PROCEEDINGS

of the

Seventh International Conference on the Ultrasonic Measurement and Imaging of Tissue Elasticity©

Lake Travis, Austin, Texas, USA
October 27 – 30, 2008

The Six National Flags That Have Flown Over Texas

Spain (1519–1685 & 1690–1821) The first European nation to claim the land that is now Texas when Cortez established a Spanish presence in Mexico, and Alonzo Alvarez de Pineda mapped the Texas coastline.

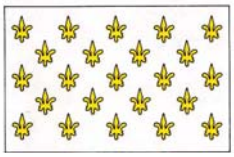

France (1685–1690) Planning to expand from French Louisiana, France planted its flag on the Texas Gulf Coast. Spanish settlements were hundreds of miles away when the first French colony, Fort St. Louis, was founded. A series of natural calamities doomed its claim.

Mexico (1821–1836) After Mexico's independence, many Hispanic pioneers went north. The Anglos from the north came and became citizens of Mexico, until Mexican General Santa Ana declared himself dictator.

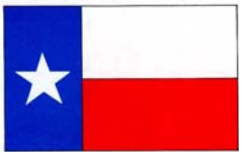

The Republic of Texas (1836–1845) Texas heritage formed in the ten years of independence. It is the birthplace of the American cowboy, the Texas Rangers. Texas joined the United States on December 29, 1845.

U.S.A. (1845–1861 & 1865–Present) Texas became the 28th star on the U.S. flag. After the Civil War reconstruction, Texas pioneers became self–reliant. The fabled Texas Longhorn, provided beef to the nation. The 20th Century found Texas's oil and technology.

Confederacy (1861–1865) When the American Civil War erupted, Texas joined the doomed South. However, Texas troops on Texas soil won the final battle of the Civil War. After the War, the great cattle–trail drives became American legends.

PROCEEDINGS

of the
Seventh International Conference
on the Ultrasonic Measurement and Imaging
of Tissue Elasticity©

Lake Travis, Austin, Texas, USA
October 27 – 30, 2008

Table of Contents

QUESTIONS OR COMMENTS ARE WELCOME AT ANY TIME AT <elasticity.conference@uth.tmc.edu>

Eighth International Conference on the Ultrasonic Measurement and Imaging of Tissue Elasticity©

Vlissingen, The Netherlands

September 14 – 17, 2009, Monday – Thursday

FOREWORD

Dear Conference Delegate:

Welcome to the 7th annual International Conference on the Ultrasonic Measurement and Imaging of Tissue Elasticity©.

The international participation in the Conference includes virtually all global entities engaged in research, development, commercialization and practice in the field. This year, as in 2005, the meeting takes place at the Lakeway Resort and Spa, which has undergone major enhancements since our last visit there.

Last year's Conference feedback was again unanimous in the desire for continuation of the tutorial series. We are pleased that Drs. Kevin Parker (USA) and Ron Daigle (USA) have agreed to present this year's exciting tutorials on the basic science and instrumentation that are involved in imaging the elastic properties of tissue. We are also continuing last year's popular format of the formal Poster Session, where each presenter has the opportunity to give a brief oral summary of his/her poster, and we thank Drs. Jeff Bamber (UK) and Marvin Doyley (USA) for their enthusiastic leadership in conducting this event.

The Tuesday evening Conference Dinner will conclude with a British Brass Band concert performed by a local Austin ensemble, the Austin Wonder Brass. The dinner and concert will take place at the Lakeway Resort and Spa's new Vistas glass pavilion overlooking Lake Travis. The closing pizza party on Thursday night will be at the Ophir's residence, which is a short car ride from the hotel.

We would like to thank all the delegates, reviewers and session chairs for their continuing support of the Conference. Special thanks are in order to our enthusiastic support staff that has worked above and beyond. Ms. Christina Andrews (USA) of the Conference Secretariat's office has handled the Conference organizational duties, correspondence and budgets; Ms. Karen Ophir (USA) volunteered to provide the strategic planning of the Conference, design the Conference's artwork, scientific program and publications, and to edit all abstracts in the Conference Proceedings; Ms. Liz Marshall (USA) has updated and greatly improved the Conference website. Mr. Yasin Jabir was instrumental in setting up and maintaining the Conference communications facilities.

The Conference is conducted under the joint auspices of the University of Rochester Center for Biomedical Ultrasound and the Ultrasonics Laboratory in the Department of Diagnostic and Interventional Imaging at the University of Texas Health Science Center at Houston. These organizations have contributed in personnel, equipment and financial support. Most funding for the Conference is derived from registration fees, and, with your continued support in abstract submissions and attendance, we are committed to improve and expand the Conference in the years to come. We appreciate your written and oral feedback that always helps us in planning for future Conferences.

We hope that you will enjoy this year's scientific and social programs as well as the Lakeway Resort and Spa and the city of Austin and beyond. Next year's Conference is planned for the Netherlands and will be hosted by Dr. Chris de Korte (NL) of the Radboud University Medical Center.

J. Ophir and K.J. Parker
Conference Organizers
Austin, Texas, October 27, 2008

CONFERENCE–AT–A–GLANCE

Seventh International Conference on the Ultrasonic Measurement and Imaging of Tissue Elasticity©
Lakeway Resort and Spa – Lake Travis, Austin, Texas, USA October 27 – 30, 2008

Monday, October 27		**10:00A – 7:30P**	
10:00A – 12:30P	**Set Up:**	Oral Presenters load presentations (CD/jump drive)	Rio Grande I
		Poster Presenters set up presentations	Rio Grande II
		Exhibitors set up exhibits	Rio Grande II
11:00A – 7:30P		Registration Desk Open	Rio Grande Foyer
12:30P – 7:30P	**Session EEX:**	Equipment Exhibit *(during breaks & Reception)*	Rio Grande II
1:30P – 3:30P	**Session TUT:**	**Tutorials**	Rio Grande I
3:30P – 4:30P		*Coffee Break*	Rio Grande Foyer
4:30P – 5:30P	**Session POS:**	**Poster Session – Live Oral Summaries**	Rio Grande I & II
5:30P – 7:30P		*Opening Dinner Reception*	Rio Grande I & II
Tuesday, October 28		**7:00A – 10:00P**	
7:00A – 8:15A		*Group Continental Breakfast*	Rio Grande Foyer
7:00A – 5:00P		Registration Desk Open	Rio Grande Foyer
8:00A – 5:00P	**Session POS:**	Posters	Rio Grande II
8:00A – 5:00P	**Session EEX:**	Equipment Exhibit	Rio Grande II
9:00A – 9:30A		*Tourist Information*	To be announced
8:15A – 8:30A		Opening Remarks	Rio Grande I
8:30A – 10:15A	**Session CAA-1:**	**Clinical and Animal Applications – I**	Rio Grande I
10:15A – 10:45A		*Coffee Break*	Rio Grande Foyer
10:45A – 12:00P	**Session MIP–1:**	**Methods for Imaging Elastic Tissue Properties – I**	Rio Grande I
12:00P – 1:30P		*Group Lunch*	Travis Restaurant
1:30P – 3:15P	**Session SIP:**	**Signal and Image Processing**	Rio Grande I
3:15P – 3:45P		*Coffee Break*	Rio Grande Foyer
3:45P – 4:45P	**Session MPT:**	**Mechanical Properties of Tissues**	Rio Grande I
7:00P – 10:00P		*Conference Dinner & Concert featuring The Austin Wonder Brass*	Vistas Ballroom
Wednesday, October 29		**7:00A – 6:00P**	
7:00A – 8:15A		*Group Continental Breakfast*	Rio Grande Foyer
7:00A – 5:00P		Registration Desk Open	Rio Grande Foyer
8:15A – 5:00P	**Session POS:**	Posters	Rio Grande II
8:15A – 5:00P	**Session EEX:**	Equipment Exhibit	Rio Grande II
8:15A – 10:00A	**Session MIP–2:**	**Methods for Imaging Elastic Tissue Properties – II**	Rio Grande I
10:00A – 10:30A		*Coffee Break*	Rio Grande Foyer
10:30A – 11:45A	**Session MMT:**	**Mechanical Measurement Techniques for Tissues**	Rio Grande I
11:45A – 1:30P		*Group Lunch*	Travis Restaurant
1:30P – 3:00P	**Session CAA–2:**	**Clinical and Animal Applications – II**	Rio Grande I
3:00P – 3:30P		*Coffee Break*	Rio Grande Foyer
3:30P – 5:00P	**Session FIP–1:**	**Forward and Inverse Problems – I**	Rio Grande I
5:00P – 6:00P		*Group Photo*	To be announced
Thursday, October 30		**7:00A – 9:00P**	
7:00A – 8:30A		*Group Continental Breakfast*	Rio Grande Foyer
7:00A – 3:30P		Registration Desk Open	Rio Grande Foyer
8:30A – 3:30P	**Session POS:**	Posters	Rio Grande II
8:30A – 3:30P	**Session EEX:**	Equipment Exhibit	Rio Grande II
8:30A – 10:00A	**Session CVE:**	**Cardiovascular Elasticity**	Rio Grande I
10:00A – 10:30A		*Coffee Break*	Rio Grande Foyer
10:30A – 11:30A	**Session FIP–2:**	**Forward and Inverse Problems – II**	Rio Grande I
11:30A – 1:15P		*Group Lunch*	Travis Restaurant
1:15P – 3:00P	**Session MIP–3:**	**Methods for Imaging Elastic Tissue Properties – III**	Rio Grande I
3:00P – 3:30P		*Coffee Break*	Rio Grande Foyer
3:30P – 4:15P	**Session INS:**	**Instrumentation**	Rio Grande I
6:00P – 9:00P		*Closing Pizza Party*	Ophir Residence

PROGRAM

Seventh International Conference
on the Ultrasonic Measurement and Imaging
of Tissue Elasticity©

Lake Travis, Austin, Texas, USA
October 27–30, 2008

Monday, October 27 10:00A – 7:30P

10:00A – 12:30P Presentation & Exhibit Set Up

All Oral Presenters load presentations onto Conference computers (CD/jump drive) Rio Grande I
Poster Presenters set up presentations Rio Grande II
Exhibitors set up exhibits Rio Grande II

11:00A – 7:30P

Registration Desk Open Rio Grande Foyer

12:30P – 1:30P 3:30P – 4:30P 5:30P – 7:30P
Session EEX: Equipment Exhibit Rio Grande II

Monday 1:30P – 3:30P
Session TUT: Tutorials

Chair: SE Salcudean, Canada *Co-Chair: L Sandrin, France* Rio Grande I

Page No.

1:30P – 2:15P

096 THE CONTINUUM OF ELASTIC RESPONSES, FROM COMPRESSION TO MRE. 22
KJ Parker[1].*
[1]University of Rochester, Rochester, NY, USA.

2:15P – 2:30P Discussion

2:30P – 3:15P

093 HIGH SPEED ULTRASOUND IMAGING USING UNFOCUSED TRANSMIT BEAMS AND PIXEL–ORIENTED PROCESSING. 23
RE Daigle[1].*
[1]Verasonics, Inc., Redmond, WA, USA.

3:15P – 3:30P Discussion

3:30P – 4:30P

COFFEE BREAK Rio Grande Foyer

Monday 4:30P – 5:30P

(Posters will be available for viewing and Coffee Break Discussion through Thursday, October 30, 3:45P)

Session POS: Poster Session – Live Oral Summaries

Chair: JC Bamber, UK *Co-Chair: MM Doyley, USA* Rio Grande II

Page No.

4:30P – 4:40P (*Live Broadcast via Internet*)

092 MR–ELASTOGRAPHY OF THE HUMAN HEART: INITIAL *IN–VIVO* RESULTS. 24
R Sinkus[1], B Robert[1], JL Gennisson[1], M Fink[1].*
[1]Laboratoire Ondes et Acoustique, ESPCI, Paris, FRANCE.

(Session POS continues on next page)

4:40P – 4:42P

003 A CLINICAL DATABASE FOR EVALUATING FREEHAND QUASISTATIC STRAIN IMAGING SYSTEMS. 25

AH Gee[1], L Chen[1], S Freeman[2], GM Treece[1], RW Prager[1], LH Berman[2].*
[1]University of Cambridge, Cambridge, England, UK; [2]Addenbrooke's Hospital, Cambridge, England, UK.

4:42P – 4:44P

011 SIMULATION OF 3D STRAIN IMAGING WITH 2D ARRAY TRANSDUCERS. 26

M Rao[1], T Varghese[1], JA Zagzebski[1].*
[1]University of Wisconsin–Madison, Madison, WI, USA.

4:44P – 4:46P

016 OPERATOR TRAINING AND PERFORMANCE DESCRIPTOR FOR PROSTATE MECHANICAL IMAGING. 27

V Egorov[1], A Sarvazyan[1].*
[1]Artann Laboratories, Trenton, NJ, USA.

4:46P – 4:48P

018 OPTICAL SKIN ELASTOGRAPHY, A CASE STUDY OF SEBORRHEIC KERATOSES. 28

J Blackann[1], Yong Zhang[1], RT Brodell[2], H Marie[1].*
[1]Youngstown State University, Youngstown, OH, USA; [2]Northeastern Ohio Universities College of Medicine, Rootstown, OH, USA.

4:48P – 4:50P

022 TRACKING ROI IN TMRI DATA USING ISO–CONTOURS OF HARMONIC PHASE. 29

T Alrefae[1].*
[1]Kuwait University, Khaldia, KUWAIT.

4:50P – 4:52P

026 VISCO–ELASTIC PROPERTIES OF *EX VIVO* AND *IN VIVO* BRAIN TISSUE BY LOW FIELD MR–ELASTOGRAPHY. 30

S Chatelin[1], J Vappou[1,2], E Breton[3], C Goetz[1,3], P Choquet[1,3], R Willinger[1], A Constantinesco[1,3].*
[1]Institut de Mécanique des Fluides et des Solides, Strasbourg, FRANCE; [2]Columbia University, New York, NY, USA; [3]Hôpital de Hautepierre, Strasbourg, FRANCE.

4:52P – 4:54P

045 DYNAMIC VISCOELASTIC PROPERTIES MEASURED BY MAGNETIC RESONANCE ELASTOGRAPHY (MRE) COMPARED TO SHEAR MODULUS MEASURED BY TRANSIENT ELASTOGRAPHY (TE). 31

J Oudry[1,2], J Vappou[2,3], R Willinger[2], P Choquet[4], L Sandrin[1], A Constantinesco[4].*
[1]Echosens, Paris, FRANCE; [2]Institut de Mécanique des Fluides et des Solides, Strasbourg, FRANCE; [3]Columbia University, New York, NY, USA; [4]Hôpital de Hautepierre, Strasbourg, FRANCE.

4:54P – 4:56P

046 CONTINUOUS WAVE DOPPLER ULTRASOUND INTERROGATION OF HARMONIC MOTION INDUCED BY FOCUSED ACOUSTIC RADIATION FORCE. 32

TZ Pavan[1], AL Baggio[1], MA Fagundes[1], AAO Carneiro[1].*
[1]Universidade de São Paulo, São Paulo, BRAZIL.

4:56P – 4:58P

060 DOPPLER IMAGE OF INCLUDED GEL PHANTOM BY MULTI–FREQUENCY VIBRATION. 33

G Marini[1], AL Baggio[1], P Nicolucci[1], JE Junior[1], AAO Carneiro[1].*
[1]Universidade de São Paulo, São Paulo, BRAZIL.

4:58P – 5:00P

076 MAGNETIC RESONANCE ELASTOGRAPHY IMAGING OF RADIATION DOSE DISTRIBUTIONS. 34

SL Vieira[1], YK Mariappan[3], JP Fernandes[1], RL Ehman[3], M Fatemi[2], AA Carneiro[1].*
[1]University of São Paulo, São Paulo, BRAZIL; [2,3]Mayo Clinic Foundation, Rochester, MN, USA.

5:00P – 5:02P

5:02P – 5:04P

5:04P – 5:06P

5:06P – 5:08P

5:08P – 5:10P

5:10P – 5:12P

(Session POS continues on next page)

(Session POS continued from previous page) Page No.

073 REAL–TIME POROELASTOGRAPHY: PHANTOM STUDIES. 44
W Khaled[1], R Zahiri–Azar[2], J Ophir[1], SE Salcudean[2].
[1]The University of Texas Health Science Center at Houston, Houston, TX, USA; [2]University of British Columbia, Vancouver, BC, CANADA.

5:12P – 5:30P **Discussion**

Monday 5:30P – 7:30P

Opening Dinner Reception *Proceedings Book Signing* Rio Grande I & II
After 7:30P *No Conference Activities*

Tuesday, October 28 7:00A – 10:00P

7:00A – 8:15A
GROUP CONTINENTAL BREAKFAST Rio Grande Foyer
7:00A – 5:00P
Registration Desk Open Rio Grande Foyer
8:00A – 5:00P **Session POS: Posters** Rio Grande II
Session EEX: Equipment Exhibit Rio Grande II
9:00A – 9:30A *Tourist Information* To Be Announced

Tuesday 8:15A – 8:30A
OPENING REMARKS
KJ Parker, J Ophir Rio Grande I

Tuesday 8:30A – 10:15A
Session CAA–1: Clinical and Animal Applications – I
Chair: W Svensson, UK *Co-Chair: W Weitzel, USA* Rio Grande I

Page No.

8:30A – 8:45A
030 MEASUREMENT OF THE MECHANICAL RESPONSE OF THE HUMAN UTERINE CERVIX. 45
M Jabareen[1], L Sultan[3], E Mazza[1], M Bauer[2], M Bajka[3], GA Holzapfel[4,5].*
[1]Swiss Federal Institute of Technology, Zurich, SWITZERLAND; [2]Medical University Graz, Graz, AUSTRIA; [3]University Hospital Zurich, Zurich, SWITZERLAND; [4]Graz University of Technology, Graz, AUSTRIA; [5]Royal Institute of Technology, Stockholm, SWEDEN.

8:45A – 9:00A
008 CLINICAL VALIDATION OF OBESE–DEDICATED PROCEDURE FOR LIVER STIFFNESS MEASUREMENT USING TRANSIENT ELASTOGRAPHY. 46
M Sasso[1], S Audière[1], V Miette[1], L Sandrin[1].*
[1]Echosens, Paris, FRANCE.

9:00A – 9:15A
015 ASSESSMENT OF THE VAGINAL WALL ELASTICITY BY MECHANICAL IMAGING. 47
V Egorov[1], HV Raalte[2], L Lipetskaia[3].*
[1]Artann Laboratories, Trenton, NJ, USA; [2]The Institute for Female Pelvic Medicine, Allentown, PA, USA; [3]St. Luke's Hospital and Health Network, Bethlehem, PA, USA.

9:15A – 9:30A
010 RELATIONSHIP BETWEEN VASCULAR COGNITIVE IMPAIRMENT AND CAROTID ATHEROSCLEROSIS. 48
T Varghese[1], BP Hermann[1], RJ Dempsey[1], H Shi[1], CC Mitchell[1], M McCormick[1], MA Kliewer[1].*
[1]University of Wisconsin–Madison, Madison, WI, USA.

Page No.

9:30A – 9:45A

032 EXAMINATION OF NONINDUCED TISSUE LESIONS WITH FREEHAND ELASTOGRAPHY: AN ANIMAL APPLICATION. 49

E Brusseau[1], J–F Déprez[1], F Duboeuf[1], F Rigout–Paulik[2], O Basset[1].*

[1]CREATIS, Université de Lyon, Villeurbanne, FRANCE; [2]Ecole Nationale Vétérinaire de Lyon, Marcy l'Etoile, FRANCE.

9:45A – 10:00A

035 A COMPARISON OF AUTOMATED AND MANUALLY DRAWN LESION BOUNDARIES FOR *IN VIVO* BREAST ULTRASOUND AND STRAIN IMAGES. 50

AM Sommer[1], A Milkowski[2], G Funka–Lea[3], GA Sisney[4], GK Hesley[5], ES Burnside[4], L Grady[3], MP Jolly[3], TJ Hall[1].*

[1]University of Wisconsin–Madison, Madison, WI, USA; [2]Siemens Medical Solutions Ultrasound Division, Issaquah, WA, USA; [3]Siemens Corporate Research, Princeton, NJ, USA; [4]Mayo Clinic, Rochester, MN, USA.

10:00A – 10:15A

042 REGIONAL ANESTHESIA GUIDANCE USING ACOUSTIC RADIATION FORCE IMAGING. 51

ML Palmeri[1], JJ Dahl[1], D MacLeod[1], S Grant[1], KR Nightingale[1].*

[1]Duke University, Durham, NC, USA.

10:15A – 10:45A

COFFEE BREAK — Rio Grande Foyer

Tuesday 10:45A – 12:00P

Session MIP–1: Methods for Imaging Elastic Tissue Properties – I

Chair: CL de Korte, The Netherlands *Co-Chair: S Aglyamov, USA* — Rio Grande I

Page No.

10:45A – 11:00A

023 HIGH QUALITY NON–INVASIVE RADIAL STRAIN ESTIMATION FOR SUPERFICIAL VESSELS USING BEAM–STEERING AND RADIAL LEAST SQUARES STRAIN ESTIMATION. 52

HHG Hansen[1], RGP Lopata[1], CL de Korte[1].*

[1]Radboud University Nijmegen Medical Center, Nijmegen, The NETHERLANDS.

11:00A – 11:15A

009 A COMPARISON OF 3D STRAIN IMAGE QUALITY USING FREEHAND 3D IMAGING AND A MECHANICALLY–SWEPT 3D PROBE. 53

RJ Housden[1], AH Gee[1], GM Treece[1], RW Prager[1], GP Berry[2], L Garcia[2], JC Bamber[2].*

[1]University of Cambridge, Cambridge, England, UK; [2]Institute of Cancer Research, Sutton, Surrey, England, UK.

11:15A – 11:30A

027 THE EFFECT OF ELASTIC CONTRAST ON ACOUSTIC RADIATION FORCE IMPULSE IMAGING AXIAL RESOLUTION. 54

MG Menon[1,2], SA McAleavey[1,2].*

[1,2]University of Rochester, Rochester, NY, USA.

11:30A – 11:45A

068 VISUALIZATION OF 3D ELASTOGRAPHY DATA. 55

R Zahiri–Azar[1], A Brant[1], SE Salcudean[1].*

[1]The University of British Columbia, Vancouver, BC, CANADA.

11:45A – 12:00P

028 FREE-SHAPE 2D KERNELS FOR IMPROVED MEASUREMENT OF ROTATIONS AND STRAINS IN SHEARING STRUCTURES. 56

RGP Lopata[1], MM Nillesen[1], HHG Hansen[1], IH Gerrits[1], JM Thijssen[1], CL de Korte[1].*

[1]Radboud University Nijmegen Medical Center, Nijmegen, The NETHERLANDS.

12:00P – 1:30P

GROUP LUNCH — Travis Restaurant

Tuesday 1:30P – 3:15P
Session SIP: Signal and Image Processing

Chair: GM Treece, UK *Co-Chair: KJ Parker, USA* Rio Grande I

Page No.

1:30P – 1:45P

004 FAST, VARIABLE SMOOTHING OF STRAIN DATA USING NONPARAMETRIC REGRESSION. 57
GM Treece[1], JE Lindop[1], AH Gee[1], RW Prager[1].*
[1]University of Cambridge, Cambridge, England, UK.

1:45P – 2:00P

043 IMPROVEMENT OF DISPLACEMENT ESTIMATION USING AUTOCORRELATION. 58
S Kim[1], S Park[1], SR Aglyamov[1], M O'Donnell[2], SY Emelianov[1].*
[1]The University of Texas at Austin, Austin, TX, USA; [2]University of Washington, Seattle, WA, USA.

2:00P – 2:15P

070 TIME–DELAY ESTIMATION USING INDIVIDUAL SAMPLE TRACKING. 59
R Zahiri–Azar[1], SE Salcudean[1].*
[1]The University of British Columbia, Vancouver, BC, CANADA.

2:15P – 2:30P

001 A MULTI–DIRECTIONAL DISPLACEMENT TRACKING ALGORITHM FOR STRAIN IMAGING. 60
L Chen[1], GM Treece[1], JE Lindop[1], AH Gee, RW Prager[1].*
[1]University of Cambridge, Cambridge, England, UK.

2:30P – 2:45P

059 A GENERALIZED SPECKLE TRACKING ALGORITHM FOR ULTRASONIC STRAIN IMAGING USING DYNAMIC PROGRAMMING TECHNIQUE. 61
J Jiang[1], TJ Hall[1].*
[1]University of Wisconsin–Madison, Madison, WI, USA.

2:45P – 3:00P

091 APPLICATION OF NON–RIGID REGISTRATION TO VALIDATE DETECTION OF PROSTATE CANCER USING THREE–DIMENSIONAL SONOELASTOGRAPHY. 62
B Castañeda[1], S Wu[1], K Hoyt[2], L Baxter[3], J Yao[3], D Pasternack[3], J Strang[3], DJ Rubens[3], KJ Parker[1].*
[1]University of Rochester, Rochester, NY, USA; [2]University of Alabama at Birmingham, Birmingham, AL, USA; [3]University of Rochester Medical Center, Rochester, NY, USA.

3:00P – 3:15P

077 PROPER POINT SPREAD FUNCTION FOR LATERAL MODULATION. 63
C Sumi[1], Y Komiya[1], S Uga[1].*
[1]Sophia University, Tokyo, JAPAN.

3:15P – 3:45P

COFFEE BREAK Rio Grande Foyer

Tuesday 3:45P – 4:45P
Session MPT: Mechanical Properties of Tissues

Chair: E Mazza, Switzerland *Co-Chair: I Sack, Germany* Rio Grande I

Page No.

3:45P – 4:00P

053 VISCOELASTIC PROPERTIES OF THE HUMAN BRAIN ANALYZED BY A NOVEL TWO–COMPARTMENT EFFECTIVE MEDIUM MODEL. 64
S Papazoglou[1], D Klatt[1], J Braun[2], I Sack[1].*
[1,2]Charité Berlin, Berlin, GERMANY.

Page No.

4:00P – 4:15P

037 MECHANICAL AND HISTOLOGICAL CHARACTERIZATION OF HUMAN FETAL MEMBRANES. 65
M Jabareen[1], J Egger[1], A Mallik[2], G Bilic[2], A Zisch[2], E Mazza[1].*
[1]Swiss Federal Institute of Technology, Zurich, SWITZERLAND; [2]University Hospital Zurich, Zurich, SWITZERLAND.

4:15P – 4:30P

007 MENSTRUAL CYCLE DEPENDENCE OF *IN–VIVO* BREAST ELASTICITY MEASURED USING ULTRASOUND INDENTATION. 66
JW Li[1], ST Chan[1], YP Huang[1], X Chen[1], YP Zheng[1,2].*
[1,2]Hong Kong Polytechnic University, Hong Kong, CHINA.

4:30P – 4:45P

067 ELASTOGRAPHIC STRAIN IMAGING OF FLUID FLOW THROUGH PERFUSED TISSUES. 67
GP Berry[1], I Rivens[1], J Civale[1], H Morris[1], J McLaughlan[1], JC Bamber[1], GR terHaar[1].*
[1]Institute of Cancer Research, Sutton, Surrey, England, UK.

4:45P – 7:00P *No Conference Activities*

Tuesday 7:00P – 10:00P

Conference Dinner & Concert *Proceedings Book Signing*

Concert: *featuring the* Austin WONDER BRASS performing traditional British Brass Band music in Austin, Texas Vistas Ballroom

Rehearsing for our concert

Tuesday 8:45P – 9:45P
Session A – INS: Acoustical Instrumentation

Chair: J Ophir, USA *Co-Chair: KJ Parker, USA* Vistas Ball Room

Page No.

8:45P – 9:00P

101 Introduction to British Brass Bands. 21
R Laguna[1].*
[1]Austin Wonder Brass, Austin, TX, USA.

Wednesday, October 29 7:00A – 6:00P

7:00A – 8:15A
GROUP CONTINENTAL BREAKFAST Rio Grande Foyer

7:00A – 5:00P
Registration Desk Open Rio Grande Foyer

8:15A – 5:00P **Session POS: Posters** Rio Grande II
Session EEX: Equipment Exhibit Rio Grande II

Wednesday 8:15A – 10:00A

Session MIP-2: Methods for Imaging Elastic Tissue Properties – II

Chair: KR Nightingale, USA *Co-Chair: E Brusseau, France* Rio Grande I

Page No.

8:15A – 8:30A

041 SHEAR MODULUS RECONSTRUCTION IN THE REGION OF EXCITATION USING ACOUSTIC RADIATION FORCE. 68

ML Palmeri[1], D Xu[1], KR Nightingale[1].*

[1]Duke University, Durham, NC, USA.

8:30A – 8:45A

033 ESTIMATING SPECTRUM VARIANCE OF ULTRASONIC SIGNAL WITH FREQUENCY SHIFT CAUSED BY THE TRANSITION BAND OF A FILTER. 69

Jian Liu[1], T Watanabe[1], N Kijima[1], M Haruta[1], Y Murayama[1], S Omata[1].*

[1]NEWCAT, Nihon University, Tamura, Koriyama, Fukushima, JAPAN.

8:45A – 9:00A

051 IS THREE–DIMENSIONAL (3D) AXIAL STRAIN IMAGING LIKELY TO BE WORTHWHILE? 70

L Garcia[1], GP Berry[1], A Woodward[2], JC Bamber[1].*

[1]Institute of Cancer Research, Sutton, Surrey, England, UK; [2]INCAT, Luton, Bedfordshire, England, UK.

9:00A – 9:15A

047 SHEAR–WAVE INDUCED RESONANCE ELASTOGRAPHY (SWIRE) OF ELLIPTICAL MECHANICAL HETEROGENEITIES. 71

E Montagnon[1], A Hadj Henni[1], C Schmitt[1], G Cloutier[1].*

[1]University of Montréal Hospital Research Center, Montréal, Québec, CANADA.

9:15A – 9:30A

072 REAL–TIME IMAGING OF BREAST TUMORS *IN VIVO* USING AXIAL AND AXIAL–SHEAR STRAIN ELASTOGRAMS: A PRELIMINARY STUDY. 72

W Khaled[1], S Chekuri[1], A Thitai Kumar[1,2], J Ophir[1], LM Mobbs[3], BS Garra[3].*

[1]The University of Texas Health Science Center at Houston, Houston, TX, USA; [2]University of Texas M.D. Anderson Cancer Center, Houston, TX, USA; [3]University of Vermont, Burlington, VT, USA.

9:30A – 9:45A

048 HARMONIC MOTION IMAGING (HMI) COMPARED TO ROTATIONAL RHEOMETRY FOR THE MEASUREMENT OF SOFT TISSUES VISCOELASTICITY. 73

J Vappou[1], C Maleke[1], J Luo[1], EE Konofagou[1].*

[1]Columbia University, New York, NY, USA.

9:45A – 10:00A

095 NON–INVASIVE ASSESSMENT OF SHEAR STRAIN IN THE ARTERIAL WALL. 74

T Idzenga[1], HHG Hansen[1], RGP Lopata[1], CL de Korte[1].*

[1]Radboud University Nijmegen Medical Center, Nijmegen, The NETHERLANDS.

10:00A – 10:30A

COFFEE BREAK Rio Grande Foyer

Wednesday 10:30A – 11:45A

Session MMT: Mechanical Measurement Techniques for Tissues

Chair: A Samani, Canada *Co-Chair: T Varghese, USA* Rio Grande I

Page No.

10:30A – 10:45A

050 MEASURING THE MECHANICAL PROPERTIES OF SOFT TISSUE OVER A WIDE FREAQUENCY RANGE BY EMPLOYING THE PRINCIPLE OF TIME TEMPERATURE SUPER–POSITION. 75

MM Doyley[1], JB Weaver[2], KD Paulsen[2].*

[1]University of Rochester, Rochester, NY, USA; [2]Dartmouth College, Hanover, NY, USA.

10:45A – 11:00A

065 ON THE ASSESSMENT OF RADIOFREQUENCY ABLATION LESION SIZE WITH ACOUSTIC RADIATION FORCE IMPULSE IMAGING. 76
SA Eyerly[1], SJ Hsu[1], GE Trahey[1,2], SH Agashe[1], Y Li[1], PD Wolf[1].*
[1]Duke University, Durham, NC, USA.

11:00A – 11:15A

020 ULTRASOUND–BASED TRANSIENT ELASTOGRAPHY COMPARED TO MAGNETIC RESONANCE ELASTOGRAPHY: A PRELIMINARY STUDY ON PHANTOMS. 77
J Oudry[1], J Chen[2], V Miette[1], K Glaser[2], L Sandrin[1], R Ehman[2].*
[1]Echosens, Paris, FRANCE; [2]Mayo Clinic, Rochester, MN, USA.

11:15A – 11:30A

006 MODELING THE TWIST MOTION OF LEFT VENTRICLE USING tMRI. 78
MD Alenezy[1], T Alrefae[2], EI Popel[1], J Shi[1], M Bilgen[3].*
[1]University of Kansas, Lawrence, KS, USA; [2]Kuwait University, Kuwait City, Kuwait; [3]Medical University of South Carolina, Charleston, SC, USA.

11:30A – 11:45A

090 *IN VIVO* INVESTIGATION OF RADIATION FORCE–INDUCED SHEAR WAVE PROPAGATION IN MYOCARDIAL TISSUE. 79
RR Bouchard[1], PD Wolf[1], SJ Hsu[1], DM Dumont[1], GE Trahey[1].*
[1]Duke University, Durham, NC, USA.

11:45A – 1:30P

GROUP LUNCH Travis Restaurant

Wednesday 1:30P – 3:00P

Session CAA–2: Clinical and Animal Applications – II

Chair: BS Garra, USA *Co-Chair: ML Palmeri, USA* Rio Grande I

1:30P – 1:45P

040 DIRECT MEASUREMENTS OF DIALYSIS FISTULA WALL STRAIN USING HIGH–RESOLUTION PHASE–SENSITIVE ULTRASOUND SPECKLE TRACKING. 80
WF Weitzel[1], K Kim[2], DW Park[1], J Hamilton[3], M O'Donnell[4], TJ Cichonski[1], JM Rubin[5].*
[1,5]University of Michigan, Ann Arbor, MI, USA; [2]University of Pittsburgh, Pittsburgh, PA, USA; [3]Pixel–Velocity Inc., Ann Arbor, MI, USA; [4]Washington University, Seattle, WA, USA.

1:45P – 2:00P

036 STRAIN VERSUS SURFACE PRESSURE FOR *IN VIVO* BREAST TISSUE. 81
AM Sommer[1], S Baker[1], LM Kiessel[1], MT Herd[1], K Nam[1], TJ Hall[1].*
[1]University of Wisconsin–Madison, Madison, WI, USA.

2:00P – 2:15P

063 TECHNICAL FEASIBILITY OF ARFI IMAGING IN THE UTERINE CERVIX. 82
M Palmeri[1], H Feltovich[2], K Nam[3], MA Kliewer[3], TJ Hall[3].*
[1]Duke University, Durham, NC, USA; [2]Minnesota Perinatal Physicians, Minneapolis, MN, USA; [3]University of Wisconsin–Madison, Madison, WI, USA.

2:15P – 2:30P

088 ACOUSTIC RADIATION FORCE IMPULSE TECHNIQUES FOR ASSESSING ELASTIC ANISOTROPY OF THE *IN VITRO* HUMAN CERVIX. 83
H Feltovich[1], TJ Hall[2], EM Hartenbach[2], JM. Harter[2], MA Kliewer[2].*
[1]Minnesota Perinatal Physicians, Minneapolis, MN, USA; [2]University of Wisconsin–Madison, Madison, WI, USA.

(Session CAA–2 continues on next page)

(Session CAA–2 continued from previous page) Page No.

2:30P – 2:45P

012 SHEAR STRAIN ELASTOGRAPHY FOR BREAST MASS DIFFERENTIATION. 84
M Rao[1], S Baker[1], AM Sommer[1], T Varghese[1], GA Sisney[1], MT Herd[1], ES Burnside[1], TJ Hall[1].*
[1]University of Wisconsin–Madison, Madison, WI, USA.

2:45P – 3:00P

056 ADVANCES AND DIFFICULTIES IN THE USE OF ULTRASOUND ELASTOGRAPHY AND INVERSE ALGORITHMS FOR GEL DOSIMETRY. 85
RA Crescenti[1], JC Bamber[1], AA Oberai[2], PE Barbone[3], JP Richter[2], C Rivas[3], NL Bush[1], S Webb[1].*
[1]Institute of Cancer Research, Sutton, Surrey, England, UK; [2]Rensselaer Polytechnic Institute, Troy, NY, USA; [3]Boston University, Boston, MA, USA.

3:00P – 3:30P

COFFEE BREAK Rio Grande Foyer

Wednesday 3:30P – 5:00P

Session FIP–1: Forward and Inverse Problems – I

Chair: A Oberai, USA *Co-Chair: S Emelianov, USA* Rio Grande I

Page No.

3:30P – 3:45P

074 NONLINEAR ELASTICITY IMAGING FOR INCOMPRESSIBLE SOLIDS. 86
S Goenzen[1], AA Oberai[1], PE Barbone[2].*
[1]Rensselaer Polytechnic Institute, Troy, NY, USA; [2]Boston University, Boston, MA, USA.

3:45P – 4:00P

021 LINEAR ELLIPTIC AND NONLINEAR LOG–ELASTOGRAPHIC PDE SOLVERS FOR SHEAR MODULUS RECOVERY FROM SINGLE FREQUENCY ELASTOGRAPHIC DATA. 87
K Lin[1], JR McLaughlin[1].*
[1]Rensselaear Polytechnic Institute, Troy, NY, USA.

4:00P – 4:15P

031 EFFICIENT BIOMECHANICAL MODELING VIA FEATURE SENSITIVITY. 88
V Mishra[1], K Suresh[1].*
[1]University of Wisconsin–Madison, Madison, WI, USA.

4:15P – 4:30P

039 A NONLINEAR MODEL FOR MECHANICAL IMAGING. 89
SR Aglyamov[1], V Egorov[2], SY Emelianov[1], A Sarvazyan[2].*
[1]University of Texas at Austin, Austin, TX, USA; [2]Artann Laboratories, Inc., Trenton, NJ, USA.

4:30P – 4:45P

057 THE LOG ELASTOGRAPHIC ALGORITHM FOR SHEAR MODULUS IMAGING USING A 2D ELASTIC SYSTEM. 90
N Zhang[1], JR McLaughlin[1].*
[1]Rensselaer Polytechnic Institute, Troy, NY, USA.

4:45P – 5:00P

062 IMPROVEMENTS IN THERMALLY–ABLATED LESION VISUALIZATION USING YOUNG'S MODULUS IMAGING. 91
J Jiang[1], C Brace[2], TJ Hall[1], T Varghese[1,3], EL Madsen[1], S Bharat[1,3], MA Hobson[1], JA Zagzebski[1], F Lee Jr.[2].*
[1,2,3]University of Wisconsin–Madison, Madison, WI, USA.

Wednesday 5:00P – 6:00P

Group Photo

TBA

After 6:00P *No Conference Activities*

Thursday, October 30 7:00A – 9:00P

7:00A – 8:30A
GROUP CONTINENTAL BREAKFAST — Rio Grande Foyer

7:00A – 3:30P
Registration Desk Open — Rio Grande Foyer

8:30A – 3:30P **Session POS: Posters** — Rio Grande II
Session EEX: Equipment Exhibit — Rio Grande II

Thursday 8:30A – 10:00A
Session CVE: Cardiovascular Elasticity

Chair: D Cosgrove, UK *Co-Chair: H Feltovich, USA* Rio Grande I

Page No.

8:30A – 8:45A

002 REAL–TIME IMAGING OF CARDIAC MECHANICAL FUNCTION USING ULTRASOUND. 92
J Hamilton[1], M O'Donnell[2], TJ Kolias[3].*
[1]Pixel Velocity Inc., Ann Arbor, MI, USA; [2]University of Washington, Seattle, WA, USA; [3]University of Michigan, Ann Arbor, MI, USA.

8:45A – 9:00A

005 THE IMPACT OF CALCIUM ON ARFI IMAGING OF ATHEROSCLEROTIC PLAQUES. 93
RH Behler[1], TC Nichols[1], EP Merricks[1], CM Gallippi[1].*
[1]The University of North Carolina at Chapel Hill, Chapel Hill, NC USA.

9:00A – 9:15A

049 PULSE WAVE IMAGING (PWI) AS A TOOL FOR THE QUANTITATIVE ASSESSMENT OF VASCULAR ELASTICITY: EVALUATION OF A QUANTITATIVE FINITE–ELEMENT MODEL AND *IN–VIVO* RESULTS IN HUMAN SUBJECTS. 94
J Vappou[1], J Luo[1], EE Konofagou[1].*
[1]Columbia University, New York, NY, USA.

9:15A – 9:30A

066 ACOUSTIC RADIATION FORCE IMPULSE IMAGING OF MYOCARDIAL PERFORMANCE, INITIAL *IN–VIVO* RESULTS. 95
SJ Hsu[1], PD Wolf[1], DM Dumont[1], RR Bouchard[1], BC Byram[1], SA Eyerly[1], Y Li[1], GE Trahey[1].*
[1]Duke University, Durham, NC, USA.

9:30A – 9:45A

075 COMPARISON OF 2D SPECKLE TRACKING AND DTI ON AN ISOLATED RABBIT HEART. 96
C Jia[1], R Olafsson[1], TJ Kolias[1], SW Huang[1], K Kim[1,2], JM Rubin[1], H Xie[3], M O'Donnell[1,4].*
[1]University of Michigan, Ann Arbor, MI, USA; [2]University of Pittsburgh, Pittsburgh, PA, USA; [3]Philips Research North America, Briarcliff Manor, NY, USA; [4]University of Washington, Seattle, WA, USA.

9:45A – 10:00A

061 ELECTROMECHANICAL WAVE PROPAGATION IN THE NORMAL AND ISCHEMIC CANINE MYOCARDIUM *IN–VIVO*. 97
J Provost[1], WN Lee[1], K Fujikura[1], EE Konofagou[1].*
[1]Columbia University, New York, NY, USA.

10:00A – 10:30A
COFFEE BREAK — Rio Grande Foyer

Thursday 10:30A – 11:30A

Session FIP–2: Forward and Inverse Problems – II

Chair: JR McLaughlin, USA *Co-Chair: T Alrefae, Kuwait* Rio Grande I

Page No.

10:30A – 10:45A

086 MULTISCALE MECHANICAL MODELING OF FLUID/SOLID MIXTURES: APPLICATIONS TO SOFT TISSUE MECHANICS. 98

R Leiderman[1], GP Berry[2], JC Bamber[2], Yixiao Zhang[3], AA Oberai[3], C Rivas[4], O Babaniyi[4], PE Barbone[4].*

[1]Federal University of Rio de Janeiro, Rio de Janeiro, BRAZIL; [2]Institute of Cancer Research, Sutton, Surrey, England, UK; [3]Rensselaer Polytechnic Institute, Troy, NY, USA; [4]Boston University, Boston, MA, USA.

10:45A – 11:00A

078 MECHANICAL SOURCE RECONSTRUCTION. 99

C Sumi[1], S Suekane[1].*

[1]Sophia University, Tokyo, JAPAN.

11:00A – 11:15A

089 SIMULATED INDENTATION OF POROELASTIC TISSUE AFFECTED BY LYMPHOEDEMA. 100

GP Berry[1], JC Bamber[1], PE Barbone[2].*

[1]Institute of Cancer Research, Sutton, Surrey, England, UK; [2]Boston University, Boston, MA, USA.

11:15A – 11:30A

094 TWO–DIMENSIONAL SHEAR WAVE SPEED AND CRAWLING WAVE SPEED RECOVERIES FROM *IN VITRO* PROSTATE DATA. 101

A Thomas[1], JR McLaughlin[1], K Lin[1].*

[1]Rensselaer Polytechnic Institute, Troy, NY, USA.

11:30A – 1:15P

GROUP LUNCH Travis Restaurant

Thursday 1:15P – 3:00P

Session MIP-3: Methods for Imaging Elastic Tissue Properties – III

Chair: TJ Hall, USA *Co-Chair: C Sumi, Japan* Rio Grande I

Page No.

1:15P – 1:30P

052 ELASTIC MODULUS RECONSTRUCTION USING A NOVEL FAST FINITE ELEMENT MODEL. 102

I Khalaji[1], K Rahemifar[2], A Samani[1].*

[1]University of Western Ontario, London, Ontario, CANADA; [2]Ryerson University, Toronto, Ontario, CANADA.

1:30P – 1:45P

054 MEASUREMENT OF TISSUE ELASTICITY USING LONGITUDINAL WAVES. 103

A Baghani[1], H Eskandari[1], SE Salcudean[1], R Rohling[1].*

[1]University of British Columbia, Vancouver, BC, CANADA.

1:45P – 2:00P

017 KRAMERS–KRONIG BASED QUALITY FACTOR FOR WAVE PROPAGATION IN TISSUE. 104

MW Urban[1], JF Greenleaf[1].*

[1]Mayo Clinic College of Medicine, Rochester, MN, USA.

2:00P – 2:15P

014 COMPARISON OF TWO METHODS FOR THE GENERATION OF SPATIALLY MODULATED ULTRASOUND RADIATION FORCES. 105

E Elegbe[1,2], SA McAleavey[1,2].*

[1,2]University of Rochester, Rochester, NY, USA.

Page No.

2:15P – 2:30P

058 PULSED MAGNETO–MOTIVE ULTRASOUND TO ASSESS VISCOELASTIC PROPERTIES OF SOFT TISSUES. 106

M Mehrmohammadi[1], SR Aglyamov[1], AB Karpiouk[1], J Oh[1], S Emelianov[1].*

[1]The University of Texas at Austin, Austin, TX, USA.

2:30P – 2:45P

069 METHODS FOR 2D SUB–SAMPLE MOTION ESTIMATION IN ULTRASOUND ECHO SIGNALS. 107

R Zahiri–Azar[1], TS Yao[1], SE Salcudean[1].*

[1]The University of British Columbia, Vancouver, BC, CANADA.

2:45P – 3:00P

071 STUDY OF THE VISCOELASTIC PROPERTIES OF NORMAL PROSTATE TISSUE USING CRAWLING WAVES: PRELIMINARY RESULTS. 108

B Castañeda[1], K Hoyt[2], T Kneezel[1], S Wu[1], J Strang[3], DJ Rubens[3], KJ Parker[1].*

[1]University of Rochester, Rochester, NY, USA; [2]University of Alabama at Birmingham, Birmingham, AL, USA; [3]University of Rochester Medical Center, Rochester, NY, USA.

3:00P – 3:30P

COFFEE BREAK — Rio Grande Foyer

Thursday 3:30P – 4:15P

Session INS: Instrumentation

Chair: V Egorov, USA — *Co-Chair: U Bae, USA* — Rio Grande I

Page No.

3:30P – 3:45P

085 TOWARDS THREE–DIMENSIONAL ACOUSTIC RADIATION FORCE IMPULSE (ARFI) IMAGING OF HUMAN PROSTATES *IN VIVO.* 109

L Zhai[1], JJ Dahl[1], KR Nightingale[1].*

[1]Duke University, Durham NC, USA.

3:45P – 4:00P

024 1D LOCAL INVERSION FOR TRANSIENT ELASTOGRAPHY OF *IN–VIVO* HUMAN LIVER. 110

Y Mofid[1], C Bastard[1,2], J Oudry[1], L Sandrin[1].*

[1]Echosens, Paris, FRANCE; [2]Université François Rabelais de Tours, Tours, FRANCE.

4:00P – 4:15P

055 FPGA–BASED REAL–TIME ULTRASOUND ELASTICITY IMAGING SYSTEM. 111

S Kim[1], S Park[1], SR Aglyamov[1], S Claffey[2], WG Scott[2], SY Emelianov[1].*

[1]The University of Texas at Austin, Austin, TX, USA; [2]WinProbe Corporation, North Palm Beach, FL, USA.

4:15P – 6:00P — *No Conference Activities*

Thursday **6:00P – 9:00P**

Closing Pizza Party

Proceedings Book Signing
Ophir Residence

Session EEX: Equipment Exhibit

Rio Grande II

Siemens Medical Solutions Ultrasound Group
Issaquah, WA, USA.

Ultrasonix Medical Corporation
Burnaby, BC, CANADA.

* *indicates Presenter*

AUTHOR INDEX

AUTHOR INDEX

The Austin Wonder Brass

under the musical direction of
Robert Laguna

AUSTIN WONDER BRASS was formed in 2005 by a group of Austin musicians to promote the enjoyment of British Brass Band music for the folks in Austin and Central Texas and to provide musicians the experience of playing this wonderful music. They have performed at the Annual Texas Community Music Festival, Sun City in Georgetown, Scholz Garten and other venues around Austin.

The brass band dates back to the early nineteenth century and England's Industrial Revolution as an outgrowth of the medieval public musicians. With increasing urbanization, employers began to finance work bands. Thus, the brass band tradition was founded. By 1860 there were over 750 brass bands in England alone.

Contests are the lifeblood of the brass band world, and rivalry has always been strong, cash prizes provide additional incentive. By the 1840s, a thriving local contest circuit had grown.

Today, two major championship events are held each year in England, the National Championship and the British Open Championship. Since 1856, the National Championship is only open to bands from England, Scotland and Wales. Since 1853, the Open Championship invites bands from all countries. Both major championships are held in the fall each year, are fiercely competitive, and it is a great honor to win either of these competitions.

Brass bands in Great Britain presently number in the thousands with many of the bands having origins prior to 1900. To this day, the bands use only non-professional musicians.

English brass bands are also popular in Japan, Australia and New Zealand; and in recent years in several European countries. Brass bands were an important part of life in nineteenth-century America. The Salvation Army was predominantly responsible for maintaining the brass band tradition in America through the 20th century. There are presently several hundred brass bands in North America, many affiliated with the North American Brass Band Association (NABBA). This returning tradition is making a valuable and unique contribution to the rich musical heritage of this country.

This evening's concert will present a taste of the traditional British Brass Band repertoire featuring styles in classical, folk song, cinematic, jazz, dance hall and popular music. Quite distinct from the American Civil War bands and, yet, more so than the New Orleans style groups, the Austin Wonder Brass' stylistic flexibility and musical optimism will be the focus of tonight's performance.

Quintet

Robert Laguna	Trumpet
Greg Kahn	Trumpet
Ted Rachofsky	Trombone
Eric White	Tuba
Stephen Kane	Horn

Band

Jason Moore	Eb Soprano Cornet
Robert Laguna	Bb Solo Cornet
Kent Stuiber	Bb Solo Cornet
Greg Kahn	Bb Solo Cornet
Philip Shanklin	Repiano Cornet
Tim Clement	2nd Bb Cornet
Pete Wilson	2nd Bb Cornet
Tom Shock	3rd Bb Cornet
Jerry Centanni	3rd Bb Cornet
Sam Acosta	Flugelhorn
Cale Montgomery	Solo Eb Tenor Horn
Charlie Schwobel	1st Eb Tenor Horn
James Barnard	1st Eb Baritone Horn
James Bland	1st Eb Baritone Horn
Ted Argos IV	1st Tenor Trombone
Guiseppe Nallagmam	2nd Tenor Trombone
Carter Cook	2nd Tenor Trombone
Ted Rachofsky	Bb Euphonium
Gordon Doig	Bass Trombone
Dan Augustine	Eb Tuba
Mike Lynch	Eb Tuba
Will Traphagan	Bb Tuba
Eric White	Bb Tuba
Jim Schwobel	Bb Tuba
Dan Wilson	Percussion I
Jack Wilds	Conductor

A detailed program will be available at the Conference Dinner in the Vistas Ballroom.
Tuesday, October 28th, 2008
Performance will start at 9:00 pm

Thanks to the American Brass Band Association for the historical information above.

ABSTRACTS

Seventh International Conference
on the Ultrasonic Measurement and Imaging
of Tissue Elasticity©

Lake Travis, Austin, Texas, USA
October 27–30, 2008

Session TUT: Tutorials Monday, October 27 1:30P – 3:30P

096 **THE CONTINUUM OF ELASTIC RESPONSES, FROM COMPRESSION TO MRE.**

KJ Parker[1]*.
[1]University of Rochester, 203 Hopeman Building, Rochester, NY, USA.

A robust variety of approaches have been proposed in the field of elastography. The experimental approaches span an impressive range from water jets that create surface forces to wide–area compression, to sinusoidal or transient shear waves. Theoretical approaches to these necessarily follow the particular conditions and excitations.

In this tutorial, we demonstrate that there is in fact a continuum of elastic behavior which relates all of the major experimental approaches. This continuum can be viewed as a function of frequency where time varying terms gradually increase their influence on the observed behavior. Although the commonality of underlying responses is significant, the particular issues of detectability, resolution, contrast and inverse solutions all shift as we move from quasi–static to high frequency excitations and responses. Examples from different approaches will be used to illustrate the continuum of elastic behavior.

Local Wave Speed Estimators

$$c = \sqrt{\frac{E}{3\rho}}$$

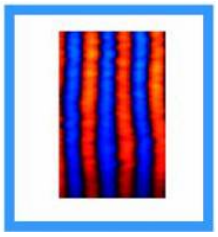

- Spatial Rate Of Phase Change (Wu et al.)
- Local Frequency Estimators (Manduca et al.)
- Arrival Time McLaughlin et al.)
- Local Autocorrelation (Hoyt et al.)
- Correlation (Castañeda et al.)

Ex Vivo Prostate Results

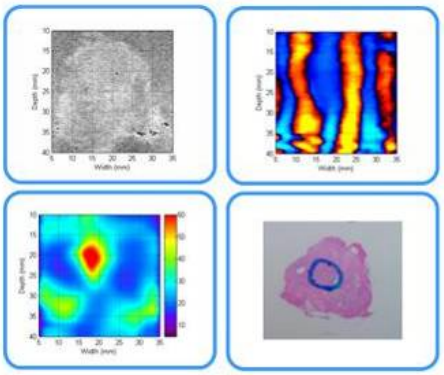

093 **HIGH SPEED ULTRASOUND IMAGING USING UNFOCUSED TRANSMIT BEAMS AND PIXEL–ORIENTED PROCESSING.**

RE Daigle[1].*
[1]Verasonics, Inc., Redmond, WA, USA.

Current ultrasound systems employ focused beams for echo imaging and Doppler applications. Composing a full image requires many transmit/receive cycles in which the focal point is moved throughout the image space. While providing lateral resolution and dynamic range benefits at the focal points, the multiple acquisition cycles limit the rate at which image frames can be produced. The use of unfocused beams for transmit (sometimes referred to as 'flash' imaging) allows insonifying large parts or all of the image space with as few as a single transmit pulse, allowing image reconstruction of the entire image space in very short time frames. This method of ultrasound acquisition can produce very high frame rates for echo and Doppler flow imaging applications, and excellent image quality can be obtained by combining information from several acquisitions.

Image reconstruction from unfocused transmit beams requires access to the received echo signals from each of the individual transducer elements and is best–performed using software processing methods. To perform these reconstructions in real–time is challenging and requires new methods of image reconstruction. A processing technique has been developed that reconstructs the signal returned from an array of points in a rectangular grid located in the 2D image space of the transducer. This technique, referred to as 'pixel–oriented processing', provides the complex signal value at each point in the array of image points, from which echo amplitude and/or Doppler phase shift information can be derived. The method reconstructs the signal only at the points of interest, using only the receive data that directly contribute to each image point. Using a single matrix operation on the selected receive data set for a given image point, the method provides the equivalent of the conventional processing operations of beamforming, signal processing and scan conversion. The efficiency of this approach allows real–time image reconstructions using only a capable commercial computing system coupled to a transmit and receive data acquisition system. Reconstruction rates as high as 50 million image points per second have been achieved using high–end desktop computers. While the pixel–oriented processing approach is ideally suited for use with unfocused transmit beams, it can also be used for conventional image scanning methods. The technique is also easily extended to 3D volume reconstructions, where the reconstruction points are voxels in the volume space of the transducer.

Applications for unfocused transmit beam acquisitions and pixel–oriented processing include the traditional ultrasound application areas, as well as a number of specialty applications. In the traditional application areas, unfocused transmit beam imaging can provide benefits such as higher frame rates for echo and Doppler flow imaging, along with improved image quality or blood velocity quantification obtained by combining multiple acquisitions. Specialty application areas include:

Elastography, where the displacements generated by induced shear waves propagating through tissue can be captured in real–time;

Vascular Imaging, where the short imaging range allows full synthetic aperture reconstructions;

and Photoacoustic Imaging, where access to individual element data allows reconstruction of internal source distributions.

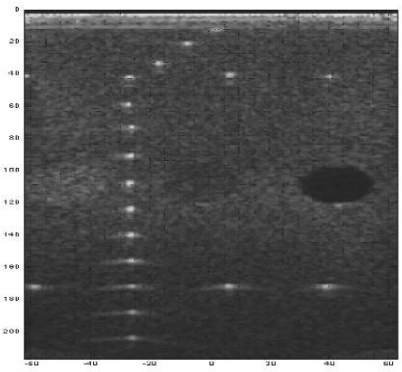

128 transmit/receive, 1 focal zone

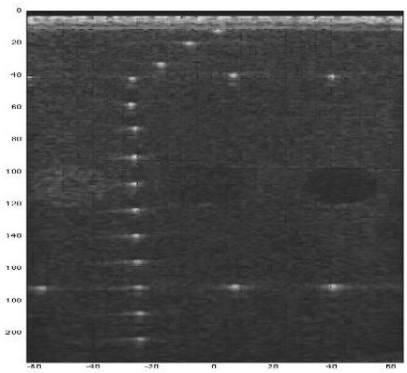

Single transmit/receive flash image

092 **MR–ELASTOGRAPHY OF THE HUMAN HEART: INITIAL *IN–VIVO* RESULTS.**

Ralph Sinkus[1], Benjamin Robert[1], Jean–Luc Gennisson[1], Mathias Fink[1].*
[1]Laboratoire Ondes et Acoustique, ESPCI, 10 rue Vauquelin, 75005 Paris, FRANCE.

Background: Information about the mechanical properties of the heart wall is of substantial interest after an infarct, for instance. Most non–invasive techniques are currently based upon strain imaging. Here, the determination of the true mechanical properties is hindered by the missing information about the stress. Dynamic MR–Elastography, which images the propagation of an externally applied steady state vibration, overcomes this limitation since both stress and strain are known.

Aims: Visualizing the propagation of low–frequency mechanical waves in the cardiac muscle.

Methods: For cardiac MRE, it is mandatory to utilize low frequency mechanical vibrations (~50Hz) which allow efficient penetration from the surface of the thorax to the heart. This contradicts the requirement to use short echo–times for cardiac MRI. We are proposing a novel MRE sequence which overcomes this limitation. It is based upon the well–known DENSE–MRI sequence which stores the magnetization in the z–direction during a mixing time in order to avoid signal loss due to T2* decay. Thus, the novelty of the new DENSE–MRE sequence lies in the fact that the MR–echo–time is disconnected from the time necessary for encoding the motion. For instance, classically a 50Hz wave requires at least 1000/50=20ms of echo–time leading to total signal loss in the cardiac muscle. Here, we use a pre–pulse of ~15ms for motion encoding which stores the magnetization mainly in the z–direction (and, thus, prevents it from decay) with a subsequent short acquisition sequence with an echo–time of ~5ms.

Results: Figure 1a shows the according anatomical image of the heart wall in short axis view, Figure 1b a snapshot of the 50Hz wave and Figure 1c the calculated speed in m/s. Results are consistent with preliminary values published using transient US–elastography [1].

Conclusions: DENSE–MRE constitutes a promising new MR–sequence capable of encoding steady–state motion at low frequencies in tissue which have short T2* values.

References:

[1] Kanai, IEEE Trans Ultrason Ferroelectr Freq Control. 2005 Nov;52(11):1931–42.

Figure 1

(a) 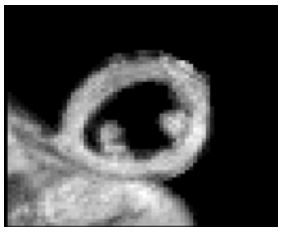

(b) 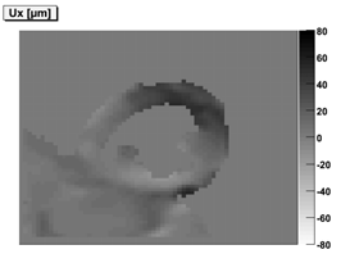

(c) 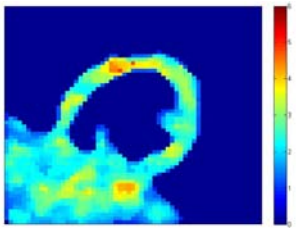

* *indicates Presenter*

003 **A CLINICAL DATABASE FOR EVALUATING FREEHAND QUASISTATIC STRAIN IMAGING SYSTEMS.**

AH Gee[1], L Chen[1], S Freeman[2], GM Treece[1], RW Prager[1], LH Berman[2].*
[1]University of Cambridge, Cambridge, England, UK; [2]Addenbrooke's Hospital, Cambridge, England, UK.

Background: Algorithms developed for quasi–static strain imaging can be evaluated using simulated, *in vitro* and *in vivo* data. Most research and development teams have ready access to the first two, but assessing strain imaging on a widely accessible, large corpus of clinically significant *in vivo* data is more problematic. There are issues related to acquiring the data with the proper ethical approval and patient consent, classifying it appropriately and disseminating the collection to the research community.

Aims: To set up a database of carefully indexed, clinical, freehand quasi–static strain data and make it available to the elastography research community.

Methods: The database comprises raw RF image sequences recorded in the Stradwin data format [1], with a simple binary file for the radio frequency (RF) samples and a plain text file for the configuration parameters. The RF samples are stored with 16–bit precision, while the sampling rate is machine specific. Each file is tagged with relevant clinical and technical information, for example:

> Sex–F; Date of scan–2007/10/24; Site–thyroid; Ultrasound diagnosis–multi-nodular goiter + dominant nodule; Biopsy–Y; Surgery–Y; Biopsy results–follicular tissue; Post–surgical histology–benign follicular adenoma; Dimensions–2D; Frames–102; Strain image quality–Good; B–scan depth–4cm; Focus–1.5cm; Probe type–Terason T3000 12L5V 7.75MHz.

The database has a web–based interface and is fully searchable using any of these fields.

Results: The database is currently populated with more than two hundred files acquired through ongoing studies into 2D and 3D freehand quasi–static strain imaging at Addenbrooke's Hospital (Cambridge, UK). Ethical approval was granted by the Cambridgeshire 3 Research Ethics Committee for the anonymized data to be disseminated to the wider research community. Patients are made aware of this at the time of obtaining informed consent. Anatomical sites currently available include head and neck, breast, testis, kidney, liver and uterus, with the forthcoming addition of intra–operative neurosurgery data obtained through collaboration with the Institute of Cancer Research and the Royal Free Hospital (London, UK).

Conclusions: The database is a potentially valuable resource for the research community.

Acknowledgements: This work was supported by Translation Award 081511/Z/06/Z from the Wellcome Trust and Research Grant EP/E030882/1 from the EPSRC.

References:

[1] http://mi.eng.cam.ac.uk/~rwp/stradwin
[2] J. E. Lindop, G. M. Treece, A. H. Gee and R. W. Prager. An intelligent interface for freehand strain imaging. Ultrasound in Medicine and Biology, in press.

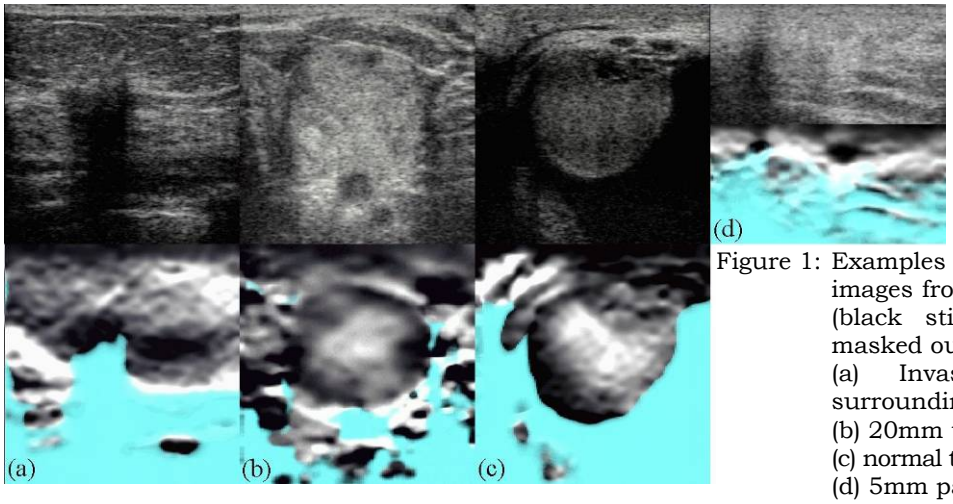

Figure 1: Examples from the database, with strain images from Stradwin's real–time algorithms (black stiff, areas of high strain noise masked out [2]).
(a) Invasive breast carcinoma with surrounding ductal carcinoma *in situ*;
(b) 20mm thyroid follicular adenoma;
(c) normal testis and epididymis with hydrocele;
(d) 5mm parotid pleomorphic adenoma.

011 **SIMULATION OF 3D STRAIN IMAGING USING 2D ARRAY TRANSDUCERS.**

M Rao[1], T Varghese[1], JA Zagzebski[1].*
University of Wisconsin–Madison, 1530 Medical Sciences Center, 1300 University Avenue, Madison, WI 53706, USA.

Background: Displacement vector and strain tensor imaging in three dimensions requires acquisition of 3D volume data in real time. Two–dimensional (2D) transducer arrays represent a promising solution for implementing real time 3D data acquisition. Previously, we described a frequency domain B–mode imaging model applicable for linear and phased array transducers [1]. In this study, we extend this model to incorporate 2D array transducers and apply it to simulate 3D strain imaging.

Aims: The aim of this study is to extend a frequency domain ultrasound simulation model to 2D array transducers and to utilize the model to generate simulated 3D strain images.

Methods: The pressure field for a 64×64 square array with element dimensions of 0.15 mm and center–to–center spacing of 0.2 mm was calculated by applying the paraxial approximation to solve the 2D Rayleigh integral for each element. We assume a rigid baffle, no apodization, a 5 MHz center frequency, and a speed of sound of 1540 m/s. A single transmit focus at 30 mm and dynamic receive focus with an F–number of 2 was utilized. The 2D array model was compared with the widely used ultrasound simulation program FIELD II, which utilizes an approximate form of the time domain impulse response function. For strain imaging, we incorporate frame–to–frame displacements using Finite Element Analysis (FEA) simulation using ANSYS software (ANSYS Inc., Canonsburg, USA). 1D, 2D and 3D motion tracking algorithms for tracking displacement vectors were compared.

Results: Discrepancies between waveforms computed using our model and FIELD II are less than 4%, regardless of the steering angle for distances greater than 2 cm (Figure 1a), yet computation times are on the order of 1/35 of that with FIELD II (Figure 1b). Modern beam–forming techniques, such as apodization, dynamic aperture, dynamic receive focusing and 3D beam steering, can also be simulated. Simulations of B–mode images provide vivid demonstrations of the ability of 2D arrays with specific imaging parameters to detect lesions of a given backscatter contrast and size. Simulated 3D strain images of the spherical inclusion phantom demonstrate that 3D tracking algorithms are required to reduce decorrelation noise induced by elevational motion when 2D array transducers are used.

Conclusions: The frequency domain approach provides an effective and feasible tool to investigate 3D strain imaging using 2D array transducers. Both the normal and shear strain tensors can be estimated for complete elastographic evaluation of lesion properties. Comparison of 3D shear strain images for bound and unbound spherical inclusion phantoms demonstrate significant differences in shear strain patterns.

Acknowledgements: This work is supported by Komen Foundation Grant BCTR0601153.

Reference:

[1] Y. Li and J. A. Zagzebski, "A frequency domain model for generating B–mode images with array transducers," IEEE Transactions On Ultrasonics Ferroelectrics and Frequency Control, vol. 46, pp. 690–699, May, 1999.

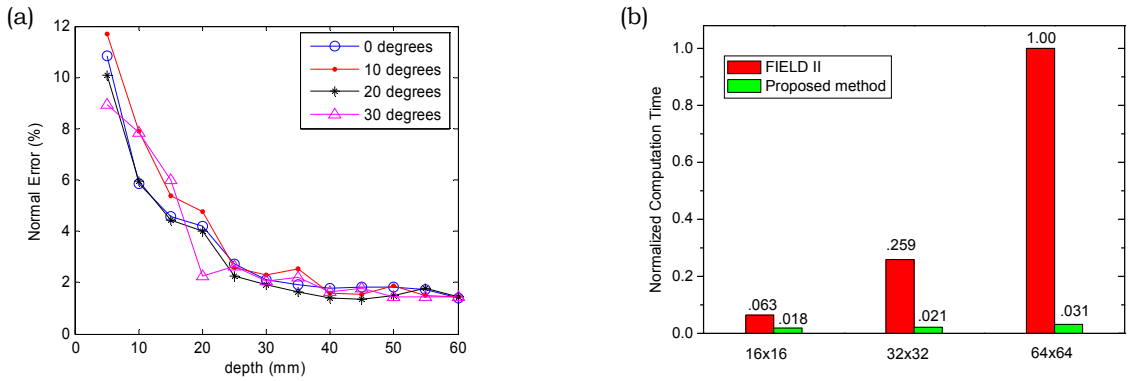

Figure1: (a) Errors between our method and FIELD II at different steering angles.
(b) Comparison of the computation time for our method and FIELD II.

* *indicates Presenter*

016 **OPERATOR TRAINING AND PERFORMANCE DESCRIPTOR FOR PROSTATE MECHANICAL IMAGING.**

Vladimir Egorov[1], Armen Sarvazyan[1].*
[1]Artann Laboratories, 1459 Lower Ferry Rd., Trenton, NJ 08618, USA.

Background: Current methods of prostate assessment include the Digital Rectal Examination (DRE), the serum Prostate Specific Antigen (PSA) blood test, TransRectal UltraSound (TRUS), computerized axial scanning tomography and endorectal magnetic resonance imaging. The most commonly employed screening techniques remain DRE and PSA, while TRUS or TRUS–guided biopsy are considered the main tools for advanced prostate cancer diagnostics. Mechanical Imaging (MI) is a new modality of medical imaging based on principles similar to those of manual palpation [1]. MI is capable of imaging and recording the sense of touch by measuring surface stress patterns using a pressure sensor array. The Prostate Mechanical Imager (PMI) is a portable PC–based device utilizing a hand–held transrectal probe with two pressure sensor arrays and an orientation tracking system. The pressure sensor array, in response to input applied pressure, produces a pressure response map analogous to that sensed by the physician's finger palpating the prostate during DRE. The composed prostate elasticity image is constructed from multiple pressure response maps using an image matching algorithm [2]. The clinical acceptance and effectiveness of PMI depends on operator skills in transrectal probe manipulation during prostate examination which must satisfy specific requirements to provide a reproducible prostate image.

Aims: The first aim of this work is to design a training setup including realistic model of male pelvic anatomy with an elastic rectum and a changeable prostate phantom mimicking variability of prostate size, elasticity and nodularity. The second aim is to develop an operator training procedure and performance descriptor to characterize the quality of prostate examination data and level of practical operator skills in prostate examination by PMI.

Methods: The MI data, including 720 examinations, were recorded for 24 prostate phantoms by 5 operators having 3 levels of training: beginning, intermediate and expert. For each examination we calculated the prostate volume, prostate baseline elasticity and elasticity contrast, maximum and average pressure over the prostate, maximum and average pressure at the sphincter, azimuth angle range, examination duration and quality of 3–D prostate image.

Results: The recorded MI data were statistically analyzed calculating average values and standard deviations for each parameter. Comparison of the calculated data sets for the 5 operators revealed correlations for the parameters with operator training level. A performance descriptor for PMI was constructed as a linear combination of the calculated parameters with an optimized set of weight factors. We found that the parameter characterizing 3–D prostate image quality must have at least a doubled weight factor in the performance descriptor. Based on this approach, we developed an operator training procedure which includes (a) training software to assist an operator in the learning process of acquiring probe manipulation skills for imaging the prostate and (b) certification software to evaluate operator skill level, calculating a score from 1 to 5 and exposing weak aspects of operator acquired PMI expertise. We stated the following additional training requirements: ability to make judgments about the PMI evaluated prostate features and recorded prostate mechanical image, ability to recognize and minimize PMI artifacts, understanding techniques in manipulating the transrectal probe to optimize the image quality.

Conclusions: Our findings demonstrate that appropriate operator training and control examinations using the designed realistic model of male pelvic anatomy may provide operator–to–operator reproducible imaging of the prostate by PMI.

Acknowledgements: This work is supported by NIH grant 5R44 CA082620–03.

References:

[1] Sarvazyan A. Mechanical imaging: a new technology for medical diagnostics. Int. J. Med. Inf. 1998; 49: 195–16.
[2] Egorov V, Ayrapetyan S, Sarvazyan A. Prostate mechanical imaging: 3–D image composition and feature calculations. IEEE Transactions on Medical Imaging 2006; 25(10): 1329–40.

018 **OPTICAL SKIN ELASTOGRAPHY, A CASE STUDY OF SEBORRHEIC KERATOSES.**

Joshua Blackann[1], Yong Zhang[1], Robert T. Brodell[2], Hazel Marie[1].*
[1]Youngstown State University, Meshell Hall, One University Plaza, Youngstown, OH, 44555, USA;
[2]Dermatology, Northeastern Ohio Universities College of Medicine, Rootstown, OH 44272, USA.

Background: Since the pioneering work of Ophir et al [1] on elasticity imaging, significant advancements have been made in both algorithms and applications. However, skin elastography has not received as much attention as in the studies of other organs, partially because that the elastic properties of skin can be obtained using more conventional biomechanical devices such as cutometers or suction chambers [2]. The biomechanical methods have drawbacks that they provide only a point–wise measurement and are invasive, hence, cannot be applied to patients with skin diseases characterized by fragility or abnormal barrier function which could lead to infection. In this paper, we present an *in vivo* imaging method (optical skin elastography) with a case study of several seborrheic keratoses in one patient.

Aims: Our aim is to develop an optical skin elastographic method that (1) is able to detect strain variations associated with the underlying tissue's biomechanical abnormalities, (2) can be applied to patients of various skin diseases and (3) is noninvasive, easy to use, and operational in most clinical settings.

Methods: There are three steps in the optical skin elastography:

(i) A high definition video camcorder is used to capture the nonrigid skin deformations;
(ii) Both horizontal and vertical motions of skin are computed using a robust optical flow algorithm;
(iii) Strain elastograms are obtained by convolving the dense motion fields with a weighted gradient filter [3]. The flow computation is usually performed using two adjacent video frames to take advantage of the small skin displacement that is required by the optical flow algorithm. However, to obtain an optimal strain elastogram, the cumulative motions between two frames of larger interval are often used.

Results: A patient with a number of seborrheic keratoses on the face and neck areas was examined. The size of seborrheic keratoses varies from less 1 mm to 10 mm in diameter. Figure 1 shows a lesion on the patient's left temple and the computed flow images and strain elastogram. This seborrheic keratosis is about 90 mm^2 in area and 2.0 mm in thickness. The patient's skin was slowly stretched to generate deformations (about 3 to 8 mm). The cumulative motions were normalized to a 0–255 grey scale, with brighter pixels for larger motions and darker pixels for smaller motions. In the strain elastogram, an area of abnormally low strain values (the dark area in Figure 1 (e)) can be clearly identified. The shape of the strain abnormality also matches well with that of the seborrheic keratosis, indicating the high sensitivity and effectiveness of the proposed method.

Conclusions: The optical skin elastography can reveal skin property abnormalities related to seborrheic keratoses. Currently, only relative property ratio can be obtained. We plan to extend the method in two aspects: (1) Acquire absolute property values using a force–deflection extensometer or a biomechanical device such as a cutometer; (2) Apply the method to patients with other skin diseases.

Acknowledgements: This work was supported by Ohio Board of Regents Research Incentive Grant #34241.

References:

[1] J. Ophir, E. I. Cespedes, H. Ponnekanti, Y. Yazdi, and X. Li, "Elastography: a quantitative method for imaging the elasticity of biological tissues", Ultrasonic Imaging, vol. 13, pp. 111–134, 1991.
[2] B. C. Murray and R. R. Wickett, "Correlations between dermal torque meter, cutometer, and dermal phase meter measurements of human skin", Skin Research and Technology, vol. 3, pp. 101–106, 1997.
[3] Y. Zhang, J. R. Sullins, D. B. Goldgof, and V. Manohar, "Computing strain elastograms of skin using an optical flow based method", 5th Inter. Conf. on Ultrasonic Measurement and Imaging of Tissue Elasticity, Utah, 2006.

(a) Original shape. (b) After deformation. (c) Horizontal flow. (d) Vertical flow. (e) Strain elastogram.

Figure 1: Sample video frames of seborrheic keratoses and the resulting optical flow images and strain elastogram.

* *indicates Presenter*

022 **TRACKING ROI IN TMRI DATA USING ISO–CONTOURS OF HARMONIC PHASE.**

T Alrefae[1].*
[1]Physics Department, Kuwait University, Khaldia, KUWAIT.

Background: Tagged magnetic resonance imaging (tMRI) has found wide–spread applications in various cardiac clinical and research areas [1–3]. The strength of this imaging modality lies in its ability to reveal regional motion of the heart wall in a set of cardiac images [1–3]. For purposes of quantification, offline algorithms are developed to track tissue motion of user–selected regions of interest (ROI). Among the most robust tracking techniques is the harmonic phase (HARP) algorithm [1,2] which utilizes phase information embedded in k–space. HARP is based on the fact that the phase angle, φ, is a material property that stays with the tissue throughout the motion. Thus, a material point located at position x_m at time t_m with an angle $\varphi(x_m,t_m)$ retains the same value for its phase angle throughout its journey to the new position of x_{m+1} at time t_{m+1}. Hence,

Equation (1) $$\varphi(x_{m+1},t_{m+1}) = \varphi(x_m,t_m)$$

To perform its tracking task, standard HARP analysis solves Equation (1) for x_{m+1} by an iterative process using numerical methods such as Newton-Raphson [1,2]. Because using numerical techniques adds to the complexity of the problem, we propose an alternative, modified HARP approach to track ROI.

Aims: The goal of this work is to develop a modified ROI tracking algorithm for tMRI data based on HARP analysis. The proposed approach utilizes image processing techniques to identify and isolate sets of points in k–space having the same value of the phase angle φ (iso–contours).

Methods: A Matlab code was developed to implement the proposed tracking method. Initially, the code executes standard HARP techniques to obtain angle images (k–space data with phase values) corresponding to vertical and horizontal motions individually (Figure 1b and 1c). Next, the code departs from standard HARP analysis by identifying iso–contours that are relevant to the user-selected ROI (Figure 1d). Thus, one ROI is associated with two iso–contours; one for the vertical motion φ_v and another for the horizontal motion φ_h. It is noteworthy that the phase values φ_v and φ_h are constants throughout the motion for a selected ROI. The location of the ROI in the first and subsequent image frames is simply identified by the intersection of φ_v and φ_h.

Results: Figure 2 shows a set of ROI successfully tracked for synthetic data undergoing deformation mimicking that observed in cardiac motion. Figure 3 shows a set of ROI successfully tracked for experimental data of a rat left ventricle undergoing systolic motion.

Conclusions: In this work, we developed a modified HARP technique that tracks user–selected ROI in tMRI data. The modified HARP technique differs from standard HARP in treating Equation 1. While standard HARP solves Equation 1 numerically using computational methods, our modified approach finds locations of constant φ by identifying iso–contours in k–space thereby simplifying the tracking process.

References:

[1] Osman, N. F., et al. IEEE Trans Med Imaging, 2000, 19(3): p. 186–202.
[2] Liu, W., et al. Magn Reson Med, 2004, 52(6): p. 1282–90.
[3] Alrefae, T., et al. *BioMedical Engineering OnLine* 2008, 7:15.

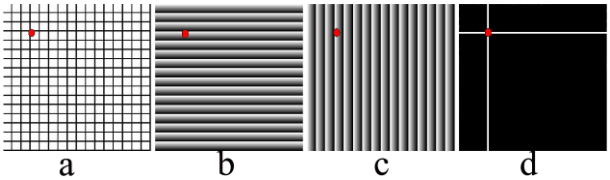

Figure 1: Computer generated grid in (a) with ROI (red). The corresponding vertical and horizontal motion angle images are shown in (b) and (c) respectively. Note that the stripe pattern in (b) and (c) are spatially analogous to grid lines in (a). Figure (d) was produced by combining Figures (b) and (c) and identifying iso–contours relevant to the ROI, namely φ_v and φ_h. The intersection of the identified iso–contours is the location of the ROI.

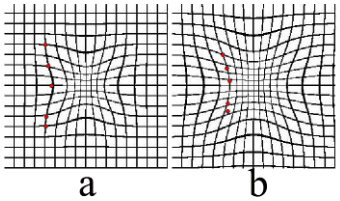

Figure 2: A set of ROI tracked for synthetic data undergoing deformation. The first and final frames are shown.

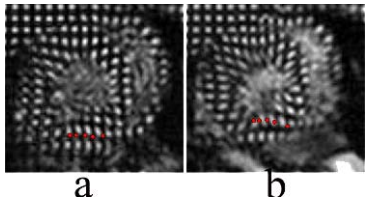

Figure 3: A set of ROI tracked for tMRI data obtained from a rat left ventricle undergoing systolic motion. The first and final frames are shown.

026 **VISCO–ELASTIC PROPERTIES OF *EX VIVO* AND *IN VIVO* BRAIN TISSUE BY LOW FIELD MR–ELASTOGRAPHY.**

S Chatelin[1], J Vappou[1,2], E Breton[3], C Goetz[1,3], P Choquet[1,3], R Willinger[1], A Constantinesco[1,3].*
[1]Institut de Mécanique des Fluides et des Solides UMR 7507 CNRS-ULP, 2 rue Boussingault, 67000 Strasbourg, FRANCE; [2]Biomedical Engineering Department, Columbia University, New York, NY, USA; [3]Service de Biophysique et Médecine Nucléaire, Hôpital de Hautepierre, Avenue Molière, 67200 Strasbourg, FRANCE.

Background: The quest for knowledge of the biomechanical behavior of brain tissue has been an essential issue for several decades [1,2]. Most of the results have been obtained through *in vitro* experimental protocols, although, recent *in vivo* studies for brain tissue have been published that use MR–Elastography (MRE) [3,4]. However, comparison between MRE and conventional mechanical techniques is missing. If available, such comparisons would allow the quantitative nature of MRE–based results to be evaluated.

Aims: We aim to validate *ex vivo* a low field MR–Elastography 2D wave inversion method for measuring the storage and loss shear moduli of brain tissue and to demonstrate that the method is practical for use *in vivo*.

Methods: In this study, we first apply a low field MRE technique compared with rotational rheometry for measuring the mechanical properties of pig brains (n=8) *ex vivo* [5]. This preliminary step is then followed by *in vivo* MRE on rat brains (n=7). The MRE tests were performed using a low field dedicated system (Bouhnik SAS, France, 0.1 Tesla) through an uni–axial modal exciter with controlled displacement, EX12 (Prodera, France), driven by a waveform generator. For comparison, mechanical rheometric shear measurements with controlled force of shear moduli were performed on an AR2000 rheometer (TA-Instruments, USA). For all MR measurements of complex wave numbers, a 2D spin echo sequence was used with inclusion of synchronized motion–sensitizing bipolar gradients. Storage (G') and loss (G") moduli were calculated from a 2D Helmoltz equation inversion algorithm [5,6] in which 8 phase steps were used for the temporal Fourier transform. Due to the limitations of both methods in terms of frequency, the *ex vivo* MRE tests were carried out from 80–140Hz with 20Hz steps, while the rheometric tests were done from 0.1-10Hz at ε=0.5% strain. For the study that deals with the *in vivo* application in rat brain, loss and storage moduli were acquired at 180Hz in 7 Sprague–Dawley rats aged from 8 to 9 weeks.

Results: MRE derived *ex vivo* pig brain values of storage (G') and loss (G") shear moduli are compared with rheometry derived values in Figure 1. It has been shown previously that rheometric results obtained from brain tissue over this frequency range can be extrapolated to higher frequencies [2]. Here such extrapolated values are found to agree well with MRE–derived values. *In vivo* maps of distributions of G' and G" in a mid–sagittal slice of a rat brain are shown in Figure 2. MRE moduli values obtained by averaging brain ROI were found to be G' = 8450 ± 410 Pa and G" = 7140 ± 610 Pa.

Conclusion: Low field MR–Elastography combined with a 2D wave inversion method provides reliable shear viscoelastic parameters in rat brain *ex vivo* and is easy to apply *in vivo*.

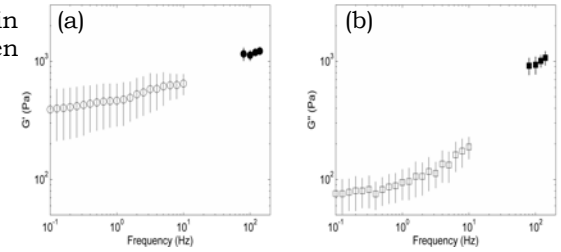

Figure 1: Storage (a) and loss (b) shear moduli versus frequency in *ex vivo* pig brain samples. Rotational rheometric data (open symbols) and MRE data (solid symbols).

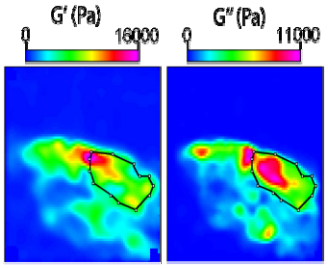

Figure 2: Distribution maps of G' and G" in a rat brain, and manually selected ROI (based on MR images of rat brain).

References:

[1] Hrapko M., et al. Biorheology 2006, vol.43, no.5, pp.313–320.
[2] Nicolle S., et al. Biorheology 2005, vol.42, no.3, pp.209–223.
[3] Sack I., et al. NMR in biomedicine 2007, DOI: 10.1002:nbm. 1189.
[4] Larrat B., et al. Proc. ISMRM 2007, p.1255.
[5] Vappou J., et al. MR Materials in Physics, Biology & Medicine 2007, 20: pp.273–278.
[6] Oliphant T.E., et al. Magnetic Resonance in Medicine 2001, 45(2):299–310.

* *indicates Presenter*

045 **DYNAMIC VISCOELASTIC PROPERTIES MEASURED BY MAGNETIC RESONANCE ELASTOGRAPHY (MRE) COMPARED TO SHEAR MODULUS MEASURED BY TRANSIENT ELASTOGRAPHY (TE).**

J Oudry[1,2], J Vappou[2,3], R Willinger[2], P Choquet[4], L Sandrin[1], A Constantinesco[4].*

[1]Echosens, Research and Development Department, 153 avenue d' Italie, 75013 Paris, FRANCE; [2]Institut de Mécanique des Fluides et des Solides, UMR7507, 2 rue Boussingault 67000 Strasbourg, FRANCE; [3]Biomedical Engineering Department, Columbia University, New York, NY, USA; [4]Service de Biophysique et Médicine Nucléaire, Hôpital de Hautepierre, Avenue Molière, 67098 Strasbourg, FRANCE.

Background: Information is missing in the literature concerning direct comparison between Ultrasound–based Elastography methods and Magnetic Resonance Elastography (MRE), while such methods are being increasingly used to estimate soft tissue stiffness.

Aims: This study aims to compare the shear modulus, G_{TE}, obtained by Transient Elastography (TE), an ultrasound–based elastography method, with the viscoelastic shear moduli (storage modulus, G'_{MRE}, and loss modulus, G''_{MRE}) obtained by MRE. This comparison is performed on the same gels in a common frequency range.

Methods: Comparison experiments were performed on 4 phantoms formed from a mixture of Styrene/Ethylene–Butylene/Styrene copolymer and mineral oil, and from additives for acoustic scattering [1]. Copolymer concentration varied between 3% and 8% of the oil mass. Gels were cylindrically shaped (8.5cm diameter, 4.5cm height). MRE experiments were performed on a low–field 0.1T magnet using a 2D spin–echo sequence including square shaped motion–sensitizing gradients. A rectangular actuator connected to a modal exciter (EX12, Prodera, France) was used to generate plane shear waves inside the gel. Shear storage, G', and loss, G", moduli were calculated from the wavelength and attenuation of the propagating plane shear wave under the assumption of homogeneity of the medium [2]. TE uses a pulse with a central frequency that can be chosen, i.e., a short duration wave train is applied as an impulse. Therefore, our TE experiments were carried out on the same gels within the 60–120Hz frequency range in order to allow direct comparison. Shear modulus, G_{TE}, was calculated from the shear wave phase velocity c_S as $G_{TE}=\rho\,(c_S)^2$, ρ being the density.

Results: For the four gels tested, the shear modulus measured by TE, G_{TE} was found to be close to the shear modulus obtained by MRE, $G_{MRE}=\sqrt{(G'^2+G''^2)}$, with an averaged relative difference of 23%. G_{TE} was also found to be in good agreement with G'_{MRE} with an averaged relative difference of 25%. This is essentially due to the fact that these gels were considerably more elastic than viscous in the considered frequency range.

Conclusions: This study compared directly TE and MRE in a common frequency range. The same MRE method was previously validated by comparing it with rheometry for the quantitative assessment of viscoelastic properties of soft homogeneous media [2]. Therefore, the good agreement found between TE and MRE on gels demonstrates the quantitative nature of TE under the assumption of incompressibility and homogeneity, and where viscous damping is small. Further research concerns the measurement of viscous losses by TE in order to compare the storage and loss moduli obtained by both methods, and the extension of this study to heterogeneous structures.

Acknowledgements: This study was partially supported by the French National Department of Research and Education.

References:

[1] Oudry et al., New Copolymer–in–oil phantom materials for Elastography, 5th International Conference on the Ultrasonic Measurement and Imaging of Tissue Elasticity, 2006.

[2] Vappou et al., Dynamic viscoelastic shear properties of soft matter by MRE using a low–field dedicated system, Journal of Rheology, 50: 531–541, 2006.

046 **CONTINUOUS WAVE DOPPLER ULTRASOUND INTERROGATION OF HARMONIC MOTION INDUCED BY FOCUSED ACOUSTIC RADIATION FORCE.**

Theo Z. Pavan[1], Andre L. Baggio[1], Marden A. Fagundes[1] and Antonio A. O. Carneiro[1].*
[1]Universidade de São Paulo, Av Bandeirantes 3900, Ribeirão Preto, São Paulo, BRAZIL.

Background: Several ultrasound elasticity imaging systems were developed in the last few years. Some of them employ acoustic radiation force as a means of internally pushing the tissue. Vibro–acoustography and Harmonic Motion Imaging (HMI) make use of Amplitude Modulated (AM) ultrasound force in order to vibrate a target [1,2]. In HMI, this vibration is promoted by a focused single element transducer, and the movement is detected through a mono–channel pulsed ultrasound [2]. In Vibro–acoustography, a confocal ultrasound transducer with two elements is employed. The ultrasound beams interact in the focal zone producing an AM force [1]. Usually the response is measured through a hydrophone [1]. However, the detection of the vibration using pulsed ultrasound is reported [4]. Continuous wave Doppler ultrasound could be an alternative to detect the vibration. This apparatus is easily found, and the response is fast since the echo is electronically processed.

Aims: To evaluate the performance of a system where a harmonic motion was induced by a modulated focused radiation force and where this movement at the focal point was measured using continuous wave Doppler ultrasound.

Methods: In the present work, the acoustic force was induced in the same way as found in Vibro–acoustography [1]. The amplitude and phase of the movement depends on the mechanical properties of the medium and were detected using a conventional continuous wave ultrasound Doppler system in which one plane ceramic is used to emit acoustic waves, another is used to detect the echoes, and the velocity and direction of induced motion is estimated by quadrature frequency demodulation of the echo signal [5]. The confocal and Doppler transducers were fixed to a three axes motorized system placed over an acoustic tank. The amplitude of the Doppler signal was recorded through a Lock–in amplifier. In order to evaluate the resolution of the method a stainless steel spherical target with diameter of 0.66 mm was fixed to a thin latex membrane. To obtain an image this sample was scanned, and the frequency of modulation adopted was 600Hz. The profile result was then compared to the PSF developed for the Vibro–acoustography system [1].

Results: Figure 1 shows the image obtained of the sphere. Figure 2 shows the experimental (solid line) and simulated (dashed line) 1D PSF of the measurement system. The FHWM of the experimental PSF was 0.46mm.

Figure 1: Image of a stainless steel sphere, 0.66 mm diameter.

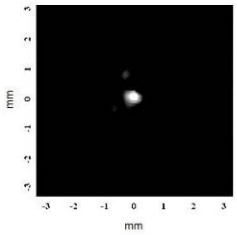

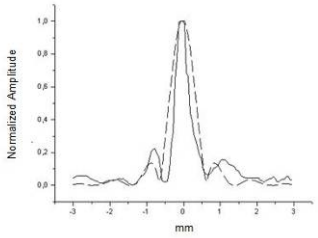

Figure 2: The experimental profile (solid line) and the theoretical point spread function of the system (dashed line) are shown.

Conclusions: The system was found to be capable of detecting vibration induced in steel spheres (embedded on a latex sheet) by a modulated acoustic radiation force. The next steps of this research are: development of a theoretical PFS taking into account both Doppler and confocal beans, and implement a pulsed tone burst excitation.

Acknowledgements: Brazilian foundations CAPES, CNPq and FAPESP.

References:

[1] M. Fatemi and J. F. Greenleaf, Vibro–acoustography: An imaging modality based on ultrasound–stimulated acoustic emission. Proceedings of the National Academy of Sciences of the United States of America 1999; 96, 6603–6608.
[2] Konofagou EE, Hynynen K. Localized harmonic motion imaging: theory, simulations and experiments, Ultrasound Med Biol 2003; 29, 1405–13.
[3] M. W. Urban, M. Bernal and J. F. Greenleaf, Phase aberration correction using ultrasound radiation force and vibrometry optimization. IEEE Transactions on Ultrasonics Ferroelectrics and Frequency Control 2007; 54, 1142–1153.
[4] Kannath A, Dewhurst RJ. Real–time measurement of acoustic field displacements using ultrasonic interferometry. Measurement Science & Technology 2004;15:N59–N66.

** indicates Presenter*

060 **DOPPLER IMAGE OF INCLUDED GEL PHANTOM BY MULTI–FREQUENCY VIBRATION.**

Gislaine Marini[1], André L. Baggio[1], Patrícia Nicolucci[1], Jorge E Junior[1], Antonio Adilton O Carneiro[1].*
[1]Universidade de São Paulo, Av Bandeirantes 3900, Ribeirão Preto, São Paulo, BRAZIL.

Background: Elastography or elasticity imaging is a new imaging modality where elastic tissue parameters related to the structural organization of normal and pathological tissues are imaged [1]. Both static and dynamic techniques have been utilized for measuring tissue elastic properties. In quasi–static elastography, radiofrequency (RF) signals acquired before and after a small amount of compression are compared. Dynamic methods, on the other hand, may image local vibrations within tissues or structures induced by externally applied oscillations using transducers or acoustic radiation force at low frequencies [2,3]. When an inhomogeneous material is vibrating with different frequencies, the velocity and amplitude of vibration in the sample will change with the local stiffness of the sample.

Aims: This work provides a new methodology to generate a Color–Flux Doppler image from soft tissue by externally dependent–frequency mechanical vibration.

Methods: In this work, the contrast of the image is related to the difference of stiffness in the internal structures of tissues. The Color Doppler image of the tissue is acquired by applying an external dynamic vibration which is an electromagnetic force with frequency ranging from 20–400Hz. The validation of the method is performed in a cubic phantom with cylindrical inclusions of different stiffness. The vibration is applied using a permanent magnet as a mechanical piston placed on the sample, and an oscillating magnetic field generated by a circular coil fixed in the surroundings and uncoupled from the magnet. The ultrasound images are obtained by a GE Logiq-Book ultrasound machine, using the Doppler color flux mode.

Results: We observed that the contrast of the Doppler image between the inclusion and the surrounding tissue changes with the vibration frequency and the stiffness of the inclusion. Figure 1 shows a series of color flux images acquired in a phantom with an inclusion for different vibration frequencies. The phantom was prepared with 12% pork gelatin Bloom 250. The inclusion was made with the same background material, but with a larger concentration so that it is 3 times harder than the surrounding medium.

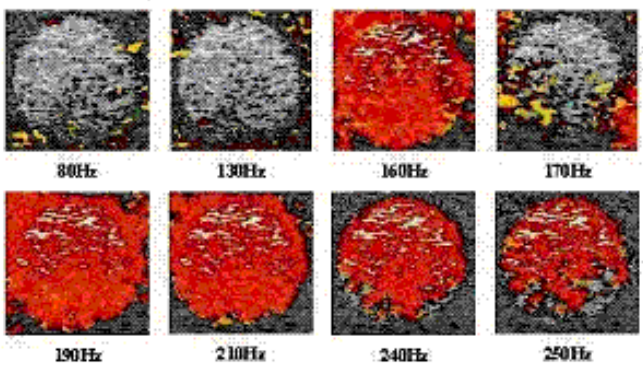

Figure 1: Color Doppler and B–mode images obtained during mechanical vibration of a phantom with a hard inclusion.

Conclusions: This study shows potential as complementary tool in clinical diagnosis of lesions in soft tissues, making use of equipment and image modalities used routinely in the clinic. The range of vibration frequencies in the internal structure of biological tissue can be applied using mechanical oscillator external to the body. Although we have evaluated the map of velocity of the internal structure in the tissue by color flux image, we can also acquire an RF map using a high frequency sampling and evaluating the displacement and deformation map.

Acknowledgements: This work was financially supported by CAPES, FAPESP and the University of São Paulo.

References:

[1] Ophir J, et al., "Elastography: ultrasonic estimation and imaging of the elastic properties of tissues", Proc Inst. Mech Engrs 213: 203–233, 1999.
[2] Nightingale KR et al. On the feasibility of remote palpation using acoustic radiation force. Journal of the Acoustical Society of America 110 (1): 625–634, 2001.
[3] Fatemi M and Greenleaf JF (1998) Ultrasound–stimulated vibro–acoustic spectrography. Science 280 (5360):82–85.

076 **MAGNETIC RESONANCE ELASTOGRAPHY IMAGING OF RADIATION DOSE DISTRIBUTIONS.**

SL Vieira[1], YK Mariappan[3], JP Fernandes[1], RL Ehman[3], M Fatemi[2], AAO Carneiro[1].*
[1]Physics and Mathematics Department, University of São Paulo, Ribeirão Preto, São Paulo, BRAZIL; [2]Ultrasound Research Laboratory, [3]Radiology Department, Mayo Clinic Foundation, Rochester, MN, USA.

Background: This work presents the Magnetic Resonance Elastography (MRE) as new technique to estimate the stiffness of irradiated gel dosimeter. Phase contrast based on measurement of small cyclic displacements was performed in a tissue–like medium which was mechanically exited by shear waves [1]. The correlation between dose distribution and the changes of shear stiffness in polymer gel dosimeters was validated using Magnetic Resonance Relaxometry (MRR) technique [2].

Aims: To investigate the feasibility of MR Elastography to evaluate dose distribution and the changes of mechanical properties (shear stiffness) in irradiated polymer gel dosimeters.

Methods: The phantoms were irradiated with 10 and 40 Gray using a 1.17 MeV radiation therapy unit. The field size in the surface of the phantom was 4 × 4 cm^2 (SSD = 80 cm). All samples were irradiated employing parallel–opposed fields to guarantee dose distribution homogeneity. The MRE data and the MRR data were acquired using a gradient–echo MRE sequence and a conventional single–spin–echo sequence, respectively on a 1.5 T GE Sigma scanner (GE Medical Systems, Milwaukee, WI, USA). The elastograms use the following imaging parameters: for two–dimensional (2D) sequences, TR: 10–300 ms; TE: 10–60 ms; acquisition time: 20–120 s; flip angle: 10–60. The number of gradient pulses used was from 2–10 cycles, and the shear waves were applied with a frequency range of 200–300 Hz to the top surface of a phantom via an actuator coil. The protocol of MRR imaging included T2–weighted transversal images obtained by a single–spin–echo sequence with echo time (TE) of 20 and 100 ms and long repetition time (TR = 4,000 ms).

Results: In Figure 1, the top and on the bottom rows correspond to a 10 and 40 Gy irradiated phantom, respectively. The isodose maps (left images), obtained from a calibrated relaxometry protocol, show the distribution of dose in the irradiated area. The center images show the displacement maps (wave offset) obtained from MRE protocol. The difference of frequency of the mechanical wave propagating into the phantom due the difference of irradiated dose is clearly seen. The shear stiffness estimated (elastograms) from the displacement maps are shown on the right of Figure 1.

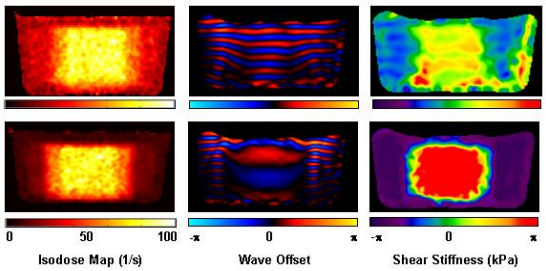

Figure 1: The isodose maps (left), displacements map or wave offset (center) and the elastograms (right).

Conclusions: Magnetic Resonance Elastography has the potential to display dose distributions. Gel dosimeters are being used for such measurements, where dose information can be obtained in spatial 3D volume with high spatial resolution. However, one important issue is standardizing a calibrating protocol to be used in different scanners; that is imperative to allow the use of MRI as a quantitative tool. A system based on polymer dosimeter gel can be used to evaluate the dose delivered by a treatment unit into the planned target volume. The results showed that MRE elasto–dosimetry could be used to evaluate complicated spatial dose distribution gel. The technique has possible applications in Stereotactic Radiosurgery and Intensity Modulated Radiation Therapy (IMRT) dosimetry gel. Elastograms from irradiation patterns, including high dose regions, could be visualized.

Acknowledgements: We gratefully acknowledge to Brazilian agencies of research: CNPq, CAPES and FAPESP for the financial support provided.

References:

[1] R Muthupillai, et al., Magnetic resonance elastography by direct visualization of propagating acoustic strain waves. Science, vol. 269: 1854–1857, 1995.
[2] AA Carneiro, GR Vilela, DB Araujo, and O Baffa. MRI Relaxometry: Methods and applications. Brazilian Journal of Physics, vol. 36, no 1A, March, 2006.

* *indicates Presenter*

064 **CALIBRATION OF THE VIBRATION AMPLITUDE MEASURED BY A SONOELASTOGRAPHIC SYSTEM.**

Benjamin Castañeda[1], Shuang Wu[1], Kenneth Hoyt[2], John Strang[3], Deborah J. Rubens[3] and Kevin J. Parker[1].*

[1]University of Rochester, 206 Hopeman Building, Rochester, NY, USA; [2]University of Alabama at Birmingham, 817 Boshell Building, 1808 7th Avenue South, Birmingham, AL, USA; [3]University of Rochester Medical Center, 601 Elmwood Ave., Rochester, NY, USA.

Background: Sonoelastography visualizes the relative stiffness of the tissue by displaying qualitative images representing the amplitude of vibration generated by an external mechanical source. The estimation of the amplitude is performed using Doppler ultrasound (US). It has been previously demonstrated that using specially designed wall filters, the sonoelastographic system can be sensitive enough to measure low–amplitude vibrations [1]. A systematic experimental study, with comparison against simulations, is given in this presentation.

Aims: This work aims to establish a relationship between the intensity values displayed by a sonoelastographic system and the actual vibration amplitude. It also investigates the effect of the wall filter (WF) and pulse repetition frequency (PRF) parameters of the system on the measurement of the displacements.

Methods: Simulations of the Doppler US signal received from a vibrating point–scatterer were made to determine the expected response of the sonoelastographic system. The simulations were corroborated with experimental results. An US transducer (M12L, GE Healthcare, Milwaukee, WI, USA) was vibrated in a sinusoidal fashion by attaching it to a piston (Model 2706, Brüel & Kjaer, Naerum, Denmark) driven by an amplifier (Model 2706, Brüel & Kjaer, Naerum, Denmark) and controlled by a function generator (Model 3511A Pragmatic Instruments, San Diego, CA, USA). A circular phantom (10cm in diameter, 10cm in depth, made of 10% pork gelatin) was located inside a container filled with water. The US transducer was positioned on top of the phantom in contact with the water but not with the phantom. A calibrated accelerometer (Model 13200B, Summit Instruments, Akron, OH, USA) was attached to the transducer. The output of the accelerometer was connected to an oscilloscope (TDS2000B, Tektronix, Richardson, TX, USA) where the amplitude of the acceleration was measured and converted to displacement. The experiment was repeated for three different combinations of WF settings ([0.55 –0.45], [0.54 –0.46], [0.525 –0.475]), PRF settings (480, 600 and 740Hz) and vibration frequencies (100, 150 and 200Hz).

Results: Experimental results agree with the point–scatterer simulations. An example of a comparison between the simulation (blue) and experimental results (green) is shown in Figure 1. A WF with higher attenuation of low frequencies sensitizes the system towards the lower vibration amplitudes but increases the noise level. PRF determines the bulk range of vibrations that can be measured.

Conclusions: WF and PRF parameters in the sonoelastographic imaging system can be set to measure a wide range of vibration amplitudes. In particular, the combination of a WF with high attenuation of low frequencies and a low PRF enables the system to measure low–amplitude vibrations (<2 μm).

Acknowledgements: This study was partly supported by NIH grant 5 RO1 AG016317–07.

References:

[1] Taylor LS, Porter BC, Rubens DJ, and Parker KJ, Three–Dimensional Sonoelastography: Principles and Practices, Phys. Med. Biol., Vol. 45, No. 6, pp. 1477–94, June, 2000.

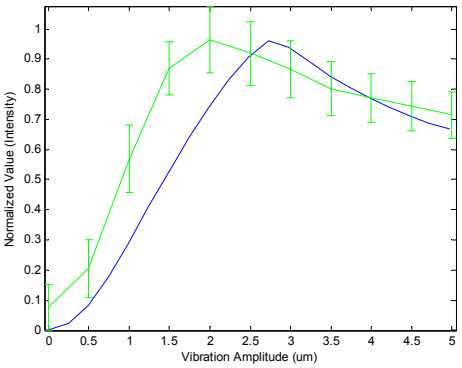

Figure 1: Comparison between the point–scatterer simulation (blue) and the experimental results (green) at vibration frequency = 200Hz, PRF = 600Hz and WF = [0.525 –0.475].

079 **THERMAL PROPERTY RECONSTRUCTION – RECONSTRUCTION OF THERMAL SOURCE AND PERFUSION.**

C. Sumi[1], T. Uchida[1], A. Minami[1], H. Kanada[1], Y. Takanashi[1].*
[1]Sophia University, 7–1, Kioicho, Chiyodaku, Tokyo 102–8554, JAPAN.

Background: A robust non–invasive technique for reconstructing the thermal properties, i.e., thermal conductivity, thermal capacity and thermal diffusivity, of living tissues and thermal quantities, e.g., thermal source/sink and perfusion for diagnosis, and monitoring and planning thermal treatments such as a high–intensity focused ultrasound (HIFU) and interstitial radiofrequency, RF, or microwave electromagnetic coagulation therapy have been reported by us [1]. Perfusion is also a measure for differentiating tumor progress. Internal tissue temperature distributions can be measured using ultrasonic imaging [2] or magnetic resonance imaging. Previously, we dealt with the case of performing reconstruction after stopping heating and perfusion [3]. That is, only the thermal properties were reconstructed. However, the region of interest (ROI) may include the thermal source. In addition, the perfusion cannot always be stopped. In such cases, by increasing the independent temperature data, the thermal source and perfusion can also be reconstructed [1]. If possible, typical property values are also used.

Aims: The feasibility of the reconstructions of thermal source and perfusion is verified by simulations.

Methods: A cubic tissue phantom (50.0mm sides) was simulated. It contained a spherical inclusion (dia = 6.0mm), which had a conductivity and a specific heat twice those of the surrounding medium, i.e., 1.0 vs 0.5W/(mK), and 8,400 vs 4,200J/(Kkg) (typical values similar to those of water; density, 1,000kg/m^3). A cubic ROI (20.0mm sides) was set at the center of the phantom with a spherical inclusion (Figure 1a). The phantom has a uniform temperature of 36.0. The time series of temperature distribution was calculated by the successive over–relaxation (SOR) method. As shown in Figure 1a, a spherical heat source Q of 0.5 or 1.0 W (dia = 6.0mm) was set at t = 0 sec such that it overlaps with the inclusion. The three sets of sequential temperatures shown in Table 1 were used. Next, the spherical heat source was changed by perfusion. Pennes' model was used (blood temperature, 36.0; specific heat, *cb*, 3,770 J/Kkg). The temperature of one surface of the phantom was increased by 6.0. For each perfusion coefficients w = 0.1, 0.3, 0.5, 1, 5, 10 kg/m^{3}K, the reconstructions of wcb were performed. Figure 1b shows the time courses of temperatures at the position 3 shown in Figure 1a. Before stopping the perfusion (t = 4,000 sec), three sets of sequential temperatures at t = 500, 1,000 and 1,500 sec were used, whereas after stopping the perfusion, two sets of sequential temperatures at t = 4,200 and 4,900 sec were used.

Results: The means and SDs of the reconstructions evaluated in the inclusion are also shown in Table 1. As shown, the thermal sources are accurately reconstructed (see also a reconstruction, Figure 2a). Figure 2 also shows the reconstructions of wcb. As shown, for $w \le 0.5$ kg/m^{3}K, the reconstructions were unstable. After stopping the perfusion, thermal conductivity was stably reconstructed regardless of w (omitted). However, when $w \le 0.5$ kg/m^{3}K, the capacity reconstruction was unstable (omitted).

Conclusions: For thermal source reconstruction, because the temperature change did not yet occur at small t in the peripheral region of the ROI, the reconstructions were unstable. In addition, a large Q could not be used since the temperature of the heated region rapidly reached to 100.0. To complete the thermal treatment in a short time, the temperature data after stopping heating should also be used. Furthermore, although it's impossible to express the perfusion of a larger blood vessel by using Pennes' model, it was suggested that the perfusion reconstruction would be effective for a large blood flow. It was also confirmed that it was difficult to reconstruct the perfusion of a small vessel.

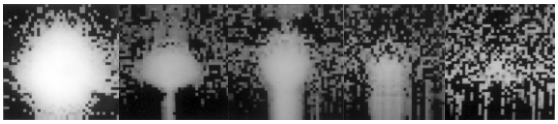

(a) (b) (c) (d) (e)

Figure 2: Reconstructions of (a) Q = 0.5 W using 299.8, 199.8 and 99.8 sec data, and wcb when w = (b) 10, (c) 5, (d) 1, (e) 0.5 kg/m^{3}K.

Q (w), (W/m^3)	Times (s)	Q (W/m^3)
0.5, 8.85e6	299.8, 199.8, 99.8	9.76e6 (2.26e6)
0.5, 8.85e6	399.8, 299.8, 199.8	8.42e6 (2.26e6)
1.0, 17.69e6	81.8, 71.8, 61.8	16.32e6 (2.29e6)

Table 1: Means and SDs of the reconstructed sources.

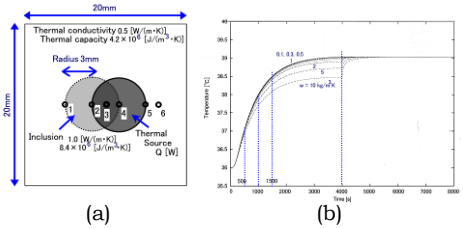

(a) (b)

Figure 1: (a) Configurations. (b) Temperatures at position 3 (perfusion).

References:

[1] C. Sumi et al., Phys Med Biol, 52, 2845, 2007.
[2] C. Sumi et al., Jpn J Appl Phys, 46(7b), 4790, 2007.
[3] C. Sumi et al., Acoustical Imaging, 29, 2007.

* *indicates Presenter*

080 **SHEAR MODULUS MICROSCOPY USING DISPLACEMENT VECTOR MEASUREMENT.**

C. Sumi[1], Y. Saijo[2].*
[1]Sophia University, 7–1, Kioicho, Chiyodaku, Tokyo 102–8554, JAPAN; [2]Tohoku University, Aobaku, Sendai, Miyagi 980–8579, JAPAN.

Background: We have been developing several strain tensor measurement methods [1,2] and several shear modulus reconstruction methods [3–5] for the differential diagnosis of diseases. Recently, we also started other applications of the shear modulus reconstructions (e.g., on normal physical motions of arms, legs, etc [6], and cultured tissues, iPS). In this context, we started to develop a shear modulus microscope using 100 MHz ultrasound (US).

For instance, the microscope can be used for evaluation of the skin shear moduli (i.e., those of the epidermis, dermis, subcutaneous tissue) of various body parts, e.g., face, arm, leg, abdomen, breast. Last year, the preliminary measurement results of the aging effect on a facial skin obtained using 7.5 MHz US were reported [7]. Such a low frequency macroscopic and high frequency microscopic evaluations will lead to developments of various techniques (e.g., using medicines, cosmetics, equipment) for skin care and culture (e.g., dry, cracked or oily skin, sun burn, etc.) as well as diagnosis of diseases.

The ability to perform a 3–dimensional (3D) displacement vector measurement enables our developed shear modulus reconstruction methods to deal with an arbitrary mechanical source (e.g., gravity, and internal, external, spontaneous or extracorporeal ones). Thus, for skin, normal and artificial deformations in an arbitrary direction can be dealt with. Various clinical applications can also be considered (e.g., cultured cardiac tissue).

Aims: The prototype microscope (Honda Electronics Co., Ltd, Japan) is used to verify the potential for accurately measuring the infinitesimal displacements and strains.

Methods: To acquire 3D echo data, the specimen is mechanically scanned using a single element transducer (100 MHz, diameter, 2.4 mm; focus, 3.2 mm). As shown in Figure 1, the focus position can also be controlled in the axial direction. That is, if necessary during the echo data acquisition, the focus position is also changed in the axial direction. The specimen is a sponge for skin culture (Johnson & Johnson). For instance, the tension was applied such that the specimen elongates in the lateral direction as shown in Figure 1. Because any lateral modulations [8] were not performed here, only the axial displacement and strain could be measured accurately [6].

Results: The axial displacement less than 0.1 μm could be accurately measured. Probably, 1×10^{-3} μm can also be measured.

Conclusions: By improving the prototype microscope, the achievable accuracy will be clarified. A proper lateral modulation will also be used to realize an accurate 3D shear modulus reconstruction. By shortening the data acquisition time, a viscous shear modulus and a micro flow parameter can also be measured. That is, a viscous shear modulus microscope and micro flow meter can also be realized. For lateral modulation, a flat element will be used. If possible, an array transducer will be used. The evaluations of anisotropic mechanical properties are also our targets.

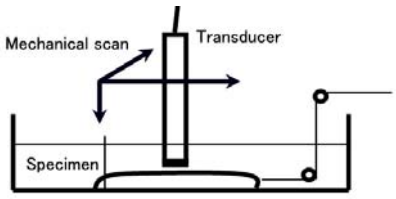

Figure 1: Experimental set up.

References:

[1] C. Sumi et al., IEEE Trans UFFC, 46, 158, 1999.
[2] C. Sumi et al., IEEE Trans UFFC, 55, 24, 2008.
[3] C. Sumi et al., IEEE Trans UFFC, 52, 1670, 2005.
[4] C. Sumi et al., IEEE Trans UFFC, 53, 2416, 2006.
[5] C. Sumi et al., IEEE Trans UFFC, 54, 2394, 2007.
[6] C. Sumi, UMB, 33, 1830, 2007.
[7] C. Sumi et al., Proc. of 6th Int Conf Ultrason Meas Imag Tissue Elasticity, p. 41, 2007.
[8] C. Sumi et al., IEEE 2007 Int Ultason symp, 1557, 2007.

081 **EFFECTIVENESS OF LATERAL DISPLACEMENT REGULARIZATION FOR SHEAR MODULUS RECONSTRUCTION.**

C. Sumi[1], T. Itoh[1].*
[1]Sophia University, 7–1, Kioicho, Chiyodaku, Tokyo 102–8554, JAPAN.

Background: We have been developing several displacement vector–measurement–based shear modulus reconstruction methods, e.g. [1]. For displacement vector measurement, we have developed the multidimensional cross–spectrum phase gradient method (MCSPGM), the multidimensional autocorrelation method (MAM) and the multidimensional Doppler method (MDM) [2]. However, to enable us to use the multidimensional shear modulus reconstruction methods practically, improved accuracy of lateral and elevational displacements must be obtained. Thus far, for the displacement vector measurement methods, we have been developing a displacement–component–dependent regularization method (DCDRM) that allows relatively accurate lateral and elevational displacement measurements to be employed [3]. Spatially variant regularization can also be implemented together as in a shear modulus reconstruction using variances [4].

Aims: The effectiveness of using the lateral displacement variance to regularize the lateral displacement is verified.

Methods: For an agar phantom that had a stiff cylindrical inclusion (inclusion 2.95 and background 1.43×10^6 N/m^2, relative shear modulus, 2.06) and was compressed in the axial direction, the lateral displacement variance was measured for 2D CSPGM, AM and DM under the assumption of a spatially local stationary measurement error. At each point, the regularization parameter for the lateral displacement was obtained by using a constant that was multiplied by all lateral displacement variances over the ROI. For the respective measurement methods, using a spatially variant regularized lateral displacement and simultaneously measured non–regularized axial displacement, a 2D shear modulus reconstruction was performed under a 2D stress assumption [1].

Results: Figure 1 shows, for the spatially variant regularizations of 2D CSPGM, AM and DM, the contrast–to–noise ratio (CNR) of the axial and lateral strains as the function of a constant multiplied by the lateral displacement variances. All CNRs of axial strain are almost constant within the range of the constant, and all CNRs of lateral strain display single maxima due to the increases in the accuracy and stability of lateral strain measurement. This behavior confirms that seen for spatially uniform regularization parameter as well [3]. For all 2D CSPGM, AM and DM, the CNRs of lateral strain obtained by spatially variant regularization are larger than those obtained by spatially uniform regularization (2D CSPGM, 2.36 vs 2.27; 2D AM, 1.90 vs 1.84; 2D DM, 1.30 vs 1.17), although the CNRs of axial strain are almost unaltered (2.29, 3.07, 0.60). Moreover, all peaks of the CNRs obtained by the spatially variant regularization are sharper than those obtained by uniform regularization (omitted), so that the best regularization parameter would be easier to detect for spatially variant regularization than for uniform regularization. For a 2D shear modulus reconstruction, the mean shear moduli are estimated to be larger and closer to the true value using spatially variant regularization than those obtained by a uniform regularization (2D CSPGM, 1.51 vs 1.50; 2D AM, 1.42 vs 1.40; 2D DM, 1.22 vs 1.21).

Conclusions: Spatially variant regularization of lateral displacement (using the lateral displacement variance) is more effective than uniform regularization in obtaining a large lateral strain CNR and an accurate 2D shear modulus reconstruction.

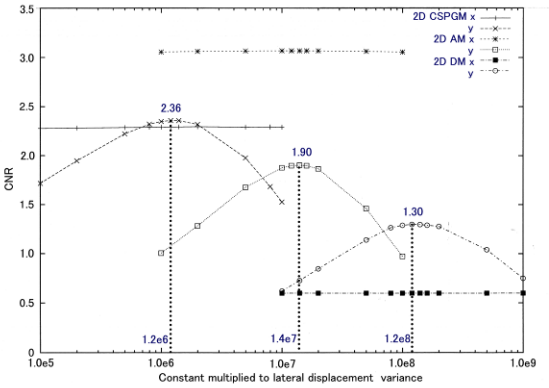

Figure 1: Axial and lateral strain CNRs for spatially variant lateral displacement regularization.

References:

[1] C. Sumi et al., IEEE Trans UFFC, 52, 1670, 2005.
[2] C. Sumi et al., IEEE Trans UFFC, 55, 24, 2008.
[3] C. Sumi et al., IEEE Trans UFFC, 55, 787, 2008.
[4] C. Sumi et al., IEEE Trans UFFC, 55, 297, 2008.

* *indicates Presenter*

082 **COMPARISON OF CONTRAST–TO–NOISE RATIOS OF AXIAL STRAIN AND SHEAR MODULUS RECONSTRUCTION BY AXIAL STRAIN RATIO – PHANTOM EXPERIMENT.**

C. Sumi[1].*
[1]Sophia University, 7–1, Kioicho, Chiyodaku, Tokyo 102–8554, JAPAN.

Background: We have been developing several displacement–measurement based shear modulus reconstruction methods, i.e., ones using a 1–dimensional (1D) displacement component [1,2] and a multidimensional (2D and 3D) [2,4] displacement vector. A statistical CNR is often used to evaluate the contrast–to–noise ratio in an image of a measured axial strain [5]. That is, the CNR is used to evaluate the detectability of a fixed sized inhomogeneity of tissue elasticity. We reported [1,6] an increase in a CNR for a 1D reconstruction by strain ratio [1,2] by setting the reference shear modulus point properly at a specific depth, i.e., in the stress concentration or stress weak region in front of and behind a stiff region and soft region. That is, we clarified that for shear modulus imaging, we should find suitable reference regions that are homogeneous and exist in the neighborhood of the target tumor by viewing B–mode and strain images.

Occasionally, by assuming a uniform stress in a region of interest, the axial strain image is used as an image of the relative shear modulus similarly to the axial strain ratio [1]. Last year, we compared the CNR of the axial strain with those of the 1D reconstruction and the inversion (i.e., the inversion of the relative shear modulus [1,2]) on simulated phantoms [6]. Consequently, we confirmed that we were able to predict the order of the CNRs using the means and SDs of measured strains in the target tumor and the surrounding region [7] without obtaining the reconstructions.

Aims: In this report, we verified the effectiveness of the prediction method by performing the same comparisons of the CNRs on an agar phantom, i.e., regarding the strain, the relative shear modulus (i.e., strain ratio) and the inversion of the relative shear modulus.

Methods: For axial strain measurements, the 2–dimensional cross–spectrum phase gradient method (2D CSPGM) [8] was used. The target phantoms (40 (axial) x 40 (lateral) x 45 (elevation) mm) had a stiff or soft inclusion (i.e., one contrast).

Results: For instance, Figure 1 shows for a phantom that had a stiff cylindrical inclusion (dia., 15 mm, relative shear modulus, 2.4), the reference position of shear modulus vs CNRs of the strain, strain ratio and the inversion. Using the above mentioned statistics of strains (i.e., those in the inclusion and the surrounding region), the order is estimated to be strain ratio > the inversion (i.e., estimated CNRs). See also, measured CNRs. As shown, the prediction was successful.

Conclusions: It was confirmed that the imaging of strain ratio is more effective than imaging axial strain. Furthermore, the evaluations of their CNRs clarified that, for local inclusions, the evaluations of means and variances of strains in the inclusion and the surrounding region [7] is effective for determining whether the strain ratio or the inversion is imaged.

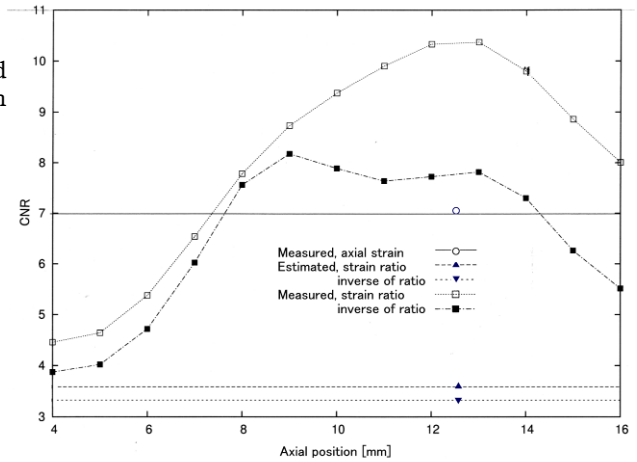

Figure 1: CNRs of axial strain, axial strain ratio and inverse of ratio obtained on agar phantom versus reference position.

References:
[1] C. Sumi et al., J Med Ultrason, 34, 171, 2007.
[2] C. Sumi, IEEE Trans UFFC, 52, 1670, 2005.
[3] C. Sumi, IEEE Trans UFFC, 53, 2416, 2006.
[4] C. Sumi, IEEE Trans UFFC, 54, 2394-2403, 2007.
[5] M. Bilgen et al., IEEE Trans UFFC, 46, 1128, 1999.
[6] C. Sumi et al., Proc. of 6th Int Conf Ultrason Meas Imag Tissue Elasticity, p. 100, 2007.
[7] C. Sumi, UMB, 33, 1830, 2007.
[8] C. Sumi, IEEE Trans UFFC, 46, 156, 1999.

087 **IMPROVING SHEAR VELOCITY ESTIMATION ACCURACY BY DETECTING POTENTIAL FALSE PEAKS IN TISSUE DISPLACEMENT RESPONSE.**

Liexiang Fan[1], Paul Freiburger[1].*
[1]Siemens Medical Solutions USA, Ultrasound Division, 22010 SE 51st Street, Issaquah, WA, USA.

Background: It has been proven feasible to detect tissue shear velocity by monitoring the shear wave arrival times at multiple locations after acoustic radiation force impulse (ARFI) excitation [1]. In [1], it is also demonstrated that accurate results can be achieved by using the peak of the tissue displacement response to track the wave front propagation. When we applied this method, we observed the appearance of two peaks in the displacement response in both phantom and *in–vivo* data. In some cases, the highest peak was a false indicator of the wave front propagation. A false peak detected before the true peak resulted in overestimation of the shear velocity, and a false peak detected after the true peak resulted in underestimation of the shear velocity. There are many possible causes for a second peak which will not be addressed in this work. Instead, we developed a method which can identify a false peak. This has enabled improved shear velocity estimation.

Aims: The aim of this work is to identify the true peak in the tissue displacement response after ARFI excitation in order to prevent over/under–estimation of shear velocity.

Methods: A set of displacements over time are generated within a region on interest (ROI) after ARFI excitation. A temporal displacement profile is generated from the median value of the displacements calculated within the ROI and is used as a reference. The highest peak is assumed to be the reference peak reflecting the average arriving time for the ROI. For each individual profile, the peak closest to the reference peak is taken as the true peak when two peaks are observed.

Results: Figure 1a shows tissue displacement responses at locations 0.83mm, 2.17mm, 3.5mm and 4.17 mm away from the center of the ARFI excitation. At location 4.17mm, there are two peaks, and the highest peak is a false peak. Figure 1b shows the results for peak occurrence times at 25 locations evenly distributed between 1.33mm to 5.33 mm from the center of the ARFI excitation pulse. The 'x' points are the peak occurrence times before the proposed method is applied, the 'o' points are the result after the proposed method is applied.

Conclusions: This work demonstrates the improvement of shear velocity detection when two peaks appear in the tissue displacement response after ARFI excitation.

Acknowledgements: We would like to thank Duke University, especially Drs. K. Nightingale and M. Palmeri for their technical communication on shear velocity estimation using ARFI.

References:

[1] Nightingale, KR et al. Shear Wave Velocity Estimation Using Acoustic Radiation Force Impulse Excitation in Liver *in–vivo*. IEEE Ultrasonic Symposium, Vancouver, Canada, October, 2006.

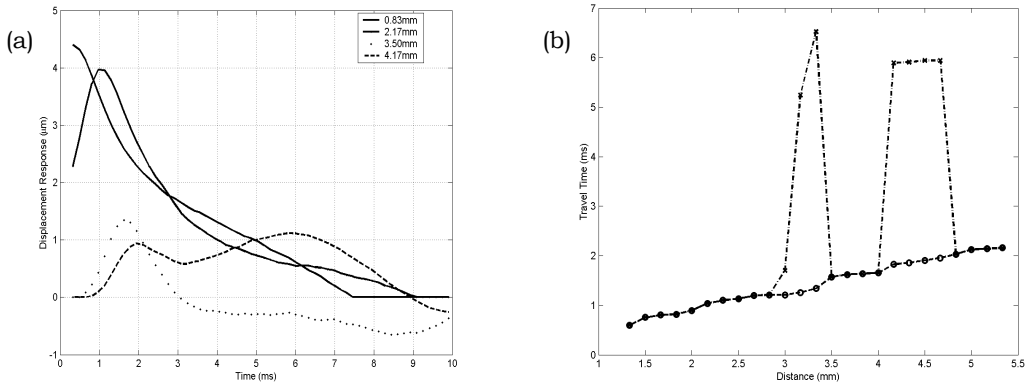

Figure 1: Tissue displacement response at four locations (a) and the shear wave travel time of 25 locations (b) after ARFI excitation.

* *indicates Presenter*

013 **ARTIFACT REDUCTION WHEN MONITORING LOCAL TEMPERATURE CHANGES WITH TRANSIENT ELASTOGRAPHY.**

Nicolás Benech[1], Carlos A. Negreira[1].
[1]Laboratorio de Acústica Ultrasonora, Instituto de Física, Facultad de Ciencias, Universidad de la República, Iguá 4225, 11400, Montevideo, URUGUAY.

Background: Transient elastography has potential to play an important role in thermal ablation therapy. Thermally induced lesions are generally stiffer than surrounding tissue, and elastography has proven to be a useful technique to evaluate their spatial extent determining the success of treatment [1]. The stiffness increase is associated with the irreversible protein denaturation process in soft tissues. However, at lower exposure levels it has been shown that shear modulus decreases with increasing temperature in a reversible process [2]. Therefore, elastographic techniques are potential candidates to monitor the tissue damage as it progresses and to detect the critical point from which cellular necrosis is produced. However, the local temperature changes produce artifacts in ultrasound based elastographic images affecting the final estimation of the local shear elasticity [3]. These artifacts are produced because the sound speed is temperature dependent. On one hand, the position at which the low frequency field is evaluated is not constant, producing an apparent spatial shift, Δ, on the elasticity image. The final value of this apparent movement depends on the temperature profile and on the material's thermodynamic properties (thermal expansion coefficient and temperature dependence of the sound speed). In agar–gelatin based phantoms, we have found that $\Delta \sim 2$mm for a 30ºC temperature change. On the other hand, the estimation of local shear elasticity requires computing the spatial derivative of the low frequency field. Therefore, the quantitative value of the local shear elasticity is also affected.

Aims: The aim of this work is to investigate and, if possible, reduce the temperature produced artifacts on the local shear modulus estimation by transient elastography.

Methods: In this work, 1D transient elastography experiments are carried out in agar–gelatin based phantoms and in fresh bovine skeletal muscle. In order to create a spatially varying temperature a 10Ω electrical resistance is placed inside the sample connected to a 10VDC source for 2 minutes. A piston–like low frequency source is employed at the free surface of the sample. Transient elastography experiments are performed every 2s around the resistor position. The local shear wave value is estimated from phase measurements of the low–frequency field with spatial resolution ~ 1mm. [4]

Results: By post processing of the ultrasound A–lines following [4], we have found that local temperature variations introduce spatial shifts Δ up to 2mm in agar–gelatin based phantoms for a 30ºC local temperature increase. The artifacts are clearly visible in Figure 1(a) where 1D transient elastography measurements were performed in an agar–gelatin phantom. The electrical resistance at position z=47mm was active between 0 and 60s. Here we propose to use the acquired RF data before the low–frequency source activation in order to introduce spatial corrections on the speckle tracking algorithm. The corrections are made using the information contained on the echo time–shift produced by the temperature profile on the consecutive A–lines. After these corrections are carried out, the heated zone is clearly visible in elastographic images (blue zone in Figure 1(b)), producing a decrease in the local shear speed value, Cs, according to previous results [2].

Conclusions: We conclude that transient elastography has potential for use in thermal therapy guidance and monitoring provided that temperature induced artifacts are taken into account and reduced. See Reviewers' Comment 5

Figure 1: (a)

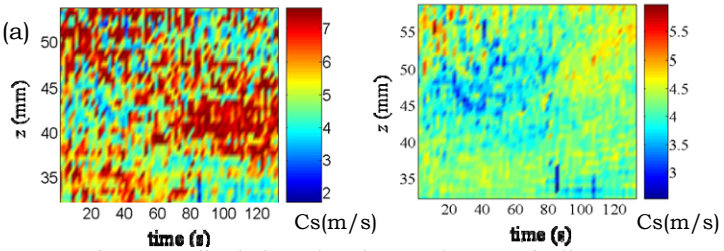

Acknowledgements: This work was supported by Programa para el Desarrollo de las Ciencias Básicas, Pedeciba, Uruguay.

References:

[1] R. Souchon, O. Rouviere, A. Gelet, V. Detti, "Visualization of HIFU lesions using elastography of the human prostate *in vivo*: Preliminary results", Ultrasound in Med. & Biol. 29, 1007–1015, (2003).
[2] T. Wu, J. Felmlee, J. Greenleaf, S. Riederer, R. Ehman, "Assessment of thermal tissue ablation with MR elastography", Magnetic Resonance in Medicine, 45, 80–87, (2001).
[3] N. Benech, C. Negreira, "Monitoring thermal changes in soft tissues by 1D transient elastography" Proceedings of the 2007 International Congress on Acoustics (ULT–13–012).
[4] S. Catheline, F. Wu, M. Fink, "A solution to diffraction biases in sonoelastography: The acoustic impulse technique", J. Acoust. Soc. Am. 105, 2941–2950, (1999).

029 **FIRST RESULTS IN THE MEASUREMENT OF RAYLEIGH ELASTICITY PARAMETERS IN PHANTOMS AND *IN–VIVO* BREAST TISSUE.**

EEW Van Houten[1], MDJ McGarry[1], JB Weaver[2], KD Paulsen[3].
[1]University of Canterbury, Private Bag 4800, Christchurch, New Zealand; [2]Dartmouth Hitchcock Medical Center, Lebanon, NH 03756, USA, [3]Thayer School of Engineering, Dartmouth College, Hanover, NH 03755, USA.

Background: The attenuating behavior of soft tissue shows evidence of providing clinical and diagnostic insight into various soft tissue disorders [1–3]. To make the most of this diagnostic capability, characterization of the damping behavior of tissue should be as accurate as possible. To date, attenuation in the case of the time–harmonic tissue behavior found in dynamic elastography has captured the damping behavior through a single parameter that takes the form of an imaginary component of a complex valued shear modulus. A more generalized damping formulation for the time–harmonic case, known commonly as Rayleigh or proportional damping, includes an additional parameter that takes the form of an imaginary component of a complex valued density. The effects of these two different damping mechanisms can be shown to be independent across homogeneous distributions and mischaracterization of the damping structure can be shown to lead to artifacts in the reconstructed attenuation profile [4].

Methods: A novel method for reconstructing the Rayleigh damping distribution of within tissue and tissue–mimicking phantoms from 3D time–harmonic displacement data obtained via MR imaging has been developed based on a subzone approach to the global inverse problem [5]. This technique has been used to evaluate the ability to assess Rayleigh damping distribution from measured data and to initiate an investigation into the potential clinical value of these measurements.

Results: The two figures below illustrate typical results for this reconstruction method in tissue mimicking phantoms and breast tissue. It can be seen that that the structure of the various reconstructed mechanical properties match structural aspects in both cases. Resulting values for real shear modulus and overall damping levels are in reasonable agreement with values established in the literature or measured by mechanical testing. The value of real density was fixed at that of water, roughly 1000 kg/m^3.

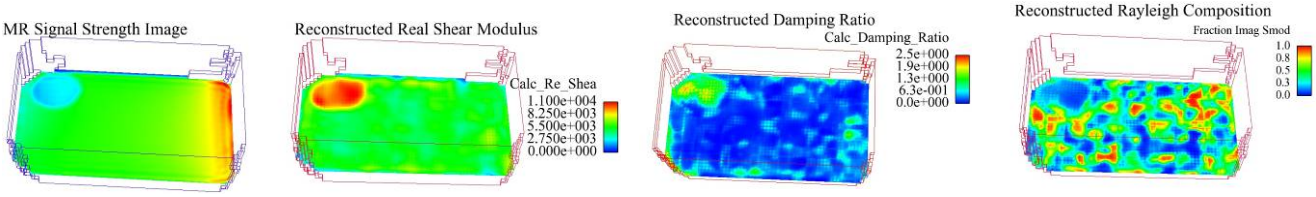

Figure 1: Rayleigh damping reconstruction from a tissue mimicking heterogeneous phantom.

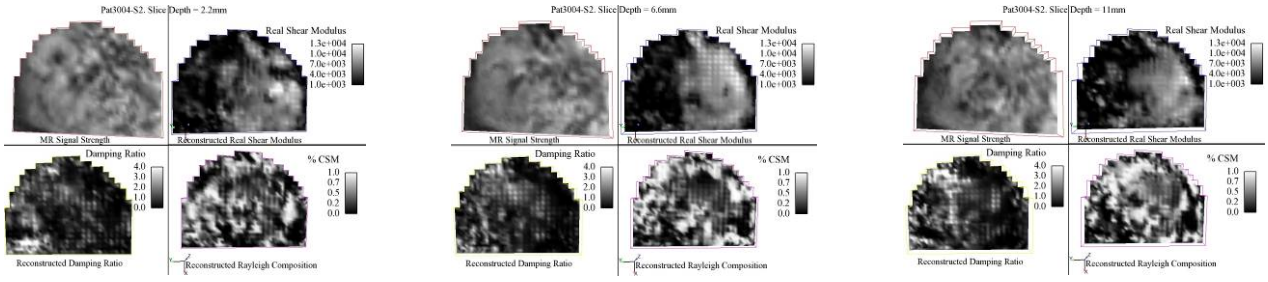

Figure 2: 3 slices of a Rayleigh damping reconstruction from breast tissue.

Acknowledgements: We gratefully acknowledge support from NIH/NIBIB R01–EB004632–02.

References:

[1] L Huwart et al., Liver Fibrosis: Noninvasive Assessment with MR Elastography versus Aspartate Aminotransferase–to–Platelet Ratio Index, Radiology, 245, 2007.
[2] R Sinkus et al., Viscoelastic shear properties of *in vivo* breast lesions measured by MR elastography, J Magn Reson Imaging, 23(2), 2005.
[3] N Salameh et al., Hepatic viscoelastic parameters measured with MR elastography: correlations with quantitative analysis of liver fibrosis in the rat, J. Magn Reson Imag, 26(4), 2007.
[4] MDJ McGarry et. al., Reconstructing spatially varying rayleigh damping parameters in magnetic resonance elastography, Sixth Int Conf Ultrason Meas Imag Tiss Elast, 54, 2007.
[5] M Doyley et al., Steady–state magnetic resonance harmonic elastography: contrast detailed analysis and preliminary clinical evaluation, First Int Conf Ultrason Meas Imag Tiss Elast, 45, 2002.

* *indicates Presenter*

038 **DETERMINATION OF ELASTIC PROPERTIES AND HEIGHT PROFILE OF LAYERED BIO–MATERIALS WITH VECTOR–CONTRAST SCANNING ACOUSTIC MICROSCOPY USING POLAR DIAGRAM IMAGE REPRESENTATION.**

Esam T. Ahmed Mohamed[1], Albert Kamanyi[1], Moritz von Buttlar[1], Reinhold Wannemacher[1], Kristian Hillmann[1], Wilfred Ngwa[2] and Wolfgang Grill[1].

[1]Institute of Experimental Physics II, University of Leipzig, Leipzig, GERMANY; [2]Physics Department, University of Central Florida, Orlando, Florida, FL 32816, USA.

Background: Acoustic phase and magnitude contrast data represented in a polar plot have been shown to provide a direct way to elucidate the elastic properties of sufficiently planar and homogenous biomedical samples of variable thickness [1]. The method is also applied to get non–contact mapping of the topography of thin film layered biomedical samples.

Aims: Non–contact mapping of the height and determination of the elastic properties of thin layered biomedical samples using phase and magnitude data represented in a polar graph.

Methods: An In–focus image of chitosan thin film deposited on glass substrate was taken using a vector contrast phase–sensitive acoustic microscope (PSAM) [2] working at 1.195 GHz.

Results: The variation in the grey value of the reflected signal was taken along the horizontal straight black line across the phase and amplitude images (Figure 1). These data were plotted in a polar graph (Figure 2). The reflectivity of the different points along the surface of the sample depends spatially on the thickness of the sample. Highest reflectivity comes from bare glass and is represented at the top of the polar graph by a point corresponding to zero phases. The reflectivity decreases along the spiral curve till its minimum value near the center of the polar plot which corresponds to maximum thickness. The attenuation increases with increased thickness. The interferences between reflections from interfaces and reflections within the sample are represented by the spirals at which the polar graph reverses its direction to delineate zones of equal acoustic path lengths and then continues toward the direction of increased thickness. The experimental data were fitted with a model based on the geometrical ray theory to get the acoustic velocity, attenuation and density of the material. These parameters were then used to calculate the shear viscosity and the elasticity (Young's) modulus of a chitosan thin film. Since the variation of the reflectivity depends basically on the variation of the thickness, the thickness of each point is deduced resulting in the height profile of the sample (Figure 3).

Conclusions: The method provides a direct way to find the acoustic parameters from which the elastic properties are derived. In addition, it allows height profiling of the thin films.

References:

[1] Ahmed Mohamed. E, et al., Determination of mechanical properties of layered materials with vector contrast scanning acoustic microscopy using polar diagram image representation. Proc. SPIE Vol. 6935, 69351Z, 2008.

[2] Grill. W, Hillmann. K, Würz. K and Wesner. J, Advances in Acoustic Microscopy, Springer Publisher, New York, 168–175, 1996.

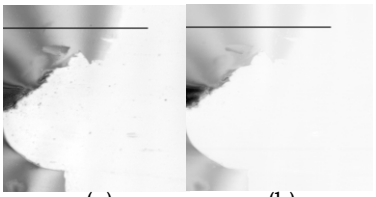

(a) (b)

Figure 1: Images in magnitude contrast (a) and phase contrast (b) of a chitosan layer of variable thickness on a glass substrate. Magnitude and phase data were taken along the horizontal black line indicated in the images and are displayed in a polar representation in Figure 2.

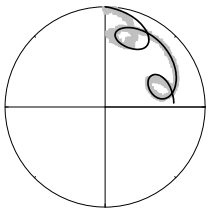

Figure 2: Polar diagram of the magnitude and phase of the reflected signal along a horizontal straight line across the images of a thin film of chitosan (grey squares) and the fit of the experimental data (black solid line).

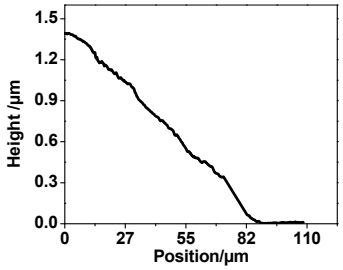

Figure 3: Height profile of the chitosan thin film drawn from the data represented in the polar graph in Figure 2.

073 **REAL–TIME POROELASTOGRAPHY: PHANTOM STUDIES.**

W Khaled[1], R Zahiri–Azar[2], J Ophir[1], SE Salcudean[2].
[1]Ultrasonics and Elastographics Laboratory, University of Texas Health Science Center at Houston, Houston, TX, USA; [2]University of British Columbia, Vancouver, BC, CANADA.

Background: The collection, retention and flow of fluids in tissues are related to their state of health and disease. Lymphedema is a condition of abnormal localized fluid retention in the interstitial space that causes swelling, most often in the arms and/or legs. Lymphedema following breast cancer treatment is one of the most common kinds of lymphedema and is a serious lifelong concern even with modern treatments. However, the current diagnostic methods are mostly qualitative in the assessment of lymphedema and cannot detect its exact location and severity. On the other hand, the feasibility of using off–line poroelastography to differentiate between lymphedematous and normal tissues has been shown in [1]. According to the biphasic theories, the porous media can be modeled as a combination of an intrinsically incompressible porous–permeable solid matrix and an interstitial incompressible fluid.

Aims: The aim of this work is to develop a real–time method for measuring the time–dependent mechanical behavior of homogeneous and inhomogeneous poroelastic materials.

Methods: The poroelastograms are computed as the ratio of the lateral and axial strain elastograms acquired from a poroelastic material undergoing stress relaxation. The data reported in this study were acquired in real–time using the Sonix–RP Ultrasound machine (Ultrasonix Medical Corp., Richmond, Canada) and the client–software first presented in [2]. The collected RF–sequences were used to calculate the concurrent local axial and lateral strains. For the qualitative validation of the method several experiments were run using different types of poroelastic tofu phantoms. The phantoms were imaged to a depth of 50 mm using a linear array transducer (128 elements and 6.6 MHz center frequency) and digitized at 40 MHz. One RF–frame was acquired and stored as the pre–compression signal. Using a mechanical compressor, the phantoms were slightly compressed axially and sustained under constant uniaxial axial strain for up to 90s. After compression, many post–compressed RF–data frames were serially captured from which axial and lateral displacements were calculated. The poroelastograms were then estimated using the ratio between lateral strain and axial strain at every point in time.

Results: Different types of tofu phantoms were tested, having different porous material properties. Figure 1 (a, b and c) show the effective Poisson's ratio elastograms for different tofu–samples with and without a cylindrical hole filled with water and plugged with gelatin or with poly–vinyl alcohol cryogel (PVA) at different times after the initial loading. The instantaneous effective Poisson's ratio at (0^+ s) computed immediately after compression is close to 0.5 for most of the samples, i.e., the porous samples behave instantaneously like incompressible materials. Then, after a short time the volume of the porous samples tends to decrease due to fluid exudation, causing a reduction of the instantaneous effective Poisson's ratio. Incompressible materials such as water or PVA did not show significant time–dependent changes in the Poisson's ratio value after a short interval.

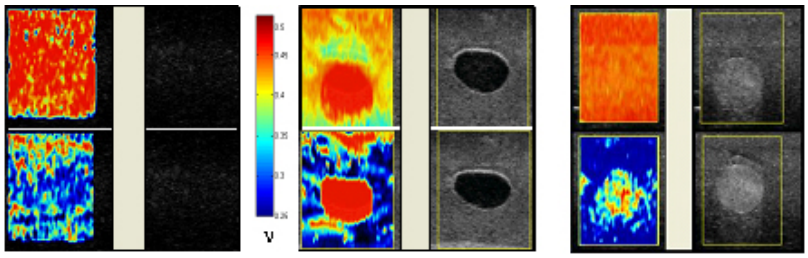

Figure 1: Poroelastograms and B–mode images: (a) Firm tofu phantom, at 0s (upper) at 90s (lower); (b) Soft tofu phantom with cylindrical hole filled with water, at 0s (upper) at 55s (lower); (c) Soft tofu phantom with cylindrical inclusion of poly-vinyl alcohol at 0s (upper) at 90s (lower).

Conclusions: The results from preliminary data sets show consistent differences in the real–time temporal behavior in the poroelastograms of uniform phantoms and phantoms containing localized incompressible inclusions. Temporal changes in inclusion/background contrast are readily visualized.

Acknowledgements: This work is supported by NIH grants CA64597–10, CA135580–01 and CA127291–01 awarded to the University of Texas Health Science Center at Houston.

References:

[1] Righetti R, et al.: The feasibility of using poroelastography techniques for distinguishing between normal and lymphedematous tissues *in vivo*. Physics in Medicine and Biology, pp. 6525–6541, 2007.
[2] Zahiri R, et al.: Real-Time Poroelastography: A Feasibility Study. Proc. 6th Intl. Conf. on the Ultras Meas and Imag of Tiss Elas, Santa Fe, NM, USA, p. 138, 2007.

* *indicates Presenter*

030 **MEASUREMENT OF THE MECHANICAL RESPONSE OF THE HUMAN UTERINE CERVIX.**

Mahmood Jabareen[1], Laila Sultan[3], Edoardo Mazza[1], Margit Bauer[2], Michael Bajka[3], Gerhard A. Holzapfel[4,5].*
[1]Mechanical Engineering Department, Swiss Federal Institute of Technology, 8092 Zurich, SWITZERLAND; [2]Medical University Graz, Obstetrics and Gynecology Department, 8036 Graz, AUSTRIA; [3]University Hospital Zurich, Obstetrics and Gynecology Department, 8091 Zurich, SWITZERLAND; [4]Graz University of Technology, Institute of Biomechanics, 8010 Graz, AUSTRIA; [5]Royal Institute of Technology, School of Engineering Sciences, 100 44 Stockholm, SWEDEN.

Background: The occurrence of cervical ripening before 34 weeks of gestation leading to preterm delivery represents a serious problem. Thus, the assessment of the mechanical properties of the cervix is an important diagnostic procedure in obstetrics. In daily practice digital palpation is used to determine consistence, effacement, dilatation and position of the cervix and is complemented by endovaginal ultrasound to describe the shape of the organ. Recently, we applied an *in vivo* aspiration experiment to evaluate the biomechanical function of the cervix. The aspiration device, [1], allows the assessment of the mechanical response of internal organs under sterile conditions without harm to the tested tissue. In a preliminary study (Medical University Graz, [2]) measurements were conducted on post–menopausal subjects before vaginal/abdominal hysterectomy.

Aims: The currently ongoing clinical study at the Clinic of Obstetrics, OB/GYN Department, University Hospital of Zurich aims to quantify the mechanical response of normal cervical tissue at different gestational ages.

Methods: A novel version of our aspiration device was developed for this study, see Figure 1. It consists of a tube (external diameter 15mm) in which the internal pressure can be controlled according to a desired negative pressure law. One end of the tube is placed in contact with the tissue. The displacement of the aspirated portion of the tissue is quantified from the images of a digital camera. Scalar parameters are used to evaluate and compare the mechanical response of different cervices. In particular, the so called "stiffness parameter" is defined as the applied pressure difference divided by the maximum displacement of the aspirated tissue. Measurements on pregnant subjects are performed during standard gynecological examinations. For determining the maximum pressure to be safely applied on the tissue, a preliminary step is performed with a ramp loading from atmospheric to 200 mbar negative relative pressure. After this, a loading cycle is applied; the pressure starts from atmospheric, reaches the minimum value, keeps at that pressure level for about 8 seconds and then goes back to atmospheric pressure. The duration of the test is 25 seconds.

Results: Tests on non–pregnant cervices showed that the proposed experimental procedure should allow detecting changes of approximately 30% of the patient–specific stiffness parameter [2]. Measurements have been performed so far on 10 pregnant subjects. Preliminary results indicate that the stiffness of the cervix of pregnant subjects is about one order of magnitude lower as compared to post–menopausal women. No pain, no irritations, no bleeding and no damage were found after the measurements.

Conclusions: The present experience confirms the feasibility of clinical studies with application of the aspiration device on pregnant subjects. The limited number of data acquired so far in the study on pregnant subjects is not sufficient to draw statistically relevant conclusions on the evolution of the cervical response in the course of pregnancy. These data and those acquired in the next months will be presented at the Conference.

(a) (b)

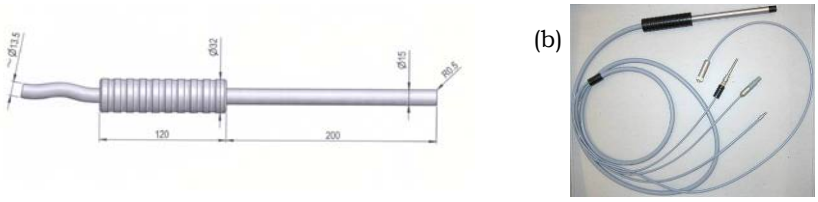

Figure 1: Drawing (a) and photo (b) of the aspiration device used for measurements on the cervix.

References

[1] Nava A., *In vivo* Characterization of the Mechanical Response of Soft Human Tissue, ETH Zurich, Dissertation No. 17060, 2007.
[2] M. Bauer, et al., *In Vivo* Characterization of the Mechanics of Human Uterine Cervices, Annals of the New York Academy of Sciences, Volume 1101, Reproductive Biomechanics: 186–202, 2007.

008 **CLINICAL VALIDATION OF AN OBESE–DEDICATED PROCEDURE FOR LIVER STIFFNESS MEASUREMENT USING TRANSIENT ELASTOGRAPHY.**

Magali Sasso[1], Stéphane Audière[1], Véronique Miette[1], Laurent Sandrin[1].*
[1]Echosens, Research and Development Department, 153 avenue d'Italie, 75013 Paris, FRANCE.

Background: Transient elastography (Fibroscan®, Echosens, Paris, France) is a non–invasive and rapid technique used to assess liver fibrosis by measuring liver stiffness. Liver stiffness measurement for chronic liver diseases in adult patients using Fibroscan® is of clinical interest. Clinical liver stiffness evaluation can be tricky in obese patients [1, 2]. Obesity is a growing public health concern which requires dedicated liver evaluation procedures due to the patients' morphology and/or the specific diseases associated with obesity.

Aims: Our study aims to show how Fibroscan® can be adapted for liver disease evaluation in obese patients.

Methods: A new Fibroscan® transient elastography probe dedicated to obese patients was developed. Seventeen (17) obese patients and Twenty–two (22) morbidly obese patients were evaluated in a clinical study using both regular and obese–dedicated probes. The success rate (SR) of liver stiffness measurement was assessed using both probes. Improvement in the measurement procedure is proposed to increase SR in patients with a large subcutaneous fat thickness (SFT).

Results: SR associated with both regular and obese–dedicated probes is presented in Table 1 and has to be compared with the SR of the general population ranging between 85 and 95%. Thanks to the use of the obese–dedicated probe, the SR improved by 20 and 100% for obese and morbidly obese patients, respectively.

Failure in liver stiffness measurement is shown to be associated with SFT (odd ratios: 17:22 and 13:13 for the regular and obese–dedicated probe, respectively). SR obtained using both probes are given in Table 2 for patients having a SFT smaller than and greater to 2.7cm. For patients with SFT less than or equal to 2.7cm, the use of the obese–dedicated probe makes all examinations valid (SR = 100%). For patients with SFT greater than 2.7cm, the SR was improved by 78%, but the failure rate is still high (59%).

To improve the number of valid Fibroscan® examinations with patients having a large SFT, we propose a modification of the examination procedure by adequately stretching the patient's skin and increasing the compression of the abdominal wall. To validate this approach, we performed tests on two–layer tissue–mimicking phantoms, finite–element simulations (Femlab, Comsol) and *in vivo* on pigs and on human volunteers.

Conclusions: Improvement of the Fibroscan® elastometry measurements are shown for obese patients. By using the obese–dedicated Fibroscan® elastometry probe, the SR is improved up to 100% for obese and morbidly obese patients with SFT ≤ 2.7cm. For patients with large SFT, we demonstrated that a modification of the examination procedure by adequately stretching the patient's skin and compressing the abdominal wall can improve the SR of liver stiffness measurement.

References:

[1] Foucher et al., "Prevalence and factors associated with failure of liver stiffness measurement using FibroScan® in a prospective study of 2114 examinations", 56th Annual Meeting of the American Association for study of Liver Disease, San Francisco, USA, 2005.

[2] Kettaneh et al., "Features associated with success rate and performance of FibroScan measurements for the diagnosis of cirrhosis in HVC patients: A prospective study of 935 patients.

Patient	Number	BMI	SR, Regular Probe	SR, Obese–Dedicated Probe
obese	17	35.8 ± 2.2	59%	71%
morbidly obese	22	48.1 ± 7.5	32%	64%

Table 1: SR associated with both regular and obese–dedicated Fibroscan® elastometry probes.

SFT	number of patients	SR, regular probe	SR, obese-dedicated probe
≤ 2.7cm	17	71%	100%
> 2.7cm	22	23%	41%

Table 2: SR associated with both regular and obese–dedicated Fibroscan® elastometry probes for patient having a SFT smaller than and greater to 2.7cm.

* *indicates Presenter*

015 **ASSESSMENT OF THE VAGINAL WALL ELASTICITY BY MECHANICAL IMAGING.**

Vladimir Egorov[1], Heather van Raalte[2], Lioudmila Lipetskaia[3].*

[1]Artann Laboratories, 1459 Lower Ferry Rd., Trenton, NJ 08618, USA; [2]The Institute for Female Pelvic Medicine, 2200 W. Hamilton St., Allentown, PA 18104, USA; [3]St. Luke's Hospital and Health Network, 801 Ostrum St, Bethlehem, PA 18015, USA.

Background: Changes in elasticity and the relative collagen composition of the vaginal wall and connecting supporting tissues are thought to be significant risk factors for the development of pelvic organ prolapse, a prevalent condition affecting at least 12% of women in the US [1]. These conditions carry a tremendous impact on the emotional and physical aspects of women's life, as well as a significant economic impact in women's health care. Consideration of the vaginal wall mechanical properties creates two predominant concerns related to pelvic floor disorders: 1) How does decrease in tissue stiffness affect the development of pelvic organ prolapse and 2) How can functional elasticity be maintained through reconstructive surgery while providing enough strength for a durable repair. Current diagnostic evaluation includes a clinical pelvic examination (palpation) for vaginal or uterine prolapse while the patient is in a supine and/or standing position. Vaginal properties are then assumed based on the degree of support and tissue strength subjectively collected by the examiner. The assessment is highly variable among providers and is likely not truly reflective of the underlying vaginal tissue properties. To date, there is no standardized, non–invasive, reproducible tool to accurately assess the circumferential elastic properties of the vagina. Mechanical Imaging (MI) is a new modality of medical imaging, based on principles similar to those of manual palpation [2]. MI is capable of imaging and recording the sense of touch by measuring surface stress patterns using a pressure sensor array. The changes in surface stress patterns as a function of pressure are closely related to elastic properties and geometry of the examined region. Analyzing these changes, MI can produce 2D/3D images of the tissue [3, 4].

Aims: The objective of this study was to evaluate applicability of MI technology a) to measure and compare mechanical properties of the vaginal wall in women with and without pelvic organ prolapse; b) to characterize local vaginal sites with increased hardness, e.g. sites against the implanted mesh graft or surrounding scar tissue.

Methods: Thirteen women were enrolled in the study and underwent transvaginal MI evaluation. The women enrolled included 5 women with normal pelvic support, 3 of which had had prior reconstructive pelvic surgery, and 8 women with current pelvic organ prolapse. MI was performed utilizing a vaginal probe comprised of pressure sensor array and orientation sensors. Imaging results were electronically recorded and then analyzed under laboratory conditions by custom developed software.

Results: Among women with and without prolapse, the slope of the scan head applied force (Fs) versus elevation angle of the probe characterized an elasticity of the vaginal wall against which the scan head has been pressed. Comparison of a woman with normal pelvic support to a woman with pelvic organ prolapse revealed Fs values of 0.18±0.01 (normal support) and 0.025±0.010 (Stage 3 prolapse) for the anterior compartment and Fs values of 0.11±0.01 (normal support) and 0.035±0.010 (Stage 2 prolapse) for the posterior compartment. The ratio of normal–to–prolapse vaginal wall elasticity was found to be 7.2 for the anterior compartment and 3.1 for the posterior compartment. For patients with prior reconstructive surgery, areas of previous scar tissue and graft placement could be easily seen on recorded 2D pressure patterns with a measurable increase in tissue rigidity. Even within the vaginal site of graft placement, areas of increased rigidity, such as mesh arms used in graft kits, could be visually discerned and quantitatively characterized.

Conclusions: Our findings suggest that MI may offer a non–invasive, quantitative evaluation of vaginal elasticity with the potential for a more comprehensive evaluation of overall vaginal support structures. The prospective gynecologic application of the MI could impact our further understanding of the etiology of prolapse, individual variations in biomechanical properties and provide insight into optimal approaches for surgical repair.

References:

[1] Boyles SH, et al. Procedures for pelvic organ prolapse in the United States. Am J Obstet Gynec 2003; 188:108–15.
[2] Sarvazyan A. Mechanical Imaging: A new technology for medical diagnostics. Int J Med Inf, 1998; 49: 195–16.
[3] Egorov V, Ayrapetyan S, Sarvazyan A. Prostate mechanical imaging: 3-D image composition and feature calculations. IEEE Transactions on Medical Imaging, 2006; 25(10): 1329–40.
[4] Egorov V, Sarvazyan A. Mechanical imaging of the breast. IEEE Transactions on Medical Imaging 2008; 27(9): 1275–87.

010 **RELATIONSHIP BETWEEN VASCULAR COGNITIVE IMPAIRMENT AND CAROTID ATHEROSCLEROSIS.**

T Varghese[1], BP Hermann[1], RJ Dempsey[1], H Shi[1], CC Mitchell[1], M McCormick[1], MA Kliewer[1].*
[1]University of Wisconsin–Madison, 1530 Medical Sciences Center, 1300 University Avenue, Madison, WI 53706, USA.

Background: Carotid artery atherosclerosis is a particular presentation of the larger systemic disease of atherosclerosis. Clinical pathophysiology of carotid atherosclerosis had originally emphasized flow stenosis. However, a second mechanism present in both the coronaries and carotids may be of great importance, i.e. artery–to–artery emboli. Because of the extreme eloquence of critical regions of the cerebral vasculature, even moderate emboli may produce devastating and clinically relevant consequences. Multiple small emboli may cause atrophy and multiple small infarcts that are not recognized as a single event but rather as a progressive decline in function and cognition.

Aims: Ischemic cerebrovascular disease and stroke remain the number three cause of death and number one cause of disability in adults in the USA. While we clearly understand that atherosclerosis plays a role in cerebral ischemic disease, identifying patients at greatest risk remains limited. In this study, we examine the relationship between structural stability of carotid plaque and cognitive impairment.

Methods: *In-vivo* data acquisition on 10 patients with carotid stenosis and plaque was performed at the University of Wisconsin–Madison Hospitals and Clinics, under a protocol approved by the UW–Madison Institutional review board. Ultrasound RF data was acquired on patients who had consented to the study, using a Siemens SONOLINE Antares (Siemens Ultrasound, Mountain View, CA, USA) equipped with the Axius direct research interface. In additional to RF data acquisition, a complete carotid clinical ultrasound study was performed with color–flow Doppler imaging to determine regions and velocities of blood flow and acquisition of ultrasound B–mode data loops. Patient scanning was done using the VFX 13–5 transducer with a center frequency of 11.43 MHz. The lateral resolution was also set to the highest value, i.e. 508 A–lines for a beamwidth of 38 mm. The sampling rate for the RF signals was 40 MHz, and a single transmit focus was set at the depth of the plaque with dynamic focusing on receive. After data acquisition, regions of interest (ROI) within plaque in the scans were identified by the radiologist. The maximum accumulated axial strain and the relative lateral shifts [1] in the plaque ROI were computed.

In addition to strain imaging, a neuropsychological assessment, namely the Repeatable Battery for the Assessment of Neuropsychological Status (RBANS) was also performed on the same patients. All patients presented with significant carotid atherosclerotic plaques based on NASCET and ACAS criteria. Patients presented with and without major motor, sensory, vision or speech clinically recognizable symptoms and were scheduled to undergo carotid endarterectomy.

Results: The RBANS Total score was regressed on the maximum accumulated axial strain for the 10 patients who had undergone assessment of both cognition and strain. There was a significant correlation between strain and RBANS Total performance (p=.03), with higher strain associated with poorer cognitive performance as shown in Figure 1. Inspection of additional RBANS scales showed similar significant associations between strain and immediate (p=.03) and delayed memory (p=.03). Relationships were in the similar direction, but weaker, across tests of visuoperception, language and attention with correlation coefficients ranging from -0.37 to -0.31.

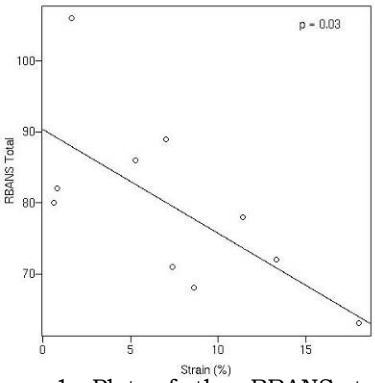

Figure 1: Plot of the RBANS total score versus the maximum accumulated frame strain.

Conclusions: These preliminary results suggest a direct relationship between increasing maximum accumulated axial strain within atherosclerotic plaque and decreased cognitive function. This is present in both classically symptomatic and asymptomatic patients. The relationship suggests that the processes, by which clinically recognizable major transient ischemic attacks or stroke symptoms of motor, vision, speech or sensation are seen, may be inadequate to recognize processes by which cognitive decline take place.

Reference:

[1] H. Shi, et al., "Preliminary *in–vivo* atherosclerotic carotid plaque characterization using the accumulated axial strain and relative lateral shift strain indices", Physics in Medicine and Biology, 2008.

** indicates Presenter*

032 **EXAMINATION OF NONINDUCED TISSUE LESIONS WITH FREEHAND ELASTOGRAPHY: AN ANIMAL APPLICATION.**

E Brusseau[1], J–F Déprez[1], F Duboeuf[1], F Rigout–Paulik[2], O Basset[1].*
[1]CREATIS UMR CNRS 5220 Inserm U630, Université de Lyon, Villeurbanne, FRANCE; [2]ENVL Ecole Nationale Vétérinaire de Lyon, Marcy l'Etoile, FRANCE.

Background: Ultrasound elastography is now recognized as a valuable tool for the early detection and for the characterization of many pathologies. Strain estimation techniques, with their specific characteristics and performance, are at the core of this recent imaging modality.

Aims: We recently developed a 2D locally regularized strain estimation technique [1] that was proven to provide good quality elastograms with simulations and fresh excised specimens of bovine livers, containing artificial lesions made of agar gel. The aims of this study are to investigate the potential of our strain estimation technique to image the deformation of non–induced dog tissue lesions as well as its relevance for the diagnosis.

Methods: Contrary to most 2D techniques that model the local tissue motion as a 2D translation, our method considers the additional variation in shape of the signal, locally modeled as an axial scaling factor. Anterior 1D studies, indeed, showed that considering a signal shape variation provides estimation methods that are more robust in terms of decorrelation noise [2]. Deformation parameters are locally determined by maximizing a similarity criterion (chosen as the normalized correlation coefficient, NCC) between a specific ROI and its deformed version after compensating for the effects of the deformation. A local regularization process is then applied to correct potentially incorrect estimates, identified as those having led to a NCC value too far from 1 (NCC<0.8). Finally, movies exhibiting the tissue deformation during the compression are generated by cumulating frame to frame deformation images. In order to investigate pathologies resulting from natural development, the dogs included in this study are not laboratory animals, but pets suffering from non–induced diseases and treated in the clinical department of the National Veterinary School in Lyon. For this first clinical study, experiments were performed with organs (livers and spleens) from euthanized dogs and characterized by different lesions, including mainly malignant tumor lesions. For each considered case, autopsy and histological reports were provided.

Results: Several cases are presented, with harder but also softer lesions. For all cases, the lesions are clearly identified in the good quality elastography movies. Moreover, in some cases, quasi–undetectable lesions in the B–mode images were clearly brought out in the elastograms with well delineated boundaries as well as high contrast that increases with compression. Heterogeneity of some lesions was also revealed during deformation imaging. The particular case of malignant tumor lesions within a dog spleen is presented in Figure 1. Results were corroborated with autopsy and histological reports.

Conclusions: The 2D locally regularized strain estimation method provides smooth elastograms with clinical data and freehand acquisition conditions. Moreover, it allows extracting information complementary to ultrasound imaging, showing its relevance for diagnosis.

Acknowledgements: The authors thank the Rhône–Alpes Region for their financial support through the I3M cluster.

References:

[1] E. Brusseau, J. Kybic, J–F. Deprez, O. Basset, "2D locally regularized tissue strain estimation from radiofrequency ultrasound images–Theoretical developments and results on experimental data", IEEE TMI, Feb 2008, pp. 145–160.
[2] S.K. Alam, J. Ophir, and E.E. Konofagou, "An adaptive strain estimator for elastography", IEEE UFFC, 1998, vol.45, n°2, pp. 461–472.

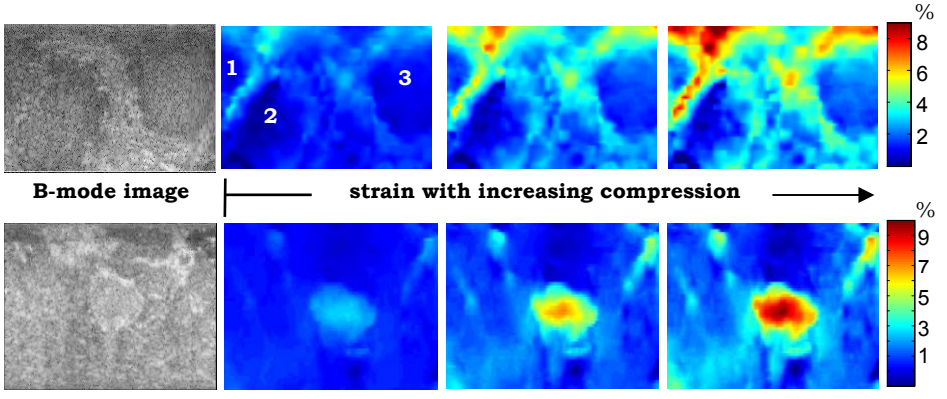

Figure 1: Dog spleen characterized by the presence of multiple malignant tumor lesions. The boundary between lesions 1 and 2 is clearly brought out in the three elastograms extracted from the sequence of elastograms, whereas it was less obvious in the B–mode images.

Figure 2: Dog liver characterized by blood stasis and vessel repletion. In some areas, the blood stasis led to tissue degeneration. A softer lesion is observable in the middle of the image.

035 **A COMPARISON OF AUTOMATED AND MANUALLY DRAWN LESION BOUNDARIES FOR *IN VIVO* BREAST ULTRASOUND AND STRAIN IMAGES.**

AM Sommer[1], A Milkowski[2], G Funka–Lea[3], GA Sisney[1], GK Hesley[4], ES Burnside[1], L Grady[3], MP Jolly[3], TJ Hall[1].*

[1]University of Wisconsin–Madison, Madison, WI, USA; [2]Siemens Medical Solutions Ultrasound Division, Issaquah, WA, USA; [3]Siemens Corporate Research, Princeton, NJ, USA; [4]Mayo Clinic, Rochester, MN, USA.

Background: A robust measure of the ratio of lesion area in strain to B–mode images is a useful criterion to improve breast ultrasound specificity, but the busy work environment of an imaging center reduces the reliability of this measure [1].

Aims: Our goal was to compare an automated lesion boundary detection method currently available on the Siemens ACUSON S2000 with radiologists' manually drawn lesion boundaries in B–mode and strain images.

Methods: Radiofrequency echo data was acquired from a Siemens Elegra with freehand scanning of *in vivo* breast tissue. B–mode and strain images were formed off–line. Forty–eight (48) benign and fifty (50) malignant lesions were selected to represent the total data set of 403 lesions. Three radiologists (A, B, and C) independently viewed the B–mode sequence, chose a representative frame, and drew the lesion boundary. The radiologists then viewed the corresponding combined B–mode and strain image sequence, chose a representative strain image and drew the lesion boundary in the strain image [2]. An automated segmentation algorithm [3], available on the Siemens ACUSON S2000, was used to obtain a lesion boundary in each of the frames selected. The displacement estimates obtained in strain image formation were used to warp four frames surrounding each selected frame back to the geometry of that selected frame. Automated boundaries were then obtained from each of these motion–compensated images as well as the averaged image. The automated boundaries from each of the motion–compensated images were compared to the automated boundary from the averaged image using the overlap measure to ensure that the automated boundary was consistent through a consecutive sequence of images. The automated and manually drawn boundaries were then compared using the overlap measure for each lesion and radiologist. The overlap measure is the area of the intersection of the two lesion boundaries divided by their union. The ratio of lesion area in strain to that in B–mode was also calculated.

Results: The automated boundaries provide a consistent lesion boundary over five consecutive images in both B–mode (0.82) and Strain (0.76). When the radiologists' boundaries were in modest agreement (overlap > 0.1), the automated boundaries were representative of the manual tracings in both the B–mode and elasticity images (B-mode–0.69, Strain–0.62). The lesion size ratio specificity at the 100% sensitivity improved when using the automated boundaries (A–35%, B–35%, C–25%) over the manual boundaries (A–2.5%, B–20%, C–12.5%).

Conclusions: The automated lesion boundaries provide a good representation of boundaries traced independently by three radiologists in the majority of cases. Thus, the automated segmentation algorithm can be used to provide a lesion boundary with minimal user input.

Acknowledgements: We are grateful for the support from the NIH (R01–CA100373), and to colleagues at the Mayo Clinic in Rochester, MN and the Charing Cross Hospital in London, UK for providing some of the data used in this study.

References:

[1] Regner, D.M., et al. Breast lesions: evaluation with US strain imaging – clinical experience of multiple observers. Radiology 2006; 238(2):425–37.

[2] Burnside, E.S., et al. Differentiating Benign from Malignant Solid Breast Masses with US Strain Imaging. Radiology 2007l 245(2): 401–10.

[3] Jolly, M.P., Grady, L. 3D general lesion segmentation in CT. IEEE International Symposium on Biomedical Imaging Book of Abstracts, May, 2008.

* *indicates Presenter*

042 **REGIONAL ANESTHESIA GUIDANCE USING ACOUSTIC RADIATION FORCE IMAGING.**

ML Palmeri[1], JJ Dahl[1], D MacLeod[1], S Grant[1], KR Nightingale[1].*
[1]Duke University, Durham, NC, USA.

Background: B–mode imaging is used to help guide anesthetic injections during regional nerve blocks. B–mode imaging relies on acoustic impedance mismatches to scatter and reflect acoustic energy to generate images. While needles can be brightly hyperechoic with significant shadowing beneath them, misalignment between the needle and the imaging plane can make visualization of the needle challenging. Nerves can also be difficult to visualize with B–mode imaging because they do not have appreciable ultrasonic contrast with adjacent soft tissues (muscle, fat, fascia). Acoustic Radiation Force Impulse (ARFI) imaging utilizes acoustic radiation force to impulsively excite tissues with a modified diagnostic scanner, and the dynamic mechanical response of the tissue is monitored using conventional ultrasonic tracking methods with the same transducer. ARFI images display relative differences in tissue elasticity/stiffness that can provide improved contrast of soft tissue structures over B–mode imaging [1].

Aims: The goal of this work is to demonstrate that ARFI imaging can improve the visualization of nerves and needles to help guide regional anesthesia procedures.

Methods: ARFI imaging was performed using a modified Siemens SONOLINE™ Antares scanner using a VF10–5 linear array (7–10 MHz) and a VF7–3 linear array (4–7 MHz). Multiple focal zone excitations ranging from 10–25 mm in depth were utilized with 100–200 cycle radiation force excitations spanning a lateral region of interest of ~20 mm. ARFI and B–mode image reconstruction was performed offline. Displacements were estimated using Loupas' algorithm on IQ data acquired with 4:1 parallel receive tracking. Imaging was performed *in situ* on cadavers and *in vivo* in human brachial plexus and femoral and sciatic nerves. B–mode and ARFI images were acquired before, during and after saline injections.

Results: ARFI images demonstrate that nerves display mechanical contrast relative to their adjacent tissue that can be much greater than their acoustic contrast in B–mode images. We have demonstrated a contrast improvement up to 600% in an ARFI image when compared with the corresponding B–mode image (0.6:0.1). Needles can be visualized as regions of decreased displacement (relatively stiff). While needles in B–mode images can be difficult to visualize at steep angles of insertion and when misaligned with the imaging plane, ARFI images are able to clearly delineate their location, allowing anesthesiologists to have better localization of needle tips relative to nerves of interest.

Conclusions: ARFI imaging can enhance the visualization of nerves, needles and injected anesthetic during regional nerve blocks by taking advantage of the mechanical contrast between these structures. This improved image guidance during nerve block procedures should improve nerve block efficacy, resulting in improved pain management and functional outcomes while reducing complications and adverse side effects.

Acknowledgements: We thank Siemens Medical Solutions for their technical support, Dr. Gregg Trahey for his valuable insights and NIH R01 CA114075.

References:

[1] K.R. Nightingale et al. On the feasibility of remote palpation using acoustic radiation force, J Acoust Soc Am 2001;110:625–34.

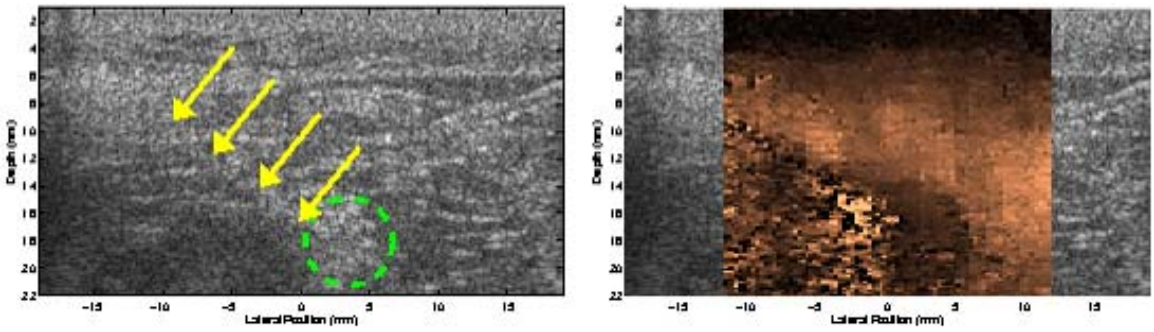

(a) B–mode Image (b) ARFI Image

Figure 1: B–mode (a) and ARFI (b) images of a cadaveric sciatic nerve (dashed circle) *in situ* with an 18 gauge needle (arrows) approaching the upper left corner of the nerve.

* *indicates Presenter*

023 **HIGH QUALITY NON–INVASIVE RADIAL STRAIN ESTIMATION FOR SUPERFICIAL VESSELS USING BEAM–STEERING AND RADIAL LEAST SQUARES STRAIN ESTIMATION.**

Hendrik HG Hansen[1], Richard GP Lopata[1], Chris L de Korte[1].*
[1]Clinical Physics Laboratory, Radboud University Nijmegen Medical Center, Nijmegen, The NETHERLANDS.

Background: Non–invasive strain imaging of superficial vessels requires a conversion from axial and lateral data to radial strains. Last year, a beam–steering approach was presented that enabled the construction of high quality radial strain images for the entire vessel cross section [1]. For each beam–steering angle, axial strains were projected in radial direction for a small segment of the cross–section. Segments were combined to form a compound radial strain image for the entire cross–section. However, a conversion of axial and lateral displacements to radial displacements, followed by deriving radial strains and compounding might increase the quality; radial strains can be derived for larger circle segments, since axial and lateral displacements can be measured up to 60° and higher with respect to the insonification angle, whereas axial and lateral strains approach zero at 45°. Consequently, fewer and smaller acquisition angles would be required to construct a compound radial strain image.

Aims: This study investigates whether the compounding of radial strains estimated from radial displacements outperforms the compounding of radial strains derived from axial and lateral strains.

Methods: Rf data of four cross–sections of a homogeneous vessel phantom (8% gelatin, 2% agar, 1% SiC scatterers) with a concentric lumen were acquired with a Philips SONOS 7500 system, equipped with a linear array transducer (11–3L). Pre and post compression data of the cross–sections were acquired at beam–steered angles of –45, –30, –15, 0, 15, 30 and 45 degrees. In addition, rf data of a cross–section of a geometrically similar phantom were simulated with Field II. A 2D coarse–to–fine cross–correlation based algorithm was applied to estimate axial and lateral displacements for each pair of pre and post compression images. The axial displacements were projected in radial direction for circle segments ranging from –60° to +60° with respect to the insonification angle. For the remainder of the cross–section lateral displacements were projected in radial direction. A 1D LSQSE was applied radially to estimate radial strains. Three radial strain images were constructed for each cross–section, using 0° data; –15°, 0° and 15° data; and –30°, –15°, 0°, 15° and 30° data, respectively. Also, a reference strain image was constructed by principal component analysis of 0° data and a compound strain image was estimated with the "old" technique using data of all 7 angles. Elastographic SNRs and CNRs were calculated for all radial strain images and compared. Finally, the technique was applied for two phantoms with an eccentric lumen: a homogeneous and a "soft plaque" phantom made up of a stiff outer layer and a softer inner layer.

Results: For the simulations, SNR_e and CNR_e increases of 4.2 dB, and 6.8 dB; 6.9 dB and 13.5 dB; and 8.3 dB, and 14.8 dB were found with respect to the reference image when using data of 1, 3 and 5 angles respectively. The "old" approach using 7 angles resulted in an improvement of only 5.8 dB, and 10.5 dB with respect to the reference image. For the concentric phantom, SNR_e and CNR_e increased with 5.5 dB ± 1.4 dB, and 18.0 dB ± 6.8 dB using 5 angles, compared to increases of 2.3 ± 1.7 dB, and 12.6 ± 5.4 dB with the "old" approach. Compound strain images for the two eccentric phantoms constructed with the new technique are shown in Figure 1. The strain pattern clearly reveals the position of the soft layer.

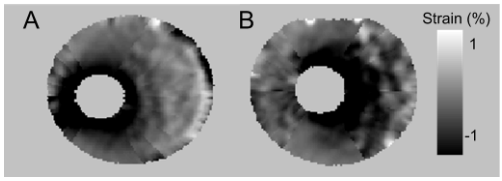

Figure 1: Compound radial strain images of A: a homogeneous phantom, and B: a 'soft plaque' phantom with an eccentric lumen

Conclusions: Compounding of radial strains estimated from radial displacements outperforms the compounding of radial strains derived from axial and lateral strains: higher image quality is achieved using fewer and smaller acquisition angles. Furthermore, the method can be applied for vessels with an eccentric lumen.

Acknowledgements: The support of the Dutch Technology Foundation (STW) and Philips Medical Systems.

References:

[1] H.H.G. Hansen, R.G.P. Lopata, and C.L. de Korte, "Compounding non–Invasively obtained strain images at large insonification angles", 6th Intl Conf on the Ultrasonic Meas & Imag of Tiss Elas, p.30, November, 2007.

* *indicates Presenter*

009 **A COMPARISON OF 3D STRAIN IMAGE QUALITY USING FREEHAND 3D IMAGING AND A MECHANICALLY-SWEPT 3D PROBE.**

RJ Housden[1], AH Gee[1], GM Treece[1], RW Prager[1], GP Berry[2], L Garcia[2], JC Bamber[2].*
[1]University of Cambridge, Engineering Department, Cambridge, England, UK; [2]Institute of Cancer Research, Sutton, Surrey, England, UK.

Background: 3D strain visualization is potentially useful for producing a complete picture of the anatomy and accurately measuring the volume of any stiff inclusion. Currently, there are two approaches to quasi–static 3D strain imaging. The freehand approach uses a tracked 2D probe to produce a sequence of B–scans located in 3D space. Pairs of images are compared sequentially to produce a set of 2D strain images covering a 3D volume [1]. Alternatively, a mechanically–swept 3D probe can be used to record two overlaid volumes of ultrasound data with a small freehand compression between them. Images from one volume are compared to corresponding images in the other volume, again producing a 3D volume of strain data [2]. There are fundamental differences between these two approaches, both in the processing that creates the strain images and the stress distribution produced by the different probe footprints. As a result, the achievable strain image quality varies between the two methods.

Aims: The aim of this work is to investigate the relative quality of 3D strain data produced using the freehand and mechanically–swept approaches.

Methods: We compared the two approaches experimentally, using a GE RSP6-12 mechanically–swept probe and an 8–16 MHz linear array probe attached to a Dynamic Imaging Diasus ultrasound machine. Both had a 3 cm depth setting and an image width of 2.7 cm. The 3D probe has a footprint of approximately 5 cm laterally by 5.5 cm elevationally. The 2D probe face is 3.5 cm × 0.9 cm. Processing of the data, including a linear depth–dependent normalization, was done using Stradwin [3].

Results: Figures 1(a–b) show sample 3D scans of a breast biopsy phantom with a stiff spherical inclusion (approx. 12 mm diameter) in a uniform stiffness background material, recorded using each of the two approaches. For comparison, Figure 1(c) shows a scan using the 3D probe in the freehand scanning protocol with the transducer fixed in the centre of the probe, effectively a freehand scan with a footprint extender. While there may be variations in the results in terms of resolution and noise level, the most noticeable artifactual differences are caused by the size of the probe face and the associated change in the stress distribution. In particular, the two results using the 3D probe (b and c) have a more significant stress concentration artifact at the top of the inclusion (the bright white region) and appear stiffer in the region just in front of the probe face. In comparison, the freehand scan (a), which has a smaller compressor area, produces images with a more uniform background. The fact that the artifacts also occur in (c) shows that the stress distribution, rather than the signal processing, is most significant.

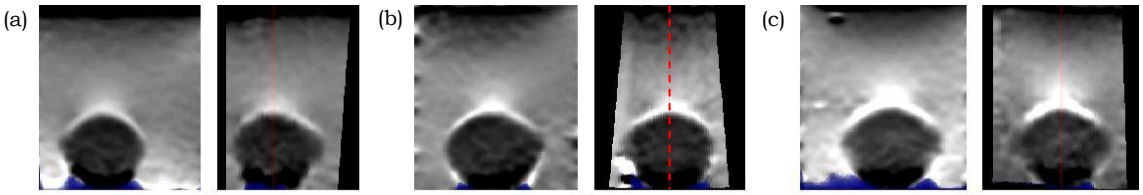

Figure 1: Axial strain images derived from three scans of a stiff inclusion using the different scanning protocols. (a) Freehand. (b) Mechanically swept 3D probe. (c) 3D probe used in a freehand scanning protocol. In each case, the left image is an axial–lateral view from the centre of the 3D data set and the right is an axial–elevational re–slice along the length of the scan. The thin dashed red line in the re–slice images indicates the intersection with the axial–lateral view. In these images, white indicates regions of high strain, while black represents lower strain. The blue at the bottom masks regions with low precision strain estimates.

Conclusions: 3D scans obtained using a mechanically–swept 3D probe produce noticeably different strain images to those obtained with a freehand scanning approach. It is therefore important to take account of the method used to obtain the scans when interpreting 3D strain data. These results indicate that the main cause of the differences is the varying stress distributions produced by probes with different footprints. Scans with a smaller compressor appear to produce better images with a more uniform background strain level, although further experimentation and simulations will be required to confirm this.

Acknowledgements: This work was supported by EPSRC grant number EP/E030882/1.

References:

[1] Lindop J, Treece G, et al. 3D elastography using freehand ultrasound. UMB 32:529–545, 2006.
[2] Treece G, Lindop J, et al. Freehand ultrasound elastography with a 3–D probe. UMB 34:463–474, 2008.
[3] http://mi.eng.cam.ac.uk/~rwp/stradwin.

* *indicates Presenter*

027 **THE EFFECT OF ELASTIC CONTRAST ON ACOUSTIC RADIATION FORCE IMPULSE IMAGING AXIAL RESOLUTION.**

Manoj G. Menon[1,2], Stephen A. McAleavey[1,2].*
[1]Biomedical Engineering Department; [2]Rochester Center for Biomedical Ultrasound, University of Rochester, Rochester, NY 14627, USA.

Background: Acoustic Radiation Force Impulse (ARFI) imaging measures the mechanical properties of tissue by generating a local acoustic radiation force using a standard diagnostic ultrasound scanner. Short duration, high intensity ultrasound pulses are used to induce impulsive acoustic radiation forces that result in micron–scale tissue displacements. Displacements are tracked using ultrasound tracking pulses and are quantified using conventional correlation–based methods. ARFI imaging may be used to find objects of various shapes and sizes, and elasticity values. The ability to detect such objects can be quantified using measures of elastic contrast (reported here in terms of Young's modulus ratio) and resolution. In this study, we were interested in measuring axial resolution of our ARFI imaging system in the physiologically relevant Young's modulus ratio range between 1 and 4 [1]. It is critical to understand the potential relationship between these measures in order to understand the limits of this modality's ability to detect local disease.

Aims: The goal of this study was to measure the axial resolution of an ARFI imaging system as a function of the ratio of Young's modulus values of the hard, and soft portion of gelatin–based tissue phantoms. The experimental results were to be verified using a computational model.

Methods: The ARFI imaging system used was a Siemens Antares ultrasound scanner (Siemens Medical Systems) and a VF10–5 linear array transducer. Each beam sequence included a 30 μs pushing pulse followed by 29–0.15 μs tracking pulses (at a pulse repetition frequency (PRF) of 12.7 kHz), both with a 6.67 MHz center frequency. For this study, we captured and analyzed images over a period of 1.2 ms after the push. Five phantoms were created with adjacent hard and soft regions (ranging between 16 to 20 kPa, and 4 to 17 kPa, respectively) which provided the contrast necessary for a step response at a depth of 2 cm from the transducer (given that the elevational and lateral foci are set at 2 cm). The elastic contrast in these phantoms had a range of 1.1 to 4.2. These experiments were also modeled using COMSOL/FEMLAB. Displacements from our FEA analysis were applied to a field of scatterers using MATLAB and FIELD II. The displacement data of both the experiment and the computational model had a 1 μm noise floor, making direct measurement of the point spread function impractical. Instead of filtering the data, and thereby artificially degrading the resolution, a representative sigmoid function was found to represent the step responses using a nonlinear least squares curve fitting routine. The derivative of the sigmoid function was calculated, and the FWHM of the resulting point response was measured and reported as the resolution.

Results: Axial resolution with a 1 mm correlation window was found to be linearly dependent on the elastic contrast. As the Young's modulus ratio decreased from approximately 4.2 to 1.1, the minimum resolution degraded from approximately 1 mm to 3 mm. Both the experimental and computational results showed agreement.

Conclusions: The linear relationship between axial resolution and elastic contrast of our ARFI imaging system was illustrated. Axial resolution was found to reduce significantly with a change in physiologically relevant values of elastic contrast.

Acknowledgements: Grants include the Wallace H. Coulter Foundation Early Career Award. In–kind and technical support was provided by Siemens Medical Solutions USA, Ultrasound Group.

References:

[1] T. A. Krouskop, T. M. Wheeler, F. Kallel, B. S. Garra, T. Hall. Elastic moduli of breast and prostate tissues under compression. Ultrasonic Imaging, Vol. 20, No. 4, pp. 260–274, 1998.

* *indicates Presenter*

068 **VISUALIZATION OF 3D ELASTOGRAPHY DATA.**

R. Zahiri-Azar[1], A. Brant[1], S.E. Salcudean[1].*
[1]The University of British Columbia, Vancouver, BC, CANADA.

Background: Recent advances in elastography make it possible to measure the mechanical properties of soft tissue not only in the cross–sectional plane but also in the entire volume [1,2]. As a result scientific visualization techniques that reveal the full anatomy in 3D and assist both scientists and physicians in understanding the underlying tissue structure are becoming necessary.

Aims: To study several visualization techniques that best depict tissue structures in 3D strain volumes.

Methods: An experiment was performed on a breast phantom using the experimental set up shown in Figure 1a. A Sonix–RP Ultrasound (US) machine (Ultrasonix Medical Corp., Richmond, Canada) with a 4DC6–3/40 motor–driven transducer was used for this study. Similarly to conventional 2D strain imaging, pre– and post–compression RF echo volumes were acquired using the Propello SDK package. A mechanical stage was used to compress the phantom in the axial direction between data acquisitions. The phantom was imaged to a depth of 60mm with a 128 element curved linear array transducer with 5MHz center frequency digitized at 40MHz with 0.5 degree frame spacing. The axial displacements between the corresponding sets of RF frames from the two volumes were estimated using the Time Delay Estimator with Prior Estimates (TDPE) [3] using 1mm x 1mm windows with 50% window overlap. Sub–sample displacement estimates were then calculated using a cosine interpolation method. The Least Squares Estimator (LSE) with a kernel size of 4 was then used to estimate the strain from the displacement data. Once 2D strain images were calculated, 3D strain volume was generated by stacking the 2D strain images.

Results: 3D displacement and strain volumes with their corresponding correlation coefficients are shown in Figure 1. Visualizing with multi–planar slicing, volume rendering with adjusted transparency, and surface fitting based on the threshold value [4] are shown in Figure 1e–f. The hard inclusion is well visualized and can be clearly detected in all the strain volumes.

Conclusions: Multi–planar slicing is the most computationally straightforward method to review data through the volume. Interactive display of planar slices offers retrospective evaluation of anatomy, particularly viewing of arbitrary planes perpendicular to the acquisition plane and orientations not possible during data acquisition, but it increases the scanning time. Surface fitting based on a certain threshold produces clear visualization of a tissue region with high strain contrast. However, artifacts can be easily introduced and misinterpreted as abnormality in the tissues by using this technique due to strain concentration or false positive and negative surface pieces. Furthermore, the selection of proper threshold plays an important role in the performance of this approach. The volume rendered images show the entire strain data set, depending on opacity and intensity values. Thus, they do not introduce ambiguity in the interpretation. However, the segmentation is not as clear as the surface fitting method.

References:

[1] T.G Fisher et al, Volume Elasticity Imaging with a 2D Capacitive Micro–Machined Ultrasound Transducer Array, Fifth Intl. Conf. on Ultrasonic Measurement and Imaging of Tissue Elasticity, Snowbird, USA, Page 125, 2006.
[2] G.M. Treece, J.E. Lindop, A.H. Gee, R.W. Prager, Freehand Strain Imaging with a 3D Probe, Sixth Intl. Conf. on Ultrasonic Measurement and Imaging of Tissue Elasticity, Santa Fe, USA, Page 66, 2007.
[3] R. Zahiri–Azar, S. Salcudean, Motion Estimation in Ultrasound Images using Time Domain Cross Correlation with Prior Estimates, IEEE Transactions on Biomedical Imaging, 53(10), pp. 1990–2000, 2006.
[4] T.R. Nelson, T.T. Elvins, Visualization of 3D Ultrasound Data, IEEE Computer Graphics and Applications, 13(6), pp. 50–57, 2002.

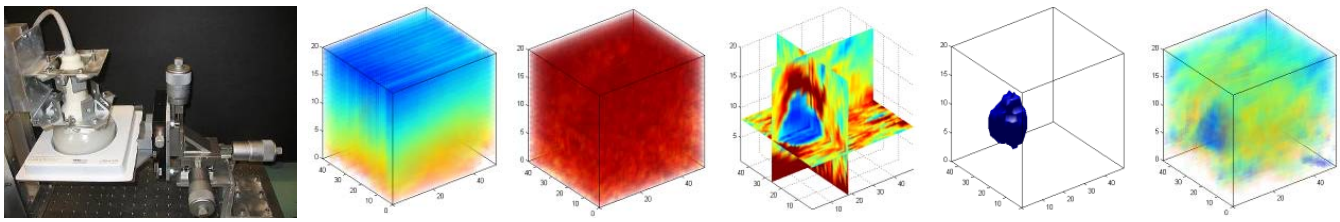

(a) (b) (c) (d) (e) (f)

Figure 1: (a) Experimental setup showing the ultrasound 4D probe and the breast phantom, (b) estimated displacement images, (c) with its corresponding correlation coefficient, and (d) generated 3D color coded multi–planer, (e) surface fitted and (f) volume rendered strain volumes obtained by stacking 2D planes estimated from echo signals are shown.

028 **FREE–SHAPE 2D KERNELS FOR IMPROVED MEASUREMENT OF ROTATIONS AND STRAINS IN SHEARING STRUCTURES.**

RGP Lopata[1], MM Nillesen[1], HHG Hansen[1], IH Gerrits[1], JM Thijssen[1], CL de Korte[1].*
[1]Clinical Physics Laboratory, Radboud University Nijmegen Medical Center, Nijmegen, The NETHERLANDS.

Background: 2D and 3D RF–based strain imaging is used in a variety of applications. However, in cardiac and vascular applications, shearing and rotational movement of tissue often occur.

Aims: This study examines the feasibility of measuring rotations using 2D kernels of RF data by using two different methods. The methods were also tested on a shearing object.

Methods: A block (5 cm x 5 cm) of 3.5 million randomly distributed scatterers was rotated for a range of angles, 0.5°, 1.0°, 2.0°, 3.0°, 4.0°, 5.0° and 10°. No deformations were applied. RF data were simulated using Field II© for a linear array with a center frequency of 7.5 MHz and a pitch of 135 μm, resulting in an image depth of 5.0 cm and width of 3.0 cm. A similar phantom was compressed 2.0% in the axial direction in combination with 2.25% axial shearing. Displacements were estimated using a coarse–to–fine 2D displacement/strain estimation algorithm with 2D parabolic interpolation for sub–sample displacement estimation and additional sub–sample aligning of kernels (Method I, [1]). A different approach was developed, in which the kernel shape was not limited to a box–shaped 2D region (Method II). Coarse axial displacement estimates were used to freely deform the kernel in the axial direction, resulting in kernels shaped such as parallelograms. Both methods were applied to the aforementioned simulation data and the displacements, rotation angles and cross–correlation values were measured.

Results: The simulation study revealed that rotations can be measured up to 5.0° using both methods. Analysis was limited to the center area of the image (2.5 cm x 2.5 cm) in order to properly compare displacements in both directions. The maximum axial and lateral displacements at 0.5° and 5.0° were ±0.15 mm and ±1.5 mm respectively. The root–mean squared error (RMSE) between the applied and measured, unfiltered, displacements was calculated. For Method I, the RMSE ranged from 0 to 0.25 mm in the axial and from 0.015 to 0.23 mm in the lateral direction. Method II yielded displacements with a lower RMSE, ranging from 0 to 0.06 mm in the axial direction and up to 0.10 mm in the lateral direction. The measured cross–correlation decreased for larger angles (0.5 to 5.0°) from 0.92 to 0.58 for Method I and from 0.92 to 0.68 for Method II. A maximum improvement of 0.13 was found for a 3.0° rotation. After reconstruction of the rotation angle, the mean angles were 0.49, 0.99, 1.97, 2.96, 3.95, and 4.88, with a mean standard deviation of 15–29%. However, reconstruction of angles revealed artifacts near the axis of rotation. Rejecting this region lowers the standard deviation to 7–9% and is angle–independent. For the shearing object, an increase in axial and lateral SNRe was found of +6 dB and 3.2 dB respectively. Both axial and axial shear strain revealed an SNRe of 28 dB.

Conclusions: The proposed new 2D method enhances the measurement of rotation and shearing movements. Findings revealed that rotations can be measured up to 5.0°. Additional validation of the method should be performed for simultaneously rotating and deforming tissue in simulation and experimental data. Furthermore, the feasibility of torsion measurements has to be examined. The preliminary findings for shearing structures are also promising.

Acknowledgements: The support of the Dutch Technology Foundation (STW) and Philips Medical Systems.

References:

[1] Lopata RGP, et al., *In vivo* 3D cardiac and skeletal muscle strain estimation. Proc. IEEE Ultrasonics Int. Conf., Vancouver, Canada, p.744–747, 2006.

** indicates Presenter*

004 **FAST, VARIABLE SMOOTHING OF STRAIN DATA USING NONPARAMETRIC REGRESSION.**

GM Treece[1], JE Lindop[1], AH Gee[1], RW Prager[1].*
[1]University of Cambridge, Cambridge, England, UK.

Background: Quasi–static strain images generally require filtering, whether explicit or implicit in the displacement tracking window or gradient estimation kernel. Such filtering can improve the SNR of the data but will reduce the resolution [1]. Nonparametric surface regression (NPR) is a promising tool for this purpose, due to its inherent ability to use all the available data in an optimal way, increasing the resolution for a given SNR [2]. Additionally, the resolution can be varied with the raw data quality, leading to strain images with uniform SNR. NPR has previously been applied to displacement data. However, optimal quasi–static strain images require some form of temporal persistence, and this is applied to normalized strain, rather than displacement, data. Furthermore, persistence does not work well over images with varying resolution, hence variable smoothing by NPR must be applied after persistence.

Aims: To apply NPR in real time to persisted, unfiltered, normalized strain data, in order to generate quasi–static strain images with good resolution and more uniform SNR.

Methods: We implement NPR for strain images using the roughness penalty approach. We minimize a cost, C, expressed in matrix form as $C = (\acute{s}-\hat{s})^T W(\acute{s}-\hat{s}) + \acute{s}MTM\acute{s}$, where $\hat{s}$ are the raw strain estimates, $\acute{s}$ the smoothed values, W is a matrix of raw strain precisions and $\acute{s}MTM\acute{s}$ expresses the sum of squares of the first derivative of axial strain in both dimensions. C is minimized by the solution of $(W+MTM)\acute{s} = W\hat{s}$. Since W is diagonal, MTM is block tri–diagonal, and the combination is symmetric positive definite, this equation can be solved very efficiently by a combination of pseudo–direct and iterative linear algebra techniques [3,4]. The performance is demonstrated on an *in vitro* scan of half an olive in agar. NPR is compared to piecewise–linear least squares regression (PLLSR) [5] and 2D precision–weighted Gaussian filtering.

Results: Strain images are shown in Figure 1, with a grid size of 127 x 291, and displacement tracking window of 8 cycles with a slight overlap. A simple difference was used for gradient estimation before NPR or Gaussian smoothing. The olive boundary is blurred by PLLSR, which also introduces artifacts such as the black–white bands at the lower centre of the image. Gaussian smoothing is more successful, but the boundary is still blurred, and the olive appears larger as the smoothing is increased. NPR generates better images in all cases: at lower smoothing levels, the higher variance data below the olive is still smoothed over, and, at higher levels, the olive boundary is still well preserved. Gradient calculation and filtering measured on a 2.4 GHz laptop averaged 11ms (PLLSR), 18ms (Gaussian) and 36ms (NPR).

Conclusions: NPR has been demonstrated, in real time on normalized strain data, to generate smoothed images which have visually better resolution and SNR than PLLSR or weighted Gaussian smoothing.

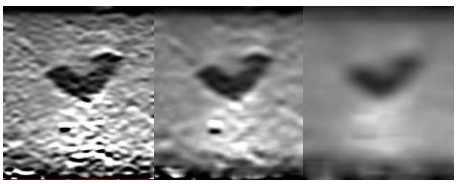

(a) PLLSR

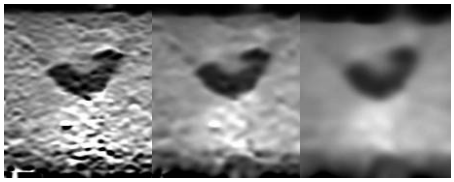

(b) Precision–weighted Gaussian

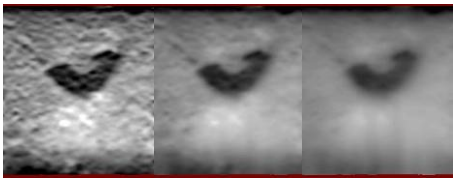

(c) NPR

Figure 1: Strain images of half–olive phantom, with three levels of smoothing. The kernel sizes for (a) and (b) and the smoothing levels for (c) have been matched visually.

Acknowledgments:
Graham Treece is supported by a Royal Academy of Engineering/EPSRC Research Fellowship.

References:

[1] JE Lindop, GM Treece et al The general properties including accuracy and resolution of linear–filtering methods for strain estimation, IEEE Trans UFFC, in press.
[2] JE Lindop, GM Treece et al Nonparametric surface regression for strain estimation, Tech. Rep. CUED/F–INFENG/TR 598, Cambridge Uni. Dept. Engineering, 2008.
[3] C Millar, A Asenov et al Excessive over–relaxation method for multigrid Poisson solvers, J. Comput Elect. 1:341–345, 2002.
[4] RS Varga Matrix Iterative Analysis, Springer, 2000.
[5] F Kallel, J Ophir A least–squares strain estimator for elastography, Ultrasonic Imag. 19:195–208, 1997.

043 **IMPROVEMENT OF DISPLACEMENT ESTIMATION USING AUTOCORRELATION.**

Seungsoo Kim[1], Suhyun Park[1], Salavat R. Aglyamov[1], Matthew O'Donnell[2], Stanislav Y. Emelianov[1].*

[1]Biomedical Engineering Department, The University of Texas at Austin, Austin, TX, USA; [2]Bioengineering Department, University of Washington, Seattle, WA, USA.

Background: In elasticity imaging, ultrasound frames acquired during tissue deformation are analyzed to estimate internal displacements and strains. Generally, it is critical to estimate sub–pixel level displacements precisely. This is especially true if the deformation rate of the tissue is small. To track integer level displacements, block matching algorithms based on correlation, sum of absolute differences (SAD), or sum of squared differences (SSD) are widely used. Then, sub–pixel level displacements are often estimated using phase–zero crossing or parabolic interpolation of the matching function.

Aims: The main objective of this study is to increase the quality of elasticity imaging via improved estimation of displacement vector components.

Methods: If the same frame is fed into the displacement estimator including integer and sub–pixel level estimates, the outputs of the estimator are non–zero although the input frames are exactly the same. Since non–zero displacement outputs are always less than one pixel, we assumed that these errors originate during sub–pixel level estimates. Consequently, the same errors are produced during displacement estimation between two neighboring frames. Therefore, by subtracting autocorrelation displacements from displacements obtained from cross–correlations (Figure 1), the errors produced during sub–pixel level estimation can be reduced. To evaluate the feasibility of this approach, we performed experimental measurements using a phantom with a single inclusion approximately 2.5 times harder than the background. The phantom was deformed in 0.3% strain increments. To track both axial and lateral displacements, a 2–D region was searched using a 2–D kernel. For the integer level displacement, the normalized cross–correlation was used. Then, the sub–pixel lateral displacement was calculated by parabolic interpolation, and axial displacement was estimated using phase–zero crossing interpolation. For fair comparison, no other post–processing, such as filtering, was applied.

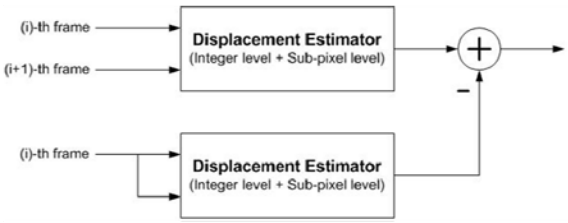

Figure 1: Block Diagram

Results: The quality of lateral displacements was dramatically improved while improvement of axial displacement was not significant in the phantom studies (Figure 2). Since the autocorrelation method removes displacement errors from parabolic interpolation, the developed approach can also be adapted to SSD or SAD methods where parabolic interpolation is used to estimate the sub–pixel displacement.

Conclusions: The results of this study suggest that autocorrelation approach can improve the displacement quality due to the elimination of errors from sub–pixel level interpolation of correlation.

Acknowledgements: This study was partially supported by the NIH under grants EB 004963 and HL 091609.

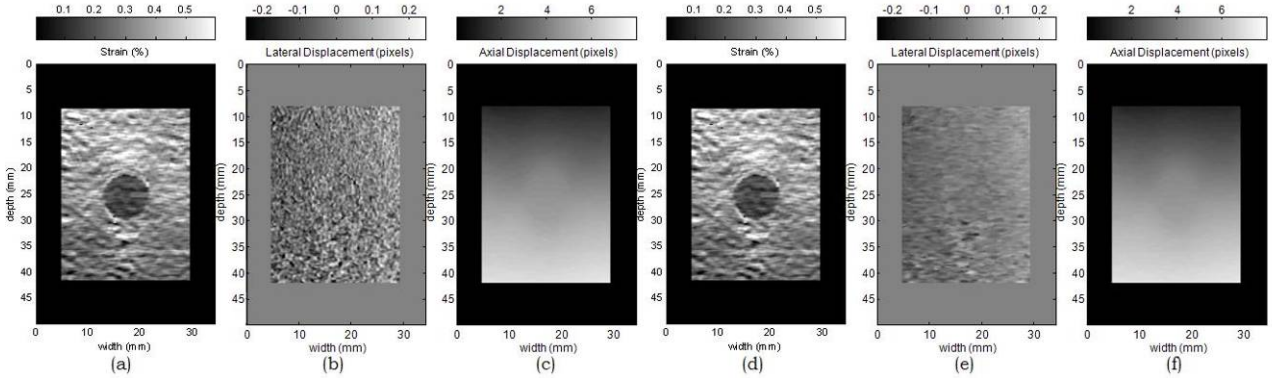

Figure 2: Phantom with an inclusion (0.29% deformation)
(a), (b), (c): strain, lateral and axial displacement images without sub–pixel level displacement error correction;
(d), (e), (f): strain, lateral and axial displacement images with sub–pixel level displacement error correction.

* *indicates Presenter*

070 **TIME-DELAY ESTIMATION USING INDIVIDUAL SAMPLE TRACKING.**

R. Zahiri-Azar[1], S.E. Salcudean[1].*
[1]The University of British Columbia, Vancouver, BC, CANADA.

Background: Typically, time–delay estimators measure the average time–shift/phase–shift/frequency–shift of a number of samples within a certain window in a delayed echo signal with respect to the reference echo signal. Alternatively features in the echo signals can be found and tracked (e.g. zero–crossing tracking, ZCT, and level–crossings tracking).

Aims: To improve the performance of time–delay estimators, for small delays, by finding the delay of every signal sample with a new class of delay estimation algorithms called Sample Tracking (ST) algorithms. With this class of algorithms, the delay of each sample in an echo signal is measured with respect to a continuous, interpolated representation of the reference echo signal.

Methods: Let $s_1[i]$ be a discrete sampling of the reference echo signal and $s_2[i]$ be a discrete sampling of the delayed echo signal, where $i=0,1,\ldots n-1$ and n is the number of samples. Let $f(t), t\in[0,\infty]$, be a continuous interpolation of s_1 (i.e. a continuous approximation of the original echo signal based on the acquired samples) such that $f(iT)=s_1[i]\forall i,$. The displacement of each individual discrete sample in the delayed echo signal $s_2[i]$, with respect to the reference signal $s_1[i]$ can be estimated by finding t such that $f(t)=s_2[i]$. These delay estimates are not subject to sampling quantization. The ST approach is illustrated in Figure 1a. For estimating time–delays larger than one sample, the coarse location of each sample needs to be available prior to running ST. In this work, normalized cross correlation NCC is used first to find the coarse estimation of the time–shifts of a number of samples. ST is then applied to find the fine sub–sample time–shift of each sample. ST algorithms can be implemented with numerous interpolation schemes to provide continuous approximations to the original signal. In this paper, ST using cosine fitting, polynomial fitting, and cubic spline fitting were implemented.

Results: Computer simulations were performed to compare the performance of the ST algorithms with the commonly used time–delay estimators in terms of bias, standard deviation, and resolution as a time delay estimator. The strain filter of the ST was also studied. The RF data were created by convolving Gaussian distributed white noise (zero mean and unit standard deviation) as scatterers with sinc-enveloped sinusoid point spread function (fs=40MHz, fe=5MHz, B=0.5). The results are shown in Figure 1.

Conclusions: ST using cubic spline fitting outperforms commonly used time–shift and phase–shift estimators in terms of bias, standard deviation, and resolution. When used as a strain estimator, the proposed method also has higher sensitivity compare to conventional methods.

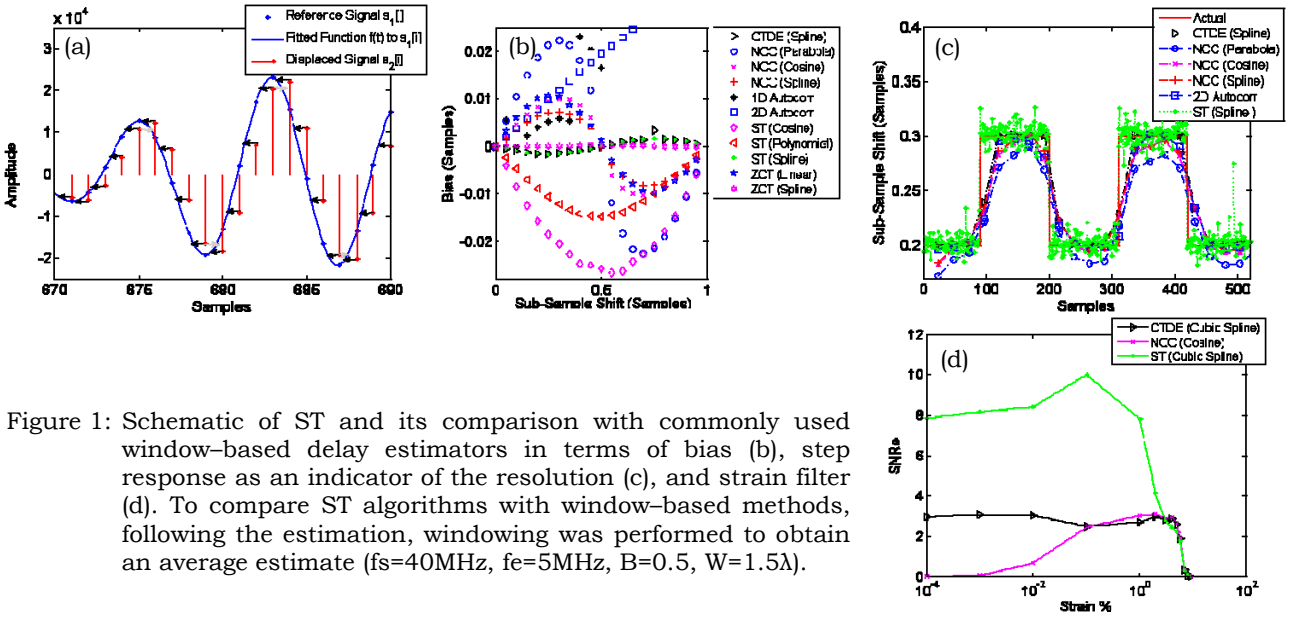

Figure 1: Schematic of ST and its comparison with commonly used window–based delay estimators in terms of bias (b), step response as an indicator of the resolution (c), and strain filter (d). To compare ST algorithms with window–based methods, following the estimation, windowing was performed to obtain an average estimate (fs=40MHz, fe=5MHz, B=0.5, W=1.5λ).

* *indicates Presenter*

001 **A MULTI–DIRECTIONAL DISPLACEMENT TRACKING ALGORITHM FOR STRAIN IMAGING.**

Lujie Chen[1], Graham M. Treece[1]. Joel E. Lindop[1], Andrew H. Gee[1], Richard W. Prager[1].*
[1]University of Cambridge, Cambridge, England, UK.

Background: Displacement estimation plays a key role in many strain imaging techniques. A displacement tracking approach can eliminate the time consuming exhaustive search from displacement estimation [1–3]. This not only enhances computational efficiency but also increases the continuity of the resultant deformation distribution. However, if a tracking path progresses in a fixed direction, it may have to traverse poorly correlated regions of the ultrasound echo signal or boundaries between regions where there is a discontinuity in the deformation. In such situations, erroneous estimates are likely to be produced and the algorithm will probably "lose track". As a result, the deformation distribution of a highly correlated region may not be correctly estimated due to errors encountered at an earlier stage.

Aims: A multi–directional displacement tracking algorithm is proposed to circumvent problems associated with tracking through geometrically irregular and disjointed regions. The algorithm is designed to track around regions of poorly correlated radio frequency (RF) data.

Methods: Prior to the multi–directional tracking process, several seeding data blocks are located in an ultrasound RF frame. This is achieved by performing exhaustive block–matching on a sparse grid of data blocks. The location of each seeding block is then added to a list, which is sorted in quality–descending order. Here, quality refers to the reliability of the estimation. We use the magnitude of the correlation between two analytic RF signals recorded pre– and post–deformation as the quality measure. The tracking path progresses in a quality–guided manner. At each step, the highest quality data block (the first one in the list) is processed by the phase–zero search algorithm [1] to obtain a refined displacement and quality. Its unprocessed 4–way neighbours are assigned the refined displacement and quality as their initial predictions and are inserted into the list based on the quality–descending order. Displacement tracking terminates when the list is empty. The algorithm is tested on homogeneous simulated data with varying noise and also on various inhomogeneous simulations and *in vivo* data sets that contain geometrically irregular regions or regions with discontinuous deformation distributions.

Results: Tests on the homogeneous data demonstrate that the proposed algorithm is as robust to additive noise as previous work [3]; while results on inhomogeneous data confirm the superior tracking ability of the multi–directional approach. An example is shown in Figure 1(a), a simulated data set with 1% uniform strain. An omega–shaped region contains white noise. Strain distributions obtained by conventional A–line tracking and multi-directional tracking are shown in Figures 1(b) and (c) respectively. Figure 2 illustrates the progression of the multi–directional tracking process. Unprocessed regions are indicated in white. Each colour indicates a region grown from a distinct seeding block. Note that the tracking paths are prevented from traversing the noisy region until the last stage of tracking.

Conclusions: The multi–directional tracking algorithm can minimize the undesired effects of noise corrupted regions in deformation estimation. This is achieved with very little additional processing time.

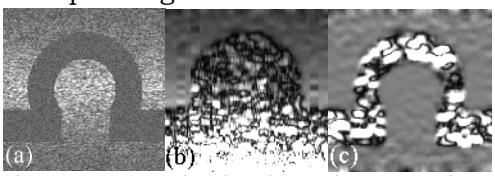

Figure 1: (a) A simulated RF data set. The omega–shaped region contains white noise only. Strain distribution obtained by (b) tracking along A–lines; (c) the multi–directional tracking algorithm with phase–zero-search [1] as the matching criterion.

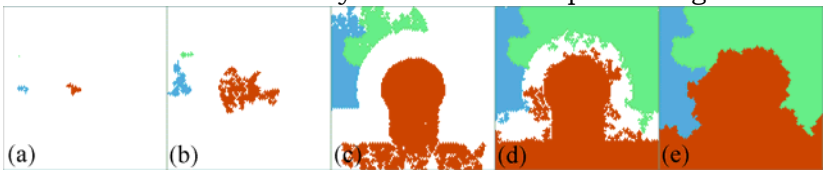

Figure 2: Propagation progress of the multi–directional tracking algorithm. Unprocessed regions are indicated in white. Each colour indicates a region grown from a distinct seeding block.

Acknowledgements: This work was funded by Translation Award 081511/Z/06/Z from the Wellcome Trust.

References:

[1] A. Pesavento, C. Perrey, M. Krueger, and H. Ermert. A time efficient and accurate strain estimation concept for ultrasonic elastography using iterative phase zero estimation. IEEE Transactions on Ultrasonics, Ferroelectrics, and Frequency Control, 46, 1057–1067, 1999.
[2] Y. Zhu and T. J. Hall. A modified block matching method for real–time freehand strain imaging. Ultrasonic Imaging, 24, 161–176, 2002.
[3] G. M. Treece, J. E. Lindop, A. H. Gee, and R. W. Prager. Efficient elimination of dropouts in displacement tracking. Proceedings of Ultrasonic Measurement and Imaging of Tissue Elasticity. Snowbird, Utah, USA, p. 68. 2006.

* *indicates Presenter*

059 **A GENERALIZED SPECKLE TRACKING ALGORITHM FOR ULTRASONIC STRAIN IMAGING USING DYNAMIC PROGRAMMING TECHNIQUE.**

Jingfeng Jiang[1] and Timothy J. Hall[1].*
[1]Medical Physics Department, University of Wisconsin–Madison, 1300 University Ave., 1530 MSC, Madison, WI, USA.

Background and Aims: Although ultrasound–based elasticity imaging is under rapid development, it is still challenging to track complex tissue motion *in vivo* in certain organs where complex anatomies (e.g. thyroid and uterine) often result in motion during scanning, which is less than ideal. This work demonstrates that speckle tracking can be regularized by a dynamic programming technique (i.e., Viterbi Algorithm) to adaptively enforce physical motion continuity, thereby allowing more accurate and robust motion tracking and axial strain image formation than conventional correlation–based algorithms.

Methods: We modeled the motion estimation task (i.e. block–matching) in a restricted solution space. The restriction/regularization in the solution space was applied to avoid inter–wave length errors resulting from false correlation peaks, since tissue motion should be reasonably continuous. A novel feature is that a set of cost functions combining correlation and various levels of motion continuity constraint targeting different organs (e.g. breast versus thyroid) were used to restrict the motion estimation. Three different cost functions (i.e., motion discontinuity versus penalty), namely total variation, approximate power law and exponent functions representing minimal (e.g., in the presence of body wall and cavity, etc.), intermediate (e.g., thyroid) and high (e.g., breast) motion continuity, respectively, were investigated. To solve the optimization problem with a reasonable time, a dynamic programming technique that does not require iterations was used to obtain displacement vectors in integer precision. Then, a sub–sample estimation algorithm was used to calculate local displacements in fractional precision. Various implementation schemes, including predictive search and multi–grid approaches, were investigated with *in vivo* breast and thyroid ultrasound echo data sets [1] and data acquired from an anthropomorphic tissue–mimicking uterine phantom [2].

Results: We found that the proposed algorithm provides more accurate displacement estimates than our previous un–regularized algorithm [3] for *in vivo* clinical data. In particular, the new algorithm is capable of tracking motion in more complex anatomy (i.e., thyroid) and increases strain image consistency in a sequence of images. Preliminary results also suggest that a significantly longer sequence of high contrast strain images could be obtained with the new algorithm compared to the previous algorithm [3]. The new algorithm can also tolerate larger motion discontinuities (e.g. cavity filled with saline in an anthropomorphic uterine phantom) with the minimal continuity cost function, as shown in Figure 1.

Conclusions: We demonstrated the proposed algorithm allows accurate motion tracking and axial strain image formation for a variety of *in vivo* data sets (imaging tasks) investigated.

Acknowledgements: We gratefully acknowledge the support by NIH grant R01CA100373. We are also grateful to colleagues at the Mayo Clinic in Rochester, MN (especially Drs. Nicholas Hangiandreou and Gina Hesley) for the *in vivo* thyroid data and the University of Wisconsin (especially Prof. Ernest Madsen and Ms. Maritza Hobson) for providing the uterine phantom data. Last, but not least, we want to thank Dr. Liexiang Fan at the Ultrasound Division of the Siemens Medical Solution (USA) Inc. for his helpful discussion on dynamic programming.

References:

[1] T. J. Hall, Y. Zhu, and C. S. Spalding, Ultrasound Med Biol, vol. 29, pp. 427–35, 2003.
[2] M. A. Hobson et al., Ultrasound Med Biol, 2008, in press.
[3] Y. Zhu and T. J. Hall, Ultrasonic Imaging, vol. 24, pp. 161–176, 2002.

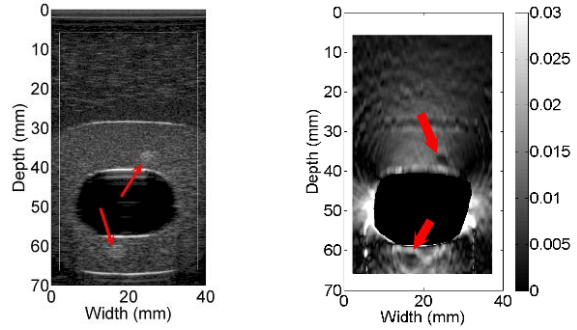

(a) B–Mode Image (b) Strain Image

Figure1: (a) B–mode and (b) strain images obtained from an anthropomorphic uterine phantom with two spherical inclusions (arrows) using the proposed speckle tracking method. The white box on the B–mode image defines the ROI from which the displacements and strains were estimated using above-mentioned algorithms. The saline with the simulated cavity causes signal decorrelation and motion tracking errors, resulting in decorrelation noise on the strain images. The simulated cavity was masked to avoid visual distraction.

091 **APPLICATION OF NON–RIGID REGISTRATION TO VALIDATE DETECTION OF PROSTATE CANCER USING THREE–DIMENSIONAL SONOELASTOGRAPHY.**

Benjamin Castañeda[1], Shuang Wu[1], Kenneth Hoyt[2], Laurie Baxter[3], Jorge Yao[3], David Pasternack[3], John Strang[3], Deborah J. Rubens[3] and Kevin J. Parker[1].*

[1]University of Rochester, 206 Hopeman Building, Rochester, NY, USA; [2]University of Alabama at Birmingham, 817 Boshell Building, 1808 7th Avenue South, Birmingham, AL,USA; [3]University of Rochester Medical Center, 601 Elmwood Ave., Rochester, NY, USA.

Background: Prostate cancer is the most prevalent type of cancer in men and the second most frequent cause of cancer death in adult males after lung cancer. Previous work has shown that sonoelastography is a promising imaging technique for tumor detection in prostate [1]. In order to validate the results from these experiments, a registration step between the sonoelastographic and the histological volumes is required. Previously, rigid registration has been proposed [2], but deformations due to histological processing of the gland suggest that non–rigid registration should obtain better results.

Aims: This work evaluates the application of non–rigid registration to validate the detection of prostate cancer when compared to histology.

Methods: Five prostate glands were received after radical prostatectomy and examined *ex vivo*. The specimens were embedded in a 10.5% gelatin mold and vibrated using an external piston at a combination of frequencies (105, 140, 175 and 210 Hz). A GE Logiq 9 ultrasound (US) scanner was used in conjunction with a positioning device to acquire B–mode and sonoelastographic volumes. The surface of the gland was segmented from the US images and the tumors from sonoelastographic images using a 3D segmentation algorithm [3]. After imaging, the gland was step–sectioned following a whole–mount histological procedure [1,2]. From these histological images, a volume was reconstructed and registered to the US and sonoelastographic volume using the surface of the gland as a marker. The registration process was composed of four steps. First, a rigid registration was used to align the volumes. Then, an affine transformation allowed compensation for shear and scale. Finally, a deformable B–spline registration with a coarse grid was applied followed by another one with a finer grid. Tumors detected with sonoelastography were compared to findings from histology. The distance between their centers of mass in the co–registered space was measured after affine and deformable registrations.

Results: Seven tumors were detected by sonoelastography in the five glands. Their average estimated diameter was 10.2±2.4 mm measured in sonoelastographic images versus 10.7±3.3 mm measured in the histological images. The average distance between the centers of mass in the sonoelastographic volumes and histological volumes was 9.8±4 mm after applying affine registration and was reduced to 7.4±3.2 mm after non–rigid registration. Figure 1 shows an example of the difference images obtained after affine and non–rigid registration. Histology revealed two other tumors which were not detected by sonoelastography with 3.9 mm and 4.2 mm in estimated diameters.

Conclusions: These preliminary results suggest that deformable registration can help in the validation process of prostate cancer detection with sonoelastography by overcoming the non–rigid deformations from the histological processing of the gland.

Figure 1: Difference images after affine (left) and non–rigid (right) registration.

Acknowledgements: This study was partly supported by NIH grant 5 RO1 AG016317–07.

References:

[1] Taylor, LS, et al., Prostate cancer: Three–dimensional sonoelastography for *in vitro* detection. Radiology, Volume 237, No. 3, December 2005, p. 981–985.

[2] Castaneda, B, et al., Prostate cancer detection based on three dimensional sonoelastography. Proceedings of the IEEE Ultrasonics Symposium, New York, NY, 2007, pp. 1353–1356.

[3] Castaneda, B, et al., Measurement of thermally–ablated lesions in sonoelastographic images using level set methods. Proceedings of SPIE Medical Imaging, San Diego, CA, 2008, Volume 6920, pp. 692018–1–692018–9.

* *indicates Presenter*

077 **PROPER POINT SPREAD FUNCTION FOR LATERAL MODULATION.**

C. Sumi[1], Y. Komiya[1], S. Uga[1].*
[1]Sophia University, 7–1, Kioicho, Chiyodaku, Tokyo 102–8554, JAPAN.

Background: We have realized the beamformings [1–3], by using steering of the multiple beams and apodization, for accurately measuring tissue or blood displacement vectors or strain tensors [4] using the multidimensional cross–spectrum phase gradient method (MCSPGM), and autocorrelation and Doppler methods (MAM and MDM). In [1–4], we reported lateral cosine modulation methods (LCMMs) that use several apodization functions in addition to the multidirectional synthetic aperture method (MDSAM) and the multiple transmitting method (MTM). As shown, the coherent superimposition of the steered beams performed in LCMM has a higher potential for realizing a more accurate measurement of a displacement vector than the synthesis of the displacement vector using the accurately measured axial displacements performed in MDSAM and MTM. However, in LMMs, MDSAM and MTM can also be used to obtain multiple steered beams. If necessary, multiple transducers are also used (e.g., for heart). These modulations can also be used for B–mode imaging simultaneously [1-3].

For these beamformings, in [1,3], we also reported more proper apodization functions than the Gaussian functions we proposed previously, i.e., parabolic functions and Hanning windows. Echo data having wider lateral bandwidths and higher signal–to–noise ratios (SNRs) can be obtained. Moreover, we also reported an optimization method [1,3] for obtaining the best apodization function in a least squares sense, i.e., the best approximated designed point spread function (PSF) can be obtained.

Aims: First, in order to gain insight about the ideal shape of the PSF, the accuracies of the 2D displacement vector measurements were compared for typical PSFs with distinct lateral envelope shapes (i.e., full width at half maximum (FWHM) and length of the feet). Next, for the PSFs used, by calculating the PSFs and spectra using a typical type transducer model and the apodization functions obtained by the respective optimization method and Fraunhofer approximation, we compare the accuracies of the realized PSFs. Thus, we report a proper apodization function that is obtained from both results.

Methods: We simulate laterally modulated echo data using the PSFs having lateral envelopes, i.e., Gaussian function (GA), Hanning window (HA) and parabolic function (PA). For the three PSFs with the same energy, the order of FWHMs is, PA > HA > GA, whereas that of the lengths of their feet is, GA > HA > PA. The PSFs with the same beamwidth are also used. For both cases, the accuracies of the 2D displacement vector measurements are evaluated. Rigid motions and strains (0.1–4%) are respectively simulated (ultrasound (US) frequency = lateral modulation frequency, fy, 1–5 MHz; axial and lateral SDs, 0.4–0.8 mm; SNR of echo, 10–30 dB). Next, for the three PSFs used, the respective Fraunhofer approximation (FA) and linear and nonlinear optimization (LO and NLO) methods [5] are used such that the corresponding apodization functions, which yield the same intensity of a transmitted US beam, can be obtained (element size, λ; height, 5.0 mm; the space between elements, 0.1 mm; beam pitch, 0.1 mm). In NLO, the feet of the apodization function are cut during the iteration of LO. The corresponding PSFs and spectra are calculated using Field II.

Results: For the simulated echo data, the orders of the measurement accuracies of displacements were, PA > HA > GA. Furthermore, all the obtained apodization functions were able to approximate the three PSFs; for PA, by comparing the lateral profiles obtained by FA, LO and NLO. Significantly, NLO yielded a wide lateral bandwidth, i.e., a more accurately approximated PSF was obtained. However, LO made the feet of the PSF slightly longer.

Conclusions: For LCMM, a PSF having a wider FWHM was ideal. Moreover, NLO yielded a wide bandwidth even for such an ideal PSF. That is, NLO was effective for realizing such an ideal PSF. In addition, NLO allowed the decrease in the channels or the confinement of the effective aperture. Other PSFs to be considered as proper ones on the basis of the results are also described in [1,2]. In addition, analogue design or dynamic programming method will also be used to realize the best PSF.

References:

[1] C. Sumi et al., Japan J. Appl. Phys., vol. 47(5B), 4137, 2008.
[2] C. Sumi et al., IEEE 2007 Int. Ultason. Symp., 1557, 2007.
[3] C. Sumi et al., IEEE Trans. UFFC (in press) 2008.
[4] C. Sumi et al., IEEE Trans. on UFFC, vol. 55, 24, 2008.
[5] C. Sumi et al., Proc. of Fall Meeting of Acoust. Soc. of Japan, 1–2–4 and 1–2–5, 2008.

053 **VISCOELASTIC PROPERTIES OF THE HUMAN BRAIN ANALYZED BY A NOVEL TWO–COMPARTMENT EFFECTIVE MEDIUM MODEL.**

Sebastian Papazoglou[1], Dieter Klatt[1], Jürgen Braun[2], Ingolf Sack[1].*
[1]Radiology Department, [2]Institute of Medical Informatics, Charité Berlin, Berlin, GERMANY.

Background: Magnetic resonance elastography (MRE) is a noninvasive imaging modality that employs the motion sensitivity of the MR phase signal to visualize externally induced shear vibrations inside the human body [1]. From the measured MRE shear wave data, the complex modulus can be deduced. Classically, the frequency dependence of the complex modulus is evaluated by rheological models comprising up to four independent viscoelastic constants [2]. However, the physical significance of those moduli with respect to tissue architecture is limited. Therefore, a new viscoelastic model is introduced accounting for material composites of pure elastic and pure viscous constituents.

Aims: To estimate the size and density of local scatterers of shear waves that fit to the modulus dispersion observed in MRE experiments of *in vivo* human brain.

Methods: To study the influence of shear wave scattering on the complex modulus dispersion a simple composite-material model is used. An elastic matrix is combined with randomly distributed and purely viscous cylindrical inclusions. Scattering is treated by considering the independent scatterer approximation (ISA) [3]. In ISA, the effective complex modulus $G_{eff}(\omega)$ reads to first order in f (filling ratio of cylinders in percent):

$$G_{eff}(\omega) = \frac{\rho\omega}{k_0^2}\left(1+\frac{f\,t}{\pi R^2 k_0^2}\right), \qquad (1)$$

where t is the forward scattering amplitude, R is the cylinder radius, ρ is the density of the matrix and k_0 is the wave number in the matrix material. Simulations are compared to experimental MRE data of *in vivo* human brain acquired at 25, 37.5, 50 and 62.5 Hz driving frequency.

Results: The results shown in Figure 1 demonstrate that modulus dispersion observed in our experiments can be explained by multiple shear wave scattering giving rise to an effective medium. The loss modulus is mainly due to the viscosity of the inclusions. Instead, accounting for purely elastic inclusions does not match the modulus dispersion of our brain MRE experiments.

Conclusions: Our model achieves a local separation of the storage properties and the loss properties of a viscoelastic material. This enables us to study tissue architecture in terms of viscous cylinders included in an elastic matrix. Although this represents a strong simplification of real tissue structures, it may help to gain information from experimental modulus data beyond classical viscoelastic constants.

References:

[1] Muthupillai R, Rossmann PJ , Lomas DJ, Greenleaf JF, Riederer SJ, Ehman RL. Magnetic resonance imaging of transverse acoustic strain waves. Magn Reson Med 1996; 36: 266–274.
[2] Klatt D, Hamhaber U, Asbach P, Braun J, Sack I. Noninvasive assessment of the rheological behavior of human organs using multifrequency MR elastography: a study of brain and liver viscoelasticity. Phys Med Biol 2007; 52: 7281–7294.
[3] Lagendijk Ad, van Tiggelen BA. Resonant multiple scattering of light. Phys Rep 1996; 270: 143–215.

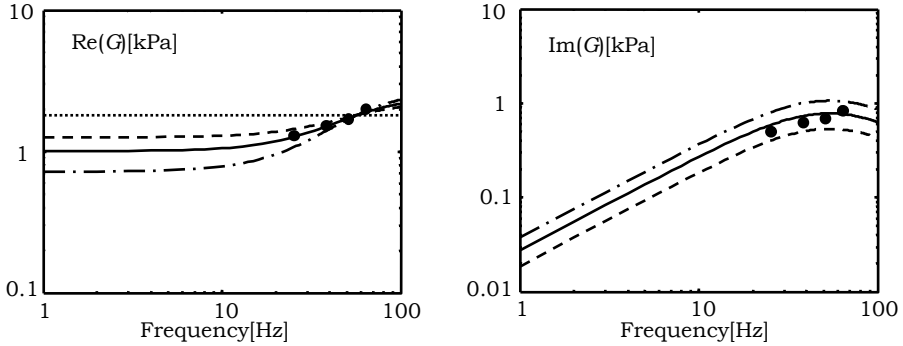

Figure 1: The complex modulus according to [1] was evaluated at 0% (dotted), 15% (dashed), 22% (straight) and 30% (dashdotted) filling ratio. The shear modulus of the matrix was chosen empirically with 1.8 kPa while the viscosity of the inclusion material was 5 Pa. Cylinder radius was R=0.5 mm. Dots represent experimental data.

* *indicates Presenter*

037 **MECHANICAL AND HISTOLOGICAL CHARACTERIZATION OF HUMAN FETAL MEMBRANES.**

Mahmood Jabareen[1], Julien Egger[1], Ajit Mallik[2], Grozdana Bilic[2], Andreas Zisch[2], Edoardo Mazza[1].*
[1]Mechanical Engineering Department, Swiss Federal Institute of Technology, 8092 Zurich, SWITZERLAND; [2]Obstetrics and Gynecology Department, University Hospital Zurich, 8091 Zurich, SWITZERLAND.

Background: Preterm premature rupture of the fetal membranes (PPROM) is a major cause of preterm birth. Until now, there is no method for repairing ruptured fetal membranes. It is, therefore, important to develop an understanding of the structural components of the human fetal membrane and their mechanical properties.

Aims: In the present study, human fetal membranes from pre–labor cesarean delivery were subjected to biomechanical testing and in parallel to biochemical and histological analysis. Specifically, biochemical analysis was performed on each tissue sample subjected to mechanical experiments, in order to correlate the measured mechanical response with tissue's microstructure (elastin and collagen content). The mechanical properties of the fetal membranes were characterized by uniaxial tensile and so called "inflation tests".

Methods: Two different types of mechanical tests were used in the present study, namely, uniaxial and inflation experiments. For the uniaxial characterization of the fetal membrane, samples were extracted and tested in a standard uniaxial tensile test setup. The samples were comfortably fixed outside the test setup on clamps equipped with sandpaper, leaving an initial gage length of 40 mm. In the inflation experiments, a piece of membrane was clamped in a ring and then fluid pressure was applied. The inflation experiment produced a biaxial state of stress, which most closely represents physiological loading conditions. Thickness of the fetal membrane was measured after histological preparation, with the Axiovert 200M Zeiss Microscope. For the biochemical analysis, different types of assays were used. Specifically, the elastin content was determined by using the fastin elastin assay.

Results: Uniaxial tests on the fetal membrane showed highly nonlinear behavior of the nominal stress versus nominal strain (see Figure 1). From the complementary histological analysis, it was found that there was good correlation between one of the material parameters of the Rubin–Bodner [1] model and the elastin content (see Figure 2). Other correlations between the parameters of the constitutive equations and the total Collagen content will be presented.

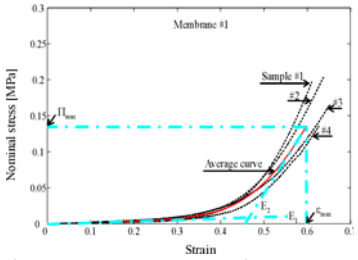

Figure 1: Stress–strain curves

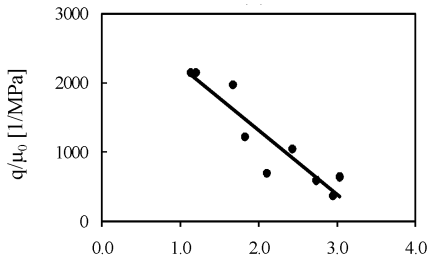

Figure 2: Correlation between the elastin content and the ratio q/μ_0

Conclusions: This study provides quantitative information on the uniaxial and biaxial mechanical response of human fetal membranes. Constitutive model parameters were determined from the experimental data. First data on the correlation between mechanical parameters and biochemical indices (e.g. elastin content) support the feasibility of a quantitative analysis of the mechanical behavior based on tissue's microstructure.

References:

[1] Rubin M. B., Bodner S. R., A three–dimensional nonlinear model for dissipative response of soft tissue, International Journal of Solids and Structures, 39, 5081–5099, 2002.

007 **MENSTRUAL CYCLE DEPENDENCE OF *IN–VIVO* BREAST ELASTICITY MEASURED USING ULTRASOUND INDENTATION.**

Jia–Wei Li[1], Suk–Tak Chan[1], Yan–Ping Huang[1], Xin Chen[1], Yong–Ping Zheng[1,2].*
[1]Health Technology and Informatics Department, [2]Research Institute of Innovative Products and Technologies, Hong Kong Polytechnic University, Hong Kong, CHINA.

Background: Ultrasound elasticity imaging using quasi–static compression has been widely used in breast tumor diagnosis. Although promising, factors such as semi–quantization without scaling the force applied [1] and physiological changes of breast elasticity during the menstrual cycle [2] may result in misdiagnosis. It has been reported that, due to female sex hormones, female breast morphology, proliferative and secretive activities, density, volume and blood flow exhibit cyclical changes during the menstrual cycle. However, there is lack of *in–vivo* information about the menstrual cycle dependence on breast tissue elasticity. One recent study based on magnetic resonance (MR) elasticity measurements showed breast elasticity variations during the menstrual cycle, however, the theory and subject position is different compared with measurements performed using ultrasound elastography [3].

Aims: This study aimed to measure elasticity of breast tissues *in–vivo* using ultrasound and to investigate the changes as a function of the menstrual cycle.

Methods: A specialized ultrasound probe with a force sensor attached was developed to record the force applied on the tissue and the corresponding deformation during the manual indentation. The elasticity index was calculated from the force–deformation data. The system validations, including force validation and temporal calibration, were performed with an electronic scale and springs respectively. The repeatability of manual indentation was tested on both silicon phantoms (n=7) and on normal female subjects (n=5, age=28±5) *in–vivo*. Ensuring that the system is consistent and repeatable, a preliminary study on two of the 5 subjects was conducted to investigate the changes over the menstrual cycle. Four quadrants were defined on both breasts for each subject. For each quadrant, five repeated tests were conducted and the results were averaged. Examinations were carried out every five to six days for one menstrual cycle.

Results: High intra–class correlation coefficients (ICC>0.95) indicated good measurement repeatability in phantoms and *in–vivo* test. Results from the two subjects indicated breast tissue elasticity changes during the menstrual cycle (Figure 1). The error bars in Figure 1 represents the SD (n=16) of the elasticity index from all quadrants of the two subjects. Differences of the breast elasticity at the four quadrants were also found (Figure 2).

Conclusions: It is believed that the results of site dependence and menstrual cycle dependence of breast tissue elasticity difference will provide a useful reference and guidance for the clinical use of ultrasound elasticity imaging. More convincing results are expected to be obtained by enlarging the sample size.

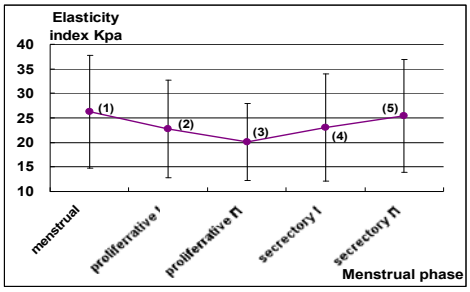

Figure 1: Tissue elasticity changes within a menstrual cycle.

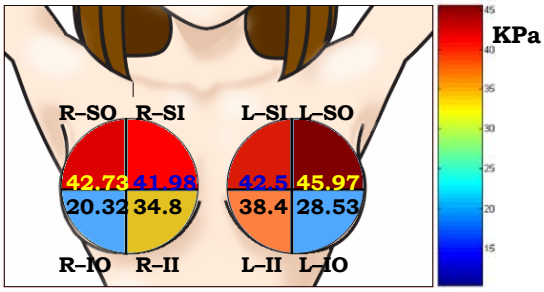

Figure 2: Differences of tissue elasticity in the four quadrants.

Acknowledgements: This project is partially supported by the HKSAR Research Grant Council (PolyU5318/05E) and the Hong Kong Polytechnic University (1–BB69).

References:

[1] Itoh A, Ueno E, Tohno E, Kamma H, Takahashi H, Shiina T, Yamakawa M, Matsumura T. Breast disease: Clinical application of US elastography for diagnosis. Radiology 239: 341–350, 2006.
[2] Wojcinski S, di Liberto A, Cassel M, Ertan AK, Schmidt W. Menstrual–cycle dependence of breast parenchyma elasticity determined by real time sonoelastography: finding the optimal time for examination. Breast Cancer Res Treat 94:208–208, 2005.
[3] Lorenzen J, Sinkus R, Biesterfeldt M, Adam G. Menstrual–cycle dependence of breast parenchyma elasticity: Estimation with magnetic resonance elastography of breast tissue during the menstrual cycle. Invest Radiol 38:236–240, 2003.

* *indicates Presenter*

067 **ELASTOGRAPHIC STRAIN IMAGING OF FLUID FLOW THROUGH PERFUSED TISSUES.**

Gearóid P Berry[1], Ian Rivens[1], John Civale[1], Hugh Morris[1], James McLaughlan[1], Jeffrey C Bamber[1], Gail terHaar[1].*

[1]Institute of Cancer Research, Sutton, Surrey, SM2 5NG, England, UK.

Background: Soft biological tissue contains mobile fluid which flows when the host tissue is compressed. Previously we investigated this coupling between fluid flow and strain in tofu [1] and in soft biological tissue *in vivo* [2]. Our investigations suggested that the combination of strain imaging with poroelastic theory could eventually be used to obtain new diagnostic information about the target tissue, specifically in relation to fluid flow characteristics. However, to further investigate the link between strain and fluid flow, it would be helpful to use an intermediate imaging medium that possesses all the biological complexity and flow characteristics of living tissue, while allowing a degree of control over its properties.

Aims: This paper describes a series of experiments in which strain images were obtained during elastographic examination of isolated perfused porcine livers through which blood was made to flow.

Methods: In total, the livers of three pigs were removed. The livers were preserved as though awaiting organ transplantation using a technique described previously [3]. The liver was then scanned using an L10–8 linear array transducer connected to a Z.one ultrasound scanner (Zonare Medical Systems Inc, Mountain View, CA, USA). A centrifugal pump was used to drive a continuous stream of perfusate through the liver before and during the examination. The perfusate consisted of oxygenated porcine blood, complete with all the nutrients necessary to maintain a functioning organ for up to 72 hours [3].

Results: Figure 1 shows a B–Mode image of one of the perfused livers. A number of echo–poor blood vessels are visible on the scan plane and clearly illustrate the inflated nature of the vasculature. Figure 2 shows a corresponding co–registered pair of freehand elastograms: one obtained during the downward phase of the freehand palpation cycle and the other during the upward phase. On compression, the large compressive strain endured by tissue close to the vessels shows that the vasculature was highly compressible. This suggests that the blood was rapidly displaced through the vasculature allowing the host tissue to locally compress. As the compression was withdrawn, the large positive strain experienced by the region around the vessels demonstrates that fluid rushed back into the vessels.

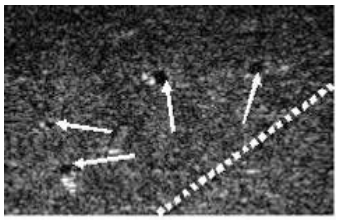

Figure 1: B–Mode image with arrows indicating the visible vasculature. Dotted line indicates the slip interface between liver segments.

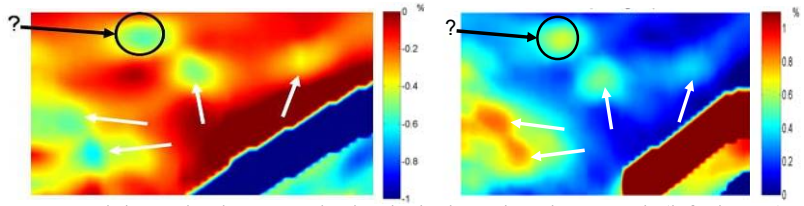

Figure 2: Axial strain images obtained during the downward (left image) and upward (right image) phases of the freehand palpation cycle. The white arrows are in the same positions as those in Figure 1 and indicate unusually high strain magnitudes. The black circle encloses a region that behaves similarly to the regions pointed to by white arrows, but which does not have an obvious vascular counterpart in the B–mode image.

Conclusions: In this study, elastography was performed for the first time on an isolated perfused organ, and the fundamental link between strain and fluid flow was demonstrated with vascular fluid flowing through living biological tissue. At each point in the B–mode image where a blood vessel was present, the corresponding region in the strain images displayed unusually high strain. Intriguingly, this pattern also occurred for a region (circled in Figure 2) that did not contain any obvious vasculature in the B–mode image. This suggests that strain imaging combined with poroelastic theory may have the potential to identify fluid flow through tissue regions even when the blood vessels are too small to be imaged directly.

Acknowledgements: We are grateful to Professor Friend and his staff for organ preparation and making their facilities available to us. This work was funded by the Engineering and Physical Sciences Research Council, UK.

References:

[1] Berry et al. Towards an acoustic model–based poroelastic imaging method: II. experimental investigation. UMB 2006;32(12):1869–1885.

[2] Berry et al. The spatio–temporal strain response of oedematous and non–oedematous tissue to sustained compression *in vivo*. UMB 2008;34(4):617–629.

[3] Butler et al. Successful extracorporeal porcine liver perfusion for 72 HR. Transplantation 2002;73(8);1212–1218.

* *indicates Presenter*

041 **SHEAR MODULUS RECONSTRUCTION IN THE REGION OF EXCITATION USING ACOUSTIC RADIATION FORCE.**

ML Palmeri[1], D Xu[1], KR Nightingale[1].*
[1]Duke University, Durham, NC, USA.

Background: Tissue stiffness (shear modulus, μ) can be used to identify pathological states in various tissues (e.g., liver fibrosis). In radiation force–based modalities, quantitative stiffness reconstruction is typically performed by monitoring shear wave propagation laterally offset (off–axis) from the region of excitation (ROE) [1]. These methods have good accuracy and are robust across different experimental parameters but typically require greater radiation force to achieve adequate SNR at laterally–offset positions and longer data acquisition times. These drawbacks motivate an "on–axis" reconstruction method that examines the displacement dynamics along the axis of symmetry in the ROE to estimate stiffness, resulting in improved SNR, decreased tissue/transducer heating and minimized temporal tracking domains to reduce motion artifacts. Given homogeneous tissue density, the displacement dynamics on–axis will have a unique correlation with tissue stiffness.

Aims: The primary goal of this work is to reconstruct elastic moduli from the dynamic displacement data along the axis of symmetry in the ROE after an impulsive acoustic radiation force excitation. Secondary goals are to identify and characterize the influence of other factors (e.g., attenuation) that affect on–axis dynamic displacement behavior.

Methods: The relationship between the on–axis displacement dynamics and stiffness (μ=1–15 kPa) were characterized using previously validated 3D finite element method (FEM) models of soft tissue response to impulsive radiation force excitations in conjunction with Field II simulations of ultrasonic displacement tracking with a CH4–1 linear array transducer (2.2 MHz excitation frequency, 3.1 MHz tracking frequency) [3]. These simulations were also used to characterize the dependence of these displacement dynamics on acoustic attenuation (0.3–1.0dB/cm/MHz) [2]. Time–to–peak (TTP) displacement data were measured as a function of depth on–axis, and the linear slope of the TTP data in the near–field (18–37mm) relative to the focal depth (49 mm) was characterized as a function of stiffness to create a lookup database. The same processing was performed on experimental data from materials of unknown stiffness, and a spline–based interpolation was performed to optimize the stiffness estimation from the database of known stiffnesses. This algorithm was validated using simulation data of different stiffnesses and attenuations and tissue–mimicking phantom data. The results of on–axis stiffness predictions were compared to off–axis (Lateral TTP [4]) reconstructions in matched datasets.

Results: The precision of stiffness reconstructions in tracked simulation data (10 speckle realizations) range from 0.1–1.4 kPa over shear moduli ranging from 1–15 kPa. Simulations demonstrate this on–axis method is accurate over a range of acoustic attenuations, with a precision of 0.1 kPa for α = 0.3-1.0 dB/cm/MHz. Reconstructed shear moduli in tissue–mimicking phantoms using this on–axis method (1.6 ± 0.1 kPa) are similar to those using our previously presented Lateral TTP (off–axis) method (1.5 ± .04 kPa) [4]. The axial region of interest (ROI) for each method is similar, but the lateral ROI is ~30x smaller for the on–axis method (0.2 mm vs. 6 mm).

Conclusions: Greater displacement magnitudes are present on–axis, resulting in greater displacement SNR. Measuring displacement dynamics on–axis, instead of at multiple off–axis locations, reduces data acquisition times (and motion artifacts) and the reduced number of transmitted radiation force excitations also reduces transducer/tissue heating. The accuracy of the on–axis method shows a minor dependence on acoustic attenuation, with reconstructed shear moduli still accurate to within ±0.1 kPa. Shear moduli reconstructed with this on–axis method are consistent with those reconstructed with our Lateral TTP method.

Acknowledgements: NIH R01 EB002132 and NIH R01 CA114075.

References:

[1] Sarvazyan et al. "Shear wave elasticity imaging: a new ultrasonic technology of medical diagnostics," Ultrasound in Med. & Biol., 24(9): 1419–1435, 1998.
[2] Palmeri et al. "A finite–element method model of soft tissue response to impulse acoustic radiation force," IEEE UFFC, 52(10): 1699–1712, 2005.
[3] Palmeri et al. "Ultrasonic tracking of acoustic radiation force–induced displacements in homogeneous media," IEEE UFFC, 53(7):1300–1313, 2006.
[4] Palmeri et al. "Quantifying hepatic shear modulus *in vivo* using acoustic radiation force," Ultras. in Med. & Biol., 34(4):546–558, 2008.

* *indicates Presenter*

033 **ESTIMATING SPECTRUM VARIANCE OF ULTRASONIC SIGNAL WITH FREQUENCY SHIFT CAUSED BY THE TRANSITION BAND OF A FILTER.**

Jian Liu[1], Takao Watanabe[1], Nobuaki Kijima[1], Mineyuki Haruta[1], Yoshinobu Murayama[1], Sadao Omata[1].*
[1]NEWCAT, Nihon University, Tamura, Koriyama, Fukushima, JAPAN.

Background: Acoustic attenuation is related to the characterization of differences in tissue structure and composition and is of important clinical value [1]. Linear attenuation coefficient is widely used for the description of attenuation. However, high–order attenuation coefficients also play roles, especially in bioacoustics. The proof of their existence is the fluctuating variance of acoustic spectrum along the propagating path (see Figure 1). Measuring the variance is helpful in providing new information about attenuating features of tissues. However, the traditional FFT–based method is time-consuming.

Aims: Motivated by this, we aim to find a method to simplify the estimation of spectrum variance.

Methods: The principle of our method is the frequency shift incurred by a signal passing through a filter. This includes:

(1) Design a low–pass filter, wherein the resonant frequency, f_c, of transducer is on the transition band of the filter;
(2) Let the raw signal, $x_1(t)$, passing through the filter generate the filtered signal, $x_2(t)$;
(3) Measure the centroid frequency $f_1(t)$ and $f_2(t)$, for $x_1(t)$ and $x_2(t)$ respectively;
(4) Assuming the spectrum of raw signal is of Gaussian shape, and the frequency response of filter H(f) near fc is approximately $\log|H(f)| = k \log f + b$, we can estimate the spectrum variance as

$$\sigma(t) = \sqrt{f_2(t)\left[f_1(t) - f_2(t)\right]/k}$$

Results: Real B–scan data on human abdomen is used to verify the method. The RF signal is acquired from the B–scan device, Aloka SSD–5500. The resonant frequency of transducer, f_c, is 3.5MHz. A first order Butterworth filter is used for filtering, with a cutoff frequency of 2.1MHz, its attenuation slope $k \approx -1$dB/dec. near f_c. For the raw signal, a Short–Time Fourier Transform (STFT) is applied, with a 128–point Hamming Window. The window slides 0.5μs per step. On each step, a 1024–point FFT is undertaken to find the centroid frequency $f_1(t)$. For the filtered signal, a similar process is applied to get $f_2(t)$. Eventually, the variance σ(t) is calculated. In the process of FFT, the real variance σ0(t) is also measured. Figure 1 is a sample RF signal from a scan line of the transducer; the result from our method is similar to that from FFT, with the correlation coefficient $\rho(f_1,f_2) = 0.8580$.

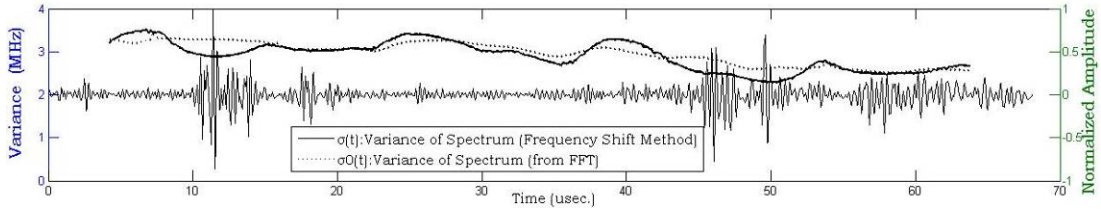

Figure1: The profile of spectrum variance for the RF Signal in a scan line. The dashed line is the variance σ0(t). The solid line is σ0(t) estimated with our method. Assuming the frequency response of tissue is Gaussian shaped, the spectrum variance of each slice of tissue can be calculated.

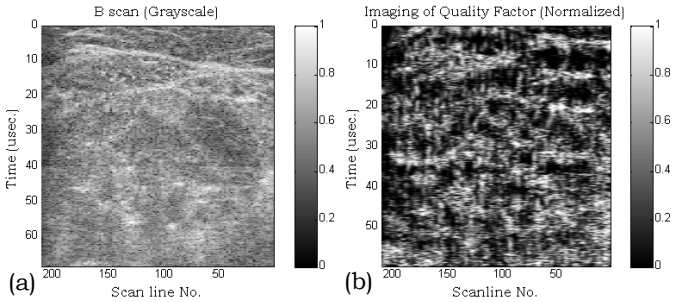

Figure 2: (a) B–scan image of human abdomen;
(b) The Q factor Image. The bright region (high Q) denotes good oscillating property (vessel, muscle, etc.); the dark region (low Q) denotes poor oscillating property (typically, body liquid). The Q factor of each part of tissue can be calculated from Q=f/Δf, where f is the central frequency of signal and Δf is the bandwidth, functionally related to the spectrum variance.

Conclusions: Our method allows a quick estimation for real spectral variance. Figure 2 is an illustration of a simple application. More attractively, with the lower requirement for the computing resources (no calculation for the second spectral moment), it is promising to be implemented as low–cost circuit modules for medical devices.

References:

[1] C. Fournier, et al, Optimization of attenuation estimation in reflection for *in vivo* human dermis characterization at 20 MHz, IEEE Transactions on Ultrasonics, Ferroelectrics and Frequency Control, 50(4),P408–418, 2003.

051 **IS THREE–DIMENSIONAL (3D) AXIAL STRAIN IMAGING LIKELY TO BE WORTHWHILE?**

Leo Garcia[1], Gearóid P. Berry[1], Andrew Woodward[2], Jeffrey C. Bamber[1].*
[1]Institute of Cancer Research, Sutton, Surrey, England, UK; [2]INCAT, Prospect Way, London Luton Airport, Luton, Bedfordshire, England, UK.

Background: Traditional ultrasound (US) elastography images the compression–induced axial strain on a two–dimensional (2D) US scan plane, with a view to understanding the elastic properties of the target tissue. However, mechanical compression is fundamentally a three–dimensional (3D) problem and thus our ultimate goal is to image the full 3D strain tensor. Nevertheless, it is appropriate to first consider whether the simpler problem of imaging the axial strain in three dimensions might be a clinically useful intermediate step, since this is achievable using current commercially available US scanners.

Aims: To investigate, using finite element modeling (FEM), the potential value of imaging axial strain in three dimensions in the presence of a 3D elasticity distribution.

Methods: Commercial FEM software (Marc/Mentat 2007r1, MSC Software Corp, Palo Alto, CA, USA) was used to construct a simple, but clinically relevant, 3D FE model consisting of a stiff spherical inclusion embedded in a softer homogeneous cubic background. Both materials were assumed to be linear elastic, isotropic and incompressible. The model was intended to represent, to a first approximation, a tumor surrounded by healthy tissue. The mechanical properties of the sphere and cube were identical, except for the Young's modulus, which was five times greater in the sphere. The model was then subjected to a 1% quasi–static unconfined compression, and the 3D behavior of the induced axial strain was predicted.

Results: Figure 1 shows a 3D representation of the compression–induced 3D axial strain, where contours are placed around particular values of strain. An outline of the tumor is also shown. It can be seen that the axial strain throughout the 3D homogeneous background material is not uniformly distributed, despite the absence of stiffness contrast in this region. The strain pattern observed represents a 3D extension of that known for a cylindrical inclusion modeled under plane strain conditions. The tumor influences the strain field in regions far beyond its own position at the geometric centre of the model. Consequently, 2D axial strain slices taken through the homogeneous background may not be uniform, as shown in Figure 2. According to the traditional elastographic interpretation, these slices suggest the presence of elastic contrast on these planes even though none is present.

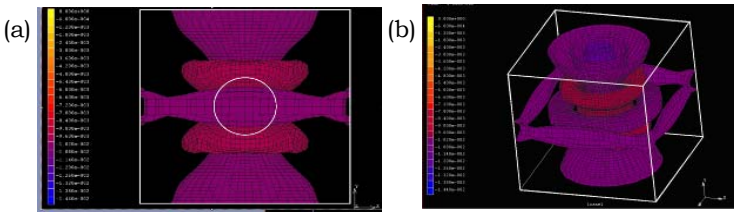

Figure 1: (a) Side view of the 3D axial strain distribution contoured around axial strain values from 0% (yellow) to -1.44% (blue). Circular outline of tumor surface also overlaid. (b) Same distribution viewed at an oblique angle where the cubic model boundary (side length of 100 mm) is also shown.

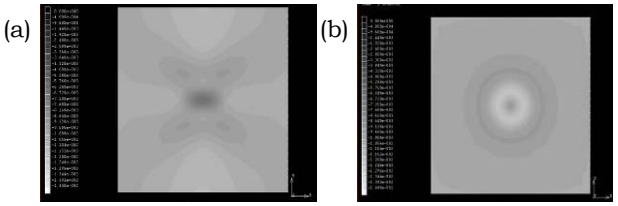

Figure 2: (a) Axial strain on a vertical plane 1 mm outside the tumor surface. (b) Axial strain on a horizontal plane 1mm above the tumor surface. The grey scale runs from 0% (black) to -1.44% (white).

Conclusions: Since traditional elastographic examination involves the display of 2D axial strain images on planes through a 3D object, the scope for clinical misinterpretation in this case is clear. More complex 3D elasticity distributions than that studied here could further complicate the interpretation. Thus, the consequences of limiting ourselves to 2D strain imaging could include the misinterpretation of tumor size or shape (both of which are important diagnostic indicators), or the appearance of stiffness structure where none should exist. However, the use of 3D axial strain imaging provides a more complete picture of the underlying strain distribution, making misinterpretation less likely. Ultimately, when used in combination with 3D elastic modulus reconstruction algorithms, this additional strain information could be used to recover the true underlying elasticity distribution. However, in the shorter term, 3D FE modeling could be used to predict 3D axial strain behavior in situations likely to be encountered clinically, so that a clinician could learn to correctly interpret these images visually in much the same way that the well–known high strain regions above and below a stiff tumor are currently ignored.

Acknowledgements: This work was supported by the Engineering and Physical Sciences Research Council, UK.

* *indicates Presenter*

047 **SHEAR–WAVE INDUCED RESONANCE ELASTOGRAPHY (SWIRE) OF ELLIPTICAL MECHANICAL HETEROGENEITIES.**

Emmanuel Montagnon[1], Anis Hadj Henni[1], Cédric Schmitt[1], Guy Cloutier[1].*
[1]Laboratory of Biorheology and Medical Ultrasonics, University of Montréal Hospital Research Center, 2099 Alexandre de Sève, H2L 2W5, Montréal, Québec, CANADA.

Background: Pathological structures, such as tumors or blood clots, have mechanical properties different than surrounding tissues [1] which can be imaged and characterized by dynamic elastography. To this end, it is relevant to exploit new kind of shear–wave interactions with complex heterogeneities. In the present work, a new technique to induce resonance of confined mechanical heterogeneities is presented.

Aims: Applied to vascular dynamic elastography, and particularly to the problem of mechanical characterization of deep vein thrombi, this study presents shear–wave induced resonance of general shaped elliptical heterogeneities.

Methods: The blood clot was modeled as an elliptic cylinder. Both inclusion and surrounding media were assumed to be isotropic, homogenous and viscoelastic. The incident plane shear wave was polarized in the *z* direction (i.e., following the cylinder axis). Solving the governing differential equation, Helmholtz wave equation, in elliptical coordinates led to the expression of the total displacement field as series of Mathieu functions [2] with unknown coefficients. Taking into account boundary conditions permitted the determination of these coefficients and, consequently, both scattered and refracted displacement fields. The computation of the displacement spectrum at a discrete position within the inclusion allowed observation of the resonance frequencies. By calculating the total displacement fields corresponding to these eigen–frequencies, we could obtain the shapes of the eigen–modes.

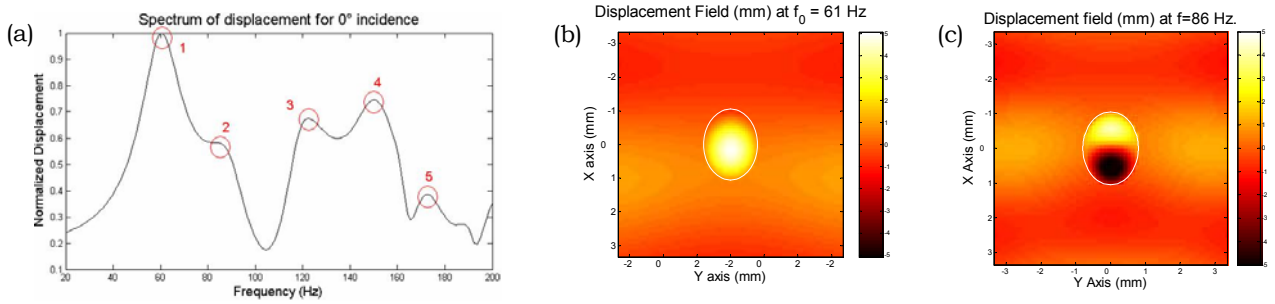

Figure 1: (a) Spectrum of displacement of an elliptical inclusion with major axis a = 10.5 mm, and minor axis b = 8 mm; (b) displacement field at the first resonance frequency of 61 Hz and (c) second eigen–mode of vibration at 86 Hz. Viscoelastic parameters were: $\mu_1=2.5\times10^3+i\omega\times0.056$ for the inclusion and $\mu_2=17\times10^3+i\omega\times0.07$ for the surrounding medium.

Results: The spectrum of displacements exhibited eigen–frequencies, which define vibrational resonances of the heterogeneity. Figure 1 presents two displacements fields: the first (b) and the second (c) vibration modes. It appears that at the first resonance frequency, the whole inclusion was vibrating in phase with the incident wave. In the second mode, displacement regions vibrating in opposite directions were observed within the inclusion on both sides of the minor axis. For both eigen–frequencies, the inclusion boundary could be clearly delimited in the stationary displacement images (at resonances).

Conclusions: A semi–analytical model of plane shear–wave scattering by elliptical cylinders has been developed. The SWIRE method permitted determining resonance frequencies of confined inclusions, as seen in the spectrum and displacements fields of Figure 1. SWIRE provides relevant advantages for dynamic elastography, such as a fast segmentation due to the increased contrast between the inclusion and surrounding media, and could allow tissue characterization, viscoelastic properties, by solving, for example, an inverse problem.

References:

[1] J.L. Gennisson, S. Lerouge and G. Cloutier, Ultrasound Med. Biol., 32, 1529–1537, 2006.
[2] A.R. Hadj Henni, C. Bacon, Journal of Sound and Vibration 299, 298–313, 2007.

072 **REAL–TIME IMAGING OF BREAST TUMORS *IN VIVO* USING AXIAL AND AXIAL–SHEAR STRAIN ELASTOGRAMS: A PRELIMINARY STUDY.**

W Khaled[1], S Chekuri[1], A Thitai Kumar[1,2], J Ophir[1], LM Mobbs[3], BS Garra[3].*
[1]Ultrasonics and Elastographics Laboratory, The University of Texas Health Science Center at Houston, Houston, TX, USA; [2]University of Texas M.D. Anderson Cancer Center, Houston, TX, USA; [3]University of Vermont, Burlington, VT, USA.

Background: Palpation of the body is a standard clinical tool used to detect the presence and nature of abnormalities that could indicate their pathological state. A deep palpation examination of the breast includes compression that is generally perpendicular to the surface, and shear motion which is tangential. Internal shear strains at tissue boundaries, with opposite shear strain signs, may arise from either compressive or tangential applied loads. Prior studies have indicated that there are differences in the way benign and malignant tumors are bonded to the surrounding host tissues [1,3].

Aims: The aim of this study is to demonstrate that real–time axial–shear strain image patterns can be visualized and confirmed as such near breast tumors.

Methods: The data reported in this study were acquired in real–time at the University of Vermont using a Sonix–RP Ultrasound machine (Ultrasonix Medical Corp., Richmond, Canada). The data included 28 patients with breast diseases: one was not biopsied, 8 were confirmed adenocarcinomas and 19 were confirmed benign tumors. The collected RF–sequences were used to calculate local axial–shear strains. Real–time axial–shear strain imaging was implemented on the ultrasound system as a client–software. The software can be used to connect to the US machine to capture RF data and B–mode images. The software can also be used to upload saved RF–data sequences and calculate real–time parameters such as axial–shear strain, effective Poisson's ratio and displacements. Time domain cross correlation with a phase sensitive motion tracking algorithm was used to estimate the displacement. The axial strain and the axial component of the shear strain were calculated using adjustable differential filters. The axial–shear strain results were spatially filtered, scan converted and displayed side by side with the corresponding B–mode images in real time at 27 frames per second. A threshold on the magnitude of the axial–shear strain value was set to be 50% of the calculated maximum axial strain. The patients were imaged with a 128 element linear array transducer with a 6.6 MHz center frequency digitized at 40 MHz. The transducer was also used for a combination of a cyclical manual compressional or dilatational actions or taken during quiet respiration only.

Results: Examples that demonstrate the ability of axial–shear strain elastograms (right, colored images) to help locate lesions in the sonograms (left), along with axial strain elastograms (second from the left) are shown in Figure 1 as patterns of changing shear strain polarity at tumor margins. Moreover, the extent of these patterns is different according to the applied compression or dilatation of the load. Differences are also shown between the axial strain regions in both types of tumors compared to the size of the tumor as seen with the white arrows. These results agree with our earlier reports on axial–shear strain elastography [3].

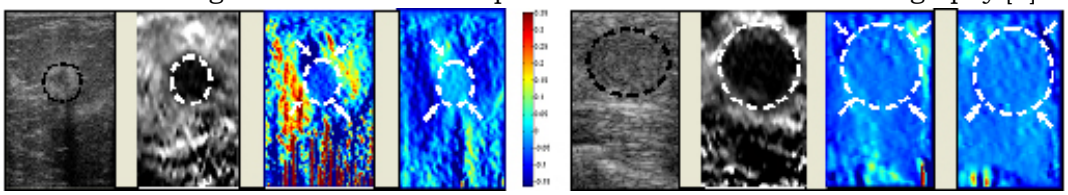

(a) Adenocarcinoma (b) Fibroadenoma

Figure 1: B–mode images, elastograms and axial–shear strain elastograms applying either compressive or dilatational loads.

Conclusions: The results from preliminary data show that the axial–shear strain elastograms can be used side by side with elastograms and B–mode images in real–time to positively identify and confirm the presence and appearance of shear strain patterns at the borders of different breast tumor lesions.

Acknowledgements: This work was supported by NIH grants P01–CA64597–10, CA127291-01 and CA135580–01 awarded to the University of Texas Medical School at Houston.

References:

[1] Chen EJ, et al., Ultrasound tissue displacement imaging with application to breast cancer, Ultras in Med and Bio 21(9), 1153–1162, 1995.
[2] Thitai–Kumar A, et al., Visualization of bonding at an inclusion boundary using axial–shear strain elastography: A feasibility study, Phys in Med and Bio 52(5), 2615–2633, 2007.
[3] Thitai–Kumar A, et al., Breast Tumor classification using axial–shear strain elastography: A Feasibility Study, Phys in Med and Bio, in press.

* *indicates Presenter*

048 **HARMONIC MOTION IMAGING (HMI) COMPARED TO ROTATIONAL RHEOMETRY FOR THE MEASUREMENT OF SOFT TISSUES VISCOELASTICITY.**

J Vappou[1], C Maleke[1], J Luo[1], EE Konofagou[1].*
[1]Biomedical Engineering Department, Columbia University, New York, NY, USA.

Background: Harmonic Motion Imaging (HMI) is a radiation force technique that induces a harmonic mechanical excitation at the focal region of a single–element focused ultrasound (FUS) transducer [1]. RF signals are simultaneously acquired by a phased array transducer, and resulting periodic displacements are estimated by using 1D cross–correlation. Therefore, this method allows obtaining a spatio–temporal displacement distribution over the entire target.

Aims: Thus far, HMI has only been validated qualitatively by showing that the displacement magnitude is inversely proportional to the stiffness in tissues *in vitro* [2] and *in vivo* [3]. In this study, the ability of HMI to measure quantitative viscoelastic properties of soft tissues is evaluated by performing comparison experiments with rotational rheometry.

Methods: Comparison experiments were performed on gelatin phantoms. Concentration varied between C=45.7g/L and C=98.6g/L. Agar powder was added to provide scattering. A 4.5 MHz FUS transducer generated a localized oscillatory force at frequency values of f=25Hz and f=50Hz. The resulting motion was imaged using a 4 MHz phased array transducer and a sampling frequency of 16 MHz. The frame rate for each acquisition was 76 frames/s. A 1D cross–correlation technique was performed to estimate and image the resulting axial displacement with a window size of 2 mm and 88% overlap. The Shear storage modulus, G', was calculated from the shear wave velocity, and the phase shift between the radiation force and the displacement allowed calculation of the ratio between shear loss modulus, G", and shear storage modulus, G'. Assuming that G'>>G", this method allowed calculation of both of these parameters. Dynamic oscillatory shear tests were performed on an ARES rheometer (TA–Instruments, New Castle, DE, USA) in a parallel–plate geometry. Cylindrical samples (1cm in diameter, 4–5mm in thickness) were tested in the 0.1–10Hz frequency range at ε=1% strain.

Results: Significant differences were found between values of shear storage modulus, G', measured by ultrasound and those measured by rheometry, whereas the difference was smaller for the shear loss modulus, G", averaged relative difference of 45% and 22% for G' and G", respectively. For example, for a concentration of C=45.7g/L gel, values of G'_{HMI}=680Pa, G''_{HMI}=240Pa were found with HMI, whereas values of $G'_{rheometry}$=1070Pa, $G''_{rheometry}$=190Pa were found by rheometry.

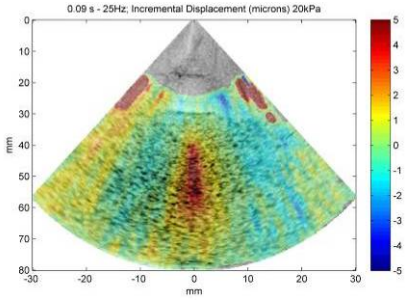

Figure1: Spatial distribution of incremental HMI displacements in the axial direction, showing the propagation of the shear wave in the lateral direction (f=25Hz, C=63.3g/L).

Conclusions: The ability of HMI to determine at least qualitatively both viscous and elastic properties of soft media was demonstrated in this study. A better agreement between HMI and rheometry was found in the case of the loss modulus. Differences that were observed have multiple causes, such as the use of slightly different frequency ranges, the differences in the mode of excitation, the poor S/N ratio leading to uncertainty in the determination of the shear wave speed and the underlying simplified physical assumptions. Ongoing work is essentially focused on improving our current methods for determining viscoelastic properties from local measurements of displacement.

Acknowledgements: This study was funded in part by NIH grants 1R21EB008521and 1KL2RR024157.

References:

[1] Maleke et al., A Single–Element Focused Transducer Method for Harmonic Motion Imaging, Ultrasonic Imaging, 28:144–158, 2006.
[2] Maleke et al., Harmonic Motion Imaging for Focused Ultrasound (HMIFU): A Fully Integrated Technique for Sonication and Monitoring of Thermal Ablation in Tissues, Physics In Medicine and Biology, 53:1773–1793, 2008.
[3] Konofagou E.E. and C. Maleke, Chapter 7: Harmonic Motion Imaging in HIFU monitoring, Biomedical Applications of Vibration and Acoustics in Imaging and Characterizations, ASME Press, 119–139, 2008.

095 **NON–INVASIVE ASSESSMENT OF SHEAR STRAIN IN THE ARTERIAL WALL.**

Tim Idzenga[1], Hendrik HG Hansen[1], Richard G.P. Lopata[1], Chris L de Korte[1].*
[1]Clinical Physics Laboratory, Radboud University Nijmegen Medical Center, Nijmegen, The NETHERLANDS.

Background: Stroke is a major cause of death and is often caused by rupture of plaques in the carotid artery. Some of these plaques are vulnerable and prone to rupture, while other plaques are stable. Vulnerable plaques mostly consist of a large lipid pool covered by a thin fibrous cap. It is hypothesised that shear stresses induced by the pulsating blood flow change the biochemical compounds of the plaque and make it more prone to rupture [1]. Furthermore, it has been hypothesized that the pulsating blood flow induces strain in the vasa vasorum surrounding the artery. These strains might be related to the vulnerability of plaques. In this study, we examined the feasibility to assess shear strains between the carotid artery and its surrounding tissue using non–invasive ultrasound.

Aims: This study is directed toward the assessment of shear strain between the arterial wall and the surrounding tissue using a Polyvinyl Alcohol (PVA) phantom and *in vivo* data of the carotid artery.

Methods: We constructed a phantom of the carotid artery with surrounding tissue from aqueous PVA solutions with SiC as scattering particles. The phantom consisted of a cube (6 x 6 x 5 mm) with a hollow tube (diameter 14 mm) made of 15 wt% PVA, freeze–thawed 3 times. The hollow tube was filled with a cylinder of 15 wt% PVA (freeze–thawed 3 times, diameter 12 mm). The remaining space was filled with 10 wt% PVA (freeze–thawed once). This resulted in an artificial vessel embedded in surrounding tissue with a movable cylinder. The phantom was placed in a water–filled container. One side of the phantom was placed against the wall of the container. The other side of the cylinder was in contact with the plunger of a syringe. We moved the plunger in ten steps of 0.2 mm to increase lateral displacement of the cylinder and induce shear strain between vessel and surrounding tissue. For each displacement, rf data of the vessel and the surrounding tissue were acquired in the longitudinal direction with a Philips SONOS 7500 system, equipped with a linear array transducer (11–3L, f_c = 7.5 MHz). A 2D coarse–to–fine cross–correlation based strain estimation algorithm [2] was applied to calculate the lateral displacements and the derivative of these displacements in the axial direction (shear strain) at each step with respect to the initial position of the plunger. In a human carotid artery, we acquired rf data and applied the same algorithm on sequential acquired frames.

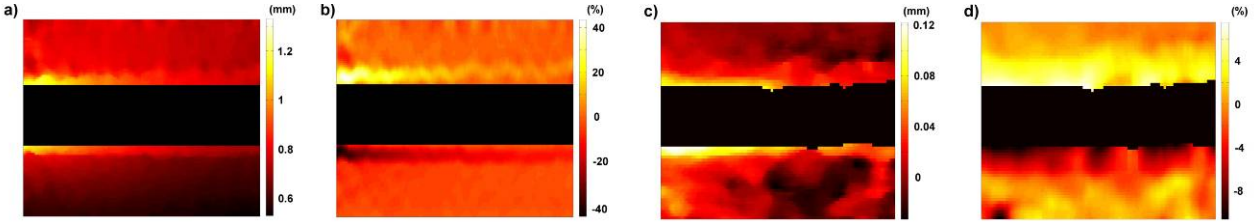

Figure 1: Examples of lateral displacement (a) and shear strain (b) in the PVA phantom and in a humane carotid artery (c and d).

Results: An example of a lateral displacement image is shown in Figure 1a. The measured lateral displacement increased linearly with the applied displacement (Linear Regression, $p<.05$). An example of the resulting shear strain is shown in Figure 1b. The shear strain at the top (bottom) decreased (increased) linearly with increasing lateral displacement (Linear Regression, $p<.05$). We also measured lateral displacement and shear strain in a human carotid artery *in vivo* (Figure 1c and d).

Conclusions: In a phantom, as well as in a human carotid artery, we have shown that the shear strain in the arterial wall can be assessed using non–invasive ultrasound. Furthermore, in the phantom we have shown that the shear strain increased with lateral displacement of the arterial wall. Similar shear strain patterns were observed in the carotid artery indicating that this technique is capable of measuring shear strain in the vasa vasorum induced by the blood flow.

Acknowledgements: The support of the Dutch Technology Foundation (STW) and Philips Medical Systems is acknowledged.

References:

[1] Slager, C.J., et al. "The role of shear stress in the generation of rupture-prone vulnerable plaques." Nat.Clin.Pract.Cardiovasc.Med. 2.8: 401–07, 2005.
[2] Lopata, R.G.P., et al. "Performance Evaluation of Methods for Two-Dimensional Strain Estimation using Ultrasound Radio Frequency Data", Ultrasound.Med.Biol., in press.

* *indicates Presenter*

050 **MEASURING THE MECHANICAL PROPERTIES OF SOFT TISSUE OVER A WIDE FREAQUENCY RANGE BY EMPLOYING THE PRINCIPLE OF TIME TEMPERATURE SUPER–POSITION.**

MM Doyley[1], JB Weaver[2], KD Paulsen[2].*
[1]University of Rochester, Rochester, NY, USA; [2]Thayer School of Engineering, Dartmouth College, Hanover, NY, USA.

Background: Phantoms plays a vital role in the development and evaluation of diagnostic imaging systems, including elastography. They are currently used to assess and optimize various stages of the elastographic image formation process and to evaluate the impact of various technological advances on image quality. To properly evaluate the performance of steady–state harmonic elastographic imaging approaches, it is important to establish methods for characterizing the performance of phantoms over a wide dynamic frequency range (up to 1kHz); a task that has proven to be difficult because of mechanical inertial effects. The main hypothesis that underpins this research is that this limitation can be circumvented by employing the principle of time–temperature superposition.

Aims: To corroborate the hypothesis that the mechanical properties of gelatin–agar based phantoms can be characterized over a wide frequency range (up to 1kHz) by employing the established principle of time–temperature super–position.

Methods: Mechanical testing was performed using dynamic mechanical analyzer on cylindrical shaped gelatin–agar and gelatin-sucrose samples. All measurements where performed using a peak–to–peak amplitude of vibration of 15 μm and a total applied stress of 0.01 N. The complex modulus of all samples was measured between 1–20 Hz at multiple temperatures (i.e., from 10–25°C, in increments of 2.5°C). Master curves and shift factors were computed by employing WLS rheological model to the thermal profiles.

Results: The results shown in Figure 1 revealed two important observations. First, the mechanical properties change can be measured up to 1kHz without incurring any inertial effects, Second, the magnitude of both shear and loss modulus are frequency dependent; noticeable increase in both storage and loss modulus was observed when frequency of vibration exceeded 50 Hz. This frequency dependence was more pronounced when gelatin was cross–linked with sucrose (30 %) than when it was cross–linked with agar (2%).

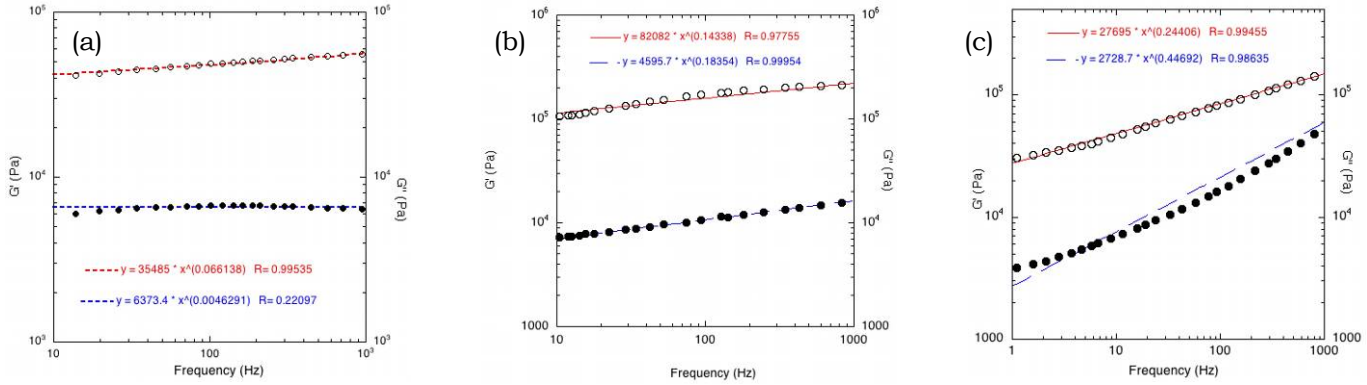

Figure 1: Master storage (open circle) and loss modulus (closed circles) curves obtained from cylindrical samples (40 mm diameter by 10 mm height) that were manufactured from pure gelatin (a), gelatin and agar (b), and gelatin and sucrose (c) by employing the principle of time–temperature superposition.

Conclusions: The results of this study revealed that the mechanical properties of gelatin samples can be measured over the frequency range commonly used in elastography by using the principle of time–temperature super–position.

Acknowledgements: This work was supported by National Cancer Institute Program Project grant P01 CA80139.

065 **ON THE ASSESSMENT OF RADIOFREQUENCY ABLATION LESION SIZE WITH ACOUSTIC RADIATION FORCE IMPULSE IMAGING.**

SA Eyerly[1], SJ Hsu[1], GE Trahey[1], SH Agashe[1], Y Li[1], PD Wolf[1].*
[1]Duke University, Durham, NC, USA.

Background: Ablation has become the preferred treatment for most cardiac tachyarrhythmias. Several studies have investigated the use of acoustic radiation force impulse (ARFI) imaging to visualize lesions created from these ablation procedures [1,2]. ARFI imaging has been demonstrated to be a suitable imaging modality in determining lesion size and continuity, as there is a high contrast in stiffness between the ablation lesion and the surrounding untreated tissue. However, an exact quantitative assessment into the accuracy of ARFI imaging of ablation lesions has not been performed.

Aims: To quantify, *in vitro*, the ability of ARFI imaging to determine the size and extent of ablation lesions within myocardial tissue.

Methods: An ablation chamber was built such that lesions, created by radiofrequency ablation (RFA) in excised myocardium, could be imaged with an intracardiac catheter and precise control of the imaging plane. Alignment slits were present so that the imaging probe could be properly aligned within a specific imaging plane. These slits were then used as guides when sectioning the identical slice plane for pathology. The lesion was then photographed along the cut plane and manually segmented based on visible discoloration within the myocardium. Once registered with the acquired B–mode and ARFI images, the sensitivity and specificity of the corresponding ARFI images were determined.

Results:

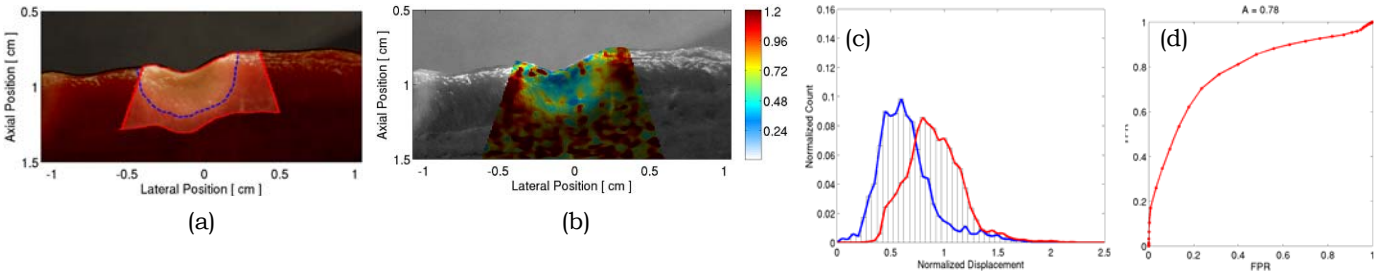

Figure 1: A typical result from these experiments is presented. (a) The pathology slice of a RFA ablation lesion is shown with (b) the co–registered ARFI image. Using time–gain compensation based methods [1], displacements within the ARFI image have been normalized with depth. By segmenting lesion boundaries based on visible tissue discoloration, probability density functions (c) show average normalized displacements within the lesion (blue line) and surrounding tissue (red line) to be: 0.58 ± 0.35, and 0.91 ± 0.26, respectively. Receiver operating characteristics analysis (d) indicates an accuracy of 78% in segmentation of the lesion with ARFI imaging.

Conclusions: We have developed a hardware and software system that provided image plane co–registration between an ultrasound system and a pathology photograph. Using this system, ARFI ultrasound images of ablation lesions were directly compared with photographs of the pathology. Analysis of additional lesions for training will allow us to identify thresholds for ARFI parameters for optimal differentiation of tissue in a real time system.

Acknowledgements: This research was funded by NIH Grants #R01–HL–075485, R01–CA–114093 and R21–EB–007741. We would like to thank Siemens Medical Solutions, USA, Inc. for their hardware and system support.

References:

[1] Fahey BJ, Nightingale KR, Wolf PD, and Trahey GE. Acoustic radiation force impulse imaging of myocardial radiofrequency ablation: Initial *in vivo* results. IEEE Trans on Ultrason, Ferroelec, and Freq Contr. 52, 631–41, 2005.
[2] Hsu SJ, Fahey BJ, Dumont DM, Wolf PD, and Trahey GE. Challenges and implementation of radiation force imaging with an intra-cardiac ultrasound transducer. IEEE Trans on Ultrason, Ferroelect, and Freq Cont 54, 996–1009, 2007.

* *indicates Presenter*

020 **ULTRASOUND–BASED TRANSIENT ELASTOGRAPHY COMPARED TO MAGNETIC RESONANCE ELASTOGRAPHY: A PRELIMINARY STUDY ON PHANTOMS.**

Jennifer Oudry[1], Jun Chen[2], Véronique Miette[1], Kevin Glaser[2], Laurent Sandrin[1], Richard Ehman[2].*
[1]Echosens, Research and Development Department, 153 avenue d'Italie, 75013 Paris, FRANCE; [2]Mayo Clinic, 200 1st Street SW, Rochester, MN 55905, USA.

Background: It is well known in clinical medicine that palpation is an effective diagnostic tool for characterizing mechanical properties of tissues. This accounts for the motivation of investigators for developing quantitative imaging techniques for noninvasively evaluating the viscoelastic properties of tissues. Comparison of a new clinical measurement technique with an established one is often needed to see whether they agree sufficiently. However, an entirely suitable "gold standard" method for quantitatively assessing tissue properties does not exist. Indeed, there are significant differences in mechanical property estimates as reported in the literature [1–3].

Aims: The goal of this work was to directly compare shear stiffness measurements obtained with two dynamic elastographic methods, namely ultrasound–based Transient Elastography (TE) with Magnetic Resonance Elastography (MRE). The comparison was performed on identical tissue–mimicking phantoms within overlapped frequency ranges.

Methods: The shear stiffness parameter μ which describes the relation between stress and strain was investigated with the simplifying assumption of homogeneous isotropic linear purely elastic medium. The shear stiffness was obtained by measurement of the elastic shear wave propagation parameters. It was estimated from the shear velocity V_S such that: $\mu = \rho V_S^2$ with ρ the density. The elastographic methods used in the study have been described in detail previously [4–5]. Basically, TE combines the use of a low frequency vibration that induces transient elastic waves in soft tissues and an ultrafast ultrasound device to follow the propagation of the elastic waves. In MRE, harmonic shear waves are applied to tissue and a phase–sensitive MRI sequence is used to image the propagating waves. For both methods, the frequency of the vibration is typically in the range of 50 to 200 Hz.

Results: Six (6) phantoms were studied and a Bland & Altman analysis was carried out to evaluate the agreement between measurement methods [6]. As shown on Figure 1, the mean difference of the shear modulus obtained from the two methods is not significant and 95% of the differences lie within the range of -1.96 SD (standard deviation) of the differences to 1.96 SD of the mean.

Conclusions: The results demonstrate no evidence of a systematic difference between TE and MRE stiffness measurements. In ongoing research, we are evaluating larger sample sizes and *in vivo* human measurements.

References:

[1] L. Huwart, et al. Liver fibrosis: non–invasive assessment with MR elastography. NMR Biomed. 2006; 19: 173–179.
[2] M. Yin, et al. Assessment of Hepatic Fibrosis With Magnetic Resonance Elastography. Clin. Gastroenterol. Hepatol. 2007; 5: 1207–1213.
[3] L. Castera, et al. Prospective comparison of transient elastography, Fibrotest, APRI, and liver biopsy for the assessment of fibrosis in chronic hepatitis C. J Gastroenterol. 2005; 128: 343–350.
[4] L. Sandrin, et al. Shear elasticity probe for soft tissues with 1–D transient elastography. IEEE UFFC 2002; 29 (4): 436–46.
[5] A. Manduca, et al. Magnetic resonance elastography: non–invasive mapping of tissue elasticity. Med. Image Anal. 2001; 5: 237–254.
[6] J.M. Bland et al. Statistical methods for assessing agreement between two methods of clinical measurement. Lancet. 1986; 8: 1(8476):307–10.

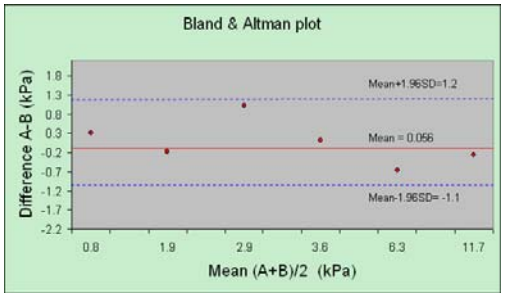

Figure 1: Difference against average of TE and MRE measurements, with 95% limits of agreement (Method A: TE, Method B: MRE)

006 **MODELING THE TWIST MOTION OF LEFT VENTRICLE USING tMRI.**

M. D. Alenezy[1], T. Alrefae[2], E.I. Popel[1], J. Shi[1], and M. Bilgen[3].*
[1]University of Kansas, Lawrence, KS, USA; [2]Kuwait University, Kuwait City, Kuwait; [3]Medical University of South Carolina, Charleston, SC, USA.

Background: During systole, the apex of the left ventricle (LV) of heart rotates clockwise as viewed from the base, while the base of the LV rotates counter-clockwise. This twisting motion, wringing, of the LV is due to the differences between the structural organization of the myocardial fibers in the epicardium and endocardium. Study of cardiac motion in the apex and base of the normal heart is of interest in gaining insight into the function of the LV that cannot be easily obtained from ordinary short– or long–axis analysis [1]. It is, therefore, important to characterize quantitatively the twisting motion of the LV in the presence of axial deformation.

Aims: This study focuses on developing a mathematical model to characterize quantitatively both the deformation and twist motions of the LV in rat heart near its apex and base by using tagged MRI (tMRI) data.

Methods: It has been shown that a Gaussian transformation is effective in describing the deformation of the LV in its mid ventricle [2]. In this presentation, we extend this deformation model to the apex and base of the LV by using a combination of Gaussian (T) and rotational (R) transformations to study the wringing of the LV during a full cardiac cycle. The Gaussian and rotational transformations are:

$$\mathbf{T} = \begin{pmatrix} 1+e^{-\frac{r^2}{\alpha^2}} & 0 \\ 0 & 1+e^{-\frac{r^2}{\alpha^2}} \end{pmatrix} \quad \text{and} \quad R = \begin{pmatrix} \cos\theta & -\sin\theta \\ \sin\theta & \cos\theta \end{pmatrix}$$

where r is the distance from the center of LV to the point of interest and $\theta(r) = \theta(r)_{apex} - \theta(r)_{base}$ is the twist angle between the apex and the base of the LV at any given point, r. Note that the rotational angle of the apex (θ_{apex}) and of the base (θ_{base}) are defined by a positive and negative angles, respectively. To test our model, we used short axis images of the apex and base of the LV of rat heart during one cardiac cycle.

Results: In Figure 1, the calculated results of the deformation and twist motion of the LV based on our mathematical model are superimposed on the short axis images of the apex and base of the LV of a rat heart, where the result from the model is represented by a two–dimensional mesh, as in [2]. The two images on the left in Figure 1 are near end–diastole, hence, there is little rotation. The two images on the right have the peak rotation of the apex (upper image) and the base (lower image) that occurred at 40% of the full cardiac cycle. These results demonstrate that our mathematical model accurately describes the deformation and rotational motions of the apex and base of the LV. Figure 2 shows the changes in θ calculated from the model at the mid point between the endocardium and epicardium wall during the cardiac cycle. The computed rotation profile is in agreement with those reported recently by another study from rat heart [3]. Compared to the published approach, an advantage of our model is that it can provide twist angle of LV at any given point on the apex by using one set of tagged MRI data obtained during a full cardiac cycle.

Conclusion: Our simple mathematical model is capable of accurately describing the dynamics of deformation and twist motion of the apex and base of LV in heart. The calculation of the twist angle based on this model is sensitive to small rotations of the apex and base. With this model, the twist angle θ as a function of r can be calculated from one set of tagged MRI data obtained during a full cardiac cycle. This model provides another dimension in the study of the twist motion of heart using tagged MRI data. Our current efforts are focused on applying the model to characterize human heart, which is clinically more relevant.

References:

[1] Notomi Y, et al. Measurement of Ventricular Torsion by Two–Dimensional Ultrasound Speckle Tracking Imaging. J.American College of Cardiology 2005, 45(12):2034–2041.
[2] Alrefae T, Smirnova I.V, Cook, and L.T, Bilgen M: A model–based time reversal of left ventricular motion improves cardiac motion analysis using tagged MRI data. Biomedical Engineering Online 2008, 7:15.
[3] Wei Liu, et al. MR tagging demonstrates quantitative differences in regional ventricular wall Motion in mice, rats, and men. Am.J Physiol Heart Circ Physiol 291:H2515–H2521, 2006.

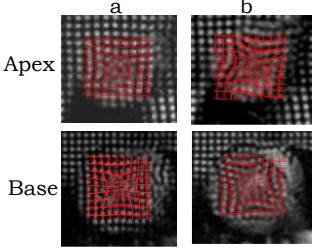

Figure 1: Short axis view of the apex and the base of the LV at the end diastole phase (a) and at 40%of cardiac cycle (b)

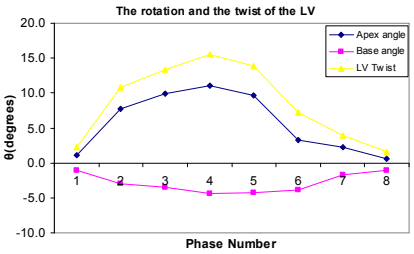

Figure 2: Average changes of rotational angle θ during a cardiac cycle versus phase number. Phase 1 is near the end diastole and phase 4 is at 40% of cardiac cycle.

* *indicates Presenter*

090 ***IN VIVO* INVESTIGATION OF RADIATION FORCE–INDUCED SHEAR WAVE PROPAGATION IN MYOCARDIAL TISSUE.**

RR Bouchard[1], PD Wolf[1], SJ Hsu[1], DM Dumont[1], GE Trahey[1].*
[1]Duke University, Durham, NC, USA.

Background: Shear wave elasticity imaging (SWEI) [1] has been shown to provide clinically–relevant stiffness information in nearly–isotropic tissues (e.g., liver) [2]. Using similar imaging techniques, Deffieux et al. compared parallel (i.e., traveling parallel to the muscle fiber direction) to perpendicular shear wave propagation velocities in skeletal muscle, a tissue which is known to be transversely anisotropic [3]. In the case of cardiac muscle, myocardial fiber direction changes laterally (i.e., at a fixed depth in the myocardium) and with depth (i.e., at a fixed lateral position), which results in a more complex structural anisotropy [4]. Yet despite the increasing degree of anisotropy observed in the heart, it is reasonable to expect that shear wave velocimetry will reflect underlying stiffness properties and structural information.

Aims: To track acoustic radiation force (ARF)–induced shear waves in the myocardium of a beating heart.

Methods: SWEI was implemented in an open–chest preparation ovine study for the purpose of measuring shear wave velocity through the myocardium in the left ventricular free wall. ECG gating was utilized to ensure that acquisition coincided with the cardiac cycle's T wave, a period of reduced physiologic motion. The transducer was attached to a vacuum–driven coupling device (to reduce lateral motion) with 1 cm standoff and was placed directly on the exposed myocardium. The long axis of the transducer's face was positioned at three distinct angles relative to the superficial fiber orientation in the exposed myocardium. Figure 1 presents shear wave velocity results as a function of depth about the transmit focus (17.5 mm) for three rotational angles: 0°, 45° and 90°.

Results:

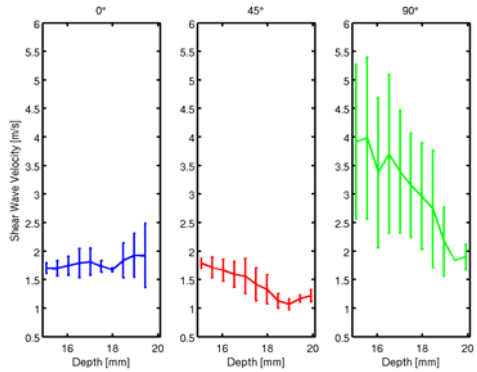

Figure 1: Shear wave velocities as a function of depth at three rotational angles in the left ventricular free wall during an open–chest preparation ovine study. Rotational angles indicate the approximate angle between the transducer's long axis and the direction of superficial fiber orientation in the exposed myocardium. Statistics (mean and standard deviation) were calculated at each depth from multiple trials (from 15–17 mm, N≥4; from 17–20 mm, N≥2 in all but one case). The linear regressions used for all shear wave velocity estimates had an R2≥0.95. At 45° and 90°, shear velocity tends to change with depth; no significant depth dependence exists in the 0° data. It is important to note that the depth values include the standoff thickness (1 cm) and do not denote the myocardial thickness alone.

Conclusions: It is possible to reliably (R2≥0.95) track ARF–induced shear waves in the myocardium of an *in vivo* ovine heart. For two rotational angles (45° and 90°), shear wave velocity appears to be depth dependent, which is consistent with phenomena one might expect given the known rotation of myocardial fibers with depth [4]. Due to the limited number of samples used in the statistical analysis, however, additional trials must be performed before it can be determined if these trends are truly significant.

Acknowledgements: This research was funded by NIH Grants R01–HL–075485 and R21–EB–007741 and by the NSF GRFP. We would like to thank Siemens Medical Solutions USA, Inc. for their hardware and system support.

References:

[1] Sarvazyan AP, et al., Shear wave elasticity imaging: a new ultrasonic technology of medical diagnostics. Ultrasound Med. Biol. 24(9): 1419–1435, 1998.
[2] Palmeri ML, et al., Quantifying Hepatic Shear Modulus *In Vivo* Using Acoustic Radiation Force. Ultrasound in Med. and Biol. 34, 2008.
[3] Deffieux T, Montaldo G, Tanter M, and Fink M. Shear Wave Spectroscopy for *in vivo* quantification of human soft tissues viscoelasticity. IEEE Trans on Ultrason, Ferroelec, and Freq Contr., (in press 2008).
[4] Hsu EW, et al., Magnetic resonance myocardial fiber orientation mapping with direct histological correlation. Am. J. Physiol. 274(5 Pt 2): 1627–1634, 1998.

040 **DIRECT MEASUREMENTS OF DIALYSIS FISTULA WALL STRAIN USING HIGH–RESOLUTION PHASE–SENSITIVE ULTRASOUND SPECKLE TRACKING.**

William F. Weitzel[1], Kang Kim[2], Dae Woo Park[1], James Hamilton[3], Matthew O'Donnell[4], Thomas J. Cichonski[1], Jonathan Rubin[5].*
[1]Internal Medicine Nephrology, University of Michigan, Ann Arbor, MI, USA; [2]Cardiovascular Institute, School of Medicine, University of Pittsburgh, Pittsburgh, PA, USA; [3]Pixel–Velocity, Inc., Ann Arbor, MI, USA; [4]Bioengineering, Washington University, Seattle, WA, USA; [5]Radiology, University of Michigan, Ann Arbor, MI, USA.

Background: The utility of noninvasive imaging to characterize fistula wall elasticity and detect stenotic lesions has been constrained by imprecise measurements of wall motion using conventional B–mode ultrasound.

Aims: This study examined the potential of high–resolution, phase–sensitive speckle tracking applied to dialysis vascular access fistulae to evaluate vascular wall strain.

Methods: With IRB approval, normal and stenotic regions of the dysfunctional native vein dialysis fistulae of two subjects were measured. Using phase–sensitive speckle tracking, strain measurements were obtained parallel and orthogonal to the radial direction of fistula motion with cardiac pulsation (i.e., top or side of vessel wall).

Results: Comparison of strain values at normal and stenotic regions of vessel walls in Subjects 1 and 2 are shown in the table below. Five measurements were taken from each region of interest (ROI) and the mean and standard deviation are displayed in the Table for each ROI. Stenotic strain values were generally less than 1% in magnitude. Compared to stenotic ROI's, strain values were approximately three times greater in normal fistula in Subject 1 and nearly twice as great in normal regions in Subject 2.

Conclusion: Phase–sensitive speckle tracking allows measurement of extremely small strain values in the vessel wall, distinguishing subtle differences in tissue hardness between diseased and normal vessel regions. While wall thickness, radius, and Young's modulus all influence strain measurements, these findings suggest that these strain measurements may add diagnostic value to ultrasound imaging in managing dialysis vascular access and allow early detection of vascular disease.

Location	Subject	ROI	Mean	STD
Side Wall	1	Normal 1	0.0334	0.0198
		Normal 2	0.0436	0.0199
		Stenosis	0.0098	0.0120
	2	Normal 1	0.0234	0.0096
		Normal 2	0.0186	0.0040
		Stenosis	0.0052	0.0013
Top Wall	1	Normal 1	–0.0196	0.0040
		Normal 2	–0.0090	0.0026
		Stenosis	–0.0032	0.0023
	2	Normal 1	–0.0170	0.0064
		Normal 2	–0.0180	0.0105
		Stenosis	–0.0104	0.0051

Acknowledgements: This work supported in part by NIH grant DK62848 and a grant from Renal Research Institute.

036 **STRAIN VERSUS SURFACE PRESSURE FOR *IN VIVO* BREAST TISSUE.**

AM Sommer[1], S Baker[1], LM Kiessel[1], MT Herd[1], K Nam[1], TJ Hall[1].*
[1]University of Wisconsin–Madison, Madison, WI, USA.

Background and Aims: Elastic modulus measurements have shown that breast tissue demonstrates a non–linear stress–strain response that is characteristic of tissue type [1]. Also, it has been demonstrated that *in vivo* fibroadenomas (FA) tend to have a changing strain contrast with increased deformation while *in vivo* invasive ductal carcinomas' strain contrast remains relatively constant [2]. Up to now the comparisons between cases were limited since the amount of initial deformation and surface pressure was unknown. The goal of this research is to compare the surface pressure versus strain for benign and malignant *in vivo* breast lesions.

Methods: Radiofrequency (RF) echo data was acquired at the University of Wisconsin Hospitals and Clinics Breast center on a Siemens SONOLINE Antares with freehand scanning of *in vivo* breast tissue using the VFX13–5 linear array transducer. A pressure sensing plate was attached to the transducer to measure the applied surface pressure during data acquisition. To date, 25 independent cases have been obtained with biopsy as the standard for diagnosis (11 – FA, 10 – Other Benign, 4 – Malignant). B–mode and strain images were formed off–line. The displacement quality measure [3] was used to select the highest quality sequence with a deformation range of roughly 10% total strain. The displacement estimates obtained for strain imaging were used to warp the strain and B–mode images back to the geometry of a reference frame within the sequence to provide stationary images. The strain was accumulated from the image with the least amount of deformation to provide a sequence of accumulated strain images. A segmentation algorithm, currently available on the Siemens ACUSON S2000, was used to obtain a lesion boundary in the total accumulated strain image. Using the lesion boundary the mean accumulated strain was calculated for the lesion for each image within the sequence. The surface pressure readings were temporally aligned with the RF data. The mean accumulated strain in the lesion was plotted as a function of surface pressure and the best fit line determined.

Results: The slope of the mean accumulated strain in the lesion versus the surface pressure tends to be larger for fibroadenomas than for the malignant lesions. Figure 1 shows the B–mode, accumulated strain image and plot of mean accumulated strain in the lesion versus surface pressure (slope = 0.25), while Figure 2 demonstrates the same for a ductal carcinoma *in situ* (slope = 0.06). Further analysis will account for differences in lesion size relative to the image depth and background tissue composition.

Conclusions: The surface pressure during strain imaging provides additional information that shows promise to aide in the distinction between benign and malignant *in vivo* breast lesions and warrants further investigation.

Acknowledgements: We are grateful for the support from the NIH (R01–CA100373).

References:

[1] Hall, T.J., Zhu Y., Spalding C.S. *In vivo* real–time freehand palpation imaging. Ultrasound in Medicine & Biology 2003; 29(3): 427–35.
[2] Wellman, P. Tactile imaging. Ph.D. dissertation, Harvard University, 1999.
[3] Jiang, J., Hall, T.J., Sommer A.M. A novel performance descriptor for ultrasonic strain imaging: A preliminary study. IEEE Trans Ultrason, Ferroelec, Freq Cont 2006; 53(6): 1088–1102.

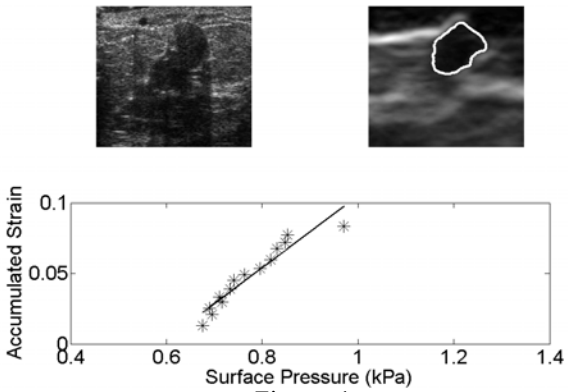

Figure 1

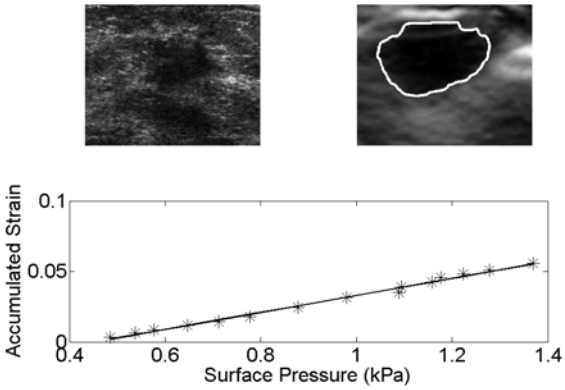

Figure 2

063 **TECHNICAL FEASIBILITY OF ARFI IMAGING IN THE UTERINE CERVIX.**

Mark Palmeri[1], Helen Feltovich[2], Kibo Nam[3], Mark A Kliewer[3], Timothy J Hall[3].*
[1]Duke University, Durham, NC, USA; [2]Minnesota Perinatal Physicians, Minneapolis, MN, USA; [3]University of Wisconsin–Madison, Madison, WI, USA.

Background: Understanding uterine cervical microstructure is critical to understanding dysfunction that leads to preterm delivery, a problem that costs the US $26 billion annually. A long, slow process of cervical softening associated with collagen fibril reorganization occurs well before active ripening in preparation for labor (preterm or term). Ripening involves synthesis of proteins, further reorganization and cervical shortening, and is irreversible prior to delivery. Interventions that treat intrauterine infection, reduce inflammation, inhibit uterine contractions or stitch closed the uterine cervix do not prevent preterm birth. Clearly, the inciting mechanism has not been elucidated. Biochemistry, molecular biology and mechanical studies suggest that collagen is responsible for cervical strength; specifically, cervical weakness and softness seems to be associated with collagen disorganization. Human *in vivo* investigation has been limited by lack of noninvasive technology sophisticated enough to detect changes in collagen. Acoustic Radiation Force Impulse (ARFI) imaging techniques are a promising approach to evaluation of cervical microstructure.

Aims: Electron microscopy and tensile strength experiments in animals shows that cervical strength is associated with collagen fibril reorganization; as the fibrils disorganize, tensile strength decreases. ARFI imaging techniques may prove to be an appropriate method for evaluation of cervical softening, which is the critical first step in cervical change and has never been objectively characterized. Mechanical characterization of the cervix with ARFI imaging may provide insight into the structure and function of the uterine cervix, creating opportunity for novel therapeutic approaches.

Methods: Three–dimensional finite element method (FEM) models of tissue heating and dynamic tissue displacement in response to impulsive acoustic radiation force excitation were performed for a Sequoia 15L8w linear array [1,2]. A 400–cycle excitation at 7.0 MHz focused at 10 mm with a F/1 focal configuration was simulated for soft tissue (c_v = 4.2 J/cm^3/°C, κ = 0.00143 cm^2/s, E = 10 kPa, ν = 0.499, α = 1.4 dB/cm/MHz). The mechanical simulations were used to determine what acoustic output (I_{SPPA}) would be necessary to generate at least 1.0 μm of displacement in peak shear wave displacement amplitude 8 mm offset from the excitation focus to insure adequate displacement SNR for shear wave speed reconstruction [3]. This I_{SPPA} value was then used in the thermal models to insure that FDA heating thresholds for fetal imaging would not be exceeded.

Results: For a Young's modulus of 10 kPa, an $I_{SPPA}|_{1.4}$ = 3000 W/cm^2 can generate a peak focal zone displacement of 6.0 μm that decays to 1.5 μm due to geometric spreading 8 mm offset from the focal point in the lateral dimension. This acoustic output leads to a peak heating of 0.08°C at the focal point per excitation. Assuming a desired lateral region of interest (ROI) of 8 mm with a line spacing of 0.2 mm and utilization of 4:1 parallel receive tracking, 10 excitations would be required to fully characterize the ROI, heating the focal point to 0.8°C, below the FDA limit of 1°C for fetal ultrasound imaging. For a more compliant cervix (E = 1 kPa, potentially indicative of collagen disorganization), this acoustic output would lead to 18 μm of focal point displacement, while in a healthier (E = 30 kPa) cervix, the focal point displacement would drop to 0.9 μm.

Conclusions: ARFI imaging has potential as a technique to evaluate the compliance of the human uterine cervix. It is possible to achieve adequate displacement magnitudes at the excitation focus without exceeding the FDA heating threshold of 1°C for fetal ultrasound imaging. The acoustic output used for generating radiation force–induced displacements can be modulated based on the expected stiffness of the cervix during pregnancy to minimize this heating. The simulated dynamic displacement fields demonstrate that shear wave propagation over 8 mm with adequate displacement SNR is possible to characterize cervical compliance during pregnancy.

References:

[1] Palmeri and Nightingale. "On the thermal effects associated with radiation force imaging of soft tissue," IEEE UFFC, 51(5):551–565, 2004.
[2] Palmeri et al. "A finite element method model of soft tissue response to impulsive acoustic radiation force," IEEE UFFC, 52(10):1688-1712, 2005.
[3] Palmeri et al. "Quantifying hepatic shear modulus *in vivo* using acoustic radiation force," Ultrasound in Med. Biol., 34(4):546–558, 2008.

* *indicates Presenter*

088 **ACOUSTIC RADIATION FORCE IMPULSE TECHNIQUES FOR ASSESSING ELASTIC ANISOTROPY OF THE *IN VITRO* HUMAN CERVIX.**

Helen Feltovich[1], Timothy J. Hall[2], Ellen M. Hartenbach[2], Josephine M. Harter[2], Mark A. Kliewer[2].*
[1]Minnesota Perinatal Physicians, 800 E. 28th Street, Minneapolis, MN, USA; [2]University of Wisconsin–Madison, 1111 Highland Avenue, Madison, WI, USA.

Background: In the United States, 1 of every 8 babies is born prematurely. Every day, 13 babies die from complications of prematurity. Besides the staggering emotional costs, preterm delivery and its complications cost the US in excess of $26 billion annually. Assessment of uterine cervical microstructure, which informs its strength and behavior, is critical to understanding dysfunction that leads to preterm delivery. The cervix is composed of an extracellular matrix (predominantly collagen with elastin and proteoglycans) and a cellular portion (smooth muscle, fibroblasts, epithelium and blood vessels). A long, slow process of cervical softening associated with collagen fibril reorganization occurs well before active ripening in preparation for labor (preterm or term). Animal data suggests that this process is associated with a progressive change from anisotropy to isotropy. Digital palpation suggests that the normal pregnant cervix softens in a distal to proximal direction throughout gestation. When the cervix fails, however, it seems to do so in a proximal to distal direction; standard B–mode imaging shows interruption of cervical integrity at its most proximal portion and cervical softness (particularly proximal) is alarming to obstetricians when noted too early in pregnancy. Despite its importance however, assessment of cervical softness currently is entirely subjective because of a lack of noninvasive technology sophisticated enough to quantitatively detect changes in tissue stiffness.

Aims: We sought to determine whether Acoustic Radiation Force Impulse (ARFI) techniques are useful for quantitative evaluation of human cervical tissue. We assessed the reproducibility of ARFI and its potential for detecting tissue stiffness differences and anisotropy based on (a) palpable distinction between cervices and (b) what would be expected within the same cervix given assumptions about cervical microstructure.

Methods: We used Acoustic Radiation Force Impulse imaging tools programmed into the Siemens ACUSON S2000 (Virtual Touch Tissue Quantification) to estimate the shear sound speed in cervical tissue from hysterectomy specimens. We used the only available arrays currently compatible with this software (4C1 and 4V1 abdominal transducers) to scan specimens in a water bath near the geometric focus of the transducer. We varied the region of interest of ARFI sampling proximally to distally along the length of the cervix to study the spatial distribution of stiffness. We also varied the orientation of the acoustic beam and the gross orientation of the cervix to the uterine corpus to study potential for anisotropy.

Results: Measurements of shear sound speed were reproducible; at the same region with the same acoustic beam angle and gross anatomical orientation, they varied about 3–10%. Shear sound speeds decreased linearly as the region of interrogation was moved proximally to distally in the same cervix; at +30° in the softer cervix, they decreased from 1.84 to 0.90m/s, and at –30° in the stiffer cervix, they decreased from 1.84 to 1.21m/s. Interrogation of the same region of the cervix with a constant acoustic beam angle but opposite gross anatomical orientation showed variation; for instance, in the midportion of the cervix with an acoustic beam angle of –15°, the shear sound speed was 3.44 for left corpus orientation versus 2.27m/s for right. Finally, interrogation of equivalent regions (with equivalent acoustic beam angles and gross orientation) in the palpably softer versus stiffer cervix showed differences in shear sound speed; at –15° with left corpus orientation in the most proximal portion of the cervix, the measurement for the palpably stiffer cervix was 4.24 versus 2.78m/s for the softer.

Conclusions: These preliminary results suggest that ARFI may be useful for evaluation of the cervix. The measurements are reproducible. The cervix that was palpably softer demonstrated slower shear sound speeds when compared to the palpably stiffer cervix. Varying the acoustic beam orientation and the gross orientation of the cervix to the uterine corpus created variations in shear sound speed while consistent orientations produced a linear decrease in shear sound speed with proximal to distal interrogation. Taken together, these suggest anisotropy, which is consistent with what is understood about cervical microstructure. This initial work suggests that ARFI is a promising approach for evaluation of the human uterine cervix.

Acknowledgements: We gratefully acknowledge the equipment loan from Siemens Medical Systems USA, Inc. Ultrasound Division and the technical support from Andy Milkowski, John Benson and Liexiang Fan of Siemens Ultrasound.

012 **SHEAR STRAIN ELASTOGRAPHY FOR BREAST MASS DIFFERENTIATION.**

M Rao[1], S Baker[1], AM Sommer[1], T Varghese[1], GA Sisney[1], MT Herd[1], ES Burnside[1], TJ Hall[1].*
[1]University of Wisconsin–Madison, 1530 Medical Sciences Center, 1300 University Avenue, Madison, WI 53706, USA.

Background: Elastography, as a strain imaging technique, has gained interest as a diagnostic tool for the detection and differentiation of breast cancer over the past decade. Konofagou et al [1] have shown that shear strain estimates may provide supplementary information on the bonding between the tumor and the surrounding tissue, characterizing different tissue elements based on their mobility. Thitai Kumar et al [2] have shown that it is feasible to extract features from axial–shear strain elastograms which may potentially be used for differentiating benign from malignant tumors using simulations and *in vivo* data on the breast.

Aims: The aim of this study is to further investigate the feasibility of *in vivo* axial–shear strain imaging for breast cancer diagnosis.

Methods: *In vivo* radiofrequency (RF) data were acquired at the University of Wisconsin Breast Center using a Siemens SONOLINE Antares real–time clinical scanner equipped with a VFX13–5 linear array transducer. Free–hand palpation imaging with deformation up to 10% was performed for acquiring pre– and post–deformation RF data to generate ultrasound strain images. A total of 38 cases have been acquired. For each case, 160 RF data frames were collected, from which we select several consecutive frames with reasonable strain image quality. In this study, we utilized 6 malignant tumors and 15 fibroadenomas to investigate the feasibility of using axial shear strain to differentiate benign from malignant tumors. Histopathology results of a biopsy were considered the diagnostic standard. Axial strain and axial component of shear strain were generated using a 2D cross–correlation based block matching algorithm. The area of the axial–shear strain region normalized to the lesion size, applied strain and strain contrast was utilized as the feature for differentiating between benign and malignant tumors [2].

Results: Figure 1 presents examples of axial–shear strain elastograms superimposed on the corresponding sonogram of (a) benign and (b) malignant breast tumor. Only those pixels that had axial–shear strain values greater than the threshold value and corresponding correlation coefficient greater than 0.75 were overlaid on the corresponding sonogram to obtain the composite image. Observe that the area of the axial–shear strain region is larger for malignant tumors when compared to benign fibroadenomas. A scatter plot of the normalized area of the axial–shear strain region demonstrates that the values of the normalized feature for cancer data are larger when compared to benign data.

Conclusions: Preliminary results demonstrate the potential to utilize axial–shear strain features to classify a tumor as benign or malignant for breast cancer imaging.

Acknowledgements: This work is supported by Komen Foundation Grant BCTR0601153.

References:

[1] E. E. Konofagou, T. Harrigan, and J. Ophir, "Shear strain estimation and lesion mobility assessment in elastography," Ultrasonics, 2000. 38(1): p.400–404.
[2] A. Thitai Kumar, T. A. Krouskop, B. S. Garra, and J. Ophir, "Visualization of bonding at an inclusion boundary using axial–shear strain elastography: a feasibility study," Physics In Medicine And Biology, 2007. 52(9): p. 2615–2633.

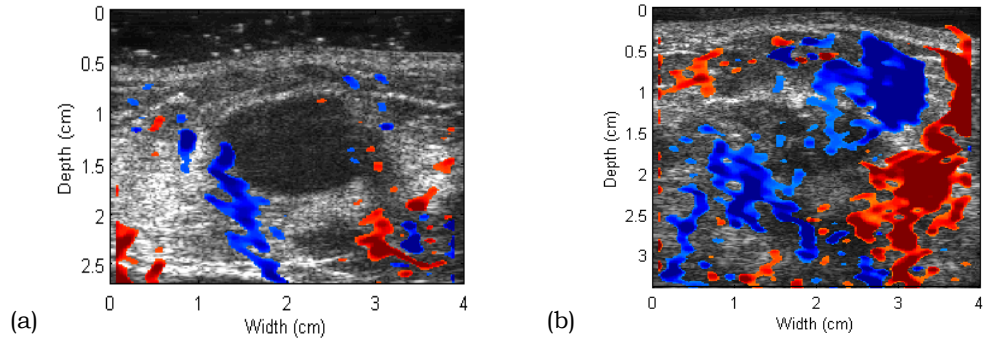

Figure1: Composite image obtained by superimposing the axial–shear strain elastograms on top of the sonogram of (a) fibroadenoma and (b) cancer.

* *indicates Presenter*

056 **ADVANCES AND DIFFICULTIES IN THE USE OF ULTRASOUND ELASTOGRAPHY AND INVERSE ALGORITHMS FOR GEL DOSIMETRY.**

Remo A. Crescenti[1], Jeffrey C. Bamber[1], Assad A. Oberai[2], Paul E. Barbone[3], Joseph P. Richter[2], Carlos Rivas[3], Nigel L. Bush[1] and Steve Webb[1].*

[1]Institute of Cancer Research and Royal Marsden NHS Foundation Trust, Downs Road, Sutton, Surrey, England, UK; [2]Rensselaer Polytechnic Institute, 110 8th Street, Troy, NY, USA; [3]Boston University, 110 Cummington Street, Boston, MA, USA.

Background: For modern radiotherapy, 3D–dosimetry is essential. Radiation sensitive polymer gels may be employed as dosimeters. Previously we have successfully determined dose contrast in such gels using ultrasound elastography combined with inverse algorithms to verify the radiation induced stiffness contrast [1]. The findings were limited to a single high dose region, and a technique was introduced to correct artifacts that were present in the background (zero–dose) gel due to the influence of mechanical conditions at the top and bottom boundaries, which were hard to control or determine.

Aims: This presentation describes advances in the above experiment, to attempt to visualize more complex dose distributions and to adjust the shape of the sample so as to render the region of interest (ROI) used for quantitative elastography less sensitive to the effect of boundary conditions.

Methods: A deliberately tall (y–axis) and narrow (x–axis) block of radiation sensitive polymer gel [2] (4 x 10 x 10 cm^3 along x, y and z–axis, respectively) was irradiated to produce a complex stiffness distribution (three rod–shaped regions along the z–axis). The block of gel was placed in a mechanical frame, which allowed expansion in the x–direction but prevented z–direction motion. The block was compressed in y–direction while RF ultrasonic echo data were acquired in one central plane. The local displacement was tracked in a ROI in the centre of this plane. The stiffness contrast between the stiff inclusions and the soft background was determined using an inverse algorithm [3] in which the ROI was modeled as an incompressible, linear elastic solid with zero shear traction boundaries, using the finite element method (the tall and narrow shape was designed so that friction at the physical top or bottom boundary would not introduce additional stress in the ROI). Independent calibration (direct stress versus strain measurement) was performed with smaller cylindrical and homogenously irradiated samples to relate stiffness with dose. The dose distribution was determined in the central plane using magnetic resonance imaging (MRI) as a reference.

Results and Discussion: All three high dose areas were detected with good spatial accuracy (Figure 1). The top and bottom boundary regions were artifact–free. However, the dose distribution was very noisy, especially at the sides. This, supposedly, was due to ultrasound beam attenuation and reflection from the sides of the sample that was just marginally wider than the ultrasound transducer. The noise combined with the smoothing characteristics of the regularized inversion caused shape distortion and incorrect estimation of the dose contrast in the high dose areas. Improvement of the experimental setup and acquisition of ultrasound data from two orthogonal directions, together with an adapted inverse algorithm that can incorporate this additional information is now under development to improve the computed estimates.

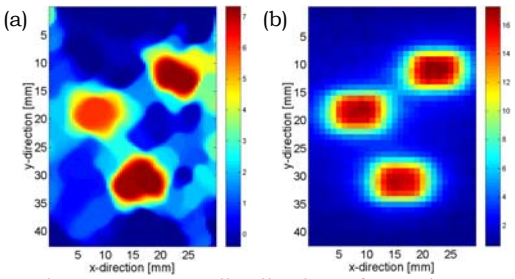

Figure 1: Dose distribution from inverse algorithm (a) and reference dose distribution from MRI (b).

Conclusions: We have simplified the imaging of irradiation–induced changes in elasticity in a polymer gel using a plane strain inverse algorithm, but the data acquisition and the inverse computing need adaptation and improvement if elastic properties are to be used for dose determination.

Acknowledgements: This project is funded by the ICR and the URP program at RPI.

References:

[1] Crescenti RA, et al., Ultrasonic elastography and plane strain inverse algorithms for polymer gel dosimetry, Proc. 2007 IEEE Ultrasonics Symposium Yuhas MP (ed.) IEEE, Piscataway, NJ, 2025–2027, 2007.

[2] Fong PM, Keil DC, Does MD and Gore JC, Polymer gels for magnetic resonance imaging of radiation dose distributions at normal room atmosphere, Physics in Medicine and Biology, 46, 3105–3113, 2001.

[3] Oberai AA, Gokhale NH, Doyley MM, Bamber JC, Evaluation of the Adjoint Equation Based Algorithm for Elasticity Imaging, Physics in Medicine and Biology, 49, 2955–2974, 2004.

* *indicates Presenter*

074 **NONLINEAR ELASTICITY IMAGING FOR INCOMPRESSIBLE SOLIDS.**

S Goenezen[1], AA Oberai[1], PE Barbone[2].*
[1]Rensselaer Polytechnic Institute, Troy, NY, USA; [2]Boston University, Boston, MA, USA.

Background: Nonlinear elasticity imaging has the potential of distinguishing different tissue types and hence improving breast cancer diagnosis. For example, *ex–vivo* data suggests that while the elastic modulus of fibroadenoma and invasive ductal carcinoma (IDC) at small strains is similar, at large strains (15%) IDC is about three times as stiff as fibroadenoma [1]. As a result, it may be possible to distinguish IDC from fibroadenoma by imaging the increase in stiffness with increasing strain. Recently we have developed an algorithm that accomplishes this by imaging the linear and nonlinear elastic parameters of tissue using quasi–static displacement data measured at two different levels of overall strain [2]. This algorithm has provided encouraging clinical results. However, it is somewhat limited in that it assumes that tissue deformation in the imaging plane is compressible (plane–stress hypothesis).

Aims: In practice, tissue deformation in the imaging plane can be nearly area–preserving if the out of plane strain component is small (plane–strain state). Further, when imaged in three dimensions, tissue deformation is always nearly incompressible. Standard finite element formulations fail to accurately model incompressible deformations, however. Motivated by these observations, in this presentation, we present an extension of our algorithm that is capable of modeling tissue as an incompressible material in two and three dimensions.

Methods: We solve the inverse problem of determining the linear and nonlinear elastic property distributions iteratively. We utilize a quasi–Newton method to minimize the difference between predicted and measured displacement fields. The overall computational cost of this algorithm is significantly reduced by employing the adjoint method and a novel material property continuation strategy. Using this approach, the cost of solving the inverse nonlinear elasticity problem is only two–to–three times that of solving the corresponding forward problem. We model tissue as an incompressible isotropic hyperelastic solid. The stress–strain response is assumed to be exponential and is given by the Veronda–Westman constitutive model. In order to handle the incompressibility constraint, we augment the finite element formulation with a stabilizing term that prevents the appearance of the spurious pressure modes and the accompanying displacement locking observed in standard finite element schemes [3].

Results: We solve benchmark forward problems with known displacement fields in order to test the effectiveness of the proposed approach in modeling the incompressible behavior of tissue. Its performance in solving inverse problems is assessed using displacement data obtained by solving the forward problem with known material property distributions and data obtained from tissue–mimicking phantoms. In all cases, it is found that the proposed approach accurately models the incompressible behavior of tissue.

Conclusions: A new, efficient approach for imaging the nonlinear elastic properties of tissue undergoing incompressible motion has been developed and tested. It is conjectured that this algorithm could play a role in improving the diagnosis of breast cancer using elasticity imaging.

Acknowledgements: We are grateful for the support from the NIH (R21–CA133488). PEB further acknowledges the support of CenSSIS (The Center for Subsurface Sensing and Imaging Systems) under the Engineering Research Centers Program of the National Science Foundation (Award No. EEC–9986821).

References:

[1] Wellman P, Howe RH, Dalton E and Kern KA. Breast tissue stiffness in compression is correlated to histological diagnosis Technical Report, Harvard Biorobotics Laboratory, 1999.
[2] NH Gokhale, PE Barbone and AA Oberai. Solution of the nonlinear elasticity imaging inverse problem: the compressible case, Inverse Problems, in presss.
[3] Klaas O, Maniatty A and Shephard MS. A stabilized mixed finite element method for finite elasticity. Formulation for linear displacement and pressure interpolation, Comp Meth in Appl Mech and Eng, 180 (1–2), 65–79, 1999.

* *indicates Presenter*

021 **LINEAR ELLIPTIC AND NONLINEAR LOG–ELASTOGRAPHIC PDE SOLVERS FOR SHEAR MODULUS RECOVERY FROM SINGLE FREQUENCY ELASTOGRAPHIC DATA.**

K Lin[1], JR McLaughlin[1].*
[1]Rensselaear Polytechnic Institute, Troy, NY, USA.

Background: Assuming that the single frequency measured displacement of the propagating shear wave satisfies the acoustic wave equation, the locally constant assumption on shear modulus is widely accepted for deriving the Direct Inversion Model from the first order partial differential equation (PDE) model, i.e. the Full Inversion Model, in the inverse problem of elastography. Previous investigation (see [1] for a rigorous proof) has shown that the solution from the Direct Inversion Method is a good approximation to the exact modulus under some hypotheses; reconstruction results from simulated data have confirmed the theoretical relative error estimate. However, when there are a number of high contrast inclusions embedded in the background, recovering the shear modulus from the Full Inversion Model can yield a more reliable image. To solve the first order PDE involved in the Full Inversion Model in a stable manner, we need to handle the complex features of the characteristics in the differential equation and capture the possible exponential growth and decay of the targeted parameter.

Aims: The goal here is to develop fast and stable finite difference based numerical solvers for shear modulus recovery from the first order PDE model in the inverse problem. We aim to establish the stability and accuracy results for our numerical schemes and compare their performances with an upwind semi–implicit numerical scheme and the Direct Inversion Algorithm. Our examples are with synthetic data with a variety of multiple shear modulus inclusions.

Methods: The first method for the inverse problem is inspired by Fattal and Kupferman [2] in their simulation of viscoelastic flows. We use a logarithmic variable transformation to establish the nonlinear log–elastographic numerical scheme for solving the differential equation as a evolution type of PDE in the inverse problem. Our second method for the inverse problem is inspired by numerical computation methods for elliptic equations. It is also based on the non–oscillatory part of the differential equation. In our forward simulation, perfectly matched layer absorbing boundary conditions are implemented to avoid artificial reflections.

Results: Stability and first order accuracy results are obtained for both the linear elliptic scheme and nonlinear log–elastographic scheme [1]. Images of shear modulus reconstructions from simulated data are presented to demonstrate cases where each of the proposed numerical schemes outperforms both the other numerical scheme and the local inversion algorithm.

Conclusions: We have constructed and analyzed two first order accurate finite difference based PDE solvers for shear modulus recovery from single frequency elastographic data. The nonlinear log–elastographic scheme is the most stable algorithm to capture the exponential growth and decay of the target value, while the linear elliptic scheme has the best performance when stiff inclusions are closely distributed along the direction of shear wave propagation.

Acknowledgements: We acknowledge NIH and ONR for partial support of this work. This work was performed at IPRPI, the Inverse Problem Center at Rensselaer Polytechnic Institute.

References:

[1] K. Lin, Ph. D. Thesis, "Error estimation for the Direct Inversion Model and numerical schemes for the Full Inversion Model in Elastography", August, 2008.
[2] R. Fattal and R. Kupferman, "Time–dependent simulation of viscoelastic flows at high Weissenberg number using the log–conformation representation", Journal of Non–Newtonian Fluid Mechanics, 126(2005) 23–37.

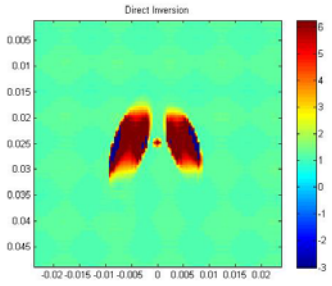

Direct Inversion Recovery

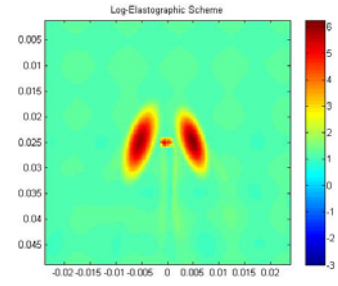

Log–Elastographic Scheme Recovery

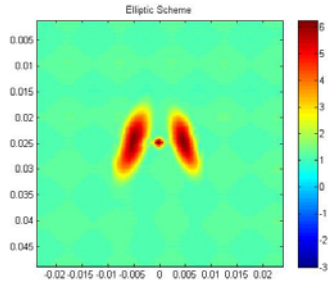

Elliptic Scheme Recovery

031 **EFFICIENT BIOMECHANICAL MODELING VIA FEATURE SENSITIVITY.**

V Mishra[1], K Suresh[1].*
[1]University of Wisconsin–Madison, 1513 University Ave, Madison, WI, USA.

Background: Shape and topology optimization techniques have flourished over the last two decades, resulting in a number of powerful mathematical concepts. One such concept is that of topological sensitivity [1] that quantifies the impact of adding infinitesimal holes (within a given continuum) on specific quantities of interest such as compliance, average stress, etc.

Aims: We recently proposed a novel generalization of topological sensitivity called Feature Sensitivity [2] that captures the change in quantities of interest when an arbitrary feature (e.g., tumor) is inserted within an existing continuum (i.e., tissue). The objective of this presentation is to discuss the biomechanical applications of Feature Sensitivity, in particular, for detecting and sizing tumors within healthy tissue.

Methods: Feature Sensitivity relies on fundamental theorems of shape sensitivity and adjoint formulations of boundary value problems. It provides an analytical expression for rapidly computing various quantities of interest such as tissue compliance, stress distribution within a region, etc., without having to rely on expensive finite element analysis (FEA).

Results: We have shown that a closed formed expression for Feature Sensitivity can be established for a large class of field problems in 2–D and 3–D. For example, Figure 1 illustrates a plane stress problem where the quantity of interest is the average vertical displacement over the region 'R'. The task lies in rapidly updating this quantity when an arbitrary feature (Example: an elliptical hole as in Figure 1) is placed within the body. While one can rely on FEA, this can be slow when numerous features need to be explored. On the other hand, Figure 2 illustrates that Feature Sensitivity (FS) provides an excellent estimate. Further, in [2], we have shown that the computational cost associated with Feature Sensitivity is negligible.

Conclusions: Feature Sensitivity can dramatically reduce the computational cost of various shape optimization and inverse problems that occur in biomechanical applications.

Acknowledgements: The authors wish to acknowledge support from support of the National Science Foundation under grants OCI–0636206, CMMI–0726635 and CMMI–0745398.

References:

[1] Novotny, A.A., Feijóo, R. A., Taroco, E., Padra, C., Topological–Shape Sensitivity Analysis. Computer Methods in Applied Mechanics and Engineering, 2003. 192(7): p. 803–829.
[2] Gopalakrishnan, S. H., Suresh, K, "Feature Sensitivity: A Generalization of Topological Sensitivity", Finite Elements in Design and Analysis, in press.

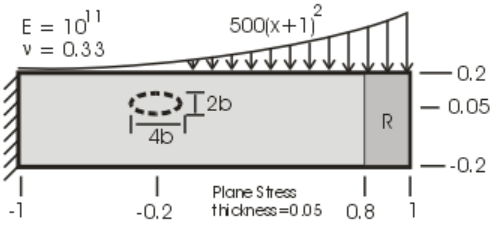

Figure 1: A plane–stress problem.

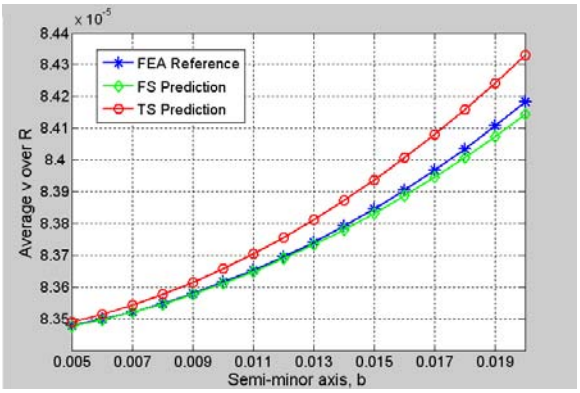

Figure 2: Accuracy of feature sensitivity.

* *indicates Presenter*

039 **A NONLINEAR MODEL FOR MECHANICAL IMAGING.**

Salavat R. Aglyamov[1], Vladimir Egorov[2], Stanislav Y. Emelianov[1], Armen Sarvazyan[2].*
[1]University of Texas at Austin, Austin, TX, USA; [2]Artann Laboratories, Inc., Trenton, NJ, USA.

Background: Mechanical imaging, one of the approaches in elasticity imaging, is based on measurements of stress patterns on the surface of the investigated tissue [1]. The distribution of surface stress provides important information about elastic composition and geometry of the underlying tissue structures. Recent studies have shown great promise for detecting breast and prostate cancers using mechanical imaging [2,3]. During clinical examination, a mechanical imaging probe consisting of a matrix of stress sensors acts similarly to human fingers mimicking manual palpation. For quantitative diagnosis of tissue pathologies, however, an accurate interpretation of the mechanical imaging data based on an adequate mechanical model is required. In addition, a mechanical model is needed for the development of the robust inverse algorithms to reconstruct internal distribution of tissue elasticity.

Aims: The goal of this study was to develop a mathematical model of mechanical imaging and to verify this model using the results of tissue–mimicking phantom experiments.

Methods: Since relatively large deformations are applied during mechanical imaging, strain energy potentials were used to model nonlinear behavior of incompressible tissue. Specifically, strain energy potentials in polynomial form with N=1 (two elastic constants) and N=2 (five elastic constants) were considered. Numerical 3D simulations were performed for a given geometry of mechanical imaging probe and phantoms using the finite element method. To explore the influence of the boundary conditions at the interface between the sensor array and the tissue surface, various combinations of boundary conditions were investigated. The experimental studies were performed using tissue–mimicking phantoms constructed from rubber and silicon. Elastic properties of the background material were chosen close to the properties of normal breast and prostate tissues with Young's modulus of approximately 4–6 kPa. The inclusions with different elastic properties and various sizes were used to mimic malignant and benign tumors. The nonlinear elastic properties of the phantom materials were estimated using a set of compression tests. A breast mechanical imager (SureTouch™, Medical Tactile Inc., CA), a compact device for real time mechanical imaging of breast pathologies, was used in mechanical imaging experiments. Using both numerical and experimental studies, the contrast in mechanical imaging was studied. The contrast in our studies was defined as the ratio between the maximum pressure signal from inclusion and a baseline signal from surrounding tissue. Note that during clinical studies, relatively large deformations are customarily applied to image the surrounding tissue and the underlying pathology.

Results: Results of the finite element modeling show that the nonlinear elastic properties play a critical role in tissue behavior during mechanical imaging experiments. A comparison between two forms of the nonlinear strain potential demonstrates that for a polynomial form with N=2, the contrast between the inclusion and the background is increasing rapidly once the applied deformation reaches 20–30%. Such behavior was observed during experimental and clinical studies. For a polynomial form with N=1, the contrast between the inclusion and the background is also increasing but at much slower rate. Finally, the linear elastic model results only in marginal contrast enhancement with large deformations. Therefore, nonlinear model is required to explain the experimental results where the high contrast was obtained for high deformation level. Using slippery boundary conditions between the probe and the object increases the contrast in comparison with non–slippery boundary conditions. This is in agreement with phantom experiments and clinical testing of mechanical imaging.

Conclusions: The results of our study show that mechanical imaging experiments can be accurately described using nonlinear mechanical model with strain energy potential in polynomial form with N=2. Furthermore, this model can also be used to assess the elastic properties of tissue.

Acknowledgements: This work was supported in part by National Institutes of Health under grants EB 004963, HL 091609, CA 091392 and CA 082620.

References:

[1] Sarvazyan A. Mechanical Imaging: A new technology for medical diagnostics. Int. J. Med. Inf., 1998, 49, 195–216.
[2] Egorov V., Airapetian S., Sarvazyan A. Prostate Mechanical Imaging: 3–D image composition and feature calculations. IEEE Trans. Med. Imag. 2006, 25(10), 1329–1340.
[3] Egorov V. and Sarvazyan A., Mechanical Imaging of the breast. IEEE Trans. Med. Imaging, 2008, 27(9), 1275–1287.

057 **THE LOG ELASTOGRAPHIC ALGORITHM FOR SHEAR MODULUS IMAGING USING A 2D ELASTIC SYSTEM.**

Ning Zhang[1], Joyce R. McLaughlin[1].*
[1]Rensselaer Polytechnic Institute, 110 Eighth Street, Troy, NY, USA.

Background: A common assumption when calculating shear stiffness images from elastographic data is the so–called locally constant assumption when derivatives of biomechanical properties are ignored. Estimates for the relative error made by this assumption are given in [1] when the mathematical model is the Helmholtz equation. This estimate (and also examples in [1]) suggests that a Full Inversion method, in this case based on the elastic system, can result in enhanced images. This Full Inversion method will be based on a mathematical model that includes first order derivatives of the biomechanical properties.

Aims: The aim is to develop a stable, accurate Full Inversion algorithm that effectively controls potential exponential growth in the error. This error can occur when solving first order linear partial differential equation systems when the coefficient of the zeroth order term in shear stiffness has the wrong sign or when all coefficients of the zeroth and first order terms are complex.

Methods: A nonlinear Log Elastographic method for recovering shear stiffness, μ, and pressure, p, simultaneously in a 2D elastic system will be presented. The underlying idea is to develop a new system for log μ and p, discretize this system to obtain a stable algorithm and selectively exponentiate the discretization resulting in a straightforward but nonlinear algorithm. A more detailed realization is as follows:

1) when the 2D displacement vector is assumed known, the Full Inversion equation for μ and p is a first order p.d.e. system;
2) we assume that, in the experiment, wave propagation occurs primarily in one direction, call it the x direction;
3) we treat the propagation direction variable, x, as a time like variable and rewrite the Full Inversion system as a p.d.e. of the form
$$(\mu_x, p_x) = (F_1(\mu, p, \mu_y, p_y), F_2(\mu, p, \mu_y, p_y)),$$ where F_1 and F_2 are both linear in μ_y and p_y;
4) we rewrite this system with log μ as the dependent variable instead of μ;
5) we discretize the new system in 4) with finite difference methods;
6) lastly, we exponentiate the discretized equation for log μ in 5) and selectively linearize the exponential terms that contain the pressure.

The final result is a new discretized nonlinear equation for μ. This algorithm gives stable and accurate results when all quantities are real, without requiring a fine discretization to control possible exponential error growth. In the complex case, an additional filtering step is made because arbitrarily high exponential growth can occur.

Results: We compare images obtained with this new algorithm and images obtained with the locally constant assumption algorithm and exhibit examples to show that Full Inversion can perform significantly better. E.g., in the figures below, (a) is the exact shear stiffness, (b) is the recovery obtained with the locally constant assumption algorithm and (c) is the recovery obtained from this new algorithm, which gives an image with better quality, including size, shape and contrast of the inclusions.

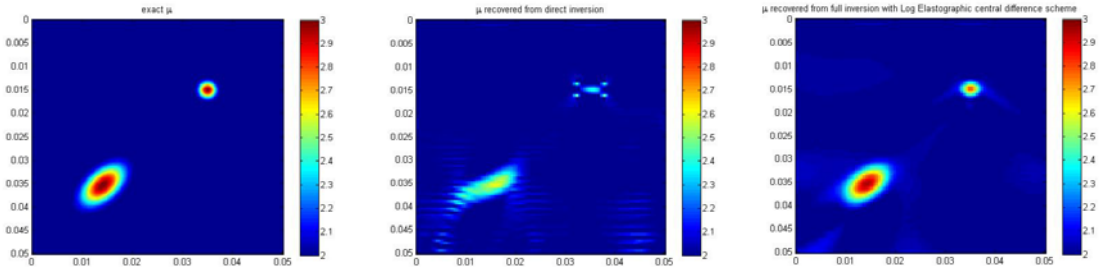

Conclusion: We have developed a new nonlinear Log Elastographic method for imaging the shear stiffness and the pressure simultaneously using a 2D elastic system, which improves the quality of the recovered images, especially for small inclusions and in the presence of multiple inclusions.

References:

[1] K. Lin, Ph. D. Thesis, "Error estimation for the Direct Inversion Model and numerical schemes for the Full Inversion Model in Elastography", August, 2008.

* *indicates Presenter*

062 **IMPROVEMENTS IN THERMALLY–ABLATED LESION VISUALIZATION USING YOUNG'S MODULUS IMAGING.**

Jingfeng Jiang[1], Chris Brace[2], Timothy J. Hall[1], Tomy Varghese[1,3], Ernest L. Madsen[1], Shyam Bharat[1,3], Maritza A. Hobson[1], James A. Zagzebski[1] and Fred Lee Jr.[2].*

[1]Medical Physics, [2]Radiology and [3]Electrical Engineering Departments, University of Wisconsin–Madison, Madison, WI, USA.

Background and Aims: Effective tumor localization and intra–procedural monitoring are critical to treatment success during thermal ablation. However, conventional B–mode ultrasound is ineffective at depicting the margin of tissue coagulation because only hyperechoic areas created by micro–bubbling and out–gassing are visible. The objective of this study is to assess whether an ultrasound based modulus imaging method using clinical ultrasound scanners can be used to determine the size and the shape of the ablated area, where protein denaturation and water vaporization cause an increase of the tissue modulus.

Methods: Following the methodology originally proposed by Kallel and Bertrand [1], we iteratively adjusted local modulus values to enforce a mechanical model to produce displacements close to those obtained from ultrasonic speckle tracking (i.e., optimization). Key refinements include obtaining more accurate displacement measurements using a robust motion tracking algorithm [2] and using an edge–preserving term in the cost function. Consistent with our experience with *in vivo* cases, the edge–preserving term numerically produces coherent thermal lesions with sharp boundaries. Validation studies were performed in tissue–mimicking (TM) phantoms and *in vivo* porcine livers. The phantom has a simulated spherical ablated zone (19 mm in diameter; elastic contrast 3.2:1) encompassing a simulated irregularly shaped liver tumor (elastic contrast 5.8:1) in a background TM material. TM materials consist of dispersions of microscopic safflower oil droplets in an aqueous gelatin matrix, and changes of stiffness were achieved by adjusting the volume percent of oil. In animal studies, thermal ablations were created in pig livers during thoracotomy using both radiofrequency and microwave applicators. In both experiments, radiofrequency ultrasound data were acquired from a Siemens SONOLINE Antares under the guidance of the eSieTouch real–time strain imaging system [3]. Ablation zones were excised and stained for viability to demarcate the zone of complete necrosis. The gross pathology images were digitally overlaid on modulus images to determine the percentage overlap in the ablated area.

Results: In phantoms, the simulated ablated region was well correlated with that seen on the Young's modulus image (>95% overlap). Ablated areas in liver as estimated from modulus reconstruction agreed with gross pathology (90%). In one case, B–mode and strain images failed to accurately depict a bifurcated ablation zone while the modulus image was able to show the bifurcation accurately, as shown in Figure 1 below. This could have resulted in an overestimate of the ablated volume that would leave viable tumor cells untreated.

Conclusions: Modulus imaging may be an effective alternative to B–mode and strain imaging to determine true ablation zone boundaries. Therefore, modulus imaging has potential for improved localization of tumors and for monitoring tissue damage during and after thermal ablation treatments.

Acknowledgements: We gratefully acknowledge the support by NIH grants R01CA100373, R01CA112192, T32CA09206 and funding from the UW–Madison.

References:

[1] F. Kallel and M. Bertrand, IEEE Trans. Medical Imaging, vol. 15, pp. 299–313, 1996.
[2] J. Jiang and T. J. Hall, IEEE Ultrasonics Symposium, 2006.
[3] T. J. Hall, Y. Zhu, and C. S. Spalding, Ultrasound Med Biol, vol. 29, pp. 427–35, 2003.

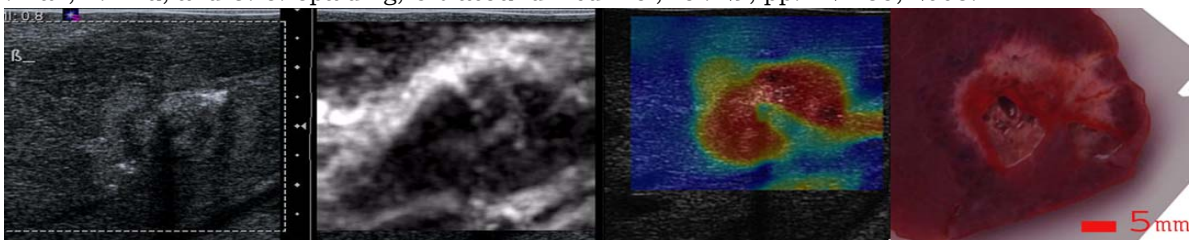

(a) (b) (c) (d)

Figure1: B–mode (a), strain (b), modulus (c) and optical (d) images obtained from a thermal lesion in an *in vivo* pig study.

002 **REAL–TIME IMAGING OF CARDIAC MECHANICAL FUNCTION USING ULTRASOUND.**

James Hamilton[1], Matthew O'Donnell[2], Theodore J Kolias[3].*
[1]Pixel Velocity Inc., Ann Arbor, MI, USA; [2]University of Washington, Seattle, WA, USA; [3]University of Michigan, Ann Arbor, MI, USA.

Background: A primary goal of clinical cardiology is regional assessment of heart muscle mechanical function. Echocardiography is well suited for evaluating myocardium performance due to its high temporal sampling, fine resolution, non–invasiveness and low cost. However, current clinical methods have several limitations. The most common is visual evaluation of B–mode (i.e., gray scale) images to determine abnormalities which is, therefore, subjective and requiring a high level of expertise. Other common echocardiographic measurements are global (e.g., ejection fraction) and are not sensitive to regional and subtle dysfunction. Doppler techniques have greatly improved measurements of cardiac dynamics but are limited by acoustical viewing geometry and suffer motion–induced artifacts. Recently, B–mode tracking applications have shown some interesting results but will not be clinically significant unless they can be made real–time with improved accuracy and robustness.

Ultrasound speckle tracking of radio–frequency (RF) data overcomes these limitations providing accurate, robust measurements of regional tissue motion and deformation. Several studies have produced promising results using RF speckle tracking for measuring heart mechanical function [1–3]. However, clinical impact and widespread use of this technology has been limited because most methods are not real–time due to the large computational requirements for real–time speckle tracking. Real–time capability is critical for efficient clinical use because it provides quick assessment of tissue mechanical conditions as well as guides image acquisition.

Aims: The goal of this research is to demonstrate real–time RF speckle tracking for accurate, regional assessment of cardiac function.

Methods: A cart–based fully functional imaging device, suitable for clinical use, was built. The system produces real–time B–mode, 2D tissue velocity, strain, strain rate and correlation magnitude images. A fast acquisition architecture provides frame rates exceeding 200 Hz for full field of view, fine resolution, cardiac imaging. Multi–resolution speckle tracking reduces computations and provides the large inter–frame tracking range needed to accommodate peak cardiac tissue velocities (>150 mm/s). Finally, suitable clinical functionality is supported by display, data archive and system control sub–systems.

Results: Images representing cardiac tissue motion and deformation were displayed in real–time from several volunteers. The device provided instant accurate assessment of regional myocardium function. Measurements of peak systolic strain, tissue velocity and strain rate were evaluated and compared for several standard echocardiographic views and multiple segments.

Conclusions: A real–time ultrasound imaging system for visualizing and measuring regional cardiac mechanical function was developed, and clinical performance was demonstrated. The accurate real–time, regional measurement capabilities of the device lay the foundation for wide spread clinical use of ultrasound based measurements of cardiac mechanics.

Acknowledgements: This work was supported in part by NIH grant 2R44HL071379.

References:

[1] J. D'hooge, E. Konofagou, F. Jamal, A. Heimdal, L. Barrios, B. Bijnens, J. Thoen, F. Van de Werf, G. Sutherland, and P. Suetens, "Two–dimensional ultrasonic strain rate measurement of the human heart *in vivo*," IEEE Trans. Ultrason., Ferroelect., Freq. Contr., 2002; 49: 281–286.
[2] Varghese T, Zagzebski JA, Rahko P, Breburda CS. "Ultrasonic imaging of myocardial strain using cardiac elastography," Ultrason Imaging. 2003; 25(1):1–16.
[3] Konofagou EE, D'hooge J, Ophir J. "Myocardial elastography–A feasibility study *in vivo*," Ultrasound Med Biol. 2002; 28(4):475–82.

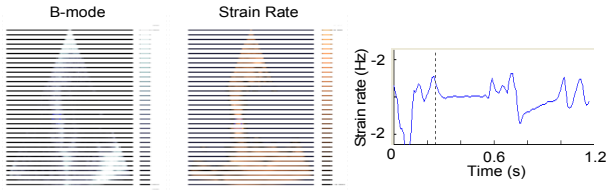

Figure 1: Apical B–mode and strain rate images of septum created by the imaging system. Graph shows strain rate variation at region of interest (blue box) through cardiac cycle.

* *indicates Presenter*

005 **THE IMPACT OF CALCIUM ON ARFI IMAGING OF ATHEROSCLEROTIC PLAQUES.**

Russell H. Behler[1], Timothy C. Nichols[1], Elizabeth P. Merricks[1], Caterina M. Gallippi[1].*
[1]The University of North Carolina at Chapel Hill, 150 MacNider Hall, CB 7575, Chapel Hill, NC, USA.

Background: Heart attack and stroke are often caused by the rupture of vulnerable coronary and carotid plaques, respectively. It is well established that a plaque's rupture potential is increased by certain compositional features including a degraded fibrous cap and a large lipid core. However, the role of calcium deposition in plaque vulnerability remains unknown. Assessing the location and severity of calcification may, in the future, aid in the risk stratification of patients with coronary or carotid stenosis [1–3]. We have previously demonstrated in a familial hypercholesterolemic (FH) pig model that Acoustic Radiation Force Impulse (ARFI) imaging detects both stenotic and non–stenotic plaques and describes their composition [4]. With immunohistochemical validation, we have shown a spatial correlation between ARFI–induced peak displacement and plaque collagen content as well as time to recovery from ARFI–induced displacement and plaque elastin content. We have also shown a relationship between radiation force–induced shear wave velocity, as in shear wave elastography imaging (SWEI), and plaque composition [5]. However, the impact of plaque calcium content on ARFI and SWEI imaging is yet to be determined. It is, thus, the focus of this work.

Aim: To test our hypothesis that calcium deposition results in smaller ARFI–induced peak displacement and faster SWEI–induced shear wave velocities relative to non–calcified plaque and arterial wall tissue.

Methods: ARFI and SWEI imaging were performed using a Siemens SONOLINE Antares™ imaging system and VF7–3 linear array transducer (Siemens Medical Solutions USA, Inc. Ultrasound Division, USA). A freshly harvested left femoral artery of an adult pig with advanced, diffuse atherosclerosis was suspended in a saline bath and hydrostatically pressurized for *ex vivo* imaging. Following imaging, the vessel was sectioned and stained for calcium, collagen, and elastin composition for spatially matched immunohistochemical validation of imaging results.

Results: Immunohistochemistry confirmed the presence of a large region of calcium deposition in the context of diffuse atherosclerosis. This plaque also contained focal collagen deposition and elastin degradation. In the area of calcium deposition, median ARFI–induced peak displacement was 3.9 μm, while median peak displacement in adjacent plaque tissue without calcium deposition was 4.9 μm. Median peak displacement in arterial wall tissue beside the plaque was 9.2 μm. SWEI derived shear wave velocity measured in the region of calcium deposition was 10.6 m/s, versus 8.9 m/s in adjacent plaque tissue and 4.7 m/s in arterial wall tissue beside the plaque.

Conclusions: Arterial calcium deposition associated with atherosclerosis resulted in diminished ARFI–induced peak displacement and accelerated SWEI–induced shear wave velocity, as predicted, in this preliminary *ex vivo* study. This supports the merit of further *in vivo* study and suggests that radiation force imaging may be relevant to identifying and localizing calcium deposition.

Acknowledgements: We thank Siemens Medical Solutions, USA Inc. Ultrasound Division for *in kind* support and Gregg Trahey, Jeremy Dahl, and Kathy Nightingale for their technical insights. This work is supported by AHA award #0765330U and NIH grants P20–RR020764 and 5K12HD001441.

References:

[1] Li Z, Howarth S, *et al.* Does Calcium Deposition Play a Role in the Stability of Atheroma? Location May be the Key. Cerebrovasc Dis 2007; 24:452–459.
[2] Thomas B. and Larson T. Quantitative Carotid Calcium Scoring and Cerebral Ischemia – A pilot Study and Review of Recent Literature. Cerebrovasc Dis 2007; 23:453–456.
[3] Li J, Zhu C, *et al.* The Role of Inflammation in Coronary Artery Calcification. Ageing Research Reviews 6(2007)263–270.
[4] Behler R, Merricks E, *et al. In Vivo* ARFI Atherosclerosis Imaging with Validation in a Relevant Pig Model of CVD. 19th International Congress on Acoustics, 2007: ULT–01–007.
[5] Sarvazyan A, Rudenko O, *et al.* Shear wave elasticity imaging: A new ultrasonic technology of medical diagnostics. Ultrasound in Medicine and Biology 24 (9): 1419–1435 Nov 1998.

049 **PULSE WAVE IMAGING (PWI) AS A TOOL FOR THE QUANTITATIVE ASSESSMENT OF VASCULAR ELASTICITY: EVALUATION OF A QUANTITATIVE FINITE–ELEMENT MODEL AND *IN–VIVO* RESULTS IN HUMAN SUBJECTS.**

J Vappou[1], J Luo[1], EE Konofagou[1].*
[1]Biomedical Engineering Department, Columbia University, New York, NY, USA.

Background: A large number of pathological conditions result in significant changes of the mechanical properties of the aortic wall. Using the Pulse Wave Velocity (PWV) as an indicator of aortic stiffness through time–delay methods has been proposed for several decades [1]. However, accuracy limitations and homogeneity assumptions do not allow the detection of localized and/or subtle changes in aortic wall mechanical properties that are characteristic of focal diseases such as atherosclerosis and aneurysms. Pulse Wave Imaging (PWI) has been developed to map and quantify the pulse wave (PW) propagation along the abdominal aortic wall and measure its local properties [2] (see Figure 1).

Aims: PWI has been performed on healthy mice and on mice with abdominal aortic aneurysms (AAA), and distinct PW propagation patterns were reported [3]. Determining the mechanical properties from such varying PW patterns is challenging. We present a finite–element-based approach that aims at improving our understanding of the PW patterns and their relationship to the underlying mechanical properties. The applicability of the PWI method to human subjects for assessment of aortic elasticity is also evaluated.

Methods: A Fluid–Structure Interaction (FSI) coupled model was developed based on idealized axisymmetric aorta geometry. Realistic blood flow boundary conditions were imposed using *in vivo* pulsed Doppler flow measurements. The accuracy of the model as well as its ability to reproduce realistic PW propagation was evaluated by performing a parametric analysis on aortic elasticity. The Young's modulus of the aortic wall was varied between 10 and 500kPa, which corresponds to the widest range of reported stiffness values in healthy and diseased aortas. Also, comparison was performed between different methods to calculate the elasticity from the PWV. A Sonix RP system (Ultrasonix Medical Corp., Richmond, Canada) was employed with a phased array in 90° sector, a depth of 11cm, a frequency of 3.3 MHz, and a line density of 128 lines. Radio–frequency (RF) signals of the healthy aortas were digitized at a sampling frequency of 20 MHz and a sampling resolution of 16 bits. 2–D full long–axis view RF frames were reconstructed from 5–7 narrow RF sector frames at the high frame rate of 481 Hz. The radial wall velocities were estimated using 1–D cross–correlation (window size = 3.5 mm, 75% overlap) and cine–loops during the entire cardiac cycle were generated.

Results: The Finite–Element model was able to predict with good accuracy the expected PWV values in different theoretical cases. The averaged error between the theoretical and the calculated Young's modulus was equal to 24%. PWV *in vivo* on human subjects was measured between 3–4 m/s, which is similar to previously reported PWV values in aortas of young subjects. Using the Moens–Korteweg equation in cylindrical geometry and based on the geometrical parameters measured on the B–mode image leads to a range of 68–96kPa for the aortic Young's modulus, which is also within the range studied in the Finite–Element model.

Conclusions: PWI is a promising technique for the characterization of the aortic wall mechanical properties. Compared to conventional wave–based elasticity imaging methods, PWI offers the advantage of using the physiologic and sharp perturbation of the pulse wave. Ongoing work deals with the refinement of the FEM, including realistic geometries and constitutive relationships, and the validation of the technique on aortic phantoms.

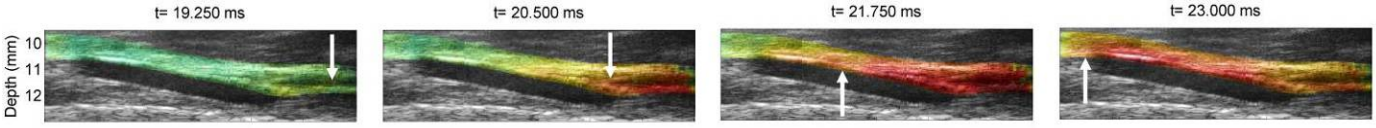

Figure 1: *In vivo* PWI on normal mouse at different times showing the propagation of the pulse wave along the abdominal aorta. Radial wall velocity is color–encoded and overlaid on the B–mode image.

Acknowledgements: This study was funded in part by NIH grants 5R01EB006042 and 1KL2RR024157.

References:

[1] Nichols, O'Rourke, MacDonald's Blood Flow in Arteries, Oxford Univesity Press (5th Ed.)
[2] Fujikura et al., A Novel, Non–Invasive Technique for Pulse–Wave Imaging and Characterization of Clinically Significant Vascular Mechanical Properties *in vivo*, Ultrasonic Imaging 29:137–154, 2007.
[3] Luo et al, Pulse wave imaging of normal and aneurysmal abdominal aortas *in vivo*, IEEE TMI (accepted).

* *indicates Presenter*

066 **ACOUSTIC RADIATION FORCE IMPULSE IMAGING OF MYOCARDIAL PERFORMANCE, INITIAL *IN–VIVO* RESULTS.**

SJ Hsu[1], PD Wolf[1], DM Dumont[1], RR Bouchard[1], BC Byram[1], SA Eyerly[1], Y Li[1], GE Trahey[1].*
[1]Duke University, Durham, NC, USA.

Background: One important parameter that reflects myocardial performance is myocardial stiffness. Several studies have associated increased myocardial stiffness with heart failure and various cardiac diseases. Variations within acoustic radiation force impulse (ARFI)–induced tissue displacement curves have shown an inverse relationship with the changes in myocardial stiffness through the cardiac cycle. Expanding on these results, we present the preliminary investigations that further establish the correlation between myocardial stiffness and performance with ARFI imaging.

Aims: To monitor the changes in myocardial performance with acoustic radiation force impulse imaging.

Methods: ARFI images were made of the left ventricular free wall of an exposed ovine heart. Preload, afterload and contractility (three determinants of myocardial performance) were varied, and the ensuing changes in relative myocardial stiffness (normalized inverse ARFI–induced tissue displacements) through multiple heartbeats were measured. Left ventricular pressures and volumes, and the global electrocardiogram were also recorded. The ARFI imaging displacement curve, measured with decreased preload, was compared with estimates of myocardial elastances derived from pressure–volume (P–V) analysis.

Results:

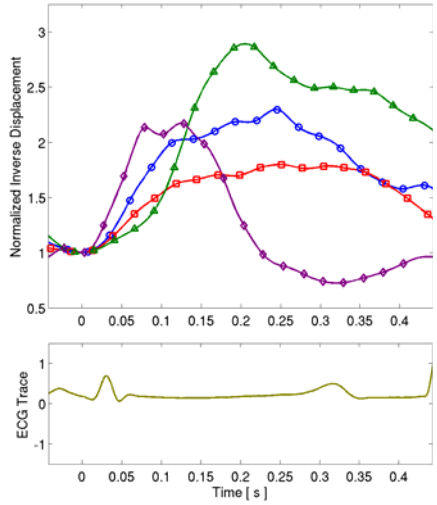

Figure 1: Average inverse displacements (normalized by the maximum end diastolic displacement) and matched ECG (below). Differences in maximum stiffening factors and rates can be observed between the baseline (○) and after decreasing preload (□), increasing afterload (◇), and increasing contractility (△).

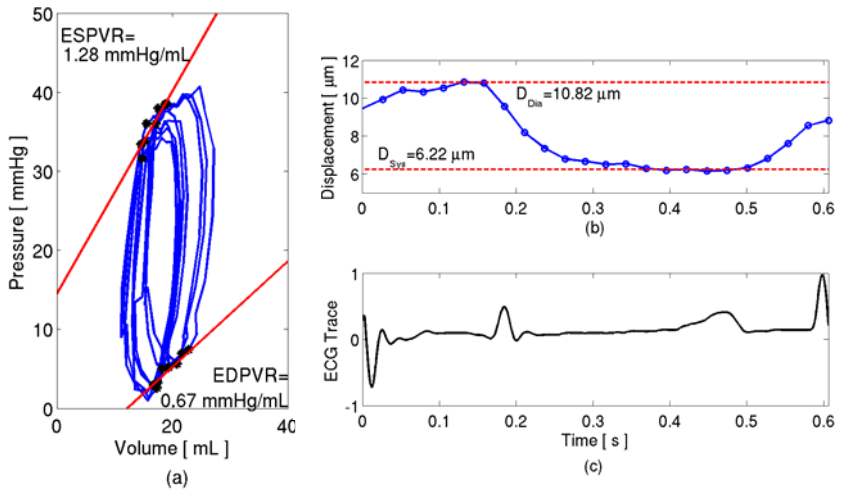

Figure 2: Comparison between pressure-volume analysis and ARFI imaging. (a) The end systolic and end diastolic pressure volume relations (ESPVR and EDPVR) are calculated via P–V analysis and venal caval occlusions. The systolic to diastolic elastance ratio (ESPVR:EDPVR) was measured to be 1.91:1. (b) The corresponding averaged ARFI imaging measured a systolic to diastolic stiffness ratio (D_{Dia}:D_{Sys}) of 1.74:1. (c) The matched ECG is shown below.

Conclusions: Changes in myocardial performance were reflected by changes within the ARFI–induced displacement curves. In the cases of varying preload and contractility, the maximum stiffening factor (with respect to the minimum end diastolic stiffness) was affected. For varying afterloads, the most apparent changes within the stiffness curves were in the rates of stiffening. The systolic to diastolic ARFI–based stiffness ratio (1.74:1) was measured to be comparable with an equivalent P–V-based elastance ratio (1.91:1). Additional investigations of cardiac ARFI imaging are necessary before more definite relations between myocardial stiffness and performance can be inferred.

Acknowledgements: This research was funded by NIH Grants #: R01–HL–075485, R01–CA–114093, and R21–EB–007741. We would like to thank Siemens Medical Solutions USA, Inc. for their hardware and system support.

* *indicates Presenter*

075 **COMPARISON OF 2D SPECKLE TRACKING AND DTI ON AN ISOLATED RABBIT HEART.**

Congxian Jia[1], Ragnar Olafsson[1], Theodore J. Kolias[1], Sheng–Wen Huang[1], Kang Kim[1,2], Jonathan M. Rubin[1], Hua Xie[3] and Matthew O'Donnell[1,4].*

[1]University of Michigan, Ann Arbor, MI 48109, USA; [2]University of Pittsburgh, Pittsburgh, PA 15213, USA; [3]Philips Research North America, Briarcliff Manor, NY 10510, USA; [4]University of Washington, Seattle, WA 98195, USA.

Background: Cross–correlation–based 2D speckle tracking (ST) [1] and autocorrelation–based Doppler tissue imaging (DTI) [2] are two major techniques for quantitatively assessing myocardial contractility. ST can estimate 2D or 3D motion, while DTI can only estimate the displacement along the beam direction. In addition, DTI suffers from low strain signal–to–noise ratio [3] because a high pulse repetition frequency (PRF) is used to reduce decorrelation due to lateral or elevational motion.

Aims: No quantitative comparison of ST and DTI has been made using the same cardiac data acquired in controlled animal experiments. Here, we aimed to evaluate ST and DTI on complex cardiac motion using a well controlled Langendorff experimental system on an isolated rabbit heart.

Methods: An isolated rabbit heart was retroperfused through the aorta with oxygenated Krebs–Henseleit buffer and paced through the apex at 3Hz. An ultrasound scanner (Sonix RP) acquired radio frequency (RF) data using a linear probe (L14–5/38). To cover the heart area, 17 partially overlapped beam packages with 13 beams per package were fired for each of the three pulse lengths: 1, 4 and 12 cycles at 5 MHz. For each package, we acquired RF data over one heart cycle at a PRF of 738Hz. The RF data acquisition, left ventricular pressure and electrocardiogram recording were synchronized to the pacing signal. DTI and 2D ST were performed on the same RF data.

Results: Figure 1 shows the estimated short–axis view velocities of heart wall using DTI (top row) and 2D ST (middle and bottom rows) at the beginning of systole. 2D ST velocities were estimated with a resolution of 1.1, 1.9 and 5.1mm axially and 2.5mm laterally for three pulse lengths. DTI estimated velocities along the beam direction (axial) with a resolution of about 0.3, 1.0 and 2.9mm. For both methods, tracking variation decreased with increased pulse length, i.e., at sacrifice of spatial resolution. The peak hops in ST results with longer pulses need to be addressed further. Although DTI– and ST– derived axial velocity maps are consistent, comparison of the ST result at 1 cycle with the DTI result at 12 cycles reveals that ST can provide better resolution and lower tracking variation than DTI.

Conclusions: Compared to DTI, 2D ST achieved better accuracy given a tracking resolution. Lack of lateral motion information with DTI induces larger registration errors when accumulating across frames. Furthermore, using 2D ST, principal deformation axes and corresponding normal strains can be derived independent of the coordinate system. The directions of principal deformation axes can be used to detect cardiac dysfunctional areas.

Acknowledgements: This work was supported in part by HL–082640, HL–67647, HL–68658, and CA–109440.

References:

[1] M.A. Lubinski, S.Y. Emelianov, M. O'Donnell, "Speckle tracking methods for ultrasonic elasticity imaging using short–time correlation," IEEE Transactions on Ultrasonics Ferroelectrics and Frequency Control 1999; 46:82–96.

[2] M J. D'hooge, et al., Echocardiographic strain and strain–rate imaging: "A new tool to study regional myocardial function," IEEE Transactions on Medical Imaging 2002; 21:1022–30.

[3] M X. Chen, et al., "3–D correlation–based speckle tracking," Ultrasonic Imaging, Vol. 27, pp. 21–36, 2005.

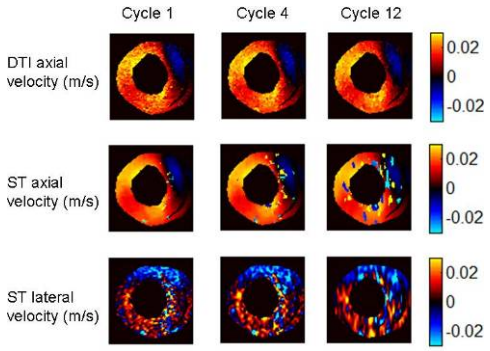

Figure 1: Velocity maps estimated using DTI and ST.

* *indicates Presenter*

061 **ELECTROMECHANICAL WAVE PROPAGATION IN THE NORMAL AND ISCHEMIC CANINE MYOCARDIUM *IN–VIVO*.**

Jean Provost[1], Wei–Ning Lee[1], Kana Fujikura[1], Elisa E. Konofagou[1].*
[1]Biomedical Engineering Department, Columbia University, New York, NY, USA.

Background: Higher temporal resolution through ECG–gated composite ultrasound and elasticity imaging techniques has been previously shown capable of detecting and mapping the electromechanical contraction wave occurring immediately after end–diastole in murine and human hearts *in vivo* [1,2]. The direction of propagation of this wave has already been shown to be dependent on the pacing origin in mice [3], hence, suggesting that the electromechanical wave imaging (EMI) technology could be used to assess conduction properties of the myocardium.

Aims: The goal of this study is to characterize the propagation of the electromechanical wave in three longitudinal planes in the normal, ischemic and infarcted canine myocardium *in vivo*.

Methods: A non–survival canine ischemic model (n=5) was performed by steadily increasing the amount of mid–distal occlusion of the left–anterior descending (LAD) coronary artery, from 0–100% at 20% increments. A pressure catheter (Millar Instruments Inc., Houston, TX, USA) was inserted and sonomicrometry crystals (Sonometrics Corp., London, ONT, Canada) were implanted in the left ventricle to simultaneously obtain pressure and volume measurements and quantify changes in global contractility.

An Ultrasonix RP system (Ultrasonix Med. Corp., Burnaby, BC, Canada) with a 3.3 MHz phased array was used to acquire RF frames at 389 frames per second (fps) using our previously reported automatic composite technique [2]. The parasternal long–axis, parasternal four chamber, and parasternal two chamber views were obtained at each occlusion level. Axial/radial displacement was computed offline using cross–correlation techniques (window size: 4.6 mm, 80% overlap). An automated contour tracking technique [4] was used to segment the myocardium. Displacement color–coded images were then overlaid on the B–mode images.

Results: In the normal case, three waves were observed in the anterior wall within 50 ms immediately after the onset of the QRS complex in the parasternal two chamber view. The first wave originated at the endocardium near the apex and propagated along the anterior wall toward the base at 0.70 m/s. The second and third waves then propagated from base to apex at –0.77 m/s and from apex to base at 1.04 m/s, respectively. Conduction velocities reported in the literature range between 0.6 and 1 m/s [5]. After partial occlusion (40%), the second wave was noted to have lower amplitude, but no significant change in velocities was observed: 0.54, –0.65, and 1.07 m/s. In the infarcted myocardium, the direction of propagation of first two waves was reversed compared to the normal case (–0.83 m/s, and 0.98 m/s, respectively) while the third wave was no longer detectable.

Conclusions: The electromechanical waves exhibited different patterns of propagation in the presence and at the site of ischemia or infarction. This supports the hypothesis that the waves imaged are closely linked to the electrical activation of the myocardium and its disruption in the case of abnormalities. Electromechanical wave imaging could, thus, be used for the detection and treatment monitoring of conduction pathologies. Examples in other echocardiographic views will also be shown.

Acknowledgements: This study was supported in part by NIH grant R01EB006042 and the Wallace H. Coulter foundation.

References:

[1] Pernot, M. and Konofagou, E.E., IEEE Proc. Symp. UFFC, 2005.
[2] Wang, S. et al., IEEE International Ultrasonics Symp., 2007.
[3] Konofagou, E.E et al. IEEE Proc. Symp. UFFC, 2006.
[4] Luo, J. and Konofagou, E.E.; IEEE Trans. UFFC 55(1), 240–248, 2008.
[5] Wikswo, JP, Jr., et al., Circ. Res. 68(2), 513–530, 1991.

086 **MULTISCALE MECHANICAL MODELING OF FLUID/SOLID MIXTURES: APPLICATIONS TO SOFT TISSUE MECHANICS.**

R Leiderman[1], GP Berry[2], JC Bamber[2], Yixiao Zhang[3], AA Oberai[3], C Rivas[4], O Babaniyi[4], PE Barbone[4].*
[1]Federal University of Rio de Janeiro, Rio de Janeiro, BRAZIL; Institute of Cancer Research, Sutton, Surrey, England, UK; [3]Rensselaer Polytechnic Institute, Troy, NY, USA; [4]Boston University, Boston, MA, USA.

Background: Roughly one in four breast cancer survivors report some degree of arm oedema. Lymphoedema is a build–up of excess lymph fluids in the tissues. Persistent lymphoedema leads to pain, diminished limb function, increased risk of infection, soft tissue fibrosis and severe cases can be grossly disfiguring. Lymphoedemous tissues contain solid and fluid phases organized on a microscopic scale that give rise to inelastic "effective" mechanical properties at the macroscale [1–6]. Elasticity imaging provides a means to image and potentially measure those properties [7].

Aims: Relate microscale properties of physiological interest, e.g., volume fraction of fluid, volume fraction of solid, tissue permeability, filtration coefficient, to macroscopically measurable properties.

Methods: We use a combination of mixture theory, homogenized models, direct numerical simulation, and phantom testing to relate microscopic properties to macroscopic properties. Mixture theories use a combination of asymptotic homogenization and variational bounds to relate macroscopic properties to microscale features. These relations give "effective" continuum models that can be used to simulate mixture deformations at the observable scale. The effective models are themselves tested against direct numerical simulations to establish the limits of their validity. Finally, the mechanical responses of two–phase phantom materials are compared to simulation.

Results: We solve benchmark forward problems. Unit cell calculations are used to extract macroscopic properties from detailed numerical simulations. Changes in porosity lead to measurable changes in the effective stiffness of phantom materials. Under favorable conditions, these properties can be reconstructed from ultrasound measured deformation fields.

Conclusions: The measured "effective stiffness" depends upon whether the tissue is drained or undrained. Ultrasound may be used to measure the effective stiffness properties. This provides the possibility of evaluating volume fractions and component properties of the individual tissue phases from ultrasound elasticity imaging.

Acknowledgements: Financial support from EPSRC and NSF via CenSSIS (Award No. EEC–9986821) is gratefully acknowledged.

References:

[1] Levick JR, An introduction to cardiovascular physiology, 4th ed. London: Arnold Publishers, 2003.
[2] Mow VC, Kuei SC, Lai WM, Armstrong CG. Biphasic creep and stress relaxation of articular cartilage in compression: theory and experiments. J Biomech Eng 1980;102:73–84.
[3] Netti PA, Baxter LT, Boucher Y, Salak R and Jain RK 1997 Macro-and microscopic fluid transport in living tissues: Application to solid tumors AIChE Journal 43(3) 818—834.
[4] M Sridhar, J Liu and M F Insana, Viscoelasticity imaging using ultrasound: parameters and error analysis, Phys. Med. Biol. 52 2425–2443, 2007.
[5] Berry GP, et al., Towards an acoustic model–based poroelastic imaging method: I. Theoretical Foundation. Ultrasound Med Biol 2006a;32:547–567.
[6] Berry GP, et al., Towards an acoustic model–based poroelastic imaging method: II. Experimental Investigation. Ultrasound Med Biol 2006b;32:1869–1885.
[7] Berry GP, et al., The Spatio–temporal strain response of oedematous and nonoedematous tissue to sustained compression *in vivo*, Ultrasound in Med. & Biol., Vol. 34, No. 4, pp. 617–629, 2008.

078 **MECHANICAL SOURCE RECONSTRUCTION.**

C. Sumi[1], S. Suekane[1].*
[1]Sophia University, 7–1, Kioicho, Chiyodaku, Tokyo 102–8554, JAPAN.

Background: We have developed various strain–measurement based shear modulus reconstruction methods, e.g., 1–dimensional [1] and multidimensional (2D and 3D) [1–3] methods. For a multidimensional reconstruction, the methods described in [2,3] use a mean normal stress as an unknown, whereas the method described in [1] uses a typical Poisson's ratio. In addition, in these methods, by using an iterative solution (e.g., conjugate gradient method) with no references, a shear modulus reconstruction being dependent of the initial estimate of the iterative solution can be obtained, whereas by using a quasi–reference shear modulus (e.g., unity) instead of an absolute shear modulus, a relative shear modulus reconstruction can be achieved [4]. Both the relative reconstructions are useful when the target tissue is deeply situated (e.g., liver, heart) because no geometrical artifacts are yielded. Although all 3D reconstructions can deal with arbitrary mechanical sources (e.g., high intensity focus ultrasound (HIFU), static compressor, vibrator, heart motion, pulsation, etc.) existing outside a region of interest (ROI) (i.e., external sources), if a mechanical source exists in the ROI (i.e., an internal source), the reconstructions cannot be achieved.

Aims: In this study, we extend the reconstruction methods such that arbitrary internal mechanical sources (i.e., expressed as a static or dynamic pressure or a force vector) can be reconstructed together with the shear modulus. However, because in 1D and 2D reconstructions, both the internal and external mechanical sources will affect the shear modulus and source reconstructions as in solo shear modulus reconstruction [1–3] due to the low dimensionalities, we also evaluate the effects of the mechanical source conditions (size, intensity, frequency etc.) on such low dimensional reconstructions.

Methods: Basically, dynamic deformation cases are dealt with. As mechanical source models, static or dynamic pressure or force vector can be dealt with together with the original unknowns (e.g., shear modulus, density, mean normal stress). However, for 3D reconstructions, the number of unknowns in equations cannot be larger than three. Thus, if necessary, a typical density will be used, or more equations will be obtained by assuming that the mechanical source is stationary or using a same mechanical source. For the methods described in [2,3], the mechanical source can be considered together with a mean normal stress or an inertia by combining them by an unknown. A tissue phantom (e.g., 50 mm side cube) and mechanical sources are simulated using successive–over–relaxation method. For instance, a spherical source (5 mm dia.) that partially overlaps a spherical region having a different shear modulus from that of the surrounding region (e.g., 2 vs 1 x 10^5 N/m^2) is used. As mechanical sources, (i) a pressure, p, (ii) a force component in a depth direction and (iii) a 3D force vector are dealt with.

Results: For 3D reconstructions, shear modulus can be accurately reconstructed together with combined or non–combined internal mechanical sources. In 1D and 2D reconstructions, the use of a small mechanical source yields smaller shear modulus values than the original. After the solo shear modulus reconstructions using external sources [1–3], internal sources can also be reconstructed using the strain tensor data.

Conclusions: We succeeded in the shear modulus and mechanical source reconstructions. The reconstruction of the mechanical source can also be used as an estimate of the point spread function for designing US beamformer for US imaging, controlling tissue deformation (i.e., elasticity imaging) and HIFU treatment [5,6]. For 1D and 2D reconstructions, mechanical sources should be large.

We should also mention the case where the reconstruction target is a stress tensor [5]. As described above, mean normal stress can be reconstructed. Hydrostatic pressure in fluid can also be reconstructed together with fluid parameters in the same manner. Thus, other stress tensor components can be evaluated using the reconstructed mechanical properties and mean normal stress or hydrostatic pressure together with the measured deformations. Viscous shear modulus reconstruction can also be performed.

References:

[1] C. Sumi et al., IEEE Trans UFFC, 52, 1670, 2005.
[2] C. Sumi et al., IEEE Trans UFFC, 53, 2416, 2006.
[3] C. Sumi et al., IEEE Trans UFFC, 54, 2394, 2007.
[4] C. Sumi et al., Acoustical Imaging, 29, 2007 (in press).
[5] C. Sumi et al., Jpn J Appl Phys, vol. 47(5B), 4137, 2008.
[6] C. Sumi et al., IEEE 2007 Int Ultason symp, 1557, 2007.

089 **SIMULATED INDENTATION OF POROELASTIC TISSUE AFFECTED BY LYMPHOEDEMA.**

Gearóid P Berry[1], Jeffrey C Bamber[1], Paul E Barbone[2].*
[1]Institute of Cancer Research, Sutton, Surrey, SM2 5NG, England, UK; [2]Boston University, Boston, MA, 02215, USA.

Background: When tissue affected by lymphoedema is gently squeezed, a temporary 'pit' or depression may form on the tissue surface which refills gradually once the applied pressure is removed. In a previous clinical study, we suggested that the occurrence of 'pitting' demonstrates that the tissue has experienced a compressive volumetric strain [1]. Via poroelastic theory, this requires that compression–induced flow of interstitial fluid away from the site of the compression must have occurred. Our long term goal is to better understand how this flow affects the local strain field so that elastographic strain imaging can be used to obtain diagnostically–useful images of quantities related to fluid mobility. However, so far, our simulation work has employed models in which the entire upper model surface is compressed. While appropriate for laboratory experiments in phantom materials, this arrangement differs from the indentation approach that is always used in a clinical situation with living tissue. The fluid flow patterns provoked are likely to differ substantially between these cases. As such, it is now appropriate to generalize these models to account for this more clinically realistic form of mechanical stimulation.

Aims: The aim of this paper is to use finite element simulation to further develop our understanding of the strain field response of lymphoedematous tissue to an applied surface pressure, by developing more realistic models capable of simulating tissue indentation.

Methods: Commercial Finite Element Modeling (FEM) software (Marc/Mentat 2007r1, MSC Software Corp, Palo Alto, CA, USA) was used to construct a cubic, homogenous, poroelastic model that was intended to represent, to a first approximation, an extended block of tissue affected by lymphoedema. The model edges were hermetically sealed, preventing the pore fluid from escaping. However, the fluid was free to redistribute inside the model as dictated by mechanically–induced fluid pressure gradients. The tissue was indented from above by any one of a set of rigid planar plates of circular cross–section. Five different plates were used with radii, r, ranging from 10–100 mm. Frictionless boundary conditions were imposed between the indentors and the model. Once applied, the indentation was sustained and the behavior of the induced strain field was predicted as a function of time.

Results: Immediately after the indentation is applied, the region directly beneath the indentor experiences a large compressive volumetric strain, yet the volumetric strain in other regions of the model is largely unaffected. As the indentation is sustained, compressive volumetric strain gradually sweeps through much of the model from the indentor towards the model peripheries. At the same time, regions very near the model peripheries experience volumetric expansion. Eventually, equilibrium is reached and no further changes occur. The time–constant of the tissue relaxation is seen to vary strongly with indentor size and shows a dependence on the square of the indentor radius (r^2). The larger the indentor, the longer the time taken to reach equilibrium. When the indentor is instantaneously withdrawn, the deep pit that is seen on the model surface gradually refills, and the volumetric strain everywhere in the model returns to zero. Poroelastic theory requires that changes in local volumetric strain must be accompanied by local fluid flow, so the volumetric strain patterns predicted by the simulation suggest that the indentation causes fluid to flow away from the site of the compression and towards the model boundaries. The r^2 dependence of the relaxation time further supports this hypothesis.

Conclusions: Predictions have been made describing the spatio–temporal behavior of the strain field during the indentation of a fluid–rich porous elastic material. The strain patterns were found to differ substantially from previous predictions where compression rather than indentation was used. This differing strain behavior indicates that the nature of the fluid flow induced in a clinical situation is more complex than previously thought. In the future, the results of this investigation will be used to help interpret the strain behavior in lymphoedematous tissue, potentially enabling the movement of interstitial fluid to be measured and mapped internally. As enhanced interstitial fluid mobility is a symptom of the presence of lymphoedema, the diagnostic applications are clear. Furthermore, the study demonstrates for the first time that pitting is a consequence of indentation–induced fluid flow, confirming frequent (but until now largely unsubstantiated) claims to this effect throughout the literature.

Acknowledgements: This work was funded by the EPSRC. PE Barbone gratefully acknowledges support from NSF.

References:

[1] Berry et al. The spatio–temporal strain response of oedematous and non–oedematous tissue to sustained compression *in vivo*. UMB 2008;34(4):617–629.

094 **TWO–DIMENSIONAL SHEAR WAVE SPEED AND CRAWLING WAVE SPEED RECOVERIES FROM *IN VITRO* PROSTATE DATA.**

Ashley Thomas[1], Joyce R. McLaughlin[1], Kui Lin[1].*
[1]Rensselaer Polytechnic Institute, Troy, NY, USA.

Background: The crawling wave experiment [1] creates a moving interference pattern from two sources oscillating at different but nearby frequencies. The crawling wave speed is a nonlinear multiple of the shear wave speed. Still, in data obtained using a phantom, imaging a known multiple of the crawling wave speed using the Arrival Time Algorithm [2] appeared to be a good estimator of the shear wave speed. However, examples can be exhibited that show the crawling wave speed can have high–speed artifacts. These artifacts are directly related to the nonlinear proportionality factor, which depends on the angle between the gradients of the phases of the two underlying, and interfering, shear waves.

Aims: The aim is to establish a fast, robust, finite–difference based algorithm and create shear wave speed images whose high–speed regions are consistent with cancerous regions identified by pathology. Data sets are obtained from the crawling wave experiment with two line sources.

Methods: The algorithm has the following steps:

(1) filter the crawling wave movie data and retain an interference pattern wave moving in one direction across the image plane;
(2) determine the crawling wave phase for the filtered interference pattern using L^1 optimization with physics–inspired constraints;
(3) using an averaging method to control the variance of the noise when taking derivatives of noisy data, [3], compute crawling wave phase wave speed;
(4) solve a first–order PDE for the phase of the shear wave emanating from one of the sources, enforcing continuity constraints;

and (5) again employ an averaging method to control the variance of the noise when taking derivatives of noisy data, as in step (3), to compute shear wave speed.

Results: We have successfully reconstructed images of both the crawling wave speed and the shear wave speed from *in vitro* prostate data. Comparison with the histology results shows that our recoveries have identified the position of the cancerous tissue. The shear wave speed images have fewer artifacts than the crawling wave speed images.

Conclusions: We have developed robust numerical solvers for shear wave and crawling wave speed recoveries from *in vitro* prostate data, which allow us to image shear stiffness, with high–speed regions coincident with cancerous regions identify by pathology, with data from the crawling wave experiment.

Acknowledgements: We acknowledge NIH, ONR, and NPSC for partial support of this work. This work was performed at IPRPI, the Inverse Problem Center at Rensselaer Polytechnic Institute, using data collected at the Rochester Center for Biomedical Ultrasound.

References:

[1] Z. Wu, D. J. Rubens, and K. J. Parker, "Sonoelastographic imaging of interference patterns for estimation of the shear velocity distribution in biomaterials," J. Acoust. Soc. Am. 120, 535–545, 2006.
[2] J. McLaughlin, D. Renzi, K. Parker and Z. Wu, "Shear wave speed recovery using moving interference patterns obtained in sonoelastography experiments," J. Acoust. Soc. Am. 121 (4), 2438–2446, 2007.
[3] R. S. Anderssen and M. Hegland, "For numerical differentiation, dimensionality can be a blessing!" Math. Comput. 68 (227), 1121–1141, 1999.

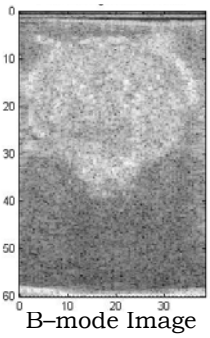
B–mode Image

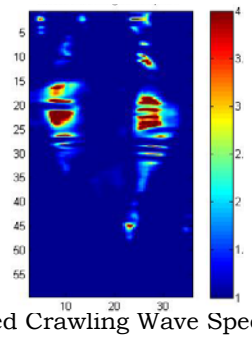
Scaled Crawling Wave Speed

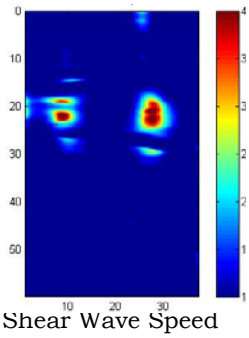
Shear Wave Speed


Histology

052 **ELASTIC MODULUS RECONSTRUCTION USING A NOVEL FAST FINITE ELEMENT MODEL.**

Iman Khalaji[1], Kaamran Rahemifar[2], Abbas Samani[1].*
[1]University of Western Ontario, London, Ontario, CANADA; [2]Ryerson University, Toronto, Ontario, CANADA.

Background: Ultrasound (US) elastograms are known to have artifacts due to the stress uniformity assumption used in strain imaging. To eliminate such artifacts, elastic modulus reconstruction techniques based on inverse problems have been developed. While accurate, such techniques are computer time demanding. This drawback would deprive US elastography from its attractive real–time feature. As an attempt to address this drawback, we introduce a novel elastography reconstruction technique. This technique is based on an accelerated finite element method (FEM) we have recently developed [1]. While sufficiently accurate, this technique preserves the attractive real–time feature.

Aims: To assess the accuracy and speed of a novel elastography reconstruction technique using a phantom study.

Methods: The proposed technique is based on the iterative reconstruction technique developed by Samani et al. [2] where the elastic modulus (E) is iteratively updated using Hooke's law in conjunction with the stress field calculated from FE analysis. To accelerate this technique, we have made two modifications: limiting the number of iterations to one and using a novel accelerated FEM. The novel FEM is based on the Statistical Shape Model (SSM) concept [3] where every shape, X, in a class of objects can be represented by the summation of the mean shape X_{mean} and a linear combination of main modes of variability P, i.e., $X = X_{mean} + Pb$. In our technique, the same concept is used in finding tissue deformation. This means that for the same class of objects, similar boundary conditions and constitutive model, the displacement field, U, can be obtained by summing the mean displacement field of the object class, U_{mean}, and a linear combination of the displacements' principal modes Q, i.e., $U = U_{mean} + Qc$. In this equation, c and Q are a weight factor vector and the displacements principal modes, respectively. The latter fields can be obtained by performing conventional FE analysis on a sufficient number of objects in the class. For a new object not included in the class, b can be obtained easily. To find U corresponding to this object, only c needs to be determined. To establish a relationship between the shape space and Finite Element space, we employed a four–layer feed–forward back–propagation neural network (NN) that outputs c for any new shape. To demonstrate this reconstruction method, we used a numerical prostate phantom, which has a stiff inclusion with an inclusion to background modulus ratio of 5.

Results: Analysis of the phantom was conducted using ABAQUS to obtain the simulated strain field. A class of 1000 prostate shapes was generated numerically by combining trigonometric functions with random amplitudes with an ellipse. The shapes were first trained and an NN relationship between b and c was obtained. For the prostate phantom (without the inclusion), b then c were calculated. Using c, U and then the stresses were calculated and combined with the simulated strains to obtain the modulus image. This reconstruction took only ~0.07 sec and compared to the strain image, the obtained image has fewer artifacts and a higher contrast such that the modulus ratio was 3.5 compared to the correct value of 5.

Conclusions: The results demonstrate the feasibility of using the novel accelerated FE technique in conjunction with Hooke's law for modulus reconstruction. Although homogeneity assumption of tissue is not correct, it shows better results compared to strain imaging, and it is almost real–time. Given the limited shape variability of organs, this approach can be applied successfully in clinical applications.

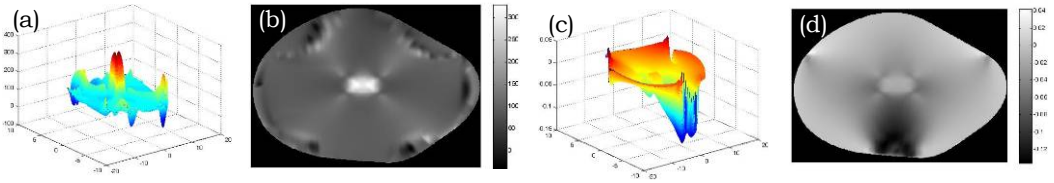

Figure 1: (a) Modulus (E) reconstruction by the proposed method; (b) Modulus (E) image; (c) εyy calculated by ABAQUS; (d) strain image.

Acknowledgements: The authors wish to thank NSERC for supporting of this research.

References:

[1] I. Khalaji, K. Rahemifar and A. Samani, "Statistical finite element model," 30th International IEEE EMBS Conference, pp.5577–5580, 2008.
[2] A. Samani et al "A constrained modulus reconstruction technique for breast cancer assessment," IEEE–TMI, 20(9): 877–885, 2001.
[3] T. F. Cootes et al, Computer Vision and Image Understanding, 61(1): 38–59, 1995.

* *indicates Presenter*

054 **MEASUREMENT OF TISSUE ELASTICITY USING LONGITUDINAL WAVES.**
A Baghani, H Eskandari, T Salcudean, R Rohling.*
University of British Columbia, Vancouver, BC, CANADA.

Background: Longitudinal wave excitation is precluded from elastography studies on the grounds of its high speed of propagation and low amplitude [1].

Aims: The aim of this study is to show, that in objects with finite dimensions, longitudinal waves propagate much slower than in infinite media. Their speed is comparable to the speed of shear waves in infinite media. At this speed, the longitudinal waves could also be tracked using ultrasound imaging systems, and elastograms formed from excitation by longitudinal waves.

Methods: Rectangular phantom blocks of different stiffness values are fabricated and their Young's modulus determined by conventional rheometry methods which are based on force–displacement behavior. The same blocks are then dynamically compressed between the plates of our elastography device (Figure 1), while being imaged by an ultrasound imaging system [2]. Axial displacements are obtained by correlation based speckle tracking [3]. The standing wave patterns are then compared with a longitudinal wave propagation model (Figure 2). By fitting this model to the experimental data, the Young's modulus is determined.

Results: The values of the Young's modulus, obtained by fitting the longitudinal wave model, matches those obtained from conventional rheometry for different test phantoms. This proves the validity of the longitudinal wave model.

Conclusions: Longitudinal waves behave differently in infinite media as compared to finite media. Finite media are free to expand on its boundaries. Therefore, a finite block of an incompressible solid has an effective stiffness significantly lower than an infinite medium of the same material. As a result, longitudinal waves propagate much slower in tissue than the ultrasound, and, in fact, could be tracked using the ultrasound itself. This proves their potential for elastography studies, in conjunction with shear waves.

Acknowledgements: This research is supported by NSERC.

References:

[1] L. Sandrin, D. Cassereau, and M. Fink, "The role of the coupling term in transient elastography," Journal of Acoustic Society of America, vol. 115, no. 1, pp. 73–83, January 2004.
[2] Hani Eskandari, Septimiu E. Salcudean, R. Rohling, "Viscoelastic parameter estimation based on spectral analysis," IEEE Trans. on Ultrasonics, Ferroelectrics and Frequency Control, 2008, to be published in July.
[3] R. Zahiri and S. Salcudean, "Motion estimation in ultrasound images using time-domain cross–correlation with prior estimates," IEEE Transactions on Biomedical Engineering, vol. 53, no. 10, pp. 1990–2000, 2006.

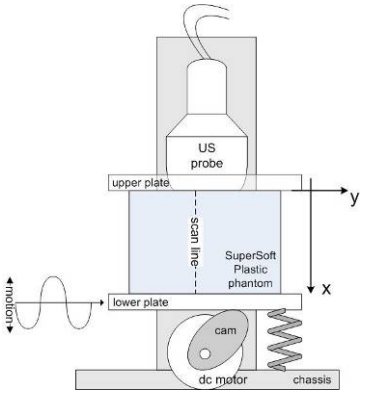

Figure 1: Schematic of the elastography device used

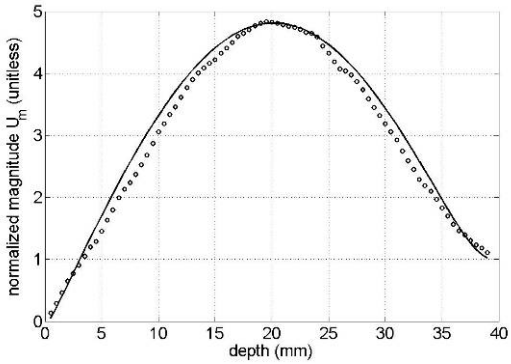

Figure 2: The measured data and the fitted model

017 **KRAMERS–KRONIG BASED QUALITY FACTOR FOR WAVE PROPAGATION IN TISSUE.**

Matthew W. Urban[1], James F. Greenleaf[1].*
[1]Mayo Clinic College of Medicine, Rochester, MN, USA.

Background: Wave propagation methods are used in elasticity imaging to evaluate the viscoelastic properties of soft tissue. The wave speed is measured, and a model is used to find the material properties. Several limitations, such as system noise, low motion amplitude and physiological or external patient motion, can affect the accuracy of the speed measurements and the material property estimates.

Aims: Assessing the quality of material property estimates is important for disease diagnosis and treatment decisions. We propose a quality factor for wave speed measurements based on Kramers–Kronig relationships.

Methods: The wave number for viscoelastic materials is a complex quantity. If it is assumed that the measurements are causal and linear, then the phase velocity and attenuation of propagating waves can be related using Kramers–Kronig (KK) relationships [1]. These relationships dictate that if the dispersive attenuation can be measured, then the phase velocity can be predicted and vice versa. This is useful because one independently measured parameter can be used to check another. Theory developed by Szabo and Wu [1] was used to assess whether shear wave attenuation values calculated from the Voigt model would yield valid predictions of wave speed when the KK relationships were used. In Shearwave Dispersion Ultrasound Vibrometry (SDUV) repeated tonebursts of ultrasound are used to create shear waves that have information at harmonic frequencies of the repetition rate of the tonebursts. The shear wave phase is measured at different positions at multiple frequencies to calculate the shear wave speed. The dispersive speed is fit to the Voigt model to extract the shear elasticity, μ_1, and shear viscosity, μ_2. An experiment using SDUV was performed on porcine muscle tissue embedded in a gelatin phantom. Shear wave speed measurements were made along and across the muscle fibers. The dispersive attenuation was measured using the motion amplitude, and the wave speed was measured using the motion phase. The shear wave attenuation values were used to predict the shear wave speed with the KK relationships, and the quality of the data was assessed based on how the measurements agreed with the predictions.

Results: The simulated shear wave attenuation in Figure 1(a) was used to successfully predict simulated values of shear wave speed using the Voigt model as shown in Figure 1(b). The predictions matched the true values very well. The KK relationships were used with the shear wave data obtained in porcine muscle. The attenuation was used to find shear wave speed predictions. These predictions were used to identify potential data points that skewed the viscoelastic property estimates. The point at 700 Hz in Figure 1(c) for the across fibers measurements would be excluded as a result of the data quality analysis.

Conclusions: The fundamental KK relationships provide a basis to assess the quality of shear wave data obtained in soft tissue. Experimental data outliers can be identified and excluded to improve the accuracy of viscoelastic estimates in tissue. Application specific quality factors could be devised and reported with each measurement to assess the quality and accuracy of a measurement.

Acknowledgements: This work was supported in part by grant EB002167 from the National Institutes of Health.

References:

[1] T. L. Szabo and J. R. Wu, "A model for longitudinal and shear wave propagation in viscoelastic media," *J. Acoust. Soc. Am.,* vol. 107, pp. 2437–2446, May 2000.

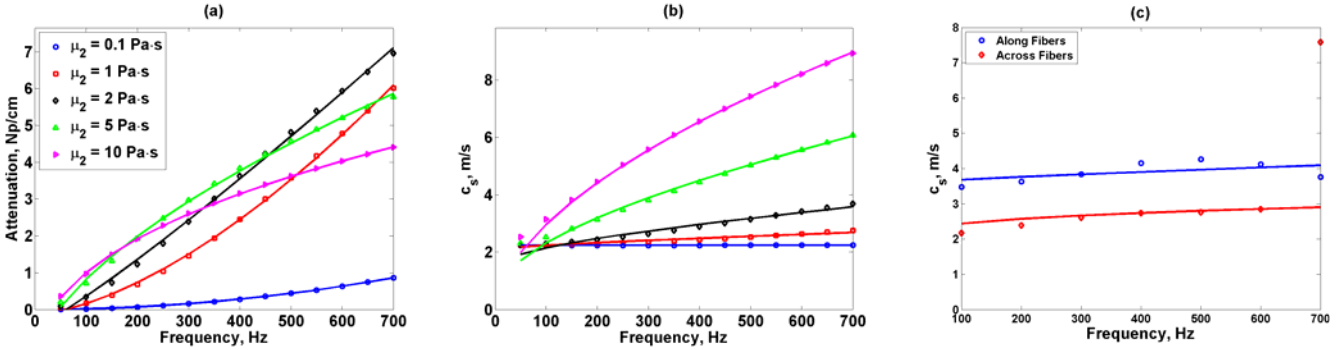

Figure 1: (a) Simulated attenuation (open symbols) and power law fits (solid lines) for μ_1 = 5.0 kPa and different values of μ_2. (b) Simulated wave speed (open symbols) and KK predictions (solid lines) for data in (a). (c) Wave speed prediction from attenuation using KK (solid lines). Experimental wave speed data in porcine muscle (open symbols) along and across the muscle fibers.

* *indicates Presenter*

014 **COMPARISON OF TWO METHODS FOR THE GENERATION OF SPATIALLY MODULATED ULTRASOUND RADIATION FORCES.**

E Elegbe[1,2], SA McAleavey[1,2].*
[1]Biomedical Engineering Department; [2]Rochester Center for Biomedical Ultrasound, University of Rochester, Rochester, NY, 14627, USA.

Background: The Spatially Modulated Ultrasound Radiation Force (SMURF) method is a technique for estimating the shear modulus of an elastic material. SMURF determines shear modulus through measurement of the frequency of shear waves of known wavelength propagating in a medium of unknown modulus. Shear modulus is then computed using the relationship $G=\rho(\lambda f)^2$.

The shear waves employed are generated by the application of an acoustic radiation force impulse of spatially varying magnitude. The spatial frequency, k, of the force variation is equal to the desired spatial frequency of the shear wave, that is, $k=2\pi/\lambda$. Because acoustic radiation force is proportional to intensity, generation of this spatially varying force is a matter of determining how to generate an equivalently varying ultrasound intensity field.

Aims: This work compares the efficacy of two methods used in creating a particular beam intensity pattern within a region of interest: the Focal Fraunhofer (FF) and Intersecting Plane wave (IP) methods [1]. This comparison is made in terms of the intensity that can be generated in the region of interest by a transducer of limited per–element power. Parameters, such as the focal depth, the width of the area of interest and the number of elements employed by each method, are compared. The widths of the beams at the transducer act as an indication of the number of elements that are employed in the beam formation process and are, thus, indicators of the ultrasound intensity that may be applied. As a result of the trade–offs associated with both techniques, we can determine a threshold that makes it easier to choose between the methods given a specific desired spatial intensity pattern.

Methods: Both methods of beam formation were simulated using Field II [2] for tissue attenuation values of 0 and 0.7dB/cm/MHz. The linear array transducer simulated in Field was similar to the Siemens VF7–3 array used in the water tank experiments. A center frequency of 5.33 MHz was used. A Siemens Antares scanner was programmed to generate the two spatially modulated beam patterns. A hydrophone (ONDA_HNV_0200 model) was mounted on a computer controlled three axis–positioner (Newport Universal Motion Controller/Driver Model ESP300) and was also connected to a pre–amplifier (ONDA AH-2020) which was in turn connected to a digital oscilloscope (LeCroy 6050A 500MHz). The ultrasound scanner and the hydrophone were properly aligned inside a water tank using a coordinate transformation matrix. The scanner continuously sent a push beam that is 10 cycles long. The three–axis positioner moved the hydrophone within the water tank in controlled increments over a desired grid of points so as to measure peak intensity values throughout the field in front of the transducer.

Results: In the FF method**,** if the desired area of focus is wide, the widths of the beams at the transducer need to be narrow. This implies that fewer elements will be employed. However, by reducing the number of elements being employed, the energy at the focus decreases accordingly. This is in contrast with the IP method where the wider ROI, the wider the apodization beams at the aperture and, thus, greater energy at the focus. The results indicate that the Intersecting Plane wave method is the more effective method except for the cases where the ROI has a width less than 4mm located at focal depths greater than 1cm.

Conclusions: To determine the shear modulus of a region of interest within tissue, the FF and IP methods of creating spatially varying ultrasound radiation forces have been developed. Due to the transducer's limited per–element power, the efficacy of both methods are compared based on the number of elements employed, and, thus, the energy generated at the ROI, for different parameters such as the focal depth and the width of the ROI. In general, the Intersecting Plane wave method seems to be more effective, especially for wider pushing regions.

Reference:

[1] McAleavey, S.A., M. Menon, et al. (2007). "Shear–modulus estimation by application of Spatially Modulated impulsive acoustic radiation force." Ultrasonic Imaging, 29(2): 87–104.
[2] Jensen, J. A. and N. B. Svendsen (1992). "Calculation of pressure fields from arbitrarily shaped, apodized, and excited ultrasound transducers." IEEE Transactions on Ultrasonics Ferroelectrics and Frequency Control 39(2): 6.

058 **PULSED MAGNETO–MOTIVE ULTRASOUND TO ASSESS VISCOELASTIC PROPERTIES OF SOFT TISSUES.**

M. Mehrmohammadi[1], S. R. Aglyamov[1], A. B. Karpiouk[1], J. Oh[1], S. Emelianov[1].*
[1]Biomedical Engineering Department, The University of Texas at Austin, Austin, TX, USA.

Background: Pulsed magneto–motive ultrasound (PMMUS) is an ultrasound imaging technique capable of detecting magnetic nanoparticles in tissues. Once the nanoparticles are delivered to tissue, an externally applied pulsed magnetic field is used to induce tissue motion detected by an ultrasound imaging system. However, the induced motion will depend on the viscoelastic properties of tissue. Therefore, the PMMUS system can be used to acquire the mechanical properties of tissue.

Aims: The goal of this study was to investigate the applicability of pulsed magneto–motive ultrasound to assess the viscoelastic properties of tissues labeled with magnetic nanoparticles.

Methods: The experiments were first performed using rigid metal spheres of various diameters and densities. The spheres were embedded into phantoms made out of gelatin (Type A, Sigma–Aldrich, Inc., St. Louis, MO, USA). Several concentrations of gelatin ranging from 3–6% (by weight) were used. The magnetic field was generated using a pulsed magnetic source (MPG5, SOTA, Inc., Penticton, BC, Canada) that supplied the current to a solenoid (Ledex 6EC, Saia–Burgess, Inc., Fort Worth, TX, USA). The solenoid consisted of an iron core to focus the magnetic field within the region of interest. Magnetic flux density measurements were performed using a Gauessmeter (DSP 475, Lakeshore, Inc., Westerville, OH, USA). The magnetic force was assumed to have the same temporal profile as the magnetic flux density squared. To measure the internal tissue motion, an ultrasound imaging system was constructed based on 25 MHz mechanically scanned single element focused ultrasound transducer (F#=2) interfaced with an ultrasound pulser/receiver (5073PR, Panametrics, Inc., Waltham, MA, USA) operating at 5–10 kHz pulse repetition frequency. The ultrasound signals were acquired using a 12 bit, 100 MS/s data acquisition card (Gage Applied, Inc., Lockport, IL, USA). The displacements were computed using cross–correlation approach. To further demonstrate the capability of PMMUS system to assess the viscoelastic properties of tissue, experiments were performed using tissue–mimicking phantoms with iron–laden inclusions. Specifically, the 5% polyvinyl alcohol (PVA) inclusions contained different concentrations of various magnetic nanoparticles, including carbon coated 20 nm diameter cobalt and nickel nanoparticles.

Results: Our studies clearly demonstrate that the displacements of the spheres/magnetic inclusions are inversely–proportional to the elasticity of the surrounding medium. Under short pulse excitation, the displacement amplitude and the time needed for the displacement to reach its peak can describe the mechanical properties of medium. Generally, the time characteristics of the induced motion depend on the time profile of the magnetic excitation force but are independent of the force amplitude.

Conclusions: The characteristics of the magnetically induced motion in iron–laden tissues are related to the elastic properties of the surrounding medium. Our studies suggest that the PMMUS system, capable of detecting the magnetically induced motion, can be used to assess the viscoelastic properties of the soft tissue.

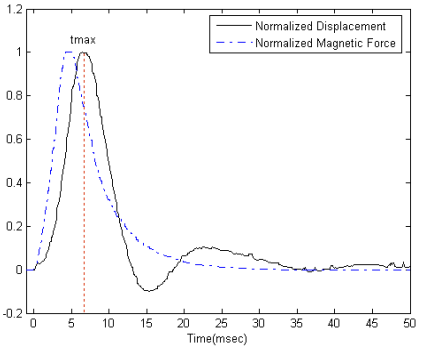

Figure 1: Temporal behavior of the displacement of a metal sphere in response to pulsed magnetic force. The 3.175 mm diameter sphere was embedded into 3% gelatin medium.

Acknowledgements: This work was supported in part by National Institutes of Health under grants EB 008821, EY 018081 and EB 008101.

References:

[1] S.R Aglyamov, et al., "Acoustic radiation force initiated motion of a solid sphere embedded in a viscoelastic medium: theoretical analysis and experimental verification," Journal of the Acoustical Society of America, 122(4), 1927–1936, 2007.
[2] M. Mehrmohammadi, et al., "Pulsed magneto–motive ultrasound imaging", Proc. 25th Ann. Hou. Conf. on Biomed. Eng. Res., The Hou. Soc. for Eng. in Med. and Bio., Houston, TX, p. 75, Feb., 2008.

* *indicates Presenter*

069 **METHODS FOR 2D SUB–SAMPLE MOTION ESTIMATION IN ULTRASOUND ECHO SIGNALS.**

R. Zahiri–Azar[1], T.S. Yao[1], S.E. Salcudean[1].*
[1]The University of British Columbia, Vancouver, BC, CANADA.

Background: Pattern matching functions (such as normalized correlation) in conjunction with sub–sample estimation techniques (such as cosine fit) are the most widely used techniques in estimating tissue motion in sequences of ultrasound echo signals. The extension of pattern matching functions to 2D is not difficult; however, the extension of sub–sample estimation techniques to 2D has received relatively little attention. Currently, the previously introduced 1D techniques are used independently in each direction to estimate the sub–sample motion in the same direction. However, this technique is only accurate if the 2D pattern matching function presents some symmetry.

Aims: To introduce interpolation techniques suitable for 2D sub–sample motion estimation.

Methods: Iterative 1D fit and 2D polynomial fit are investigated in this work as new estimation approaches in order to estimate the sub–sample motion from the 2D cross–correlation function, which is quantized on a 2D grid. In the first approach, the 2D sub–sample motion estimation is carried out by first implementing a 1D interpolation in one direction. New correlation coefficients are then interpolated at the estimated location. Utilizing these new coefficients, the sub–sample motion in the second direction is then estimated by using the second 1D fit. Further iterations of this approach showed improvements to the estimations. For the purpose of this work, cosine fit is employed for iterative 1D fit. In the second approach, a 2D polynomial is fitted to the discrete 2D cross–correlation function. The 2D sub–sample motion estimations are then simultaneously estimated by analytically finding the maximum of the fitted polynomial $f(x,y)= a + bx+ cy + dxy+ ex^2+ fy^2 + gxy^2+ hx^2y + ix^2y^2$. For the purpose of this work, Newton's algorithm is used to find this maximum.

Results: Simulations using the Field II ultrasound simulation software and experiments using a SonixRP ultrasound machine (Ultrasonix Med. Corp., Richmond, BC, Canada) were performed to acquire RF frames from a linear probe corresponding to a 2D grid of sub–sample motions. The estimators were then used to estimate the 2D motions from corresponding RF frames. The performance of each estimator was considered in terms of its bias and standard deviation as a function of sub–sample shift in both axial and lateral directions. Results from both simulations and experiments showed that the proposed iterative 1D method significantly outperformed the independent 1D fit method. The axial and the lateral biases of the proposed iterative method were measured to be less than 1µm and 5µm, respectively, in both the simulated and the experimental data as opposed to 1µm and 25µm for independent 1D interpolation.

Conclusions: The proposed methods significantly outperform current methods in estimating 2D motion.

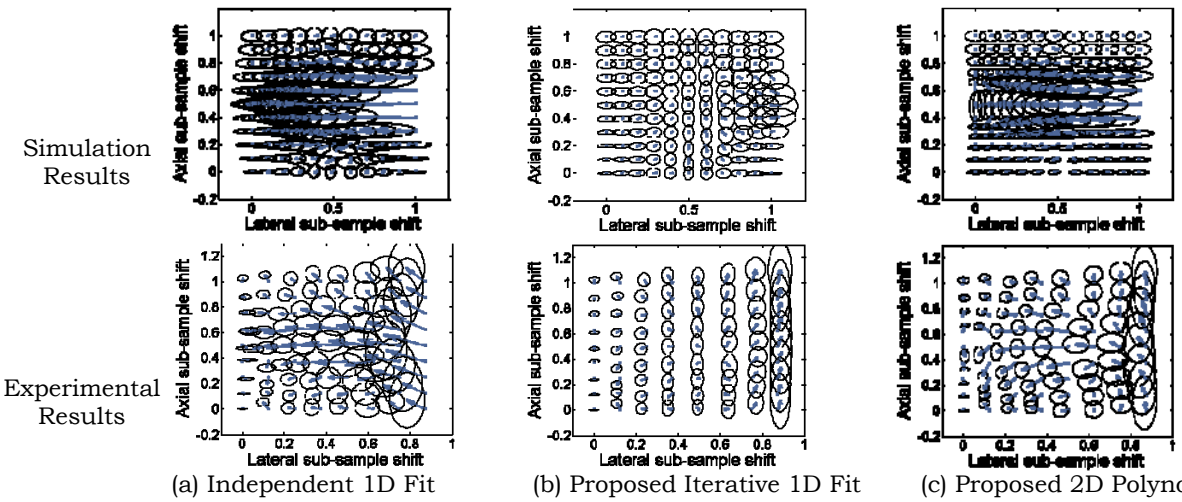

(a) Independent 1D Fit (b) Proposed Iterative 1D Fit (c) Proposed 2D Polynomial Fit

Figure 1: The bias vectors and standard deviation ellipses are shown for different interpolation techniques on an 11×11 simulated grid (Simulation Results) and a 9×8 grid captured from an ultrasound machine (Experimental Results). Smaller vectors correspond to smaller biases and smaller ellipses correspond to smaller standard deviation in estimating the motion in both the axial and lateral directions. For better visualization, the axes of ellipses for experimental data are scaled by half. A total of 1000 realizations were used to generate each bias vector with its corresponding standard deviation ellipse. (Fs = 40MHz, Fe = 5MHz, B = 0.5, W = 1mm × 1mm, ΔW = 0%).

071 **STUDY OF THE VISCOELASTIC PROPERTIES OF NORMAL PROSTATE TISSUE USING CRAWLING WAVES: PRELIMINARY RESULTS.**

Benjamin Castañeda[1], Kenneth Hoyt[2], Timothy Kneezel[1], Shuang Wu[1], John Strang[3], Deborah J. Rubens[3] and Kevin J. Parker[1].*

[1]University of Rochester, 206 Hopeman Building, Rochester, NY, USA; [2]University of Alabama at Birmingham, 817 Boshell Building, 1808 7th Avenue South, Birmingham, AL,USA; [3]University of Rochester Medical Center, 601 Elmwood Ave., Rochester, NY, USA.

Background: Crawling wave (CrW) sonoelastography [1] is a technique capable of locally estimating the shear wave speed in tissue and, therefore, can provide a quantitative estimation of the Young's modulus for a given vibration frequency. It has been successfully applied to detect radiofrequency ablated hepatic lesions *in vitro* [2] and to characterize human skeletal muscle *in vivo* [3].

Aims: The objective of this study is to establish a protocol based on CrW sonoelastography to quantify the viscoelastic properties of normal prostate tissue *in vitro*.

Methods: Fifteen prostatic glands were obtained after radical prostatectomy and embedded in a 10.5% gelatin mold. Two pistons were located at each side of the mold to create shear vibration. The ultrasound transducer was positioned on top of the gelatin mold and equidistant from the vibration sources. Each gland was imaged at three positions (apex, middle gland and base) at three vibration frequencies (100, 120 and 140 Hz) with an offset of 0.25 Hz between the sources. The site for the three cross–sections was marked, and the corresponding histological slices were obtained. The cross–sections without any cancerous tissue were processed using a two–dimensional shear wave speed estimator [2]. The autocorrelation variance for the estimator was used as a quality metric. All the estimates which had a low variance were included in the computation of the average and standard deviation of the shear wave speed (and elasticity modulus) of the tissue.

Results: Out of the fifteen glands, only four had cross–sections without cancerous tissue. Preliminary results from these slices are shown in Table 1. These values agree with previous reports of the elasticity of normal prostate tissue based on mechanical testing [4]. Furthermore, the increase in shear wave speed estimates with vibration frequency is suggestive of a viscoelastic effect.

Conclusions: These preliminary results suggest that the protocol based on CrW sonoelastography can be adapted to estimate the viscoelastic properties of prostate tissue.

Acknowledgements: This study was partly supported by NIH grant 5 RO1 AG016317–07.

References:

[1] Zhe Wu, Kenneth Hoyt, Deborah J Rubens, Kevin J Parker, Sonoelastographic imaging of interference patterns for estimation of shear velocity distribution in biomaterials. J of the Acoust Soc of Am, Vol. 120, Iss 1, July, 2006, pp. 535–545.

[2] Kenneth Hoyt, Benjamin Castaneda, Kevin Parker, Two–dimensional sonoelastographic shear velocity imaging. J of Ultras in Med and Bio, Vol 34, Iss 2, Feb., 2008, pp. 276–288.

[3] Kenneth Hoyt, Benjamin Castaneda, Kevin J. Parker. Muscle Tissue Characterization Using Quantitative Sonoelastography: Preliminary Results. Proc of the IEEE Ultrasonics Symp, NY, 2007, pp. 365–368.

[4] Man Zhang, et al., Quantitative characterization of viscoelastic properties of human prostate correlated with histology. J of Ultras in Med, Published online 13 February 2008.

	100Hz	120Hz	140Hz
Shear Wave Speed (m/s)	1.7±1.1	1.9±1.1	2.0±1.0

Table 1: Estimated shear wave speeds for normal prostate tissue.

* *indicates Presenter*

085 **TOWARDS THREE–DIMENSIONAL ACOUSTIC RADIATION FORCE IMPULSE (ARFI) IMAGING OF HUMAN PROSTATES *IN VIVO*.**

Liang Zhai[1], Jeremy J Dahl[1], Kathy R Nightingale[1].*
[1]Biomedical Engineering Department, Duke University, Durham NC, USA.

Background: Imaging techniques capable of visualizing prostate structures and abnormalities can play an integral role in prostate cancer management. However, it has been a challenging task for current imaging modalities to reliably identify cancerous regions within the prostate. Under the guidance of transrectal ultrasound (TRUS), the false negative rates range from 25–45% based on the first time biopsy [1]. Past studies have showed that prostate cancer is stiffer than normal prostate tissues [2], which provide opportunities for elasticity imaging techniques to detect prostate lesions. Recent studies reported improved prostate cancer detection rates for elastography-guided needle biopsies [3]. Our initial *ex vivo* study has demonstrated that ARFI imaging is able to visualize the internal anatomy and suspicious lesions in the excised human prostate [4].

Aims: The objective of this study is to implement ARFI techniques on a 3D wobbler transducer (EV9F4), and evaluate its performance of guiding prostate needle biopsy.

Methods: A modified Siemens Antares™ scanner and a 3D wobbler rectal probe, EV9F4, were used for this study. The ARFI excitation pulses utilized a focal depth 20 mm, F/#2.7, center frequency 4.0 MHz and 2 × 200 cycles. 4:1 parallel receive was used to reduce the number of push locations. The intensity field was measured in water. Linear extrapolation of derated small signal values was used to estimate the *in situ* intensity, which was then compared to that of the VF10–5 linear array with settings that were used for the previously presented *ex vivo* prostate studies. ARFI images were acquired with both probes in a homogeneous tissue–mimicking phantom to compare the displacements. During 3D ARFI imaging, the internal wobbler motor was programmed using varying delays between data acquisitions. In order to evaluate motion artifacts, a heterogeneous tissue–mimicking phantom was imaged with the delay time ranging from 1s to 30s between two adjacent elevational planes. Volumetric views were computed from the inverted 3D displacement dataset. Finally, the system was tested with excised human prostate specimens.

Results: The extrapolated derated (α= 0.7dB/cm/MHz) *in situ* I_{SPPA} at the focal depth was 3216 W/cm^2, which is about 47% of that used in our *ex vivo* study with the VF10–5 linear array. The corresponding ratio of maximum displacements is 42%. No motion artifact is observed in any of the delay settings during the motion test. All 5 spherical inclusions (E = 31kPa, D = 3mm) in the heterogeneous phantom (background E = 4kPa) were clearly visualized in the volumetric views, as shown on the left. With 50 excitation locations (7cm in lateral FOV), the system can perform 3D data acquisition for an average human prostate within 3 minutes with the minimum delay setting (1s) between adjacent planes. The system generates an average displacement of 4μm within the peripheral zone in excised human prostates for structural visualization.

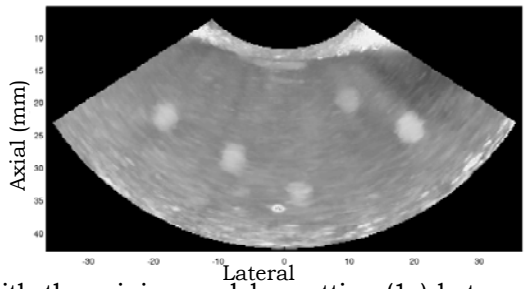

Conclusions: With fast 3D data acquisition and sufficient displacements in the peripheral zone of human prostates for structural visualization and lesion detection, the system will be adequate for imaging human prostates *in vivo*.

Acknowledgements: The authors would like to thank Dr. Gregg E. Trahey and Dr. Mark L. Palmeri for their valuable insights for this project and Siemens Medical Ultrasound for their technical support. This work is supported by NIH 1R01 CA–114075 and US ARMY Prostate Cancer Research Program (W81XWH–08–1–0132).

References:

[1] Svetec D, McCabe K, et al. "Prostate rebiopsy is a poor surrogate of treatment efficacy in localized prostate cancer", J Urol, vol 159, pp. 1606–1608, 1998.
[2] Zhang M, Nigwekar P, et al. "Quantitative characterization of viscoelastic properties of human prostate correlated with histology", Ultrasound in Med. & Biol., Vol 34, 2008.
[3] Konig K, Scheipers U, et al. " Initial experiences with real–time elastography guided biopsies of the prostate", J Urol, vol 174, pp. 15 – 117, 2005.
[4] Zhai L, Madden J, et al. "Visualizing the anatomic structures of human prostates using acoustic radiation force impulse (ARFI) imaging", Proceedings of 2007 Ultrasonics, Ferroeletrics and Frequency control Joint Symposium.

024 **1D LOCAL INVERSION FOR TRANSIENT ELASTOGRAPHY OF *IN–VIVO* HUMAN LIVER.**

Yassine Mofid[1], Cécile Bastard[1,2], Jennifer Oudry[1], Laurent Sandrin[1].*
[1]Echosens, Research and Development Department, 153 avenue d'Italie, 75013 Paris, FRANCE; [2]INSERM U930, CNRS FRE 2448, Université François Rabelais de Tours, UFR de Médecine–Bât. Vialle, 10 Boulevard Tonnellé, 37032 Tours Cedex 1, FRANCE.

Background: Current hepatic fibrosis diagnosis with the Fibroscan® transient elastography based device (Echosens, Paris, France) consists of measuring the mean velocity (V_s) of the shear wave induced in the liver by a low frequency mechanical vibration applied on the inter–costal space via an ultrasound single element transducer. The Young's modulus is then estimated ($E=3\rho V_s^2$) and is correlated to the pathological state of the liver [2]. The Fibroscan® is successfully used to characterize homogeneous fibrosis in the liver [1] and its adaptation to assess heterogeneous pathologies would be interesting.

Aims: In this study, we show the performance of the Fibroscan® to estimate the shear wave velocity as a function of depth in healthy human liver *in vivo* and its potential to be used for hepatic heterogeneous fibrosis diagnosis.

Methods: 1D local inversion is performed on data acquired with a standard Fibroscan® probe composed of a 3.5 MHz single transducer mounted on a low frequency vibrator. A 50 Hz mechanical vibration is generated with the transducer placed in the inter–costal space and the RF lines are acquired at a PRF of 6000 Hz during 80 ms.

The direct 1D inversion algorithm is applied on the axial component (ε_z) of the estimated strain field. The shear velocity is computed as the square root of the ratio between the strain's temporal and spatial second–order derivatives:

$$V_s = \sqrt{\frac{\partial^2 \varepsilon_z}{\partial t^2} \Big/ \frac{\partial^2 \varepsilon_z}{\partial z^2}}$$

Results: The algorithms are successfully validated on homogeneous and heterogeneous phantoms. The Young's modulus values in 1D estimation obtained for the liver *in vivo* on healthy volunteers were close to the mean elasticity values estimated by the Fibroscan® device (Figure 1).

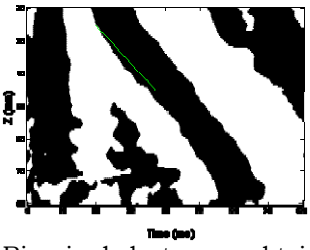

(a) Binarized elastogram obtained for a healthy human liver: the mean shear velocity is obtained geometrically by calculating the shear wave front slope ($\Delta z/\Delta t$). The Fibroscan® shows a mean elasticity value of 4 kPa.

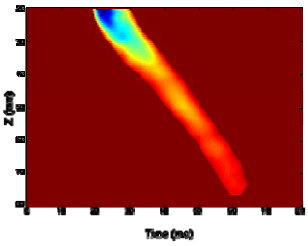

(b) Shear wave front (strain front) used to calculate second order derivatives.

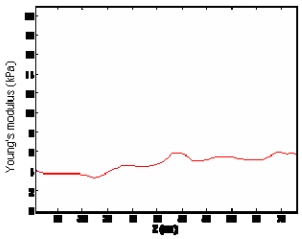

(c) Young's modulus estimation in 1D.

Figure 1: Comparison between the current Fibroscan® measurement and the 1D estimation of the shear wave velocity (or Young's modulus: $E=3\rho V_s^2$).

Conclusions: The feasibility of the use of the Fibroscan® device to measure the shear wave propagation in 1D was investigated. This simple approach presents a great potential to use this device for the characterization of heterogeneous fibrosis in human liver.

References:

[1] L. Sandrin et al., Transient elastography: a new non–invasive method for the assessment of hepatic fibrosis, Ultrasound in Medicine and Biology, Vol. 29, No.12, 2003.
[2] L. Sandrin et al., Shear elasticity probe for soft tissues with 1–D transient elastography, IEEE Trans. on ultrasonics, ferroelectrics, and frequency control, Vol. 49, No.4, April 2002.

* *indicates Presenter*

055 **FPGA–BASED REAL–TIME ULTRASOUND ELASTICITY IMAGING SYSTEM.**

Seungsoo Kim[1], Suhyun Park[1], Salavat R. Aglyamov[1], Steve Claffey[2], W. Guy Scott[2], Stanislav Y. Emelianov[1].*

[1]Biomedical Engineering Department, The University of Texas at Austin, Austin, TX, USA; [2]WinProbe Corporation, North Palm Beach, FL, USA.

Background: In ultrasound elasticity imaging, block–matching algorithms are used to estimate the displacement and, therefore, strain. One of the implementations of displacement estimator is based on 2–D cross-correlation method requiring a large number of multiplications. To efficiently implement the real–time 2–D cross–correlator, parallelized processing units are desired. Since Field Programmable Gate Arrays (FPGAs) have enormous resources compared to general purpose processors such as micro–processors and Digital Signal Processors (DSPs), implementing the real–time ultrasound elasticity imaging system in FPGAs can be a viable solution.

Aims: The main objective of our study, focused on efficient implementation of the real–time elasticity imaging system in FPGAs, was to design the hardware architecture and to optimize the process sequence.

Methods: For integer level displacement estimates, the normalized cross–correlation with a 2–D kernel and a 2–D search was used. The subvpixel level displacement was calculated by parabolic interpolation in both lateral and axial directions. The target frame rate was set to at least 30 frames per second. Also, Xilinx FPGA (XC4VSX55) having 512 MAC (Multiplication and Accumulation) units and operating at maximum 500 MHz (256G MACs/sec) was chosen for implementation of the real–time displacement estimator.

Results: Using 2–D (K_L by K_A) kernel and 2–D (S_L by S_A) search area, the normalized cross–correlation engine requiring approximately $(K_L \times K_A \times S_L \times S_A) \times 2$ multiplications per one output is needed. If one frame has ($F_L \times F_A$) samples, there are ($F_L \times F_A$)×FR outputs per second where FR is the frame rate. Therefore, overall $(K_L \times K_A \times S_L \times S_A) \times 2 \times (F_L \times F_A) \times FR$ multiplications per second are needed for real–time elasticity imaging. Using 5 by 31 kernel, 5 by 7 search range, 256 by 4096 for frame and 30 frames per second, 340 billion MAC operations per second will be needed. However, by optimizing the hardware architecture of the normalized cross–correlation engine, the impact of K_A can be removed. Therefore, MAC operations were reduced to ~11 billion per second. Furthermore, to improve the robustness and quality of the displacement estimates, two step (coarse and fine) search and autocorrelation–based error correction method can be performed. Within the given processing time for one line, 2–D cross–correlation using envelope data for coarse search is performed first, and then the radiofrequency (RF) data is used for both fine search and displacement error correction. No additional hardware resources are required because all calculations utilize the same correlation engine consecutively. Figure 1 shows the top–level architecture of real–time FPGA–based displacement and strain estimator. The designed real–time elasticity imaging approach was implemented in WinProbe system (Figure 2).

Conclusions: We have designed the real–time elasticity imaging system using the FPGA–based platform. This cross–correlation based imaging system is capable of elastographic imaging at 30 frames per second.

Acknowledgements: This work was supported by the National Institutes of Health under grant HL 091609.

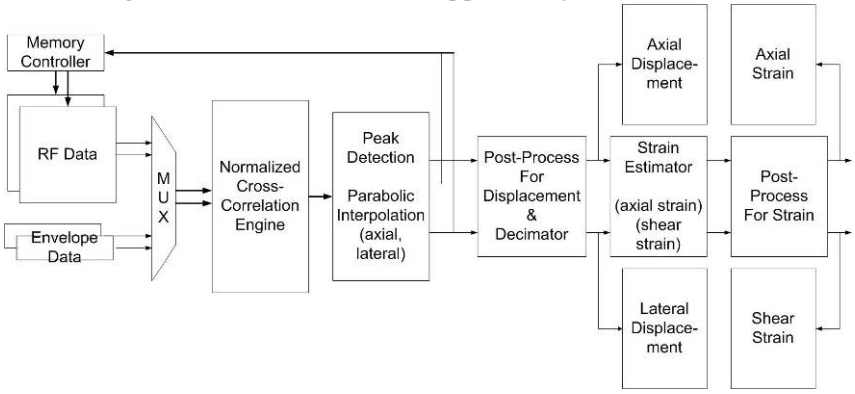

Figure 1: Top–Level Architecture.

Figure 2: WinProbe System.

Lakeway Conference Center Floor Plan

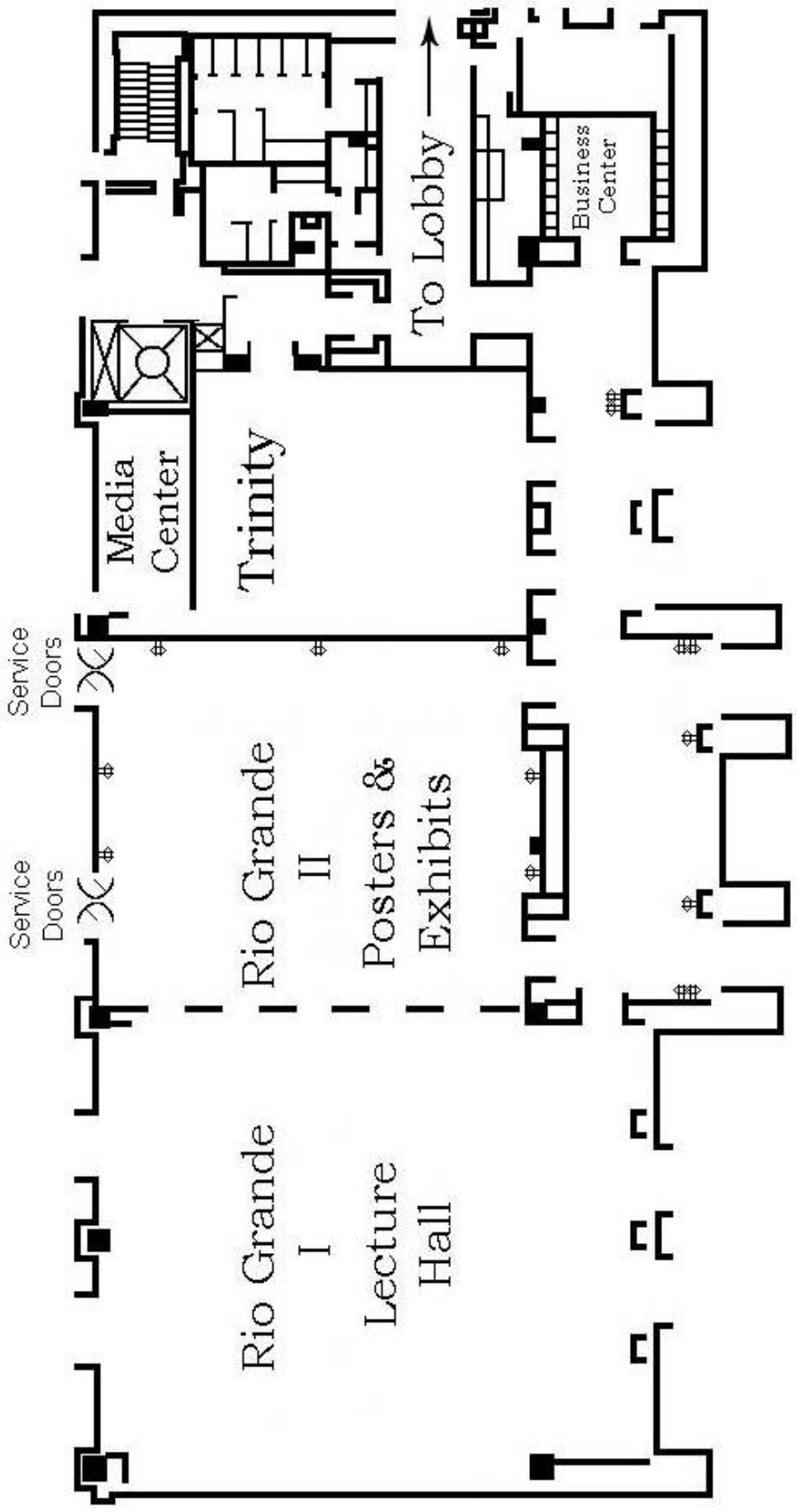

Please Fill Out Both Sides

Conference Evaluation and Questionnaire

OVERALL CONFERENCE

	Poor		Mid		Excellent
Overall Conference Evaluation	1	2	3	4	5
General comments:					

SCIENTIFIC PROGRAM

	Poor		Mid		Excellent
Quality of the Presentations	1	2	3	4	5
Relevance of Presentations to the Conference's Theme	1	2	3	4	5
Time Allotted for Presentations	1	2	3	4	5
Time Allotted for Discussion	1	2	3	4	5
Poster Session	1	2	3	4	5
Tutorials	1	2	3	4	5
Equipment Exhibit	1	2	3	4	5
Student Participation	1	2	3	4	5
Additional comments:					

CONFERENCE MATERIALS

	Poor		Mid		Excellent
Printed Proceedings Book	1	2	3	4	5
CD Proceedings	1	2	3	4	5
Other Registration Materials	1	2	3	4	5
Additional comments:					

CONFERENCE FACILITIES & SOCIAL PROGRAM

	Poor		Mid		Excellent
Lecture Hall	1	2	3	4	5
Registration Desk	1	2	3	4	5
Meals: Dining facilities	1	2	3	4	5
Conference Breakfasts and Lunches	1	2	3	4	5
Conference Dinner and Concert	1	2	3	4	5
Coffee Breaks	1	2	3	4	5
Opening Dinner Reception	1	2	3	4	5
Closing Pizza Party	1	2	3	4	5
Audio–Visual: Screen Visibility	1	2	3	4	5
Sound Level	1	2	3	4	5
Presentation Transition	1	2	3	4	5
Wireless Internet Connectivity:	1	2	3	4	5
Additional comments:					

Please Fill Out Both Sides

Conference Evaluation and Questionnaire

VENUE AND HOTEL

	Poor		Mid		Excellent
Venue – Lake Travis, Lakeway, Texas and Environs	1	2	3	4	5
Would you return to this city?	Yes		Perhaps		No
Area Attractions	1	2	3	4	5
Hotel: Overall	1	2	3	4	5
Reservations	1	2	3	4	5
Transportation and Accessibility	1	2	3	4	5
Reception and Check–In	1	2	3	4	5
Accommodations	1	2	3	4	5
Facilities	1	2	3	4	5
Parking	1	2	3	4	5
Would you return to this hotel?	Yes		Perhaps		No
Additional comments:					

CONFERENCE ADMINISTRATION

	Poor		Mid		Excellent
Website	1	2	3	4	5
Registration off–site	1	2	3	4	5
Registration on–site	1	2	3	4	5
Administrative staff	1	2	3	4	5
Correspondence	1	2	3	4	5
Additional comments:					

GENERAL INFORMATION

I am a Returning Delegate	Yes		No
I plan to attend the next conference	Yes	Perhaps	No
and present a paper(s) / poster(s)	Yes	Perhaps	No
Other(s) from my lab would attend the next conference	Yes	Perhaps	No
and he/she / they would present a paper(s) / poster(s)	Yes	Perhaps	No
How did you learn of this conference? (Check all that apply)	☐ Email Announcement		
☐ Internet	☐ Website		
☐ Other	☐ Colleague		
Tutorial Topic Suggestions for next year:			
Additional Comments:			

If you would be willing to host the Conference in your city, please give your name to the Conference Staff.

Questions or comments are welcome at any time at <elasticity.conference@uth.tmc.edu>

Thank You!